Investigation of the Incorporation of Trigonal Planar Oxyanions in Inorganic Oxide Materials

By

Joshua Deakin

Supervisors: Prof. Peter Slater &

Prof. Paul Anderson

A thesis submitted to the University of Birmingham
for the degree of Doctor of Philosophy

The School of Chemistry

College of Engineering and Physical Sciences

The University of Birmingham

31st August 2021

Abstract

The work presented in this thesis focuses on the potential incorporation of carbonate into different materials, showing how care must be given to consider its possible inclusion when synthesising materials ≤1000°C. Other oxyanion investigations are also presented for the likes of sulphate and borate.

A new layered perovskite structure was synthesised with the formula $Ba_3Yb_2O_5CO_3$. The presence of carbonate was first confirmed by Raman spectroscopy and the new structure was determined by the Rietveld refinement using Neutron diffraction data. It was then proven that this system could be extended to a range of other rare earths. Further investigation shows how this layered structure is also seen with the partial inclusion of sulphate, provided there was stabilisation from the addition of zinc.

Carbonate incorporation was also determined in the cobalt deficient $Ba_2Co_{1-x}O_{4-\delta}$ systems, where a structural change is seen from monoclinic to orthorhombic-like upon increasing the amount of deficiency. This carbonate incorporation may also be seen in the iron equivalent $Ba_2Fe_{1-x}O_{4-\delta}$ systems, whilst sulphate incorporation into these iron systems was also demonstrated leading to materials with higher thermal stability. The inclusion of carbonate/sulphate was confirmed through Raman spectroscopy and structure refinement.

Various smaller investigations into the potential carbonate incorporation of other systems are also presented, including TiO_2, and Nb_2O_5. Although not conclusive, the results suggest that carbonate could also be present at low temperature in polymorphs of these compounds.

Interesting borate systems, $Sr_{4-x}Ba_xNa(BO_3)_3$, $Sr_{4-x}Ba_xLi(BO_3)_3$, were synthesised. These systems have been previously reported, but we show for the first time here that they have perovskite-like superstructures. In these materials the borate groups are shown to provide all the oxygen atoms in the structure, illustrating the flexibility of the perovskite structure to accommodate oxyanion groups. The new $Sr_{4-x}Ba_xNa_{0.5}Li_{0.5}(BO_3)_3$ series was also prepared and whilst investigating other potential isostructural systems, a new strontium/calcium A site cation ordered $Sr_{2.2}Ca_{1.8}Li(BO_3)_3$ system was discovered.

Acknowledgements

First and foremost I would like to dedicate my work to the memory of my mother, without whom I would not be where I am, from her love, support and guidance.

I would like to thank my supervisor Peter Slater for all his help, insight and patience given to me over all my years of studies as well as all the belief he has had in my ability to complete this project. I have enjoyed my time studying with him, along with the numerous bands we have seen together over the years and many a brewery visited.

Many thanks to the rest of the Slater group past and present of which there are too many to name all personally, but I have enjoyed my time and experiences with you all. A big thank you to Abbey and Ivan in particular, for not only helping and supporting me during my PhD studies but also my Masters project. There is also much appreciation given to Mark and Bo for putting up with me for the last year and ensuring things went as smoothly as possible.

Thank you to all others who are apart of Floor 5 making it an enjoyable group to be a part of, especially Dan who has supported me a lot over the years. I would also like to thank my desk buddies Saule and Azusa for the random excursions.

I would also like to thank Evin for not only keeping the facilities up and running but also being there to listen to any of my worries and grievances as well as the weird conversations every now and then.

I would like to thank Alodia Orera and Maria Louisa Sanjuan for helping run some of the Raman studies. Also, a thank you to Alexandra Gibb and Jose Porras-Vasquez for collection the neutron diffraction.

A massive thank you to my father, brother, Jake and Matt for all their support and belief in me during my studies, and also a thank you to the rest of family and friends who have been beside me all these years.

Finally, I would like to thank the Leverhulme Trust for funding this project.

Table of Contents

1. Introduction

This project is focussed on an investigation into the potential carbonate (and other oxyanions) incorporation into mixed metal oxide materials. In the initial stages of the investigation, particular attention was paid to the potential incorporation of carbonate into materials that may be of interest for fuel cell applications, and so a background to fuel cells will now be given.

1.1 History of Fuel Cells

Sir Anthony Carlisle and William Nicholson are considered to be the first to produce a chemical reaction using electricity. This process used is in this reaction is now known as water electrolysis and is the decomposition of water into hydrogen and oxygen. Water electrolysis is the inverse reaction to that of the reaction used in hydrogen fuel cells.[1]

The idea of a fuel cell has been around since 1838 when William Grove first wrote about the development of the first crude fuel cell. Grove placed the ends of two platinum electrodes into sulphuric acid with the other ends placed into separately sealed containers of oxygen and hydrogen whilst both containers also containing water. He found that a current would flow between the electrodes and the water level would rise. By connecting several sets of these electrodes in series he was able to produce higher voltages.[2][3] Towards the end of the 19th century William Grove still did not quite fully understand the working of his findings.

Friedrich Wilhelm Ostwald experimentally determined the interconnection of the various components in the fuel cells, taking into account electrodes, electrolyte, oxidising and reducing agents, anions and cations. Through this investigation Ostwald was able to confirm the speculation of Groves that the reactions occurred at the point of contact between electrode, gas and electrolyte.[4] From this research William W. Jacques developed the first fuel cell with practical applications, and in 1900 zirconium dioxide (ZrO_2) was first used as a solid electrolyte by Walther Nernst.[5]

In 1933 Thomas Francis Bacon developed the first fuel cell for practical use combining oxygen and hydrogen through an electrochemical process to produce electricity. Subsequently he began his research into alkali fuel cells which despite their high cost, proved reliable enough to be acquired and used by Pratt and Whitney in the Apollo space missions.[4]

Following on from these events many other advances and applications have been found for fuel cells; a range of electrolyte and electrode systems have been investigated forming the many types of fuel cell systems known today. These applications range from use in mobile technology, to powering automotive vehicles, as well as other electrical appliances such as traffic signals, and finally on to large scale applications such as hospitals and police stations generating electrical power for their facilities.[4][6-9]

1.2 Differing Types of Fuel Cell

All fuel cells consist of two electrodes; a cathode and anode, and an electrolyte which separates these. Inside the fuel cell an electrochemical reaction takes place where the oxidant and fuel are supplied simultaneously to the cell producing electricity, with ions produced at one of the electrodes transported through the electrolyte to the other electrode. The basic set up for a fuel cell can be seen in ***Figure 1.1***.

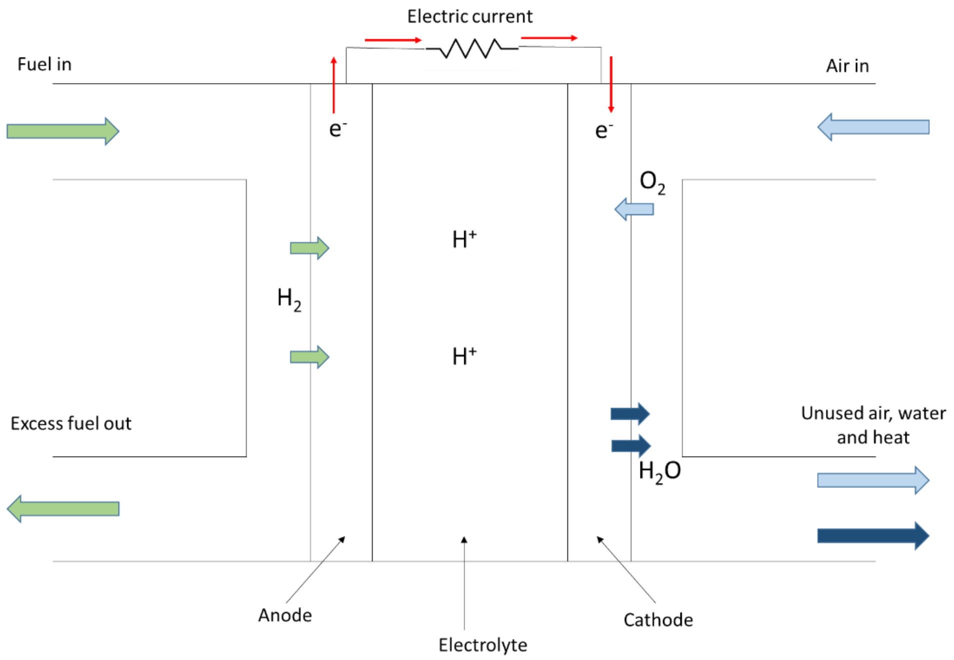

Figure 1.1 Basic fuel cell set up used for PAFCs, PEMFCs and some SOFCs.

It is desirable for electrolytes used in fuels cell to have high ionic conductivity, negligible electronic conductivity, impermeability to gases, good mechanical qualities and be chemically stable in contact with the electrode materials. For electrodes to be optimal in fuel cells they are required to be porous, electronic and ionic conductors, have a good chemical stability under reducing (anode) or oxidising (cathode) atmospheres, whilst also being electrochemically active, as well as being compatible with the electrolyte and have a high surface area for maximum catalytic efficiency.

There are a number of different classes of fuel cells, which are characterised by the electrolyte used; Alkaline Fuel Cell (AFC), Molten Carbonate Fuel Cell (MCFC), Phosphoric Acid Fuel Cell (PAFC), Proton Exchange Membrane Fuel Cell (PEMFC) and Solid Oxide Fuel Cell (SOFC). The reactions that occur for each electrode for a given fuel cell are given in ***Table 1.1***.

Table 1.1 Types of Fuel Cell and the specific reactions for each

Fuel Cell Type	**Anode Reaction**	**Mobile Ion**	**Cathode Reaction**
AFC	$H_2 + 2OH^- \rightarrow 2H_2O + 2e^-$	OH^-	$1/2O_2 + 2H_2O + 2e^- \rightarrow 2OH^-$
MCFC	$H_2 + CO_3^{2-} \rightarrow H_2O + CO_2 + 2e^-$	CO_3^{2-}	$1/2O_2 + CO_2 + 2e^- \rightarrow CO_3^{2-}$
PAFC	$H_2 \rightarrow 2H^+ + 2e^-$	H^+	$1/2O_2 + 2H^+ + 2e^- \rightarrow H_2O$
PEMFC	$H_2 \rightarrow 2H^+ + 2e^-$	H^+	$1/2O_2 + 2H^+ + 2e^- \rightarrow H_2O$
SOFC*	$H_2 + O^{2-} \rightarrow H_2O + 2e$	O^{2-}	$1/2O_2 + 2e^- \rightarrow O^{2-}$

*Solid oxide fuel cells utilising a H^+ conducting electrolyte are also known

AFCs operate at low temperature around 100°C and have the capability to reach 60% - 70% efficiency. The electrolyte used in this fuel cell is a concentrated aqueous solution of potassium hydroxide (KOH) which transports the negatively charged OH- ions created at the cathode to the anode. Although this fuel cell has a quick start up time it is sensitive to CO_2 as it reacts with the KOH electrolyte and therefore reduces the conductivity as well as the K_2CO_3 formed blocks the electrode sites.[10][11]

MCFCs operate at high temperature between 600°C – 700°C and can have an efficiency of 50% - 60%. They use a eutectic mixture of molten carbonates such as Li_2CO_3/K_2CO_3 which transports CO_3^{2-} from the cathode to the anode. Compared to the AFC, it has a relatively slow start up and the added drawback of being intolerant to S containing impurities in the fuel which affects the efficiency of the cell. However, an advantage to running at high temperatures is that internal reforming of fuel is possible (***Equation 1***) [10-13]:

$$\mathbf{CH_4 + H_2O \rightarrow CO_2 + 3H}$$

Equation 1.1 Internal Reforming Reaction

PAFCs were the first commercially available fuel cells and make use of a phosphoric acid liquid electrolyte which transports H^+ from the anode to the cathode.[11] The PAFC operates between 175°C - 200°C and is relatively tolerant to impurities in the H_2 fuel. The main issue with the use of PAFC is its high cost, as it requires platinum catalysts in the electrodes due to its low operating temperature.[11][12][14] PAFCs have an efficiency of around 40% which is low in comparison to the other fuel cells already mentioned.

The PEMFC is comparable to the PAFC except for the use of a different electrolyte. PEMFCs use polymer electrolytes to transport the H^+ between the porous electrodes. This fuel cell operates at around 100°C and has an operating efficiency around 40% – 45% which again is relatively low in comparison to other fuel cells. As with the PAFC, the PEMFC also uses platinum catalysts making the cost of the fuel cell expensive. It also has another added disadvantage in that it is intolerant to CO impurities in the H_2 fuel which decreases its efficiency.[12][15]

More recently alkaline polymer electrolytes have also been developed and are used in fuel cells known as alkaline polymer electrolyte fuel cells (APEFCs) or alkaline membrane fuel cells (AMFCs). These fuel cells combine the basic advantages of PEMFCs and AFCs whilst also improving stability towards CO_2 and potentially decreasing the cost of PEMFCs as platinum catalysts may not be required.[16]

SOFC’s are high temperature fuel cells which run at around 600°C - 1000°C with an efficiency of 50% - 60% which is high in comparison to the PAFC and PEMFC. They make use of a solid ceramic inorganic oxide as an electrolyte, such as yttria stabilized zirconia (YSZ) or doped CeO, which transports O^{2-} from the cathode to the anode. As the temperature of the fuel cell is high, internal reforming of fuel is possible in the same context as for the MCFC. Waste heat from this process can also be used to make more electricity through cogeneration, or be used for heating buildings (combined heat and power).[12][17][18]

The focus of the initial work in this project is on perovskite and perovskite related materials determining whether various oxyanions may be incorporated into these systems and their effect, if any, on properties valued for use in fuel cells.

1.3 The Perovskite Structure

The first perovskite, $CaTiO_3$, was discovered by Gustav Rose in 1839 from samples found in the Ural Mountains and was named after a Russian Mineralogist, Count Lev Alekesevich von Perovski.[19] The perovskite system itself has been found to have many applications including energy production in SOFC technology[20], environmental containment of radioactive waste[21], as dielectric resonator materials for communications[22] and as high T_c superconductors[23].

The perovskite system has the ideal general formula ABX_3 and its structure can be seen in ***Figure 1.2***.

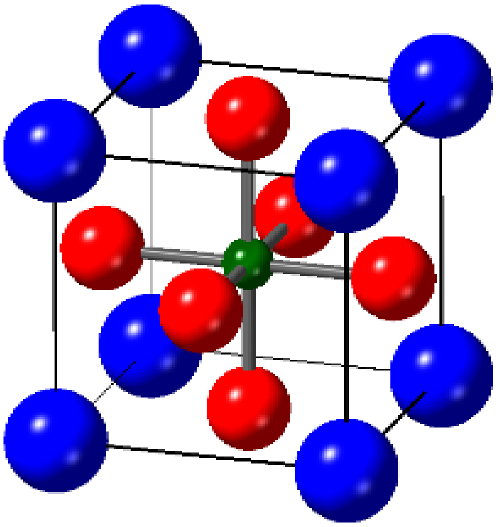

Figure 1.2 Ideal cubic perovskite (ABX_3) system with space group $Pm\bar{3}m$ (Blue = A, Green = B, Red = X)

In this figure the larger A cations sit on the corner sites of the unit cell with a 12-fold coordination to the anion, whilst the smaller B cations sit in the centre of the unit cell in a 6-fold coordination to the anion X.

The potential formation of a perovskite system and the nature of any distortions can be predicted through the application of the Goldschmidt tolerance factor which is given by the following ***Equation 1.2*** for an oxide system [24-26]:

$$t = (r_a + r_o) \ / \ \sqrt{2}(r_b + r_o)$$

Equation 1.2 Goldschmidt tolerance factor equation for the perovskite structure

This equation takes into account the radii of the ions on the A, B and oxide sites and for an ideal cubic perovskite (space group of $Pm\bar{3}m$) then $t = 1$.[27] If the radius of the cation on the B site is too large then $t < 1$ and the octahedra of anions surrounding the B cation distort and tilt towards the central A cation in order to release the strain on the system, resulting in a lower symmetry unit cell.[28][29] This is even the case with the first found $CaTiO_3$ which exhibits an orthorhombic structure with the space group *Pnma*.[30-32] In other cases (eg. $LaAlO_3$, $NdAlO_3$ and $LaCr_{1-x}Co_xO_3$), distortion to give a rhombohedral structure with the space group $R\bar{3}c$ has been observed.[27][32][33] Going the opposite way, if $t > 1$ then this means that the B cation is too small for the system and a hexagonal cell with face sharing octahedral can result.[24-26][34] With even more distortion the perovskite cell system is no longer observed.[35]

The perovskite structure is quite versatile when changes in stoichiometry are considered, as this structure can readily incorporate oxide ion vacancies brought about through doping onto cation sites. These vacancies can allow oxide ion conduction or the ability to incorporate water into the systems which can lead to the observation of proton conductivity in these materials. [36] However in some cases the oxygen vacancies may order giving rise to other structures such as the brownmillerite structure, which has alternating layers of tetrahedral and octahedral coordination around the smaller B cations and is seen in the $Ba_2In_2O_5$ and $A_2Fe_2O_5$ (A = Sr, Ca) systems. At low temperatures, these systems show poor oxide ion conduction but at higher temperatures these oxide ion vacancies disorder and a substantial increase in conductivity is seen.[37-39]

1.4 The Ruddlesden-Popper Structure

By changing the ratio of A:B cations, a system where consecutive perovskite (ABX_3) layers are separated by a rock salt layer (AX) can be obtained. Named after S. N. Ruddlesden and P. Popper who were the first to synthesise $Sr_{n+1}Ti_nO_{3n+1}$ (n = 1, 2, and 3)[40,41], phases with the general formula $A_{n+1}B_nX_{3n+1}$[40] are now known as Ruddlesden-Popper phases, where A and B are cations, X is an anion and n specifies the number of perovskite layers separating the rock salt layers. Examples of Ruddlesden-Popper structures can be seen in ***Figure 1.3***.

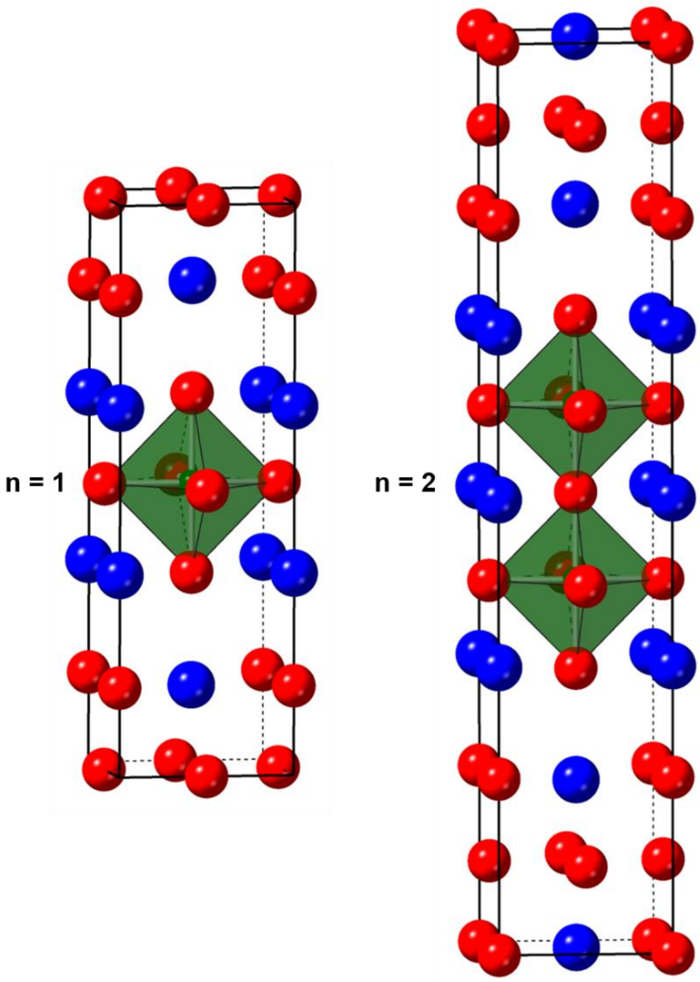

Figure 1.3 $A_{n+1}B_nX_{3n+1}$ *Ruddlesden-Popper structure (n = 1, 2) with space group I4/mmm (Blue = A, Green = B, Red = X)*

In this structure the larger A cations have two distinct coordination environments: situated on the perovskite layer with 12-fold coordination to the anion and 9-fold coordination when positioned between the perovskite and rock salt layers. The smaller B cations have similar coordination being in the centre of the perovskite layer with 6-fold coordination to the anion X.[42, 43]

When considering Ruddlesden-Popper oxides $A_{n+1}B_nO_{3n+1}$ (X = O), the A cation is generally a group 1, group 2 or rare-earth metal whilst cation B is usually a transition metal or other small cation. Like the ABX_3 structure, stability and distortions of the Ruddlesden-Popper phase can be predicted using the Goldschmidt tolerance factor mentioned in the previous section.

Systems where n = 1 (A_2BO_4) are also known as K_2NiF_4 structures and form when the A cation is slightly larger than the B cation (e.g. Sr_2TiO_4, Sr_2CoO_4)[40,44] . If the A cation size is increased (e.g. Ba_2TiO_4, Ba_2CoO_4)[45-46] then the structure deviates from the Ruddlesden-Popper structure due to the tolerance factor being >1 and instead a β-K_2SO_4 structure is formed (***Figure 1.4***).

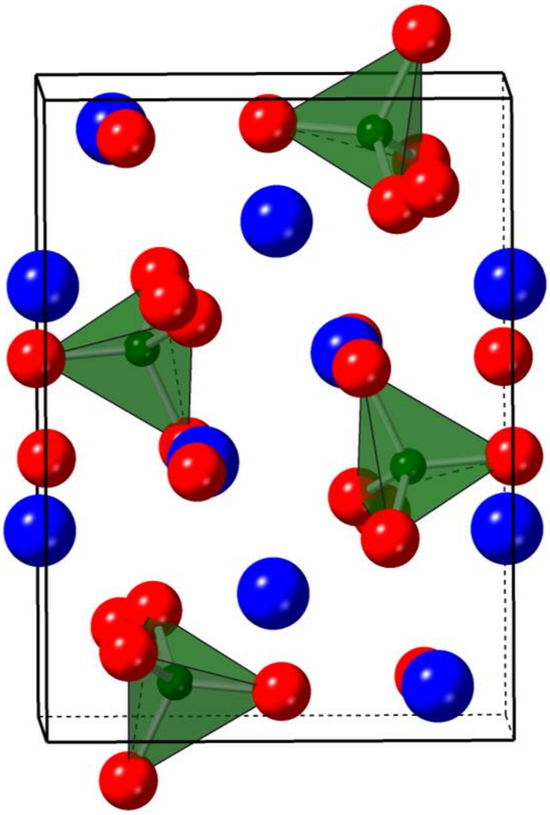

Figure 1.4 Ba_2TiO_4 as ɓ-K_2SO_4 Structure with space group P 1 21/*n* 1
(Blue = Ba, Green = Ti, Red = O)

In this structure, the A cations have 6-fold coordination to O anions, whilst the B cations are 4-fold coordination. β-K_2SO_4 has a monoclinic cell but materials with this structure-type may also be orthorhombic arising from an ordering of the B cation tetrahedra in the monoclinic super structure.

Perovskite and perovskite related materials have many uses including (but not only) their use as fuel cell materials, in particular oxide ion conducting electrolytes, such as $Ba_2In_2O_5$[39], $Ba_3In_2MO_8$ (M=Ce, Hf, Zr)[39] and $La_{0.9}Sr_{0.1}Ga_{0.8}Mg_{0.2}O_{3-x}$)[47]. Other oxide materials that are commonly used in fuel cells include those with the fluorite structure (Yttria-stabilised Zirconia (YSZ)[47] and lanathanide-doped ceria[47]) which have what is known as the fluorite structure. In these materials mentioned oxide ion vacancy defects allows a pathway for oxide conduction to occur. There is also an interest in apatite-type oxide ion conductors ($La_{9.33+x}(Si/GeO_4)_6O_{2+3x/2}$)[48] as these allow for a large range of substitutional possibilities where high conductivities can be seen where oxygen excess and/or cation vacancies are implemented.

1.5 Ion Conduction Mechanisms

When considering solid electrolyte materials for fuel cells one of the many main properties required is that of a good ionic conductivity. There are several mechanisms in which ion conduction can occur. These mechanisms are affected by the materials crystal structure which includes defects, frameworks, and partially occupied sites. Typically, ion conduction occurs through either vacancy hopping or interstitial-type mechanisms. Vacancy hopping ionic conduction pathways require the structure to contain vacancies, which can be introduced by either defects or distinct structural features, such as, partially occupied sites. The most common defects in crystal lattices are Schottky defects, where both a cation and an anion vacancy are formed, and Frenkel defects, where an ion leaves its site to occupy an interstitial site leaving a vacancy in its original position.

During the hopping mechanism an ion migrates (hops) into a vacant site leaving its original site vacant and available for another neighbouring ion of the same species to migrate into the newly vacant site, this process can then continue to move through the structure and hence a conduction pathway is seen. Vacancy hopping can be achieved by both anions and cations; however, anions (such as oxygen) are typically larger and less mobile and therefore require a greater activation energy.

If a crystal structure has ions occupying interstitial sites (as seen in Frenkel defects), an interstitial mechanism for ion migration may be preferable. If a nearby interstitial site is vacant, an ion can either migrate from its interstitial site directly or indirectly. Indirect interstitial migration occurs when one ion forces a nearby ion to move onto the vacant interstitial site from its site and is known as correlated migration where the migration of one ion directly influences the migration of another.

When considering proton (H^+) conduction another mechanism can also be described. This is known Grotthuss mechanism[49] and entails the diffusion of protons through a hydrogen bond network of water molecules. A proton attaches to a molecule of water forming H_3O^+, this molecule is then required to rotate into a position where one of the excess protons can bond to a neighbouring water molecule which then becomes H_3O^+. This process may continue through the structure and is also known as proton tunnelling.

The ionic conductivity of a material can be determined through ***Equation 1.3***:

$$\sigma = nq\mu$$

Equation 1.3 Conductivity of an ion (1.3)

n = number density of charge carriers

q = charge

μ = mobility of charge carriers

The number of mobile charge carriers, n, depends on the number of ions which have sufficient thermal energy to overcome the bonding interaction of their neighbours and have somewhere to move to and is therefore proportional to the number of vacancies within a structure. The likelihood that a mobile ion adjacent to a vacancy successfully makes the hop is governed by the mobility, μ. This value depends on the distance between the two sites and the energy barrier the ion must overcome to migrate. Both the mobility and the number of mobile ions have a temperature dependence which results in the ionic conductivity exhibiting an Arrhenius temperature dependence given by ***Equation 1.4***.

$$\sigma = \sigma_0 \exp\left(\frac{-E_a}{k_B T}\right)$$

Equation 1.4 Arrhenius representation of ionic conductivity

σ_0 = pre-exponential factor

E_a = activation energy

k_B = Boltzmann constant

T = temperature

To achieve a high ionic conductivity, materials need to have an optimum number of charge carriers with high mobility and a pathway with a low activation energy. When comparing oxide and proton conduction activation energies, the energy required for the migration of oxide ions through a solid structure is greater than that required for the migration of protons. However, proton migration is seen to happen slower than expected which is mostly likely due to the rotation required for proton tunnelling to occur. The number of charge carriers can initially be increased by increasing the temperature or via aliovalent substitution.

1.6 Aliovalent doping of SOFC Materials

As already mentioned, oxide ion conductivity, which commonly happens through a vacancy hopping mechanism,[50-55] greatly depends on the amount of oxide ion vacancies present within the structures and how they are ordered, with vacancy ordering leading to lower conduction. Therefore, there is a lot of interest in increasing the amount of oxide ion vacancies and one way of doing this is through the aliovalent doping of systems.

The doping of cathode materials has been investigated, with most research being focused on perovskite materials which have been found to attain generally high electronic conductivities and catalytic activities.[56-60]

Many perovskite materials have been doped for use as cathodes, most of which are based on Lanthanum in the A site. Some examples of this include but are not exclusive to, strontium doped $LaCoO_3$ ($La_{0.7}Sr_{0.3}CoO_3$) which allows formation of oxygen vacancies for greater ion conductivity and oxidation of the cobalt leading to greater electronic conductivity [61], strontium doped $LaMnO_3$ ($La_{0.4}Sr_{0.6}MnO_3$) shows improved electrical conductivity through oxidising manganese but does not form additional oxide ion vacancies[60]; doping $LaFeO_3$ with both strontium on the lanthanum sites and cobalt on the iron sites to simultaneously give rise to an increase in both ionic and electronic conductivities and the formula $La_{0.8}Sr_{0.2}Fe_{0.8}Co_{0.2}O_3$. [63-64]

All systems mentioned so far are classed as oxide ion conductors or mixed electronic/oxide ion conductors, but other systems can also act as proton conductors which have an advantage over the oxide ion conductors as they can typically operate at lower temperatures.

$BaCeO_3$ has attracted a lot of interest in this respect and there has been many attempts of doping Ce^{4+} with a large list of trivalent cations [65-77] which increase the amount of oxide ion vacancies within the structure. Such oxide ion vacancies then allow for water incorporation and hence proton conduction. The main issue with doped $BaCeO_3$ systems is that they tend to be unstable in the presence of CO_2 and humid atmospheres. Co-doping on this system has been seen to improve this stability [78], whilst another method of making a solid solution between doped $BaCeO_3$ and another cubic perovskite system, doped $BaZrO_3$ also enhances stability.[67]

Aliovalent doping has also shown to be able to stabilise the perovskite related Ruddlesden-Popper structures, $A_{n+1}B_nO_{3n+1}$, in particular, the difficult to prepare n = 3 systems. Chen et al. determined that formation $Sr_4Mn_3O_{10}$ was not possible without impurity, but by partially substituting on either the A site ($Sr_{4-y}Ca_yMn_3O_{10-\delta}$) or B site ($Sr_4Mn_{3-x}Fe_xO_{10-\delta}$) they obtained the desired Ruddlesden-Popper structure.[79] A similar study was also performed by Jarvis et al., who showed that while synthesis attempts to give the n = 3 $Sr_4Fe_3O_{10}$ system would produce a mixture of the simple perovskite and n = 2 systems, the desired n = 3 phase could be obtained by Cr doping to give $Sr_4Fe_{3-x}Cr_xO_{10-\delta}$.[80]

1.7 Oxyanion doping of SOFC Materials

When it comes to the perovskite materials used for SOFCs it is known that the cubic perovskites generally show higher oxide ion conductivities. This is due to long range disorder of oxide ion vacancies. One new way being researched to help to disrupt long range ordering of oxide ion vacancies in perovskites is through doping with oxyanions. Such research has investigated the use of borate, sulphate, silicate, phosphate and carbonate, showing promising results in terms of both electrolyte and electrode materials. [81-86]

In this doping strategy the central "cation" of the oxyanion dopant substitutes onto the B cation site. However, whilst the B cation is normally bound to 6 oxygens in a perovskite forming an octahedron, these oxyanion only fill 3 (for borate, nitrate and carbonate) or 4 (for sulphate, phosphate and silicate) of the 6 available oxygen sites. This appears to help to disrupt long range ordering of oxygen vacancies making for the improved ionic conductivity. One of these dopants, carbonate, is of particular interest, due to the fact that it may naturally be present in the system in the absence of deliberate doping.

Despite being expected to be too small to sit on the B cation site, carbonate has been successfully incorporated into a range of cuprate perovskites,[87, 88] although the resultant thermal stability is an issue, and so most prior synthesis work has involved the use of sealed tubes to prevent CO_2 loss. Much of this early work focussed in the cuprate systems due to interest at the time in high T_c superconductors, with the first reported carbonate containing cuprate system was the perovskite $Sr_2CuO_2CO_3$ which has carbonate layers between the CuO_2 layers (***Figure 1.5***). [87-89]

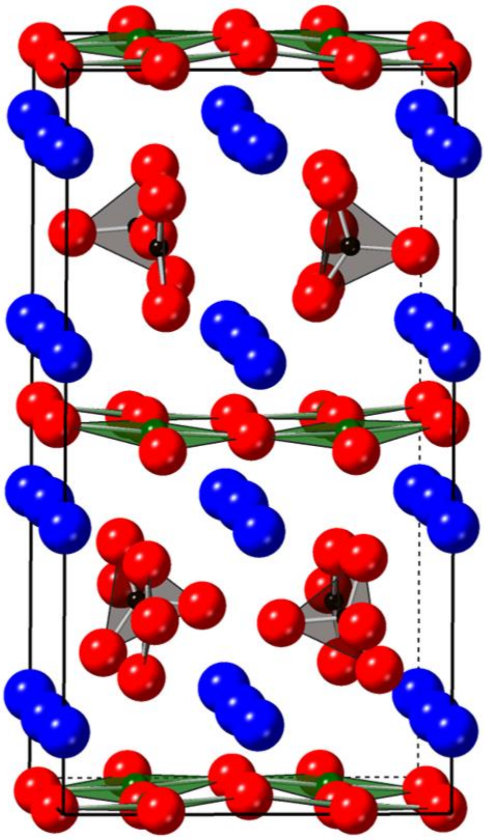

Figure 1.5 $Sr_2CuO_2CO_3$ structure with space group I -4, showing the separation of CuO_2 layers by CO_3^{2-} [91]
(Blue = Sr, Green = Cu, Black = C, Red = O)

This material has the key characteristics to support superconductivity, except for the lack of mixed valency. However, partially substituting the CO_3^{2-} groups for BO_3^{3-} groups, which have identical geometry to that of carbonate provides the partial oxidation of the CuO_2 layers leading to superconductivity.[89-88] Another perovskite cuprate carbonate system was indirectly found through analysis of potential impurities when making $YBa_2Cu_3O_{7-x}$. $Ba_3YCu_2O_x$ was assumed to be a simple perovskite structure until neutron diffraction studies showed that there was short distances to O present around one of the B cation sites which is characteristic of carbonate incorporation. The compound was hence identified as having the formula

$Ba_4YCu_{2+x}O_y(CO_3)_z$. Further investigation helped prove the sample contained carbonate, as an attempt was made to make this system only using oxide starting materials in an oxygen atmosphere, which produced an alternative cubic perovskite, $Ba_4YCu_3O_{8.5+x}$.[81, 92] Similar carbonate containing phases are also obtained when replacing the Y in the systems with Ca.[82, 93]

Other studies have shown that CO_3^{2-} can be incorporated in place if the square planar Cu sites in $YBa_2Cu_3O_{7-x}$ type materials. Moreover, the incorporation of carbonate can also lead to stabilisation of $YSr_2Cu_3O_{7-x}$ system, which cannot be prepared under ambient pressure.[94-96] Previously, due to the local strain created when replacing Ba for Sr to produce $YSr_2Cu_3O_{7-x}$, this could only be prepared via a high pressure synthesis route. However, by the incorporation of carbonate the phase can be synthesised at ambient pressure. The reason for the ready ability of cuprate systems to accommodate carbonate may be due to the Jahn Teller nature of the Cu^{2+} which allows distortion of the system to accommodate the long bond between Cu and the oxygen in the carbonate group. Further research found that nitrate could be incorporated in place of carbonate, but the nitrate containing systems proved even more difficult to control the nitrate content within a system due to even lower thermal stability. In both carbonate and nitrate cases, this can be remedied by the synthesis of these systems in sealed tubes to better allow control over the stoichiometry.[97-99]

More recent work has extended oxyanion doping to non-cuprate systems. In this respect, it has also been shown that the brownmillerite structure of $Ba_2In_2O_5$ is able to incorporate different oxyanions, such as sulphate, phosphate and silicate.[38, 87, 100] This brownmillerite structure has oxide ion vacancies that are ordered in such a way that at room temperature the structure consists of alternating layers of InO_4 tetrahedra and

InO_6 octahedra. Due to this ordering a low oxide ion conductivity is seen at low temperatures, but a large increase in oxide ion conductivity occurs when the temperature is raised to ~930°C as a result of a structural change from orthorhombic to tetragonal. This results in greater disordering of the oxide ion vacancies and hence an increased oxide ion conductivity.[101, 102] At even higher temperatures the phase becomes cubic where all the oxide ion vacancies are now completely disordered, and a much greater oxide ion conductivity is seen. Consequently, there has been a lot of interest in stabilising the high temperature highly conducting system at lower temperatures.[37, 39, 103-108]

Such work showed that the most successful strategy shown to help stabilise this cubic phase is through doping on the In site with higher valence cations, such as Ti, Mo, V, W and Sn,[103-106] although many of these doped systems have been shown to be unstable in humid atmospheres as well as in the presence of CO_2. Recently Slater et al have shown the stabilisation of the highly conducting cubic phase through the incorporation of phosphate groups, PO_4^{3-}, producing $Ba_2In_{2-x}P_xO_{5+x}$ as well as silicate groups, SiO_4^{4-}, producing $Ba_2In_{2-x}Si_xO_{5-+x}$ and sulphate groups, SO_4^{2-}, producing $Ba_2In_{2-x}S_xO_{5+x}$ These oxyanions were chosen due to their greater thermal stability in comparison to CO_3^{2-}, as high thermal stability is required for the high temperature sintering of the samples for SOFC applications. The results showed that by increasing the amount of PO_4^{3-} up to a value of x = 0.3 the structure changed from orthorhombic to cubic at room temperature.[38][100] These oxyanion doped phases also showed an increase in stability towards CO_2 at operating temperatures whilst also showing high proton conductivity due to water incorporation (***Equation 1.5***). The amount of water incorporated was seen to be affected by the amount of phosphate incorporated. As the phosphate value increases, the amount of water incorporated decreased.[38] The results suggested that it was not possible for water to “fill” the oxide ion vacancies around the oxyanion group.

/ ¡ ڈ ط 6¡ ĦɆ ط (. / P ς/ (¡ Ɇ

Equation 1.5 Kröger-Vink notation for water incorporation into oxide vacancies

Silicon is generally noted as a poison in SOFC electrolytes[109-111], but in the case of doping $Ba_2In_2O_5$ with SiO_4^{4-} led to a change from the low oxide ion conducting orthorhombic phase to the highly conducting cubic phase at room temperature. However, at higher dopant values, $x > 0.2$, the formation of an impurity was noted being Ba_2SiO_4, indicating that no more than 10% of In could be doped with Si. The Si doping was found to increase the oxide ion conductivity due to greater disorder of the oxide ion vacancies, as well as giving high proton conductivity through water incorporation and improved CO_2 stability.

Similar work was undertaken concerning the $Ba_2Sc_2O_5$ system which was reported to form an oxygen deficient perovskite structure that was unstable above 1000°C where it instead transformed to $Ba_3Sc_4O_9$. Here it was shown that 20%-30% of the Sc could be doped with PO_4^{3-}, SO_4^{2-} and SiO_4^{4-} to form the desired cubic perovskite phase. With the good thermal stability of these oxyanions allowing for high temperature sintering, high oxide ion conductivity was observed for these systems as well as increased proton conductivity in comparison to the non-doped system.[112, 113] Further studies also indicated that undoped $Ba_2Sc_2O_5$ contained carbonate, and so actually was $Ba_2Sc_{2-x}C_xO_{5+x/2}$ which explained the thermal instability of this compound.

Other research has found borate and carbonate can be incorporated into Ruddlesden Popper systems with borate and carbonate being incorporated into manganese containing $SrMnO_3$ systems and carbonate been incorporated into Ruddlesden popper type $Sr_4Fe_{3-x}(CO_3)_xO_{10-4x}$.[114-118]

1.8 Project Aims

SOFCs have gain a lot of interest over the years due to their high efficiency, operating temperatures that allow for internal fuel reforming and use of relatively cheap electrode materials in comparison to other fuel cells. Commonly, fuel cell materials are prepared by low temperature routes (e.g. sol gel) in order to deliver small particle sizes, particularly for the electrode material.

With the knowledge that the perovskite and perovskite related systems can accommodate significant levels of oxyanions, one aim of this research was to prove the inclusion of carbonate within new and existing systems. This was to place a focus on the extra consideration when synthesis techniques utilising lower temperatures (<1000°C) were used.

Given the reports suggesting carbonate incorporation in the $Ba_2Sc_2O_5$ system [109, 113], the possible incorporation of oxyanions to deliver new perovskite phases for rare earths was examined.

The work was then extended to look at systems in other areas, where the incorporation of CO_3^{2-} may be present. One such system, Ba_2TiO_4, is known to form into two different polymorphs, a low temperature monoclinic structure, which is isostructural to β-K_2SO_4 structure and a high temperature orthorhombic structure [119][120]. Recent work indicates that the low T phase actually contained carbonate, hence why a transformation for higher synthesis temperatures is seen, showing how Ba_2TiO_4 can incorporate CO_2/CO_3^{2-} [121]. Therefore an investigation was implemented on the related

$Ba_2(Co/Fe)O_4$ systems which have similar monoclinic/orthorhombic variations. The aim of this investigation is to prove the existence of carbonate within the Ba_2CoO_4 system and how this can affect the polymorph produced. A short study of sulphate incorporation was also investigated.

Throughout the course of this project many other systems were investigated for the possible inclusion of carbonate or other oxyanions in which various analytical techniques were used to determine the success or failure of each individual investigation. A key aim was whether the presence of carbonate could be confirmed in these systems through structure refinement.

2. Experimental Techniques

2.1 Synthesis Techniques

2.1.1 Solid State Chemistry[122]

The solid-state method is the most common and widely used method of synthesis and involves the mixing and heating of solid reagents at generally high temperatures (500 - 1500°C). These high temperatures are required to facilitate the migration of ions through the solid to reach a reactive interface. In this method a range of materials may be used; whilst simple oxide materials can be used as reagents, they tend to be hygroscopic and/or unstable in an open atmosphere picking up CO_2 and so precursors (such as metal carbonates) are used which decompose to their respective oxides upon heating.

Reagents are initially dried to remove moisture and then weighed into stoichiometric amounts depending on their desired product and then mixed together until a uniform powder is formed and then heated. Reactions during this technique occur at the interface of the reagents, meaning greater surface area (smaller grain) leads to a more uniform reaction with shorter synthesis times. If the interfaces become saturated with product, it is much more difficult for reaction to occur and so regrinding of the powder is generally required to create new interfaces with multiple heating steps to ensure a single phase is produced.

2.1.2 Sol-Gel Synthesis[123]

The sol-gel method of synthesis is a popular technique in the formation of oxides in ceramic chemistry due to providing a greater control over product homogeneity and purity as well being able to synthesise materials at lower temperatures than what would be required for its respective solid-state synthesis.

The method relevant to this work begins with the hydrolysis of stoichiometric amounts of metal nitrate salts which are dissolved in gently heated deionised water. Once all the reagents are dissolved a chelating agent, in this case citric acid, is added and stirred sufficiently ensuring complete chelation of the metal ions. Ethylene glycol is then added, reacting with the chelated citric acid forming a polymer network within the solution. Further heat is then applied to remove enough water from the system to leave a viscous gel. This gel is then fired to break down and burn off the organic framework and the resultant material is ground down into a powder and analysed. Further heating may then be required at higher temperatures to ensure the formation of a single phase product.

2.2 Structural Determination

2.2.1 Crystallography[124, 125]

A crystalline solid is a three-dimensional system with a long-range order of atoms known as a lattice. A crystal lattice can be described by the unit cell of a system, which is the smallest possible structural unit that exhibits the greatest symmetry and can be translationally repeated in all directions and show the full symmetry of the complete crystal structure. Differing length and angles can be used to describe the size and shape of the unit cell, which are also known as lattice parameters. Because of symmetry effects on the unit cell, every crystalline solid can be describe as one of 7 different crystal systems. These different systems are described through ***Figure 2.1*** and ***Table 2.1***.

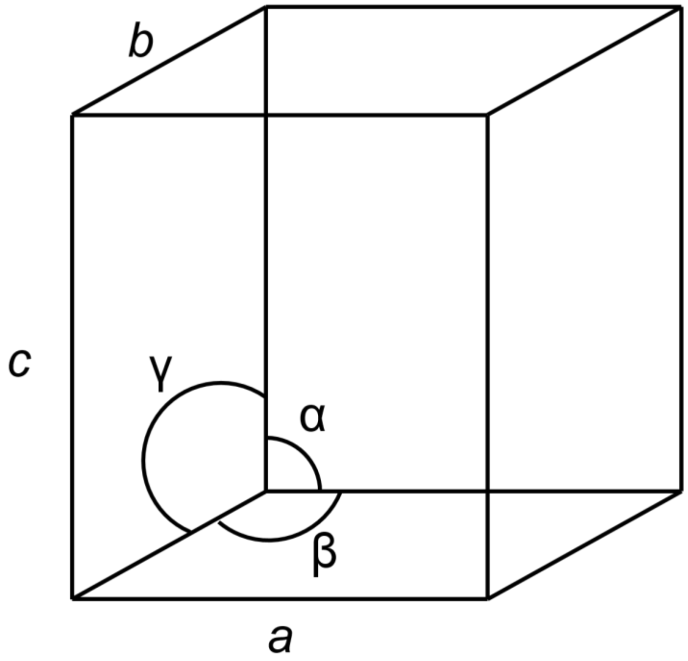

Figure 2.1 Standard unit cell showing all variable lengths and angle

Table 2.1 Seven crystal structures with their variations of lengths and angles

Cubic	a = b = c α = β = γ = 90°
Tetragonal	a = b ≠ c α = β = γ = 90°
Orthorhombic	a ≠ b ≠ c α = β = γ = 90°
Monoclinic	a ≠ b ≠ c α = γ = 90° β ≠ 90°
Triclinic	a ≠ b ≠ c α ≠ 90° β ≠ 90° γ ≠ 90°
Hexagonal	a = b ≠ c α = β = 90° γ = 120°
Rhombohedral	a = b = c α = β = γ ≠ 90°

Whilst these values describe the crystal systems, when combined with a lattice lattice; of which there are four: Primitive (*P*), Body-centred (*I*), Face-centred (*F*) and Base-centred (*C*), a total of 14 Bravais lattice types are possible (***Figure 2.2***).

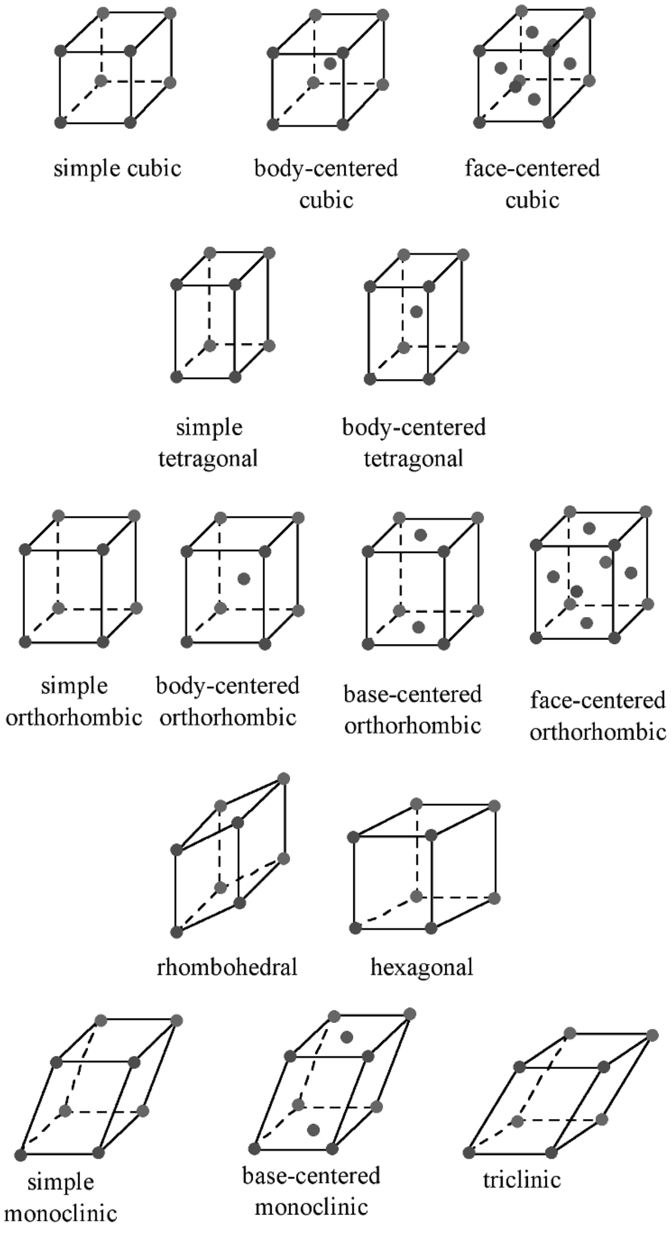

Figure 2.2 Bravais Lattices[126]

Considering all elements of symmetry for a crystal structure when atoms are also included, there are a total of 230 different ways of possibly describing the crystal structure through what are classified as space groups.

Crystal systems can also be described by their lattice planes using a notation called Miller indices. These planes are denoted as (h k l) where h, k and l are reciprocals of the plane where it intercepts the *a, b* and *c* axis. Depending on the symmetry of a system some planes may be equivalent. For example, in a cubic system all lattice parameter lengths are equal and so the (1 0 0) plane is also equivalent to the (0 1 0) and (0 0 1) plane, whereas in a tetragonal system only two of the lengths are equal, meaning whilst (1 0 0) is equivalent to (0 1 0) it is no longer equivalent to (0 0 1).

2.2.2 Powder X-Ray Diffraction

Diffraction techniques are the most important methods available for the determination of structures whilst also being non-destructive meaning the samples can be analysed further with a subsequent technique. Crystalline solids consist of regular arrays of atoms, ion, or molecules with an interatomic spacing in the order of 1 Å (100 pm) which is similar to the wavelength of radiation used in diffraction methods. When a crystalline solid is bombarded with X-rays having a similar fixed wavelength (λ), elastic scattering of the X-rays occurs undergoing constructive or destructive interference creating a diffraction pattern when detected.

Constructive interference occurs, when Braggs law (derived from ***Figure 2.3***) is fulfilled and the value of n in Braggs equation (***Equation 2.2***) is an integer.

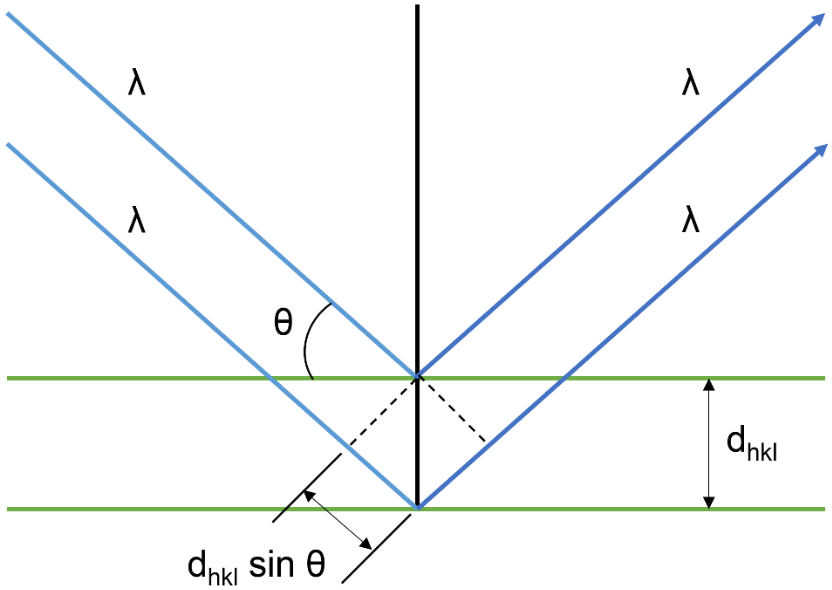

Figure 2.3 Derivation of Braggs Law

$$n\lambda = 2d_{hkl}\sin\theta$$

Equation 2.1 Braggs Equation

The term d_{hkl} represents the spacing between parallel Miller indices, also known as the d spacing. When *n* is an integer d_{hkl} can be calculated from the rearrangement of this equation, which is important as d_{hkl} could be utilised in ***Equation 2.2*** for a cubic crystal system where all lengths are equal to determine the lattice parameter (a_0).

$$\frac{1}{d_{hkl}^2} = \frac{h^2+k^2+l^2}{a_0^2}$$

Equation 2.2 Expression of d_{hkl} spacing for a cubic crystal system

This d_{hkl} value can also be used for all of the other crystal systems, as each has their own specific equation for determining lattice parameters.

Generally, X-rays are produced in labs through applying a voltage to a tungsten filament cathode which becomes heated and generates electrons. These electrons are accelerated towards a target anode (for this work Copper was most used). When these accelerated electrons hit the metal target, they ionise inner shell electrons of this metal producing vacancies. Electrons which have greater energy in outer shells of the metal target then jump from the outer shell to fill these inner shell vacancies, emitting radiation upon this relaxation. Most of this radiation ends up in the form of heat with very little energy being radiated as X-rays. Each target material has its own characteristic X-ray wavelength.

As mentioned, most X-ray diffractometers used during investigations utilised a Copper metal target which has a characteristic K_α wavelength of 1.54 Å. However, some utilised a diffractometer with a Cobalt metal target which has a characteristic K_α wavelength of 1.79 Å.

Powder materials consist of large numbers of crystallites in random orientations, and so it is necessary to bring the lattice planes into orientation with the Bragg angle. In this work most data was collected using the reflection technique (Bragg-Brentano) where the X-ray beam and detector move around the sample detecting diffraction maxima signal when they align with lattice planes.

The amount of X-ray scattering determined from atoms depends heavily on the amount of electrons they have in their orbits. This means that diffraction patterns can be weighted heavily in favour of larger elements, making it difficult to determine the positions of lighter atoms.

2.2.3 Neutron Diffraction

The idea behind neutron diffraction is much similar to that of X-ray diffraction, where Bragg’s law still applies and diffraction occurs where the wavelength of the neutron is similar to that of the separation of atoms or ions in the crystal. The main advantage of using neutron instead of X-rays is that neutrons are diffracted by the nuclei rather than the surrounding electrons. Whilst the scattering of X-rays is highly dependable on the atomic number of the atoms, the scattering of neutrons depends on the properties of the nucleus meaning that it is not dominated by the heavier elements and actually the scattering from light atoms are similar to that of the heavy atoms. Therefore, the lighter elements contribute significantly to the intensities in the diffraction pattern making it much more reliable to determine the positions and parameters of lighter atoms (such as H, O, Li, C) whilst also helping distinguish between isoelectronic atoms.

Neutron beams utilised for this type of diffraction are generated either by fission in a nuclear reactor where ^{235}U nuclei breakdown releasing neutrons in the process or through a process known as spallation (***Figure* 2.4**). During spallation a high energy proton is targeted at generally a heavy nucleus which fragments under the stress of the collision releasing neutrons. However, both generation techniques produce neutrons with too great an energy to be used for diffraction and so must first be slowed down or “moderated” to make them more suitable.

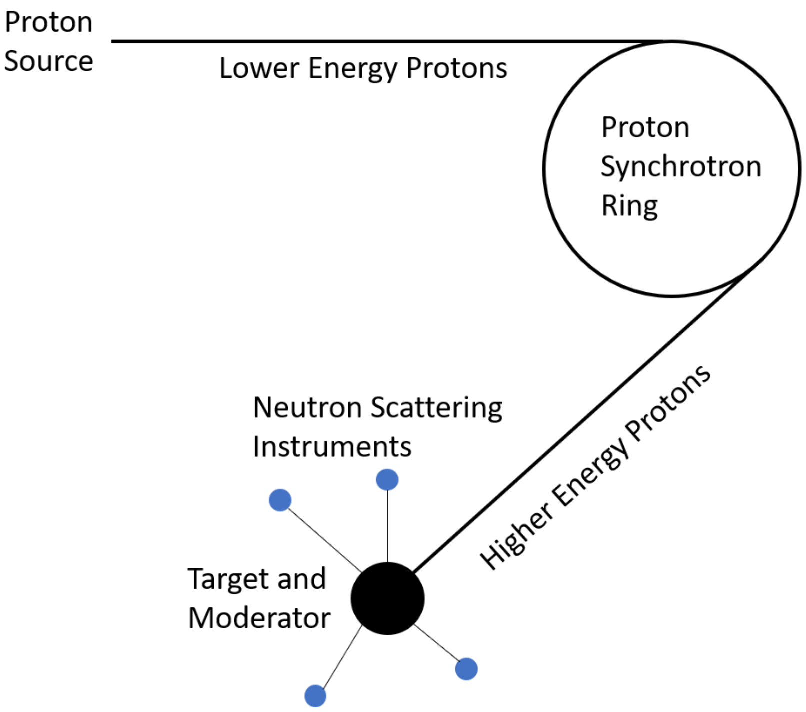

Figure 2.4 Set up for the production of neutrons through spallation

2.2.4 Rietveld Refinement[127-129]

The Rietveld refinement method was first published in 1962 by Hugo Rietveld. The basis of this method is that each point in a diffraction pattern can be analysed as the sum of contributions from background as well as Bragg peaks. A calculated powder diffraction pattern of a model crystal structure is compared to real powder diffraction pattern and Rietveld refinement is used to minimise any difference seen between the two patterns.

When calculating a pattern the peak positions are determined through the use of Bragg's law with modifications applied due to sample displacement and detector zero-point error. The intensity (y_{ic}) at any point (i) is the sum of contributions from Bragg peaks plus contribution from the background and can be calculated through the equation:

ώ̰ سي ھمج جىٓY ھمج ÜÜ ί ŞQج Ş‰ ϛ—ϳ طي ϛ—ί Ũί Öصصط ώ̰ ت
ح أ

n = number of phases present in the pattern

K = Bragg peaks near to point i

S = scale factor for the overall pattern as well as any phase fractions

L = Lorentz-polarisation correction at $2\theta_i$

M_K = multiplicity for peak K

F_K = Structure factor corrected for atomic displacements

Φ = Peak profile function for phase n

P_K = Preferred orientation correction

A = Absorption factor

y_{ib} = Background intensity at point i

This Lorentz-polarisation correction is a combination of the Lorentz factor and polarization factor. The Lorentz factor takes into account certain geometrical factors related to the reflecting planes in the crystal whilst the polarisation factor is the degree of plane polarisation of the incident X-ray beam. All atoms vibrate with a dependency of temperature, the higher the temperature the more the atoms will vibrate, and so the structure factor must be corrected to take this into account thermal displacement. The peak function defines the shape of the peaks in which many factors can contribute including X-ray/neutron source characteristics, instrumental optics, detector and sample effects (such as microstrain, crystallite size, transparency, ect). The absorption factor depends upon sample geometry as well as the elements present within the system. For X-rays, the greater the average electron density, the more the sample will absorb.

Once the model has been used to calculate a powder diffraction pattern it is compared to the observed pattern (y_{io}) and the difference is minimised through refinement of many parameters. These parameters include instrument profile functions, background, zero-point correction, sample displacement, sample transparency, sample absorption, unit cell parameters, scale factor, phase fractions (for mixed samples), crystallite size, strains, atomic position, thermal parameters, site occupancies and preferred orientations. This model is then modified using the least-squares method until the differences between the observed and calculated diffraction patterns are minimised. This is done by minimising the residual value S_y from the equation:

$$S_y = \sum_i w_i (y_{io} - y_{ic})^2$$

w_i = weighting of each data point and is equivalent to $1/y_{io}$

y_{io} = observed intensity at the i^{th} point

y_{ic} = calculated intensity at the i^{th} point

In order to determine whether a model fit is “good”, this can either be done by visually seeing the difference profile or there are several calculations mainly used to show this in numerical fashion:

$$R_{wp} = \left(\frac{\sum_i w_i \left(y_i(obs) - y_i(calc) \right)^2}{\sum_i w_i \left(y_i(obs) \right)^2} \right)^{\frac{1}{2}}$$

$$R_{exp} = \left(\frac{N - P + C}{\sum_i w_i \left(y_i(obs) \right)^2} \right)^{\frac{1}{2}}$$

N = number of data points

P = number of varied parameters

C = number of constraints

$$\chi^2 = \left(\frac{R_{wp}}{R_{exp}} \right)^2$$

It is known that numerically a great fit is seen as the values become closer to/less than 1 but care must be taken as high background and impurities can severely affect the values of R_{wp} adding justification why x^2 (goodness of fit) is generally used to represent numerically.

There are several computer programme suites that perform this refinement technique and during this research the GSAS – ii programme was used. GSAS – ii can perform Rietveld refinements on both X-ray and neutron data with the option to refine all parameters mentioned. Initially an observed diffraction pattern is loaded along with an instrument file giving specific values (such as zero-point, wavelength) for that specific instrument. Then a model is loaded and parameters are chosen for refinement, it is important to pay close attention to the refinement as convergence at a local minimum will not give a true structure and may halt any more progress of the refinement. After each refinement a report (.lst) file is produced/overwritten giving full numerical details of the refinement including error values and once a good is fit determined the programme is also able to export results in many formats including Crystallographic Information Files (CIF).

2.3 Raman Spectroscopy[130]

The study of the interaction between matter and light is known as spectroscopy. Raman spectroscopy is a vibrational spectroscopy which can help determine chemical compositions and likely structure for a compound whilst also being useful in the measurement of bond properties.

There are several ways in which light can interact with matter which include refraction, reflection, absorption, transmission, fluorescence and scattering (***Figure 2.5***); the latter four interactions mentioned being of the most relevance for Raman Spectroscopy. Absorption occurs where some incident wavelengths of light are partially absorbed in the sample (which may cause unwanted heating of the sample) whilst other wavelengths can transmit through the sample without much loss of intensity. On some occasions incident wavelengths of light may be absorbed and then reemitted in as longer, different wavelengths to that of the incident, this is known as fluorescence. Scattering may be elastic meaning that the scattered light has the wavelength as the incident light. There is also inelastic scattering where small exchanges of energy can happen between the light and matter meaning the scattered light has a change in frequency and wavelength, it is this inelastic scattering that is utilised in Raman spectroscopy.

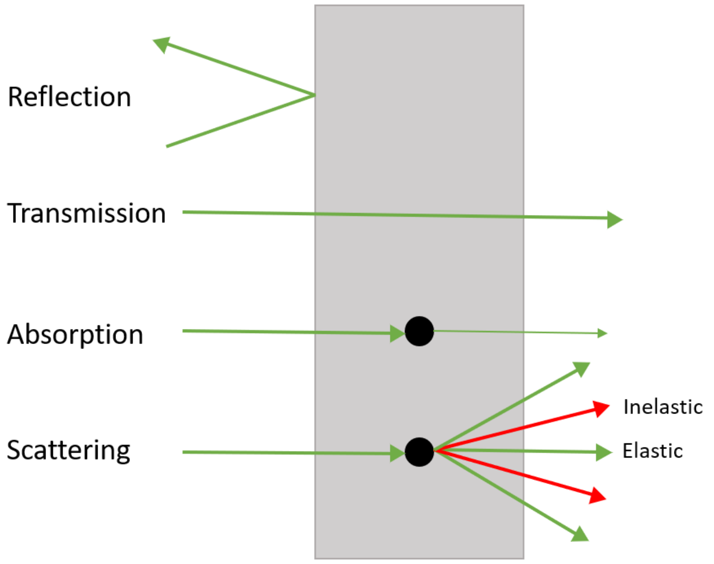

Figure 2.5 A visual representation of the ways in which light can interact with material.

There are three main scattering processes that are important for Raman spectroscopy (***Figure 2.6***). The most dominant process is known as Rayleigh scattering, this is an elastic interaction which does not change the energy state of a molecule and so the scattered photon has the same wavelength as the incident photon. Rayleigh scattering is very overwhelming and must be removed from collected data as it would obscure any Raman signals. As mentioned, inelastic scattering is utilised in Raman spectroscopy and known as Stokes and Anti-Stokes Raman scattering. Stokes Raman scattering is where the exact amount of energy required to excite a molecular vibration is transferred from the incident photon to the vibration of a molecule, meaning that the resultant scattered photon has a higher wavelength and lower energy than the incident photon. Anti-Stokes Raman scattering occurs where a specific amount of energy is transferred from the vibration of a molecule to the incident photon meaning that the scattered photon has a shorter wavelength and higher energy than that of the incident photon. In both cases energy is transferred to the molecular vibration creating a virtual state of excitement it is during the relaxation of this state that that photons emitted will have a different energy and hence wavelength to that of the incident. Of the two, Stokes and Anti-Stokes, the former process is the more common of the two (despite also being rare) which is exploited to produce a Raman spectrum. Changes in photon energy seen depends of the frequency of the vibration with high frequency vibrations showing a larger change and low frequency vibrations showing a much smaller change in scattered photon energy.

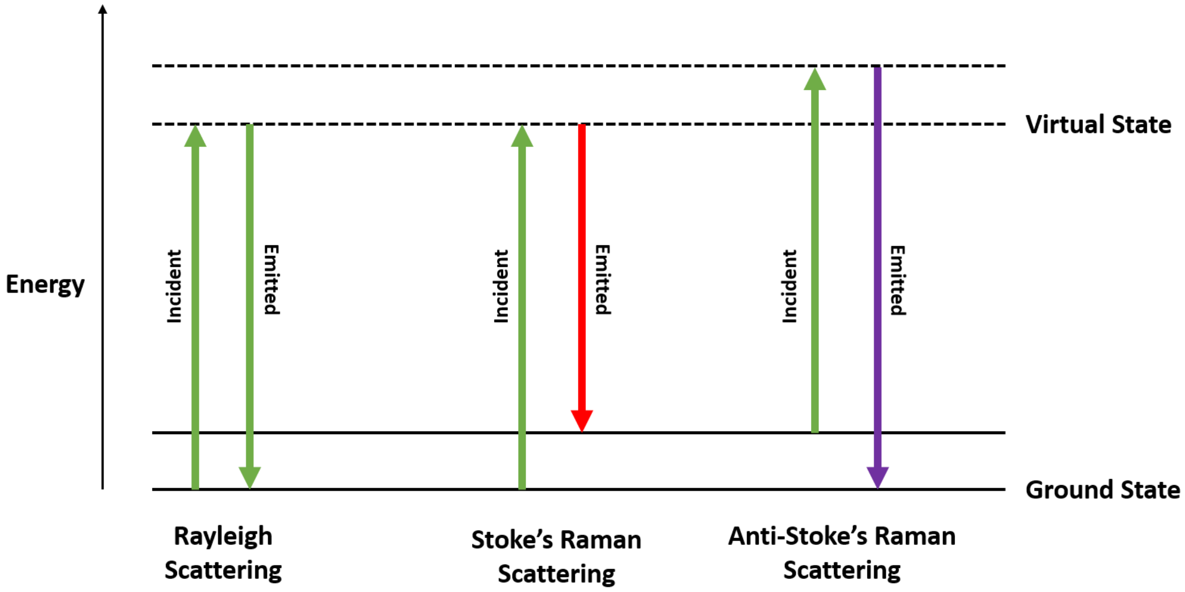

Figure 2.6 The main process of which light scattering can occur in Raman spectroscopy.

In order for a molecular vibration to be seen in Raman spectroscopy it must be Raman-active. Molecular vibrations are Raman-active when they produce a change in the polarizability of a molecule. Polarizability describes how easily the electronic cloud of a molecule can be distorted and examples that may cause this are symmetric stretching, asymmetric stretching and bending modes (***Figure 2.7***).

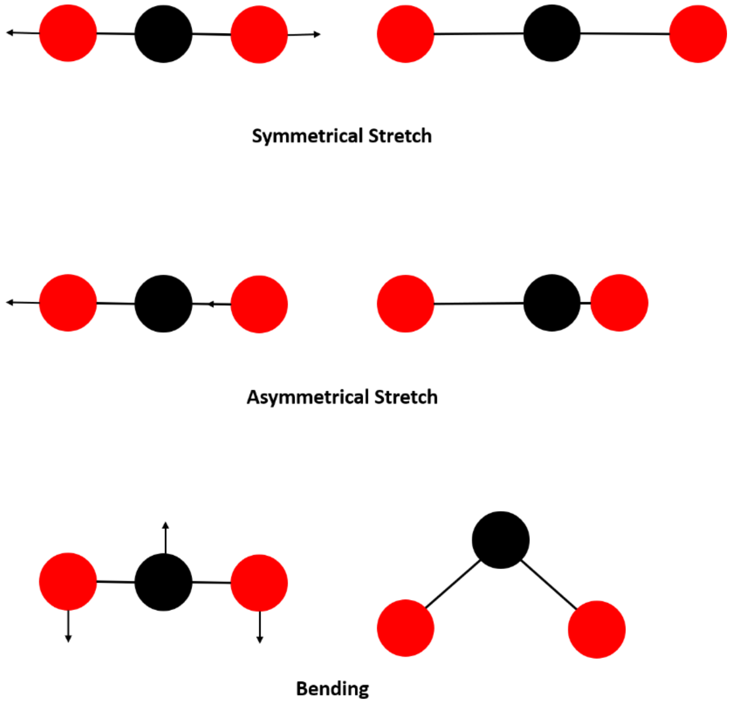

Figure 2.7 A visualisation of the vibrational modes seen for a 3 atom molecule.

Raman spectra are commonly depicted graphically where the intensity of scattered light or "count" (y – axis) is plotted against the wavenumber or "Raman shift" (x – axis). The data found in a Raman spectrum can be used to help identify a material through characteristic Raman shifts of functional groups. Spectra recorded from different positions of a sample reveal the homogeneity of a material and can help determine impurities as well as reaction completion. Individual band changes seen can provide information about stresses in a sample, variations in crystallinity as well as the amount of materials present.

Throughout this research two different Raman spectrometers were used: a Renishaw inVia Raman microscope utilising a 532nm or 633nm laser and the second using a DILOR XY spectrometer with a CCD detector at the University of Zaragoza. All measurements were taken at room temperature using varying laser line power.

2.4 Thermogravimetric Analysis (TGA)/Differential Thermal Analysis (DTA)[131]

Thermogravimetric analysis (TGA) measures changes in mass in relation to changes in temperature. This measured mass change curve can give information on changes in the sample composition, thermal stability of a sample and kinetic parameters for chemical reactions in the sample. The mass of a sample can be lost or even gained. Where mass loss occurs, this can be caused by decomposition of a sample, evaporation of volatile substituents and elevated temperatures, reduction of a sample or desorption. Mass gain can be seen if the sample undergoes oxidation, absorption or adsorption.

Differential thermal analysis (DTA) can also be performed along side TGA. During this the sample and an inert reference are made to undergo identical thermal cycles with difference in temperature profiles being recorded as the cycles progress. When the sample experiences an energy change associated with physical change or chemical reaction a difference in temperature profile is recorded helping to determine a thermal profile of the sample. Whilst TGA only measures changes of mass, with the addition of DTA, we can gain insight of the specific temperatures showing changes in state or crystal structure.

In these studies thermogravimetric analysis was with mass spectroscopy (TGA-MS) to give information about any gases coming off the sample upon heating. Data was collected through a Netsch TGA-MS using varying temperature ranges between 40° - 1300°C with the implementation of various heating programmes. All experiments were undertaken under a N_2 atmosphere and a Platinum crucible was used as the inert reference. Mass spectroscopy was used in the determination of H_2O and CO_3^{-2} content of the samples.

3. Carbonate Incorporation of $Ba_3Ln_2O_5CO_3$ Rare Earth Systems and Potential Sulphate Incorporation

3.1 Introduction

Perovskite materials have attracted considerable interest due to a wide range of technologically important properties displayed by materials with this structure-type, including superconductivity, ionic conductivity, colossal magnetoresistance, ferroelectric properties, and the ability to catalyse a range of reactions. In addition to this rich wealth of properties, perovskites also display a wealth of interesting and, at time, unexpected structural diversity. In particular, research on high T_c cuprate superconductors showed the ability of the perovskite structure to accommodate carbonate and other oxyanions (borate, nitrate, sulfate, phosphate).[132-142] In these situations, the C, B, N, P, S of the oxyanion group resides on the perovskite B cation site, while the oxide ions of this group fill 3 (C, B, N) – 4 (P, S) of the available 6 oxide ion positions around this site, albeit displaced so as to achieve the required geometry for the oxyanion. The incorporation of oxyanions into other perovskite transition metal containing systems has also subsequently been reported, e.g. $Sr(Co/Fe/Mn)O_{3-\delta}$, $La_{1-x}Sr_xCo_{0.8}Fe_{0.2}O_{3-\delta}$, $Ba_{1-x}Sr_xCo_{0.8}Fe_{0.2}O_{3-\delta}$, $CaMnO_3$ and $La_{1-x}Sr_xMnO_3$-type materials.[143-160] Recently the incorporation of sulphate and phosphate have also been reported in $Ba_2(In/Sc)_2O_5$ leading to new cubic perovskites with high oxide ion conductivity/proton conductivity.[161-162] Moreover, phosphate doping was shown to stabilise new cubic perovskite phases, eg. $Ba_2Yb_{1.5}P_{0.5}O_{5.5}$.[163]

Despite these observations that carbonate and other oxyanions can be incorporated into the perovskite structure, there is a surprising lack of consideration in the literature for the possibility that carbonate may be present in perovskite systems prepared at lower temperatures.

In this chapter, an investigation is conducted into whether a perovskite phase could be formed in the $BaCO_3$:Yb_2O_3 phase diagram at lower temperatures ($\leq$1000°C) where carbonate incorporation can be maintained. The work led to the synthesis, identification and structural characterisation of a new phase with $BaCO_3$:Yb_2O_3 ratio of 3:1, which represents a carbonate containing perovskite system while also illustrating its formation for a range of rare earths. Also contained in this chapter is the investigation into whether this new structure was also viable for other oxyanions (BO_3^{3-}, SO_4^{2-}, PO_4^{3-}).

3.2 Experimental Procedure

High purity $BaCO_3$ (Alfa Aesar 99.8%), Yb_2O_3 (Sigma-Aldrich 99.99%) were used to prepare $Ba_3Yb_2O_5CO_3$. The powders were intimately ground in a 3:1 $BaCO_3$:Yb_2O_3 ratio and heated initially to 900°C for 12h in air. They were then reground and reheated to 1000°C in air for a further 24h with regrinding every 12h. After the initial synthesis in air, we also investigated the formation of this compound under dry N_2 in order to allow higher temperature heat treatment by reducing CO_2 loss through reaction with moisture in the air. In this case, it was found that $Ba_3Yb_2O_5CO_3$ could be prepared in a shorter timescale (12h) by employing a higher temperature (1050°C). Note also that heat treatment in air at 1050°C leads to large $Ba_3Yb_4O_9$ impurities due to carbonate loss. These synthesis routes were then used to make a wider range of isostructural $Ba_3Ln_2O_5CO_3$ systems (Ln = Lu, Tm, Er, Ho, Dy, Y) prepared using $BaCO_3$ (Alfa Aesar 99.8%) and the appropriate Ln_2O_3 (Sigma-Aldrich 99.99%) reagrents.

For $Ba_3Ln_2O_5(ZnO_4)_{0.33}(SO_4)_{0.67}$ systems, high purity $BaCO_3$ (Alfa Aesar 99.8%), Ln_2O_3 (Ln = Yb, Tm, Er, Ho,Dy) (Sigma-Aldrich 99.99%), ZnO (ReagentPlus® 99.9%) and $(NH_4)_2SO_4$ (ACS Reagent ≥99.0%) were used in a respective ration mixture of 9:3:1:2. These samples were initially heated at 900°C for 12h in air before being reground and heated at 1150°C for 24h with regrinding every 12h.

Phase identification and initial structure determination was carried out by Rietveld profile refinement using powder X-ray diffraction data (XRD) collected on a Panalytical Empyrean diffractometer (Cu Kα radiation) or a Bruker D2 diffractometer (Co Kα radiation).

For the detailed structure determination of $Ba_3Yb_2O_5CO_3$, time of flight powder neutron diffraction (NPD) data were recorded on the HRPD diffractometer HRPD at the ISIS pulsed spallation source (Rutherford Appleton Laboratory, UK). Structure refinements using the NPD data was performed using the Rietveld method with the General Structure Analysis System GSAS-II suite of programs. [164]

Carbonate and sulphate identification was also confirmed through Raman spectroscopy data collected on a Renishaw inVia Raman microscope using a 532 nm laser, unless specified otherwise.

3.3 Results and Discussion

3.3.1 Synthesis and Structural Characterisation of $Ba_3Ln_2O_5CO_3$ (Ln = Yb, Lu, Tm, Er, Ho, Dy, Y)[191]

3.3.1.1 $Ba_3Yb_2O_5CO_3$ (Ln = Yb)

3.3.1.1.1 Powder X-Ray Diffraction

Initially a range of $BaCO_3$:Yb_2O_3 mixtures with different ratios were investigated, and it was found that a new phase was observed with an optimum $BaCO_3$:Yb_2O_3 ratio of 3:1. The formation of this phase was shown to be very sensitive to the synthesis temperature (***Figure 3.1***).

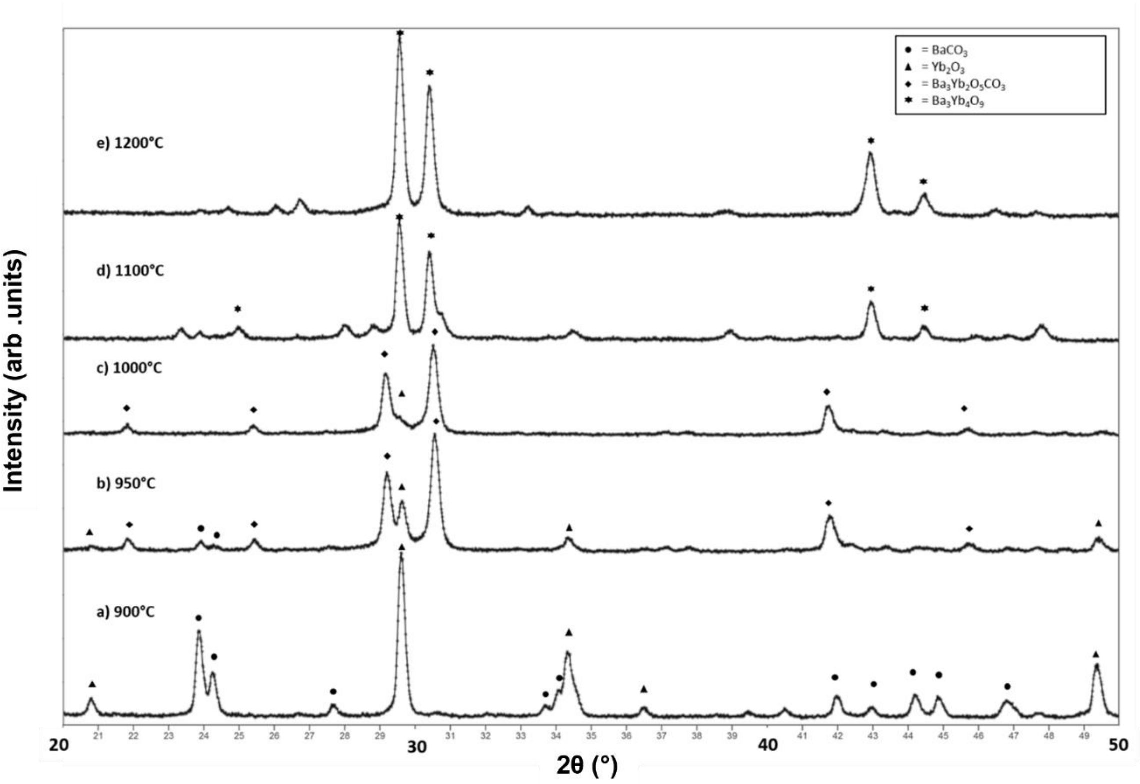

Figure 3.1 X-ray diffraction patterns for a 3:1 mixture of $BaCO_3$: Yb_2O_3 heated at different temperatures, showing the formation of a layered new perovskite phase, $Ba_3Yb_2O_5CO_3$ between 950-1000°C, with decomposition of this phase to give $Ba_3Yb_4O_9$ at higher temperature

At temperatures up to 900°C, no reaction was observed, and the XRD pattern simply showed the presence of the starting materials, $BaCO_3$ and Yb_2O_3. Heating to 950°C led to the appearance of a new phase, with the purity improving by heating at 1000°C. At temperatures above 1000°C, this compound was shown to decompose, and the formation of the simple oxide $Ba_3Yb_4O_9$ was observed, which suggested that the initial phase contained carbonate.

Indexing the pattern for this new phase (***Figure 3.2***) gave a tetragonal perovskite-related cell which was tripled along the *c* direction. From the unit cell parameters obtained, a structure was then postulated based on the prediction that the Yb would maintain a coordination of six. This predicted structure consisted of double Yb-O layers separated by carbonate layers and is shown in ***Figure 3.3***.

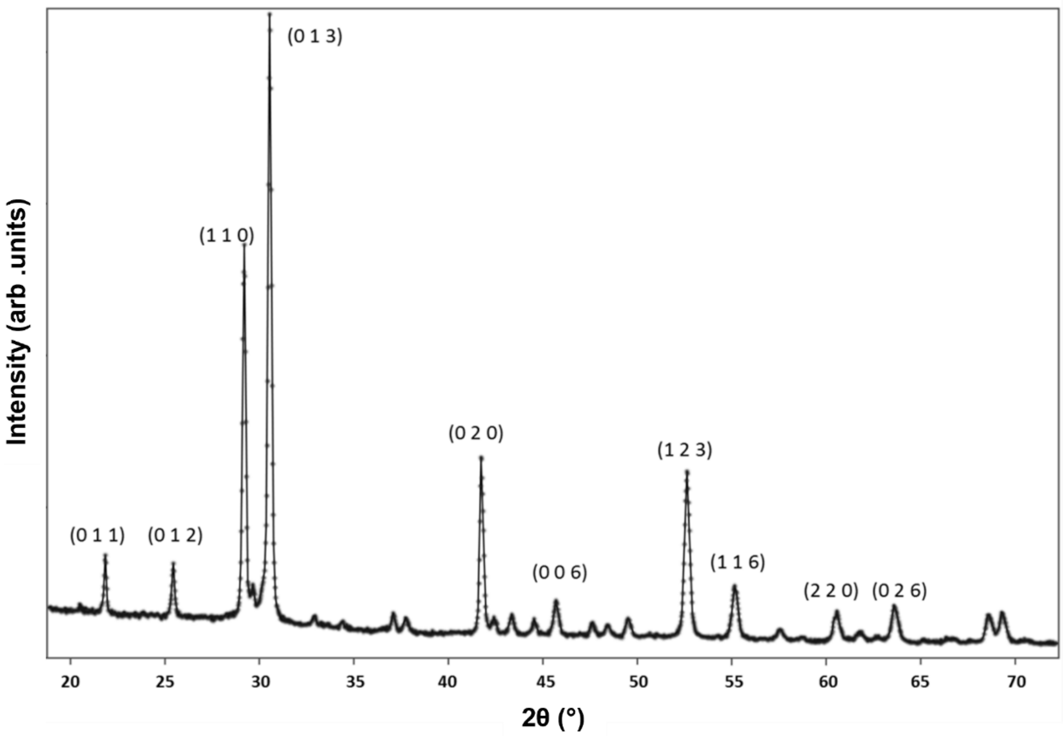

Figure 3.2 X-ray diffraction pattern of $Ba_3Yb_2O_5CO_3$ synthesised at 980°C detailing the main Miller Indices of the P4/mmm space group

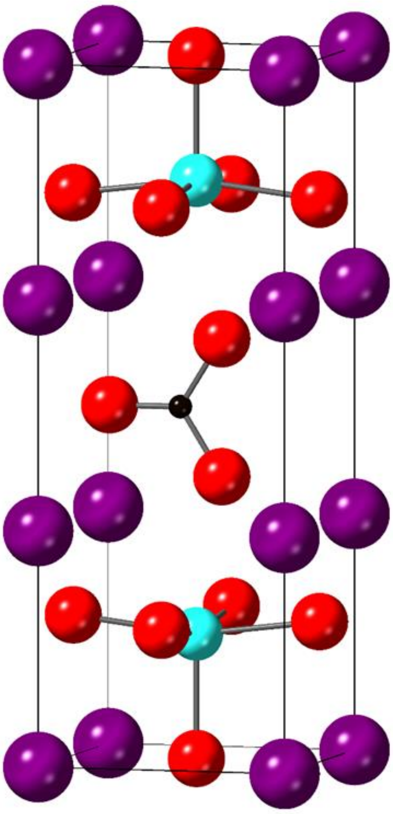

Figure 3.3 Predicted structure of $Ba_3Yb_2O_5CO_3$ using the P4/mmm space group showing triple layers with carbonate occupying the central layer

3.3.1.1.2 Synthesis Under N_2 Atmosphere

Despite being able to consistently make the $Ba_3Yb_2O_5CO_3$ system, synthesis of this phase in air would sometimes vary in the amount of time required between 24 – 48hrs at 1000°C. It is believed that this is caused by the increased rate of CO_2 loss caused by reaction with moisture in the air. Utilising a dry N_2 synthesis approach to limit the rate of loss of CO_2 and hence maintain the presence of carbonate in the sample, the $Ba_3Yb_2O_5CO_3$ system could be synthesised at the higher temperature of 1050 - 1100°C at a much more consistent 12hrs with XRD patterns shown in ***Figure 3.4***.

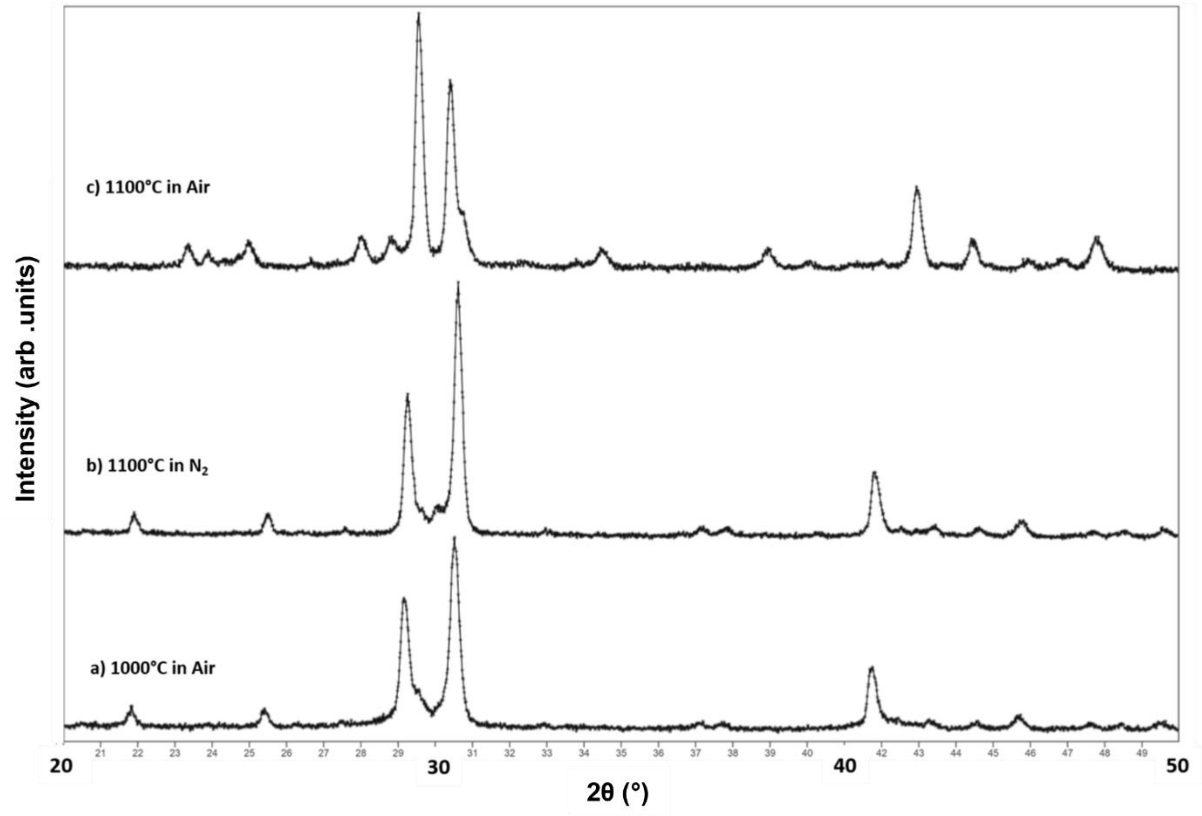

Figure 3.4 Comparison of X-ray diffraction patterns of $Ba_3Yb_2O_5CO_3$ heated at 1100°C in Air/N_2 showing a stabilisation of the synthesis when performed under N_2 atmosphere (in air at higher temperature, $Ba_3Yb_4O_9$ is formed).

3.3.1.1.3 Rietveld Refinement using Neutron Diffraction Data

This postulated structure was then used as the starting point for the Rietveld refinement using neutron diffraction data. The refinement (***Figure 3.5***) was performed using the GSAS-II programme and constraints were placed upon the carbonate group within the system which included O – C – O angles constrained to 120° and C – O bond lengths constrained to 1.28 Å, in line with those expected for carbonate. In addition, since prior studies of carbonate containing cuprate systems,[132,133] had shown significant orientational disorder in the carbonate groups, a nuclear density map was determined and from this, it was clear that there was indeed some disorder in the orientation of the carbonate group. There was also evidence for displacements of some of the other oxygen positions, most likely related to variations in the tilting of the YbO_6 octahedra with the changing orientation of the carbonate group. In line with expectations that the Yb would be 6 coordinate, the carbonate group was indeed shown to be orientated with two of its oxygens coordinated to Yb, with, the remaining oxygen equatorial to the carbonate layer.

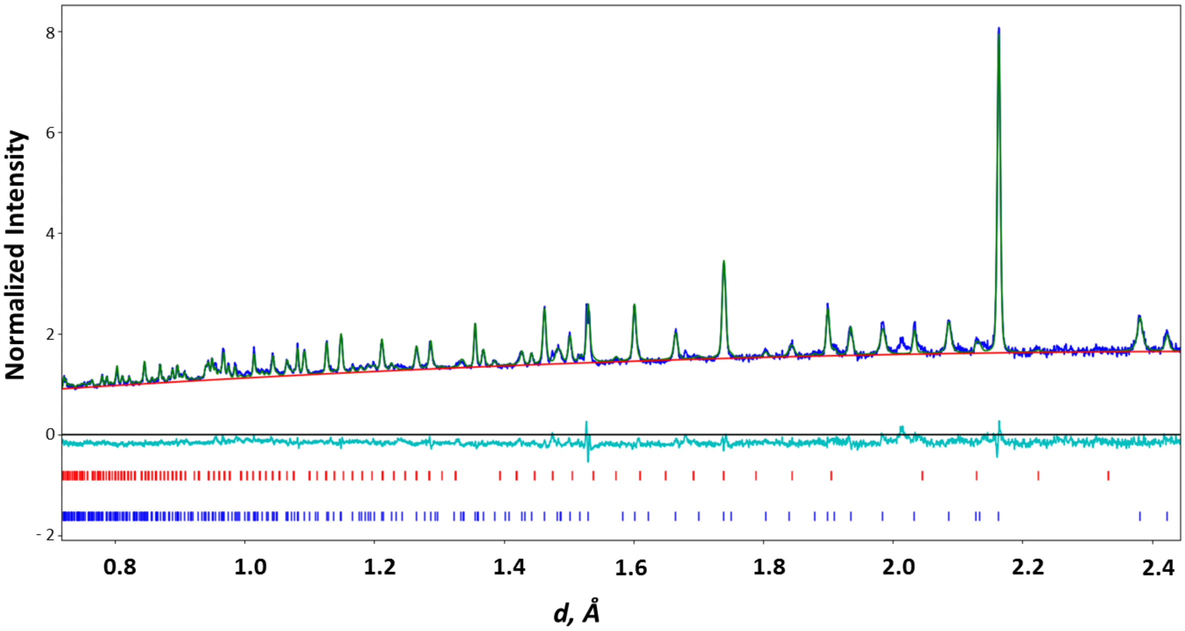

Figure 3.5 Observed, calculated and difference profiles of $Ba_3Yb_2O_5CO_3$ *neutron data (Lower tick marks ï* Yb_2O_3 *(2.5wt%), upper tick marks* $Ba_3Yb_2O_5CO_3$ *(97.5wt))*

This revised structure was then used for the final Rietveld refinement of the $Ba_3Yb_2O_5CO_3$ neutron data to determine the structure, both the O – C – O angles and C – O were now unconstrained in comparison to previous refinement. This led to a good fit with the data (the data indicated a small amount (2.5wt %) of Yb_2O_3 impurity, which was included in the final refinement) and structural parameters and bond distances are given in ***Table 3.1*** and ***Table 3.2*****.** Larger anisotropic values U_{33} for O1 and U_{11}/U_{22} of O2 support that tilting is present for YbO_6 octahedra dependant on the carbonate orientation.

Table 3.1 Refined structural values of $Ba_3Yb_2O_5CO_3$ neutron data

Atom	x	y	z	Site Occupancy	Wyckoff Position	U_{iso}
C1	0.5	0.435(2)	0.5	0.250	4o	0.009(1)
Ba1	0.0	0.0	0.0	1.000	1a	*
Ba2	0.0	0.0	0.336(1)	1.000	2g	*
Yb1	0.5	0.5	0.177(1)	1.000	2h	0.018(1)
O1	0.0	0.5	0.200(1)	1.000	4i	*
O2	0.5	0.5	0.0	1.000	1c	*
O3	0.5	0.148(3)	0.5	0.210(14)	4o	*
O4	0.397(2)	0.5	0.402(1)	0.270 (7)	8t	*

* Anisotropic Atomic Displacment Parameters

Atom	U_{11}	U_{22}	U_{33}	U_{12}	U_{13}	U_{23}
***Ba1**	0.034(1)	0.034(1)	0.015(3)	0.000	0.000	0.000
***Ba2**	0.024(1)	0.024(1)	0.030(2)	0.000	0.000	0.000
***O1**	0.008(1)	0.026(1)	0.071(1)	0.000	0.000	0.000
***O2**	0.088(1)	0.088(1)	0.004(2)	0.000	0.000	0.000
***O3**	0.020(5)	0.020(5)	0.008(5)	0.000	0.000	0.000
***O4**	0.043(2)	0.052(2)	0.052(2)	0.000	-0.013(1)	0.000

R_{wp} = 2.93% GOF = 1.71 (*P4/mmm* *a* = 4.3258(2) Å, *c* = 11.9036(5) Å)

Table 3.2 Selected interatomic distances of $Ba_3Yb_2O_5CO_3$

Bond	Bond Length / Å	Bond	Bond Length / Å
C1 – O3	1.242(16) (x1)	**Ba2 – O3**	2.985(5) (x2)*
C1 – O4	1.376(10) (x2)	**Ba2 – O4**	2.871(7) (x4)*
Ba1 – O1	3.212(2) (x8)	**Yb1 – O1**	2.179(1) (x4)
Ba1 – O2	3.059(1) (x4)	**Yb1 – O2**	2.110(3) (x1)
Ba2 – O1	2.704(5) (x4)	**Yb1 – O4**	2.711(11) (x1)

*dependent on orientation of carbonate group

The final structural model is shown in ***Figure 3.6*** and consists of double YbO_6 octahedra separated by carbonate layers, representing a new example of an ordered perovskite stabilised through carbonate incorporation.

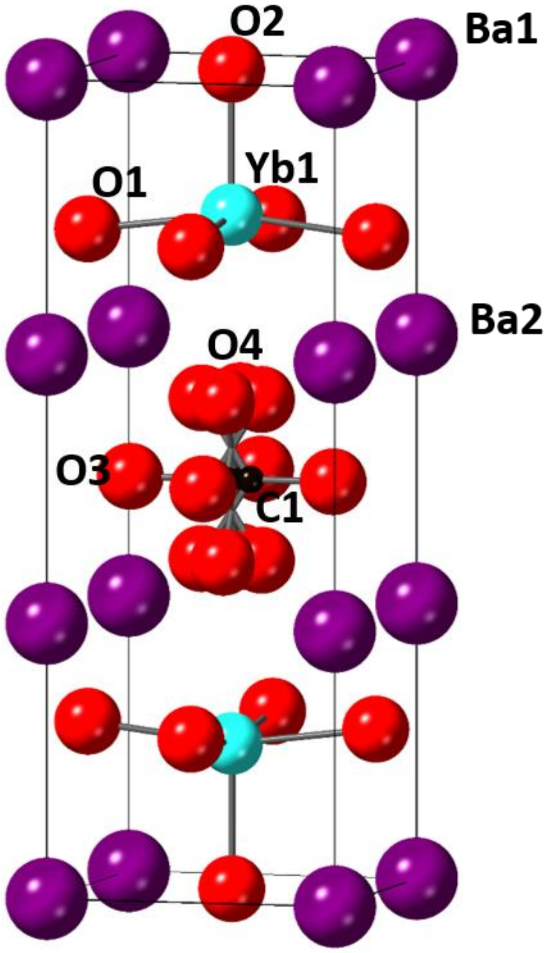

Figure 3.6 Refined structure of $Ba_3Yb_2O_5CO_3$ using the P4/mmm space group showing triple layers with carbonate occupying the central layer

3.3.1.1.4 Raman Spectroscopy

A Raman spectroscopic study was also performed (***Figure 3.7***) to confirm the presence of carbonate in the system, comparing to values of carbonate recorded for the reagent $BaCO_3$ (***Table 3***).

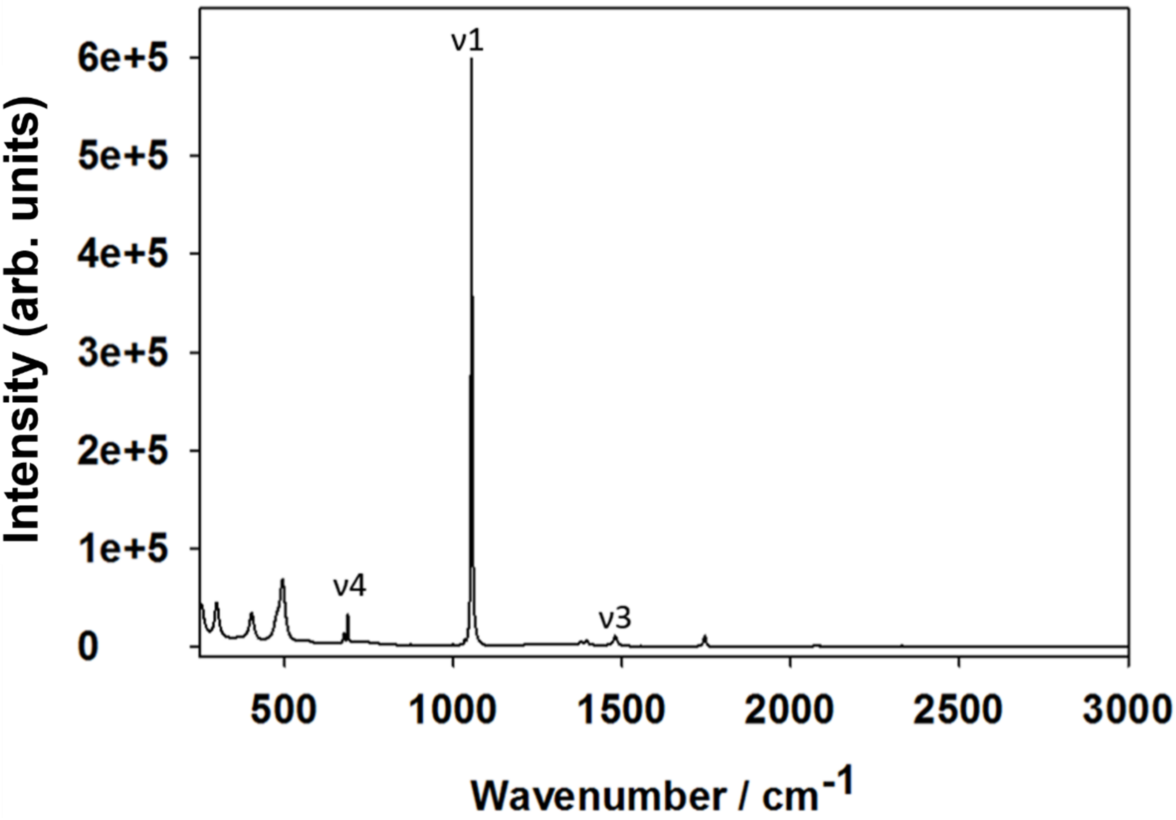

Figure 3.7 Raman spectroscopy data for $Ba_3Yb_2O_5CO_3$ detailing specific Raman bands seen for carbonate vibrational modes

Table 3.3 Raman band wavenumbers for carbonate vibrational modes of $BaCO_3$ and $Ba_3Yb_2O_5CO_3$

System	**ν 1 /$^{-1}$ cm**	**ν 3 /$^{-1}$ cm**	**ν 4 /$^{-1}$ cm**
$BaCO_3$	1059.5	1420.2 1508.1	690.8 699.2
$Ba_3Yb_2O_5CO_3$	1054.5	1395.1 1478.9	678.1 687.6

The Raman data confirms the surmised structures' inclusion of carbonate in the $Ba_3Yb_2O_5CO_3$ system with the appearance of the expected v_1 (symmetric stretch), v_3 (doubly degenerate asymmetric stretch) and v_4 (doubly degenerate asymmetric bend) carbonate vibrational modes[165] with the bands recorded for these being shifted to lower wavenumbers in comparison to those seen in $BaCO_3$. This shift is important in providing evidence that carbonate is indeed a part of the structure and not from reagent $BaCO_3$, with the decrease in wavenumber suggesting longer bond lengths/weakening of the carbonate bonds. Whilst these are not the only Raman bands seen, these were of the most importance in the determination of carbonate presence with the other more prominent bands (250-500 cm^{-1}) being associated with Yb-O vibrational modes.

Further work was then performed to see if this phase could be prepared for other rare earths.

3.3.1.2 $Ba_3Lu_2O_5CO_3$ (Ln = Lu)

3.3.1.2.1 Powder X-Ray Diffraction

A 3:1 reagent ratio of $BaCO_3$:Lu_2O_3 was used to successfully synthesis the $Ba_3Lu_2O_5CO_3$ system in air at 1000°C with the XRD pattern shown in ***Figure 3.8***. As for its Ln = Yb counterpart, heating at temperatures above 1000°C, led to decomposition due to the loss of CO_2, and the formation of the simple oxide $Ba_3Lu_4O_9$ was observed.

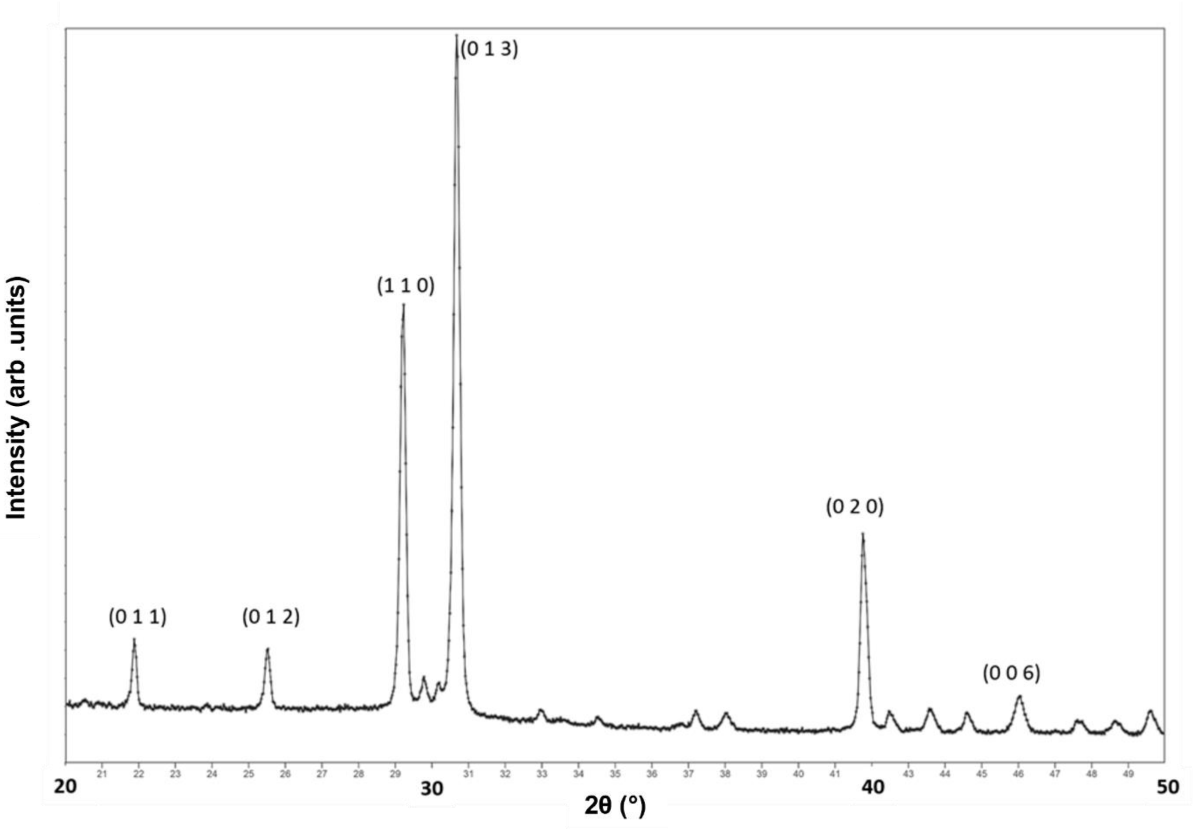

Figure 3.8 XRD pattern of $Ba_3Lu_2O_5CO_3$ synthesised at 980°C detailing the main Miller Indices of the P4/mmm space group

3.3.1.2.2 Rietveld Refinement using XRD Data

Using the Ln = Yb structural model (replacing Yb with Lu), a Rietveld refinement was performed using the XRD data for the Ln = Lu system. Structure refinement using XRD data comes with the downfall that X-ray scattering occurs from interaction with electrons, meaning that larger atoms are weighted much greater making it difficult to determine refinement values for lighter atoms such as C and O. To compensate for this, certain restrictions were applied to the refinement such as softly restrained (allowing for some deviation from the ideal values) carbonate bond lengths (1.28 Å) and angles (120°), as well as equally constrained U_{iso} values (C1 = Lu1, O1 = O2 = O3 = O4). The observed, calculated and difference profiles are shown in ***Figure 3.9*** with structural parameters and bond distances given in ***Table 3.4*** and ***Table 3.5*.**

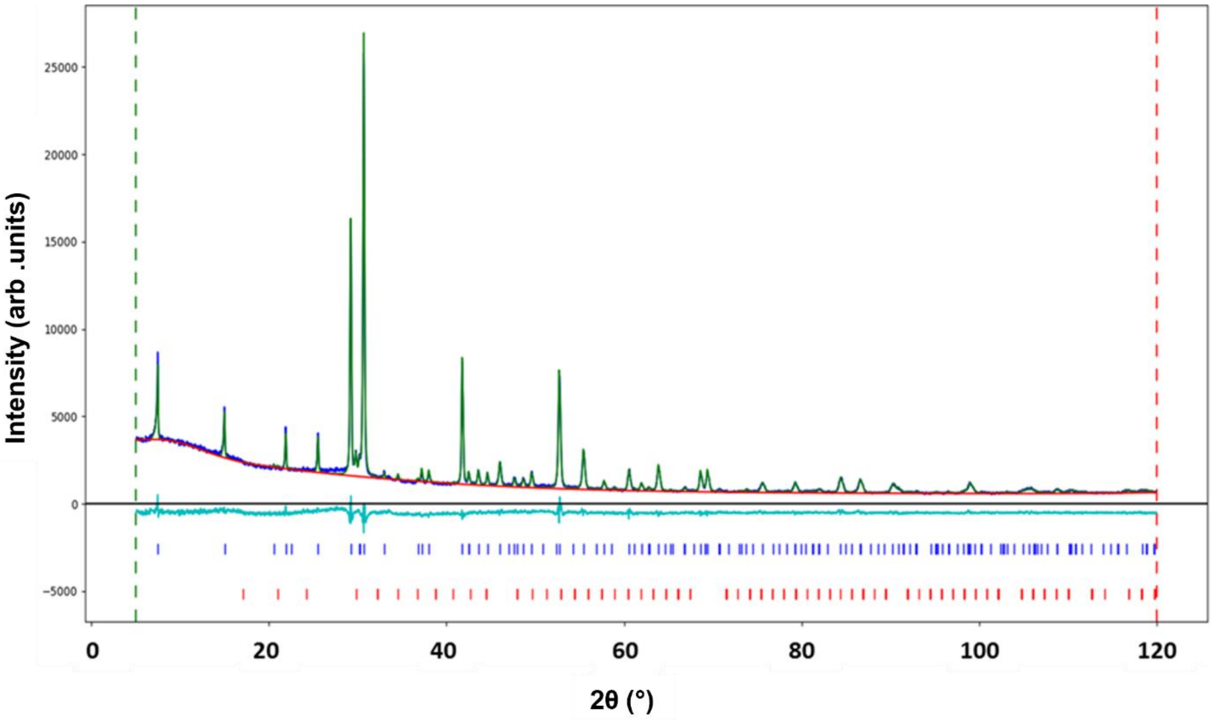

Figure 3.9 Observed, calculated and difference profiles of $Ba_3Lu_2O_5CO_3$ XRD data (Lower tick marks ï Lu_2O_3 (4wt%), upper tick marks $Ba_3Lu_2O_5CO_3$ (96wt%))

Table 3.4 Refined structural values of $Ba_3Lu_2O_5CO_3$ XRD data

Atom	**x**	**y**	**z**	**Site Occupancy**	**Wyckoff Position**	**Uiso**
C1	0.5	0.357(4)	0.5	0.250	4o	0.006(1)
Ba1	0.0	0.0	0.0	1.000	1a	0.015(1)
Ba2	0.0	0.0	0.337(1)	1.000	2g	0.008(1)
Lu1	0.5	0.5	0.176(1)	1.000	2h	0.006(1)
O1	0.0	0.5	0.199(1)	1.000	4i	0.074(5)
O2	0.5	0.5	0.0	1.000	1c	0.074(5)
O3	0.5	0.099(17)	0.5	0.210	4o	0.074(5)
O4	0.490(6)	0.5	0.404(1)	0.270	8t	0.074(5)

R_{wp} = 4.54% GOF = 1.72 (*P*4/*mmm* *a* = 4.3226(1) Å, *c* = 11.8295(3) Å)

Table 3.5 Selected interatomic distances of $Ba_3Lu_2O_5CO_3$

Bond	**Bond Length / Å**	**Bond**	**Bond Length / Å**
C1 – O3	1.275(45) (x1)	**Ba2 – O3**	2.931(5) (x2)*
C1 – O4	1.307(18) (x2)	**Ba2 – O4**	2.962(25) (x4)*
Ba1 – O1	3.198(10) (x8)	**Lu1 – O1**	2.179(1) (x4)
Ba1 – O2	3.057(1) (x4)	**Lu1 – O2**	2.080(2) (x1)
Ba2 – O1	2.703(8) (x4)	**Lu1 – O4**	2.658(13) (x1)

*dependent on orientation of carbonate group

Structure refinement indicated a small amount (4wt %) of Lu_2O_3 impurity. Attempts were made to reduce this rare earth oxide impurity by compensating with a greater excess of $BaCO_3$, however, this led to quicker formation and larger impurities of the simple oxide $Ba_3Lu_4O_9$. It should be noted that this was the case for all $Ba_3Ln_2O_5CO_3$ systems and so the +3% excess of $BaCO_3$ was kept throughout.

When compared to that of the Ln = Yb system there appears to be significant positional shifts in relation to the carbonate atoms (C1, O3, O4) as well as significant error values for these positions. These values can be attributed to the difficulties mentioned previously regarding structure refinement using XRD data, application of the restrictions or as it is such a large variation in the position of the carbonate may have a different orientation in this system. The unit cell volume of the Ln = Lu system is less than that of the Ln = Yb system as expected due to the smaller atomic radii of six coordinate Lu^{3+} (0.861 Å) in comparison to six coordinate Yb^{3+} (0.868 Å).[171]

3.3.1.2.3 Raman Spectroscopy

Raman data (***Figure 3.10***) supports the inclusion of carbonate in the $Ba_3Lu_2O_5CO_3$ system with the appearance of the expected v_1 (symmetric stretch), v_3 (doubly degenerate asymmetric stretch) and v_4 (doubly degenerate asymmetric bend) carbonate vibrational modes[165] recorded with the bands at lower wavenumbers in comparison to those seen in $BaCO_3$ (***Table 3.6***) suggesting longer bond lengths/weakening of the carbonate bonds, albeit this shift is not as great as those seen for the Ln = Yb system.

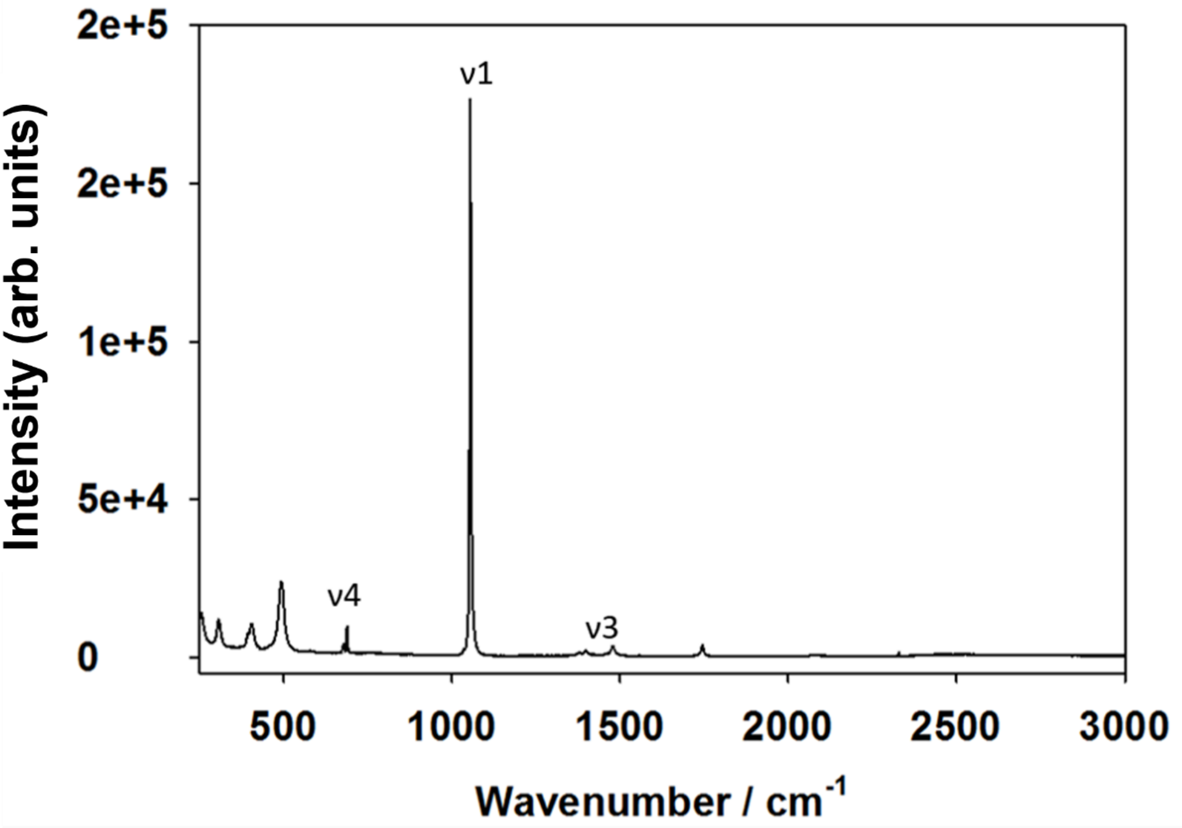

Figure 3.10 Raman spectroscopy data for $Ba_3Lu_2O_5CO_3$ detailing specific Raman bands seen for carbonate vibrational modes

Table 3.6 Raman band wavenumbers for carbonate vibrational modes of $BaCO_3$ and $Ba_3Lu_2O_5CO_3$

System	**ν 1 /$^{-1}$ c m**	**ν 3 /$^{-1}$ c m**	**ν 4 /$^{-1}$ c m**
$BaCO_3$	1059.5	1420.2 1508.1	690.8 699.2
$Ba_3Lu_2O_5CO_3$	1054.5	1398.2 1478.9	678.1 688.6

3.3.1.3 $Ba_3Tm_2O_5CO_3$ (Ln = Tm)

3.3.1.3.1 Powder X-Ray Diffraction

A 3:1 reagent ratio of $BaCO_3$:Tm_2O_3 was used to successfully synthesise the $Ba_3Tm_2O_5CO_3$ system in air at 1000°C with the XRD pattern shown in ***Figure 3.11***. As for its Ln = Yb counterpart, heating at temperatures above 1000°C, this compound was shown to decompose, and the formation of the simple oxide $Ba_3Tm_4O_9$ was observed.

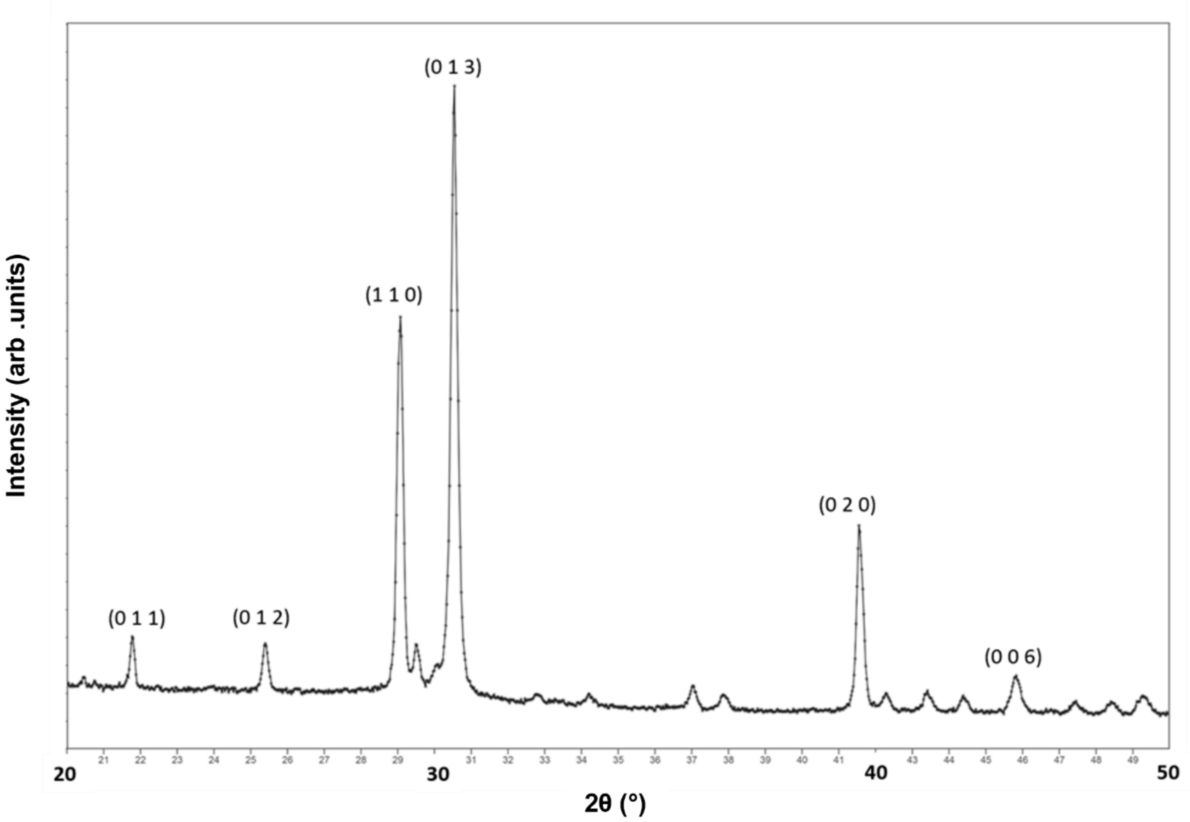

Figure 3.11 XRD pattern of $Ba_3Tm_2O_5CO_3$ synthesised at 980°C detailing the main Miller Indices of the P4/mmm space group

3.3.1.3.2 Rietveld Refinement Using XRD Data

Using the Ln = Yb structural model (replacing Yb with Tm), a Rietveld refinement was performed using the XRD data of the Ln = Tm system. Carbonate bond lengths (1.28 Å) and angles (120°) were softly restrained, with U_{iso} values being equally constrained

(C1 = Lu1, O1 = O2 = O3 = O4). The observed, calculated and difference XRD profiles are shown in ***Figure 3.12*** with structural parameters and bond distances given in ***Table 3.7*** and ***Table 3.8***.

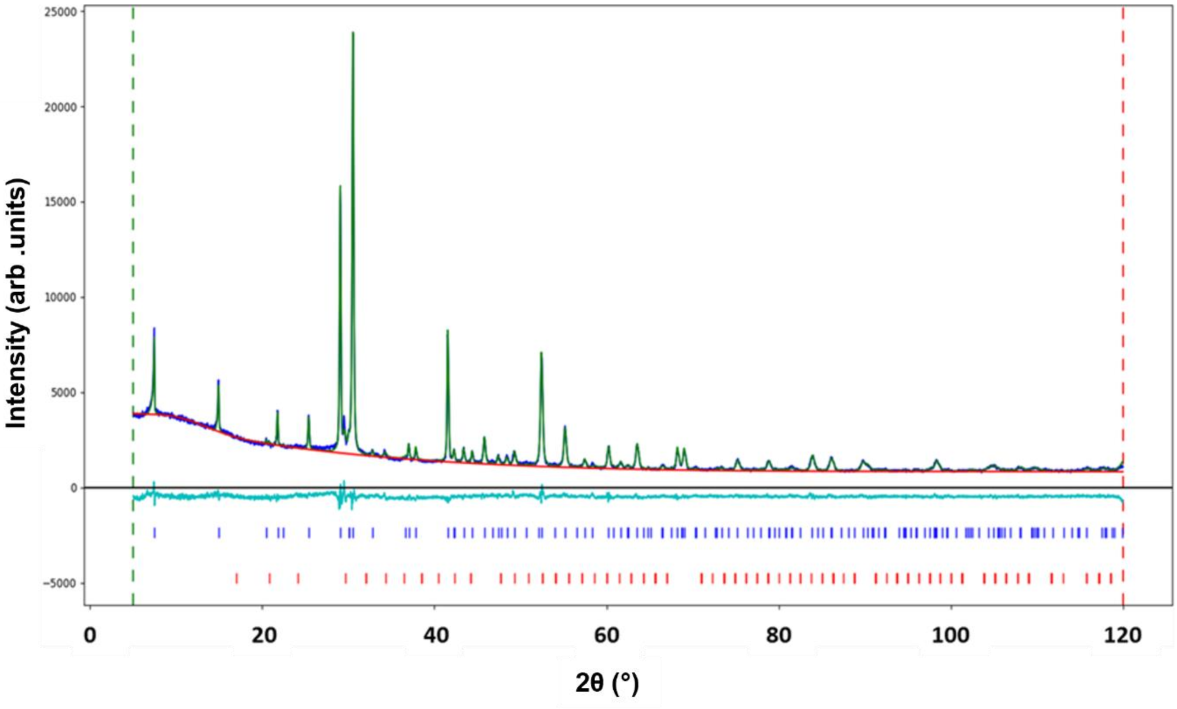

Figure 3.12 Observed, calculated and difference profiles of $Ba_3Tm_2O_5CO_3$ XRD data (Lower tick marks ï Tm_2O_3 (4wt%), upper tick marks $Ba_3Tm_2O_5CO_3$ (96wt%))

Table 3.7 Refined structural values of $Ba_3Tm_2O_5CO_3$ XRD data

Atom	x	y	z	Site Occupancy	Wyckoff Position	Uiso
C1	0.5	0.470(8)	0.5	0.250	4o	0.008(1)
Ba1	0.0	0.0	0.0	1.000	1a	0.014(2)
Ba2	0.0	0.0	0.336(1)	1.000	2g	0.014(1)
Tm1	0.5	0.5	0.177(1)	1.000	2h	0.008(2)
O1	0.0	0.5	0.204(1)	1.000	4i	0.037(5)
O2	0.5	0.5	0.0	1.000	1c	0.037(5)
O3	0.5	0.174(9)	0.5	0.210	4o	0.037(5)
O4	0.371(7)	0.5	0.404(1)	0.270	8t	0.037(5)

R_{wp} = 4.08% GOF = 1.66 (*P*4/*mmm* *a* = 4.3442(1) Å, *c* = 11.8803(4) Å)

Table 3.8 Selected interatomic distances of $Ba_3Tm_2O_5CO_3$

Bond	Bond Length / Å	Bond	Bond Length / Å
C1 – O3	1.286(52) (x1)	**Ba2 – O3**	3.012(28) (x2)*
C1 – O4	1.321(19) (x2)	**Ba2 – O4**	2.808(18) (x4)*
Ba1 – O1	3.256(12) (x8)	**Tm1 – O1**	2.196(2) (x4)
Ba1 – O2	3.072(1) (x4)	**Tm1 – O2**	2.101(3) (x1)
Ba2 – O1	2.680(9) (x4)	**Tm1 – O4**	2.709(14) (x1)

*dependent on orientation of carbonate group

Structure refinement using the XRD data indicated a small amount (4wt %) of Tm_2O_3 impurity. When compared to that of the Ln = Yb system there is some positional shift in relation to the carbonate atoms but by a smaller magnitude of that seen for Ln =Lu as well as significant error values for these related positions. These values could be attributed to the difficulties mentioned previously regarding structure refinement using XRD data and/or the addition of the refinement restrictions. The unit cell volume of the

Ln = Tm system is larger than that of the Ln = Yb system, which is to be expected due to the larger atomic radii of six coordinate Tm^{3+} (0.880 Å) in comparison to six coordinate Yb^{3+} (0.868 Å). [166]

3.3.1.3.3 Raman Spectroscopy

Raman data (***Figure 3.13***) confirmed the inclusion of carbonate in the $Ba_3Tm_2O_5CO_3$ system with the appearance of the expected v_1 (symmetric stretch), v_3 (doubly degenerate asymmetric stretch) and v_4 (doubly degenerate asymmetric bend) carbonate vibrational modes[165]. The bands were at lower wavenumbers in comparison to those seen in $BaCO_3$ (***Table 3.9***) suggesting longer bond lengths/weakening of the carbonate bonds, however this shift is greater than those seen for the Ln = Yb, Lu systems.

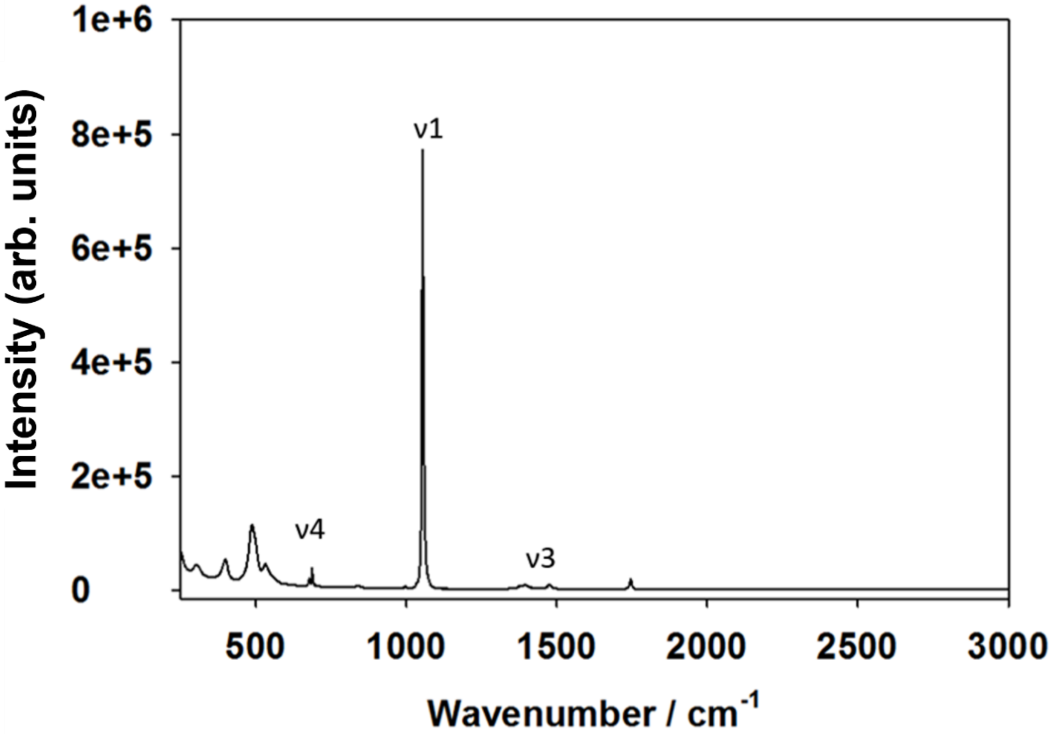

Figure 3.13 Raman spectroscopy data for $Ba_3Tm_2O_5CO_3$ detailing specific Raman bands seen for carbonate vibrational modes

Table 3.9 Raman band wavenumbers for carbonate vibrational modes of $BaCO_3$ and $Ba_3Tm_2O_5CO_3$

System	**ν 1 /$^{-1}$ c m**	**ν 3 /$^{-1}$ c m**	**ν 4 /$^{-1}$ c m**
$BaCO_3$	1059.5	1420.2 1508.1	690.8 699.2
$Ba_3Tm_2O_5CO_3$	1053.5	1394.4 1476.1	678.1 687.6

3.3.1.4 $Ba_3Er_2O_5CO_3$ (Ln = Er)

3.3.1.4.1 Powder X-Ray Diffraction

A 3:1 reagent ratio of $BaCO_3$:Er_2O_3 was also used to successfully synthesise the $Ba_3Er_2O_5CO_3$ system in dry N_2 at 1050°C with the XRD pattern shown in ***Figure 3.14***, however it is apparent some reagent remains; longer heating at the synthesis temperature may reduce these but also may give rise to issues with further Ba volatility. Like its Ln = Yb counterpart, heating at temperatures above 1050°C in N_2 led to decomposition, and the formation of the simple oxide $Ba_3Er_4O_9$.

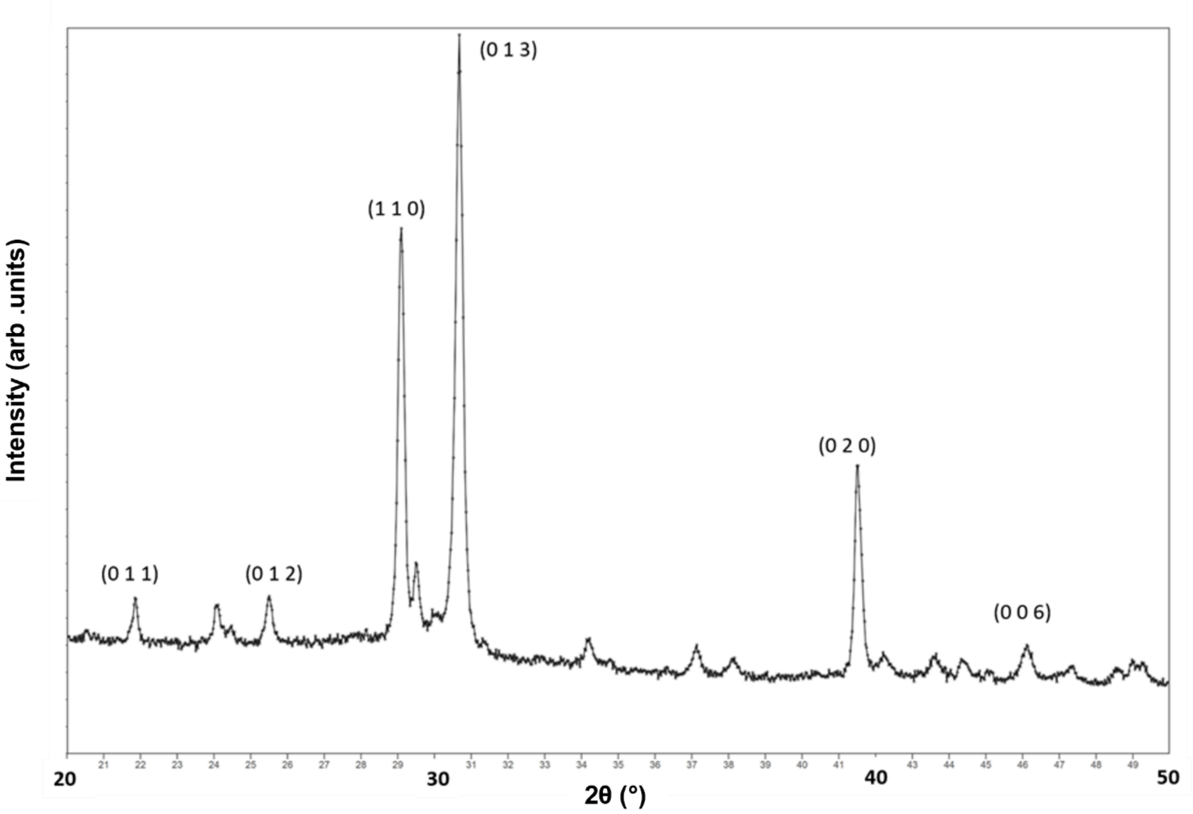

Figure 3.14 XRD pattern of $Ba_3Er_2O_5CO_3$ synthesised at 980°C detailing the main Miller Indices of the P4/mmm space group

3.3.1.4.2 Rietveld Refinement Using XRD Data

Using the Ln = Yb structural model replacing Yb with Er, a Rietveld refinement was performed using the XRD data of the Ln = Er system. Carbonate bond lengths (1.28 Å) and angles (120°) were softly restrained, with U_{iso} values being equally constrained (C1 = Lu1, O1 = O2 = O3 = O4). The observed, calculated and difference XRD profiles are shown in ***Figure 3.15*** with structural parameters and bond distances given in ***Table 3.10*** and ***Table 3.11***.

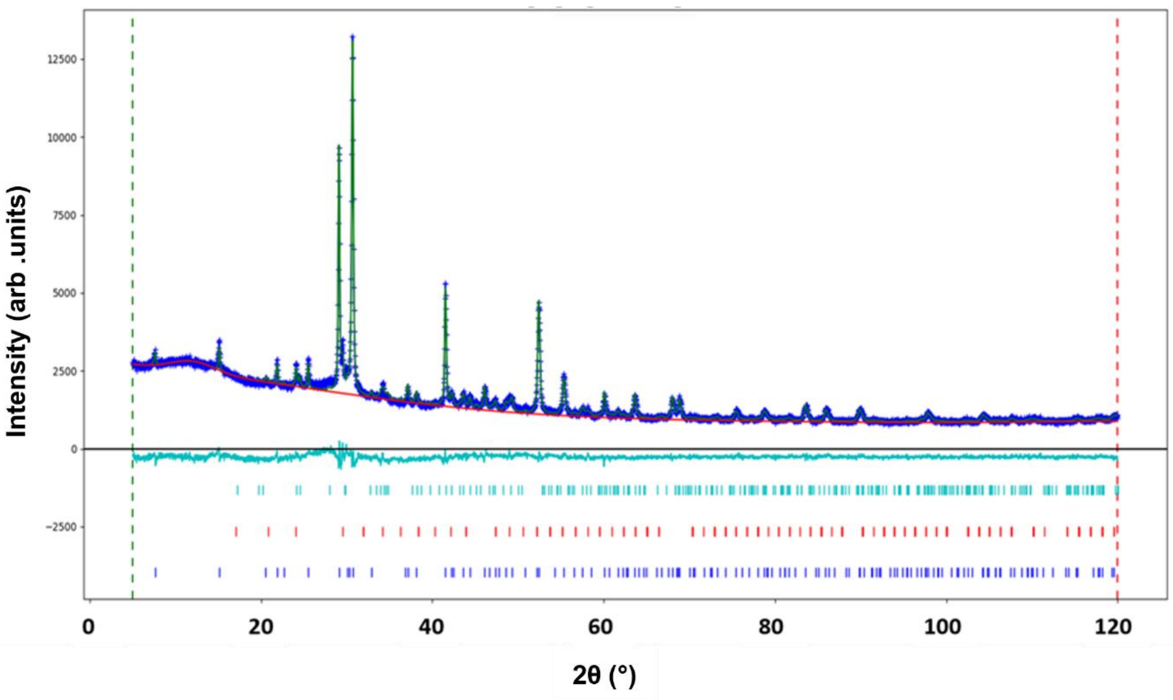

Figure 3.15 Observed, calculated and difference profiles of $Ba_3Er_2O_5CO_3$ XRD data (Lower tick marks ï $Ba_3Er_2O_5CO_3$ (86wt%), middle tick marks ï $BaCO_3$ (7wt%), upper tick marks - Er_2O_3 (7wt%))

Table 3.10 Refined structural values of $Ba_3Er_2O_5CO_3$ XRD data

Atom	x	y	z	Site Occupancy	Wyckoff Position	Uiso
C1	0.5	0.444(14)	0.5	0.250	4o	0.012(2)
Ba1	0.0	0.0	0.0	1.000	1a	0.016(2)
Ba2	0.0	0.0	0.337(4)	1.000	2g	0.016(2)
Er1	0.5	0.5	0.178(1)	1.000	2h	0.012(2)
O1	0.0	0.5	0.221(2)	1.000	4i	0.068(8)
O2	0.5	0.5	0.0	1.000	1c	0.068(8)
O3	0.5	0.150(14)	0.5	0.210	4o	0.068(8)
O4	0.396(13)	0.5	0.400(1)	0.270	8t	0.068(8)

R_{wp} = 3.94% GOF = 1.53 (*P4/mmm* *a* = 4.3675(3) Å, *c* = 11.86266(6) Å)

Table 3.11 Selected interatomic distances of $Ba_3Er_2O_5CO_3$

Bond	Bond Length / Å	Bond	Bond Length / Å
C1 – O3	1.284(86) (x1)	**Ba2 – O3**	2.989(14) (x2)*
C1 – O4	1.296(26) (x2)	**Ba2 – O4**	2.884(34) (x4)*
Ba1 – O1	3.415(19) (x8)	**Er1 – O1**	2.242(6) (x4)
Ba1 – O2	3.088(1) (x4)	**Er1 – O2**	2.117(5) (x1)
Ba2 – O1	2.579(13) (x4)	**Er1 – O4**	2.664(15) (x1)

*dependent on orientation of carbonate group

Structure refinement using the XRD data indicated a significant amount of Er_2O_3 (7%) and $BaCO_3$ (7%) impurities which may be remedied by further heating. When compared to that of the Ln = Yb system there is slight positional shift in relation to the carbonate atoms. Significant error values on carbonate atomic positions could be attributed to the difficulties mentioned previously regarding XRD data refinement, application of the restrictions or disorder in the carbonate orientation. The unit cell volume of the Ln = Er system is larger than that of the Ln = Yb system which is expected due to the larger atomic radii of six coordinate Er^{3+} (0.890 Å) in comparison to six coordinate Yb^{3+} (0.868 Å).[166]

3.3.1.4.3 Raman Spectroscopy

The Raman spectrum for this sample is shown in ***Figure 3.16***. In this case it was difficult to ascertain the positions of any expected v_1 (symmetric stretch), v_3 (doubly degenerate asymmetric stretch) and v_4 (doubly degenerate asymmetric bend) carbonate vibrational modes[165]. The difficulty most likely lies with the presence of Er^{3+}, as this is well known for its photoluminescent properties absorbing energy from the 532 nm laser and reaching an excited state.[167] Upon relaxation from this state, the

Er^{3+} releases photons with varying energy (depending on relaxation route) which are then detected by the Raman Spectrometer causing these large and wide bands. Close inspection of this spectrum does indeed support the presence of the most prominent v_1 (symmetric stretch), in this case as a small shoulder of a much larger band (1071.6 cm^{-1}) but this information must be taken with caution. If true, then the v_1 band recorded appears at lower wavenumbers in comparison to that seen in $BaCO_3$ (***Table 3.12***). In support of this assignment this shift would keep in the trend of being greater than those seen for the Ln = Yb, Lu, Tm systems.

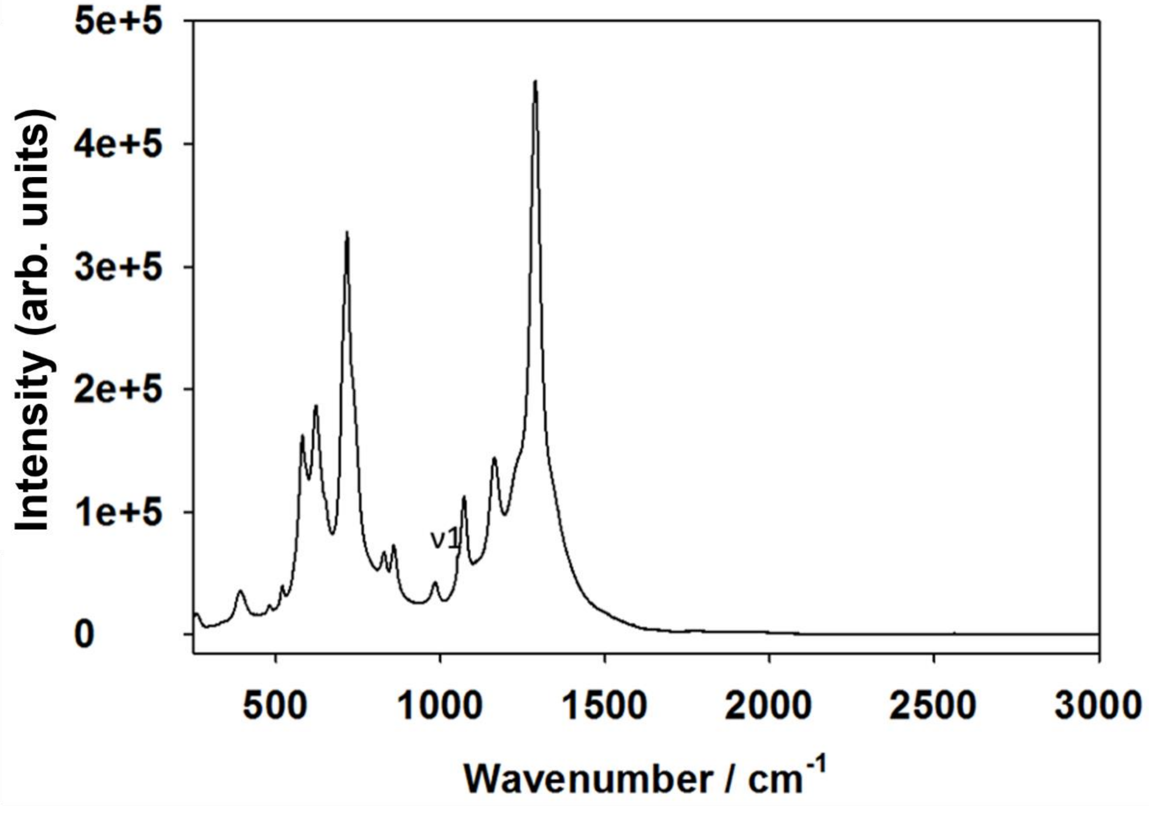

Figure 3.16 Raman spectroscopy data for $Ba_3Er_2O_5CO_3$ detailing specific Raman bands seen for carbonate vibrational modes

Table 3.12 Raman band wavenumbers for carbonate vibrational modes of $BaCO_3$ and $Ba_3Er_2O_5CO_3$

System	**ν 1 /$^{-1}$ c m**	**ν 3 /$^{-1}$ c m**	**ν 4 /$^{-1}$ c m**
$BaCO_3$	1059.5	1420.2 1508.1	690.8 699.2
$Ba_3Er_2O_5CO_3$	1052.5	- -	- -

Raman data was also recorded using a 633 nm laser (***Figure 3.17***); however, this spectrum also experiences the same issue of photoluminescence from Er^{3+} ions.

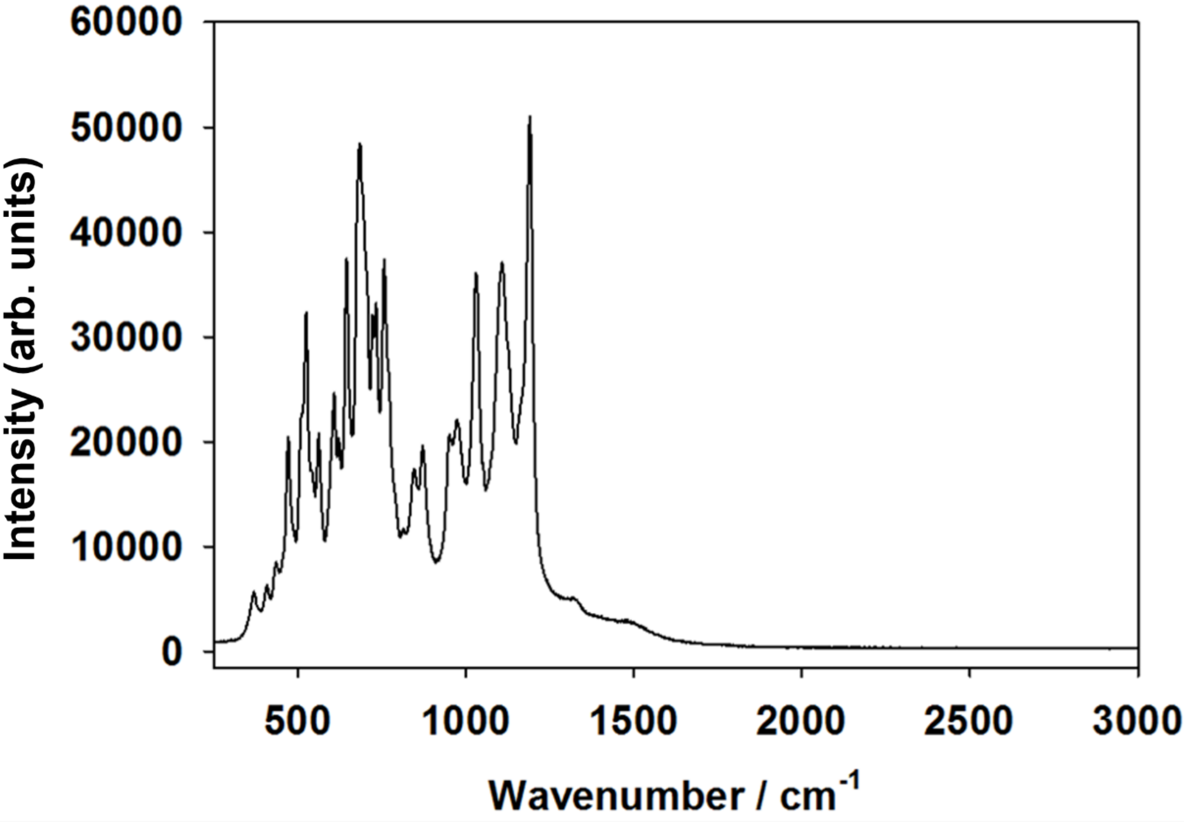

Figure 3.17 Raman spectroscopy data for $Ba_3Er_2O_5CO_3$ showing multiple peaks which makes it difficult conclusively determine any carbonate vibrational mode Raman bands

3.3.1.5 $Ba_3Ho_2O_5CO_3$ (Ln = Ho)

3.3.1.5.1 Powder X-Ray Diffraction

A 3:1 reagent ratio of $BaCO_3$:Ho_2O_3 was used to successfully synthesise the $Ba_3Ho_2O_5CO_3$ system in dry N_2 at 1000°C with the XRD pattern shown in ***Figure 3.18***. Synthesis of this system in air at 1000°C leads to the formation of large amounts of $Ba_3Ho_4O_9$ and $BaHo_2O_4$ impurities. Heating at temperatures above 1000°C in dry N_2 also causes decomposition of this system and formation of the simple oxide $Ba_3Ho_4O_9$.

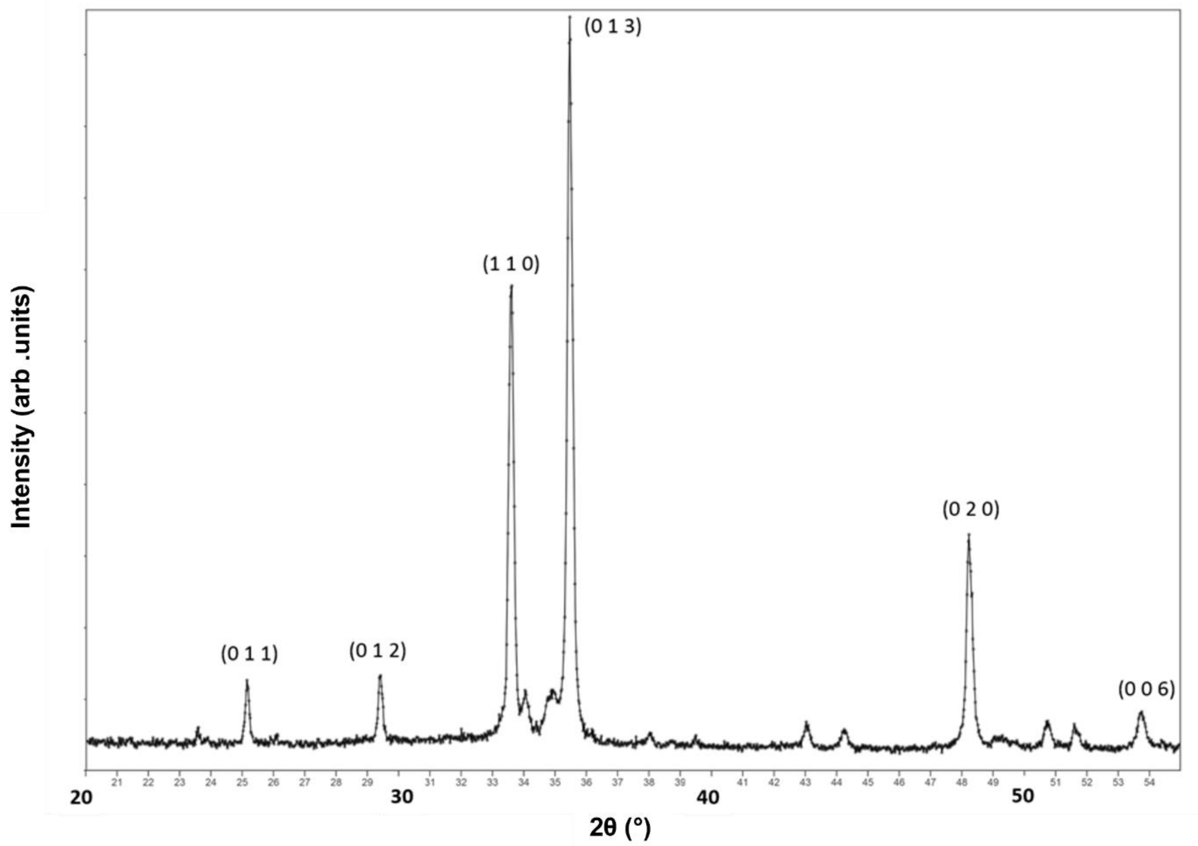

Figure 3.18 XRD pattern of $Ba_3Ho_2O_5CO_3$ synthesised at 980°C detailing the main Miller Indices of the P4/mmm space group

3.3.1.5.2 Rietveld Refinement Using XRD Data

Using the Ln = Yb structural model (replacing Yb with Ho), a Rietveld refinement was performed using the XRD data of the Ln = Ho system. Carbonate bond lengths (1.28 Å) and angles (120°) were softly restrained, with U_{iso} values being equally constrained (C1 = Lu1, O1 = O2 = O3 = O4). The observed, calculated and difference XRD profiles are shown in ***Figure 3.19*** with structural parameters and bond distances given in ***Table 3.13*** and ***Table 3.14***.

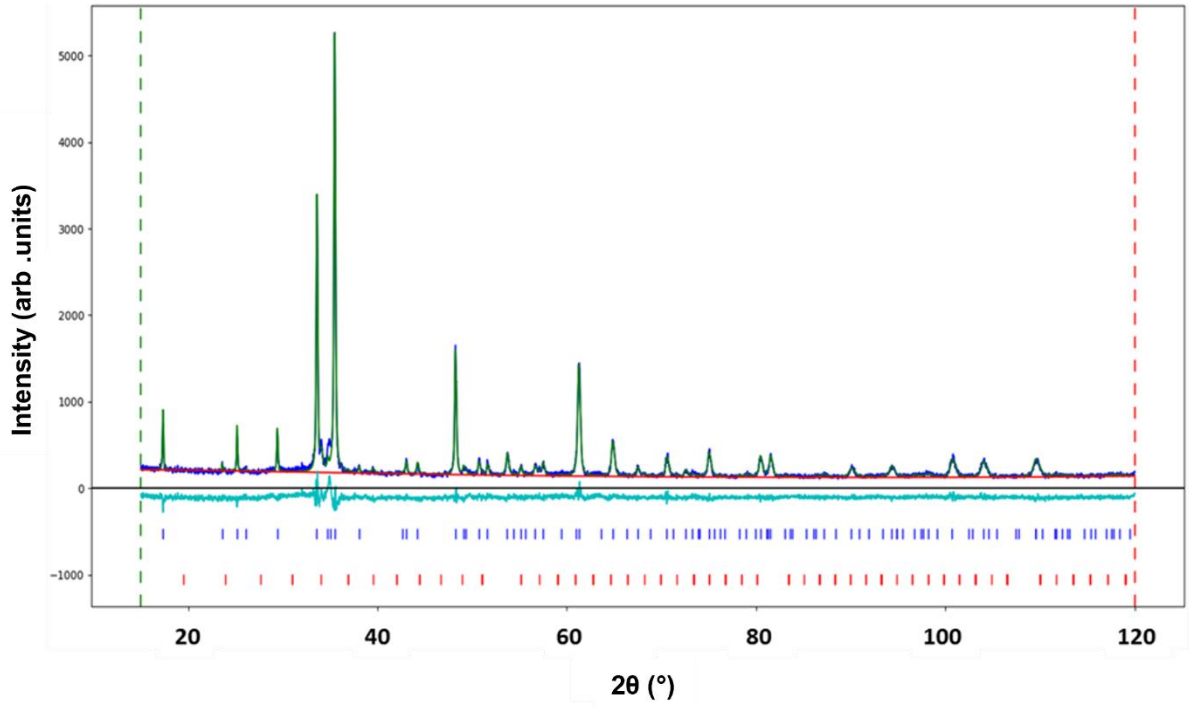

Figure 3.19 Observed, calculated and difference profiles of $Ba_3Ho_2O_5CO_3$ XRD data (Lower tick marks ï Ho_2O_3 (3wt%), upper tick marks $Ba_3Ho_2O_5CO_3$ (97wt%))

Table 3.13 Refined structural values of $Ba_3Ho_2O_5CO_3$ XRD data

Atom	x	y	z	Site Occupancy	Wyckoff Position	Uiso
C1	0.5	0.355(18)	0.5	0.250	4o	0.002(1)
Ba1	0.0	0.0	0.0	1.000	1a	0.012(2)
Ba2	0.0	0.0	0.337(3)	1.000	2g	0.013(2)
Ho1	0.5	0.5	0.177(3)	1.000	2h	0.002(1)
O1	0.0	0.5	0.208(2)	1.000	4i	0.081(6)
O2	0.5	0.5	0.0	1.000	1c	0.081(6)
O3	0.5	0.072(18)	0.5	0.210	4o	0.081(6)
O4	0.484(22)	0.5	0.403(3)	0.270	8t	0.081(6)

R_{wp} = 9.07% GOF = 1.33 (*P*4/*mmm* *a* = 4.3814(2) Å, *c* = 11.8875(4) Å)

Table 3.14 Selected interatomic distances of $Ba_3Ho_2O_5CO_3$

Bond	Bond Length / Å	Bond	Bond Length / Å
C1 – O3	1.284(11) (x1)	**Ba2 – O3**	2.944(9) (x2)*
C1 – O4	1.293(46) (x2)	**Ba2 – O4**	3.151(65) (x4)*
Ba1 – O1	3.300(20) (x8)	**Ho1 – O1**	2.221(4) (x4)
Ba1 – O2	3.098(1) (x4)	**Ho1 – O2**	2.105(3) (x1)
Ba2 – O1	2.675(15) (x4)	**Ho1 – O4**	2.693(32) (x1)

*dependent on orientation of carbonate group

Refinement of the data indicated a small amount (3wt %) of Ho_2O_3 impurity. When compared to that of the Ln = Yb system there appears to be significant positional shifts in relation to the carbonate atoms which could be attributed to the difficulties mentioned previously regarding XRD data refinement, application of the restrictions or as it is such a large variation in position, carbonate may have a different orientation in this system. The unit cell volume of the Ln = Ho system is larger than that of the Ln = Yb system which is expected due to the smaller atomic radii of six coordinate Ho^{3+} (0.901 Å) in comparison to six coordinate Yb^{3+} (0.868 Å).[166]

3.3.1.5.3 Raman Spectroscopy

Figure 3.20 shows the inclusion of carbonate in the $Ba_3Ho_2O_5CO_3$ system with the appearance of the expected v_1 (symmetric stretch) carbonate vibrational modes[165] with no prominent bands between 1350 – 1500 cm^{-1} to accurately determine the v_3 (doubly degenerate asymmetric stretch) vibrational mode positions. Like the Ln = Er system, Ho^{3+} also has well known photoluminescent properties causing large and broad bands below 1000 cm^{-1} making it difficult to determine any v_4 (doubly degenerate asymmetric bend) carbonate vibrational modes. Towards the high end of the spectrum (>2600 cm^{-1}) it can be seen that another large band not seen for other Ln systems is present. This suggests the presence of water (O – H stretch) in this sample, which likely required further drying before this analysis. The v_1 band recorded appears at lower wavenumbers in comparison to that seen in $BaCO_3$ (***Table 3.15***) as for the other systems.

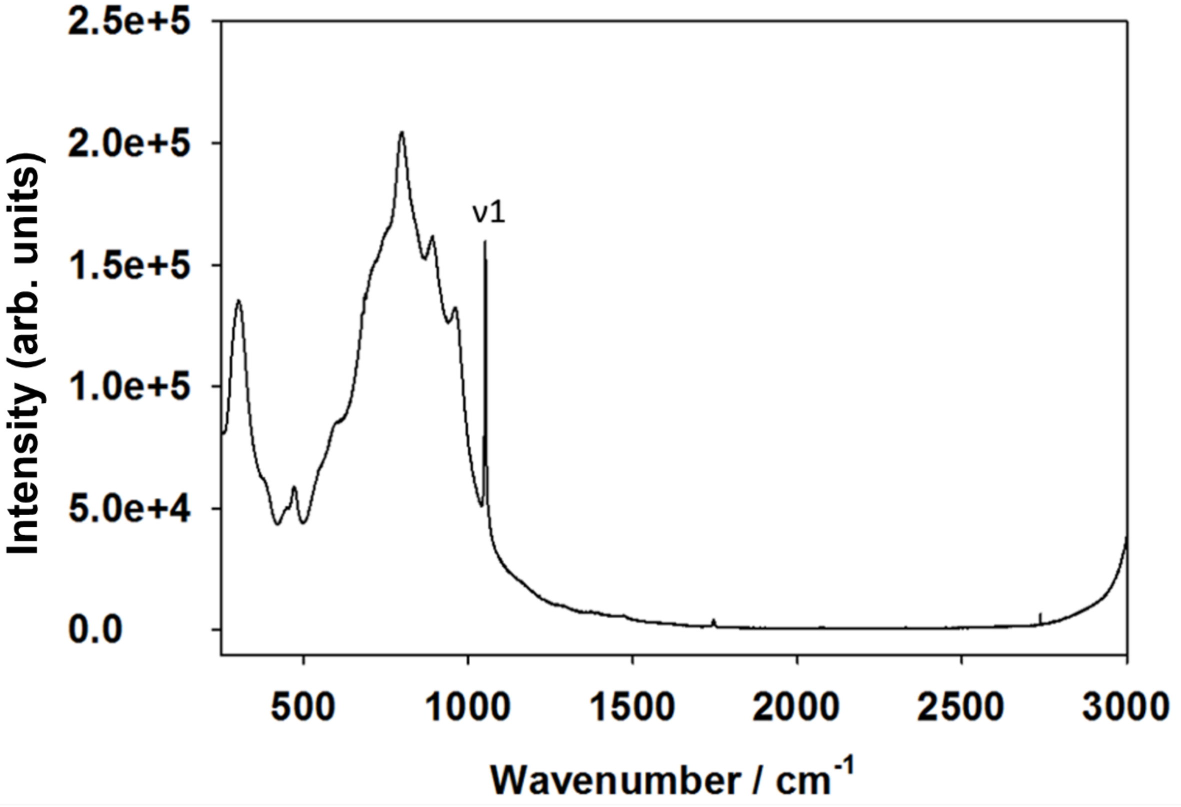

Figure 3.20 Raman spectroscopy data for $Ba_3Ho_2O_5CO_3$ detailing specific Raman bands seen for carbonate vibrational modes

Table 3.15 Raman band wavenumbers for carbonate vibrational modes of $BaCO_3$ and $Ba_3Ho_2O_5CO_3$

System	**ν 1/ cm^{-1}**	**ν 3 /$^{-1}$ c m**	**ν 4 /$^{-1}$ c m**
$BaCO_3$	1059.5	1420.2 1508.1	690.8 699.2
$Ba_3Ho_2O_5CO_3$	1051.5	- -	- -

3.3.1.6 $Ba_3Dy_2O_5CO_3$ (Ln = Dy)

3.3.1.6.1 Powder X-Ray Diffraction

A 3:1 reagent ratio of $BaCO_3$:Dy_2O_3 was used to successfully synthesise the $Ba_3Dy_2O_5CO_3$ system in dry N_2 at 1000°C with the XRD pattern shown in ***Figure 3.21***, Synthesis of this system in air at 1000°C leads to the formation of larger amounts of $Ba_3Dy_4O_9$ and $BaDy_2O_4$ impurities. Heating at temperatures above 1000°C or for a prolonged amount of time in dry N_2 causes decomposition of this system and formation to the simple oxides, $Ba_3Dy_4O_9$ and $BaDy_2O_4$.

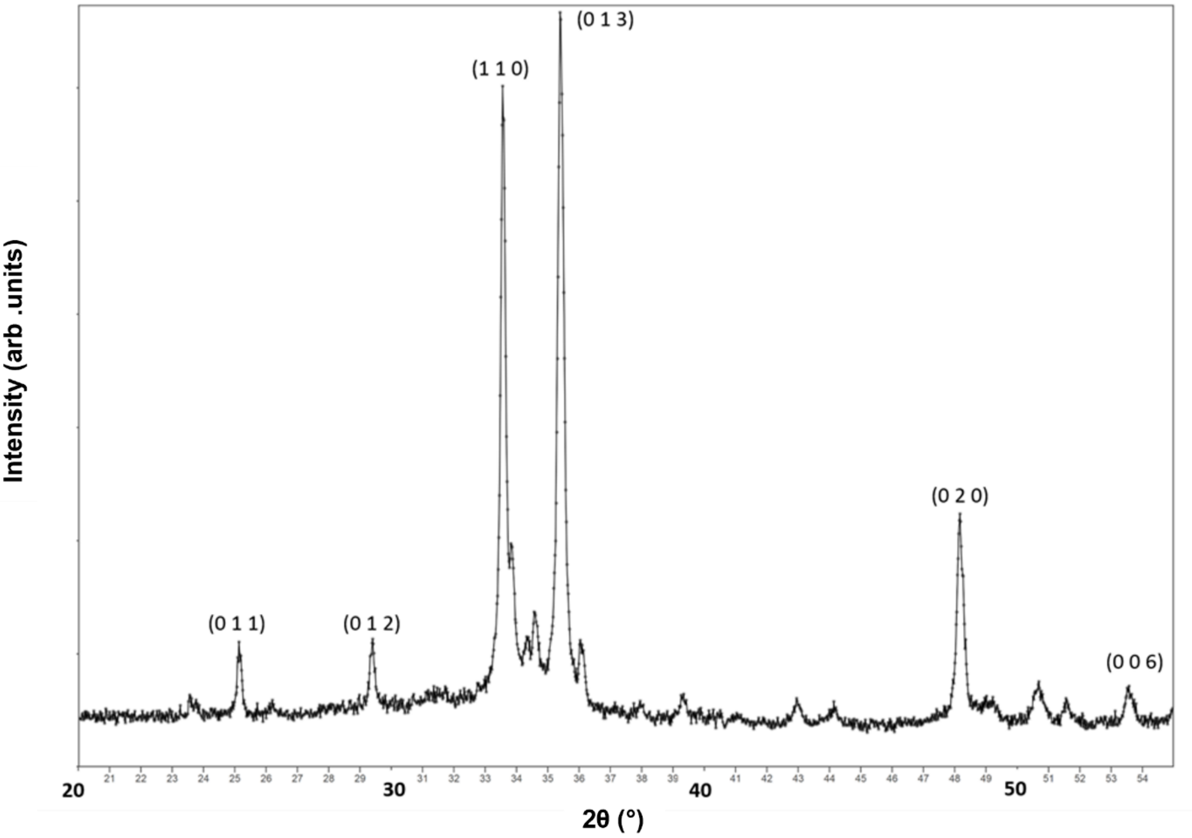

Figure 3.21 XRD pattern of $Ba_3Dy_2O_5CO_3$ synthesised at 980°C detailing the main Miller Indices of the P4/mmm space group

3.3.1.6.2 Rietveld Refinement Using XRD Data

Using the Ln = Yb structural model replacing Yb with Dy, a Rietveld refinement was performed using the XRD data for the Ln = Dy system. Carbonate bond lengths (1.28 Å) and angles (120°) were softly restrained, with U_{iso} values being equally constrained (C1 = Dy1, O1 = O2 = O3 = O4). The observed, calculated and difference XRD profiles are shown in ***Figure 3.22*** with structural parameters and bond distances given in ***Table 3.16*** and ***Table 3.17***.

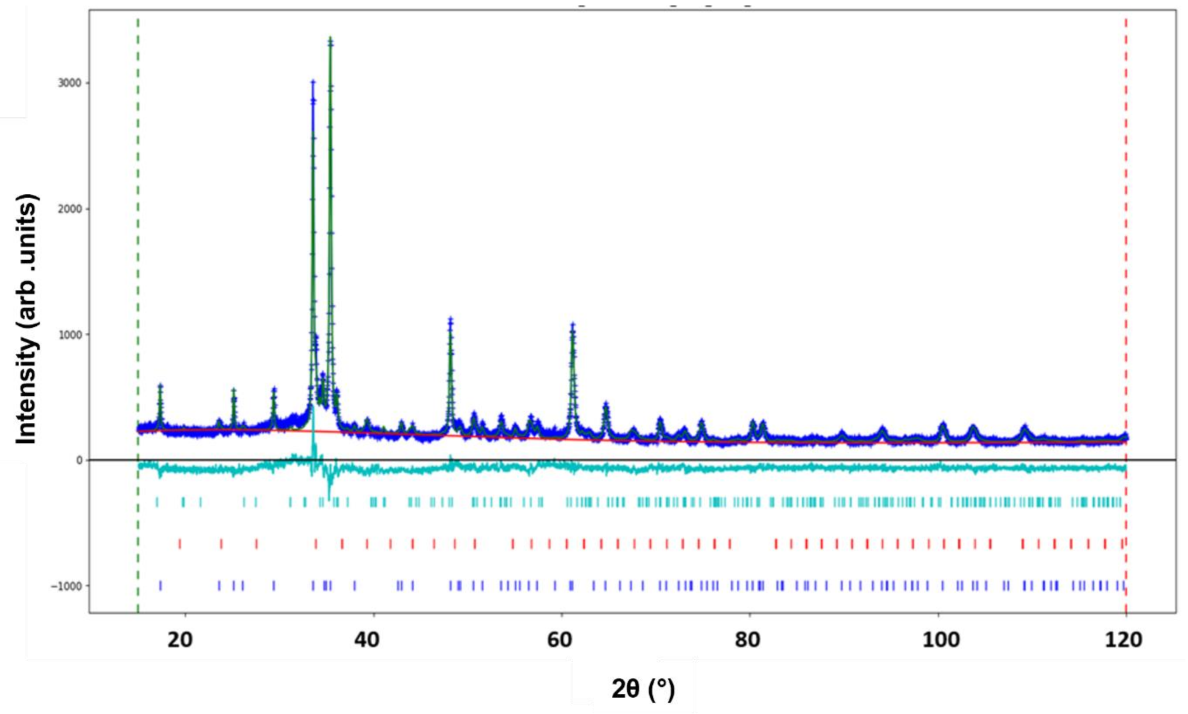

Figure 3.22 Observed, calculated and difference profiles of $Ba_3Dy_2O_5CO_3$ XRD data (Lower tick marks ï Dy_2O_3 (10wt%), middle tick marks ï $Ba_3Dy_4O_9$ (10wt%), upper tick marks $Ba_3Dy_2O_5CO_3$ (10wt%))

Table 3.16 Refined structural values of $Ba_3Dy_2O_5CO_3$ XRD data

Atom	x	y	z	Site Occupancy	Wyckoff Position	Uiso
C1	0.5	0.403(32)	0.5	0.250	4o	0.004(2)
Ba1	0.0	0.0	0.0	1.000	1a	0.034(4)
Ba2	0.0	0.0	0.339(1)	1.000	2g	0.014(3)
Dy1	0.5	0.5	0.176(1)	1.000	2h	0.004(2)
O1	0.0	0.5	0.214(4)	1.000	4i	0.105(14)
O2	0.5	0.5	0.0	1.000	1c	0.105(14)
O3	0.5	0.114(32)	0.5	0.210	4o	0.105(14)
O4	0.446(35)	0.5	0.403(3)	0.270	8t	0.105(14)

R_{wp} = 9.55% GOF = 1.44 (*P*4/*mmm* *a* = 4.3897(3) Å, *c* = 11.9239(8) Å)

Table 3.17 Selected interatomic distances of $Ba_3Dy_2O_5CO_3$

Bond	Bond Length / Å	Bond	Bond Length / Å
C1 – O3	1.273(118) (x1)	**Ba2 – O3**	2.953(22) (x2)*
C1 – O4	1.293(58) (x2)	**Ba2 – O4**	3.039(114) (x4)*
Ba1 – O1	3.366(36) (x8)	**Dy1 – O1**	2.241(9) (x4)
Ba1 – O2	3.104(1) (x4)	**Dy1 – O2**	2.099(3) (x1)
Ba2 – O1	2.656(27) (x4)	**Dy1 – O4**	2.675(29) (x1)

*dependent on orientation of carbonate group

Structure refinement using the data indicated a significant amount of Dy_2O_3 (10wt %) and $BaDy_2O_4$ (10wt %) impurities which would suggest that this system would require a slightly shorter heating time or even perhaps a slightly lower heating temperature. Large amount of impurity seen for this system, in particular $Ba_3Dy_4O_9$, could suggest that the Dy ionic radius is too large to be completely stable within this system. When compared to that of the Ln = Yb system there is slight positional shift in relation to the carbonate atoms. Significant error values; particularly with regard to the carbonate atomic positions could be attributed to the difficulties mentioned previously regarding XRD data refinement, application of the restrictions or disorder in the carbonate orientation. The unit cell volume of the Ln = Dy system is larger than that of the Ln = Yb system which is expected due to the larger atomic radii of six coordinate Dy^{3+} (0.912 Å) in comparison to six coordinate Yb^{3+} (0.868 Å).[166]

3.3.1.6.3 Raman Spectroscopy

Figure 3.23 shows the inclusion of carbonate in the $Ba_3Dy_2O_5CO_3$ system with the appearance of the expected v_1 (symmetric stretch) and v_4 (doubly degenerate asymmetric bend) carbonate vibrational modes[165]. Although there is a wide band between 1350 – 1500 cm^{-1} no band is prominent to accurately determine the v_3 (doubly degenerate asymmetric stretch) vibrational mode positions. Those bands that were recorded appeared at lower wavenumbers in comparison to those seen in $BaCO_3$ (***Table 3.18***) suggesting longer bond lengths/weakening of the carbonate bonds, however this shift is greater for v_1 than those seen for the Ln = Yb, Lu, Tm and Er systems. Whilst these are not the only Raman bands seen, these are of the most importance in the determination of carbonate presence, with the other more prominent bands (250-500 cm^{-1}) being associated with Dy-O vibrational modes.

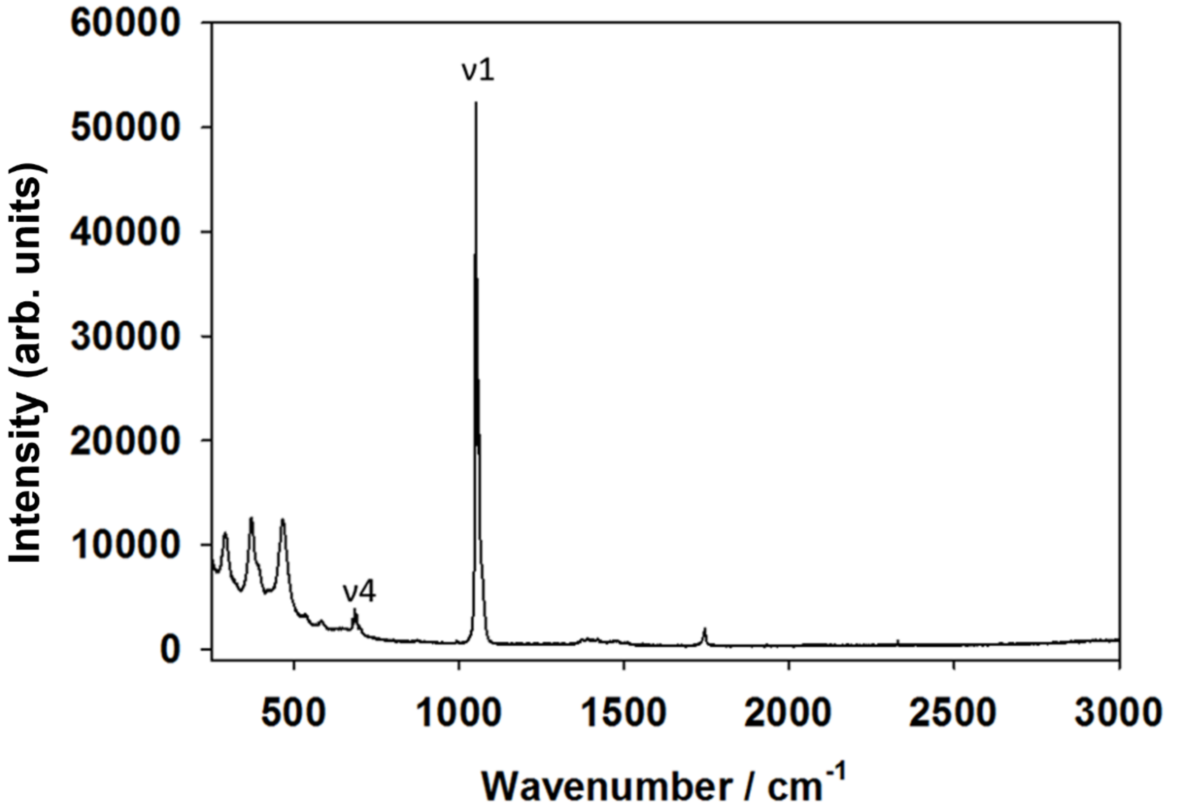

Figure 3.23 Raman spectroscopy data for $Ba_3Dy_2O_5CO_3$ detailing specific Raman bands seen for carbonate vibrational modes

Table 3.18 Raman band wavenumbers for carbonate vibrational modes of $BaCO_3$ and $Ba_3Dy_2O_5CO_3$

System	ν 1 /$^{-1}$ cm	ν 3 /$^{-1}$ cm	ν 4 /$^{-1}$ cm
$BaCO_3$	1059.5	1420.2 1508.1	690.8 699.2
$Ba_3Dy_2O_5CO_3$	1051.5	- -	673.8 684.4

3.3.1.7 $Ba_3Y_2O_5CO_3$ (Ln = Y)

3.3.1.7.1 Power X-Ray Diffraction

A 3:1 reagent ratio of $BaCO_3$:Y_2O_3 was used to synthesise the $Ba_3Y_2O_5CO_3$ system in dry N_2 at 1000°C with the XRD pattern shown in ***Figure 3.24***, albeit showing the appearance of some impurity. Synthesis of this system in air at 1000°C leads to the formation of large amounts of $Ba_3Y_4O_9$ and BaY_2O_4 impurities, showing difficulties in its synthesis.

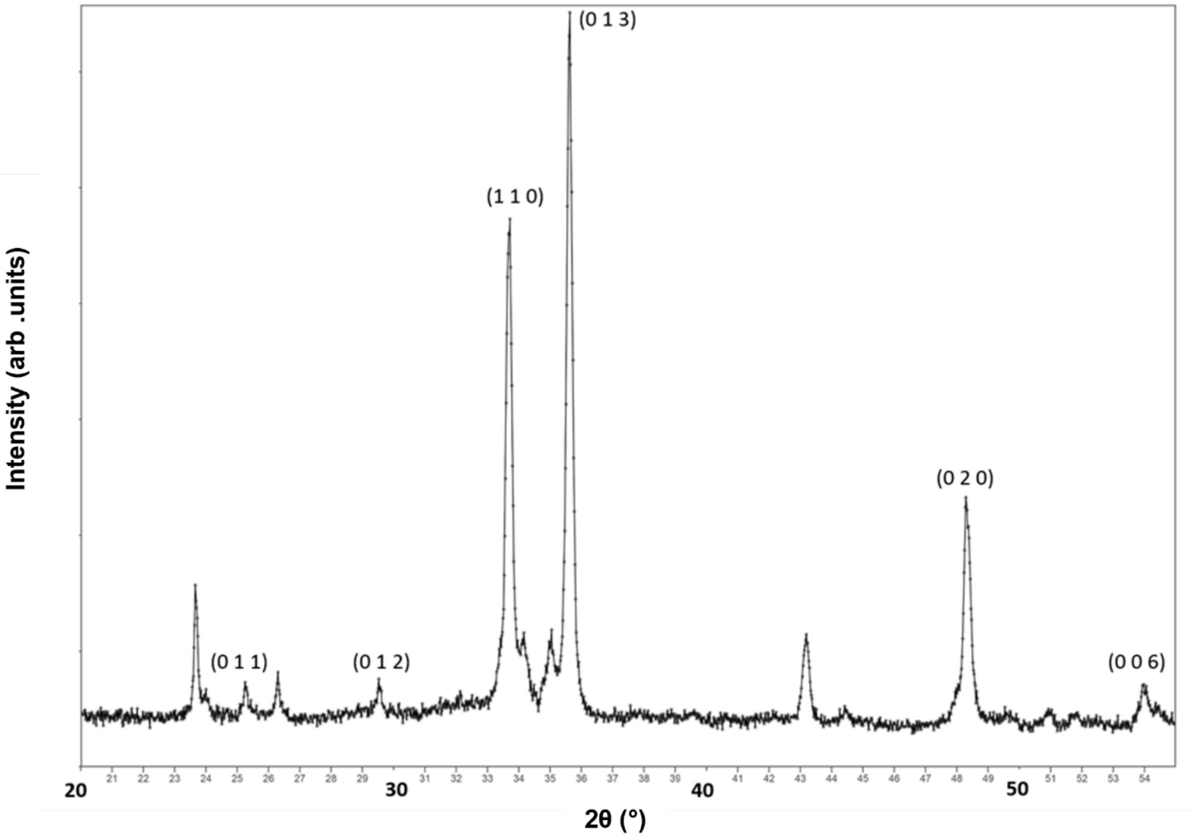

Figure 3.24 XRD pattern of $Ba_3Y_2O_5CO_3$ synthesised at 980°C detailing the main Miller Indices of the P4/mmm space group

3.3.1.7.2 Rietveld Refinement Using XRD Data

Using the Ln = Yb structural model replacing Yb with Y, a Rietveld refinement was performed using the XRD data for the Ln = Y system. Carbonate bond lengths (1.28 Å) and angles (120°) were softly restrained, with U_{iso} values being equally constrained (C1 = Dy1, O1 = O2 = O3 = O4). The observed, calculated and difference XRD profiles are shown in ***Figure 3.25*** with structural parameters and bond distances given in ***Table 3.19*** and ***Table 3.20***.

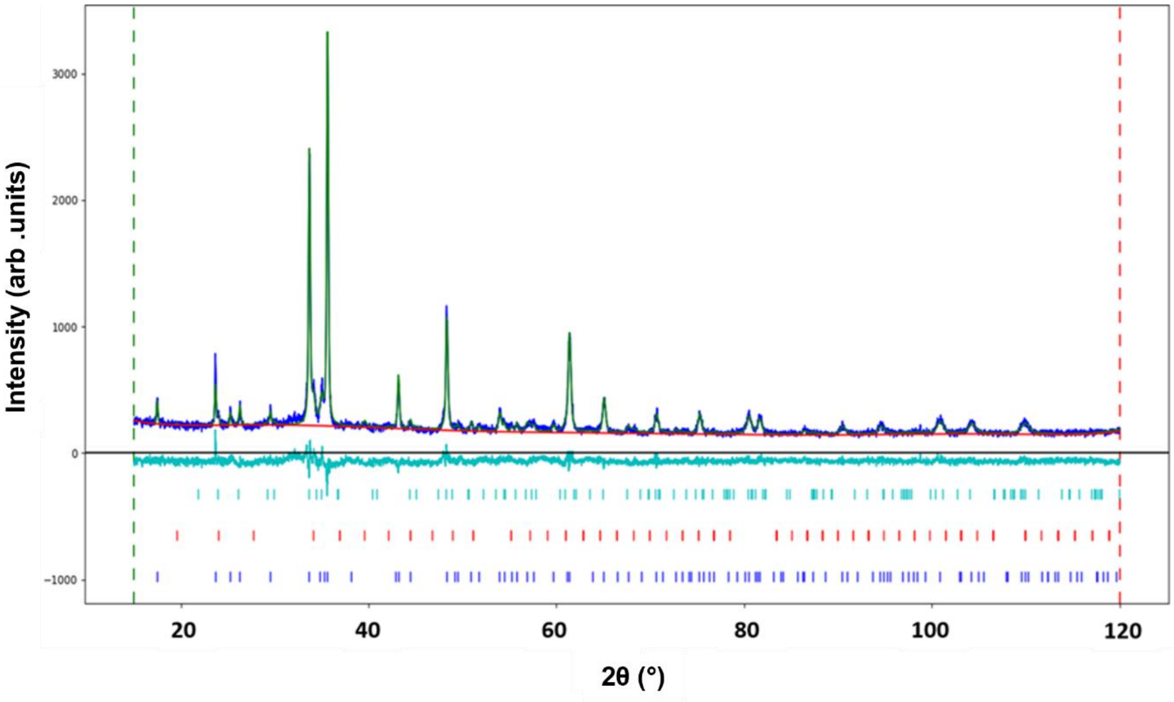

Figure 3.25 Observed, calculated and difference profiles of $Ba_3Y_2O_5CO_3$ XRD data (Lower tick marks ï Y_2O_3 (5wt%), middle tick marks ï $Ba_3Y_4O_9$ (8wt%), upper tick marks ï $Ba_3Y_2O_5CO_3$ (87wt%))

Table 3.19 Refined structural values of $Ba_3Y_2O_5CO_3$ XRD data

Atom	x	y	z	Site Occupancy	Wyckoff Position	Uiso
C1	0.5	0.433(17)	0.5	0.250	4o	0.005(3)
Ba1	0.0	0.0	0.0	1.000	1a	0.021(4)
Ba2	0.0	0.0	0.339(1)	1.000	2g	0.014(3)
Y1	0.5	0.5	0.180(1)	1.000	2h	0.005(2)
O1	0.0	0.5	0.197(2)	1.000	4i	0.053(10)
O2	0.5	0.5	0.0	1.000	1c	0.053(10)
O3	0.5	0.142(17)	0.5	0.210	4o	0.053(10)
O4	0.417(17)	0.5	0.398(1)	0.270	8t	0.053(10)

R_{wp} = 8.78% GOF = 1.31 (*P*4/*mmm* *a* = 4.382(3) Å, *c* = 11.855(8) Å)

Table 3.20 Selected interatomic distances of $Ba_3Y_2O_5CO_3$

Bond	Bond Length / Å	Bond	Bond Length / Å
C1 – O3	1.275(105) (x1)	**Ba2 – O3**	2.974(16) (x2)*
C1 – O4	1.299(29) (x2)	**Ba2 – O4**	2.938(56) (x4)*
Ba1 – O1	3.206(21) (x8)	**Y1 – O1**	2.200(3) (x4)
Ba1 – O2	3.099(1) (x4)	**Y1 – O2**	2.138(8) (x1)
Ba2 – O1	2.758(18) (x4)	**Y1 – O4**	2.603(18) (x1)

*dependent on orientation of carbonate group

Structure refinement using the XRD data indicated a significant amount of Y_2O_3 (5wt %) and $Ba_3Y_4O_9$ (8wt %) impurities which would suggest that this system would require a slightly shorter heating time or even perhaps a slightly lower heating temperature. When compared to that of the Ln = Yb system there is slight positional shift in relation to the carbonate atoms. Significant error values; particularly in regard to carbonate atomic positions could be attributed to the difficulties mentioned previously regarding

XRD data refinement, application of the restrictions or disorder in the carbonate orientation. The unit cell volume of the Ln = Y system is larger than that of the Ln = Yb system which is expected due to the larger atomic radii of six coordinate Y^{3+} (0.900 Å) in comparison to six coordinate Yb^{3+} (0.868 Å).[166]

3.3.1.7.3 Raman Spectroscopy

Raman data (***Figure 3.26***) supports the inclusion of carbonate in the $Ba_3Y_2O_5CO_3$ system with the appearance of the expected v_1 (symmetric stretch) and v_3 (doubly degenerate asymmetric stretch) carbonate vibrational modes[165]. Although there is a collection of prominent bands between 500 – 800 cm^{-1} it is difficult to determine accurately the v_4 (doubly degenerate asymmetric bend) vibrational mode positions. Those bands that were recorded appeared at lower wavenumbers in comparison to those seen in $BaCO_3$ (***Table 3.21***) suggesting longer bond lengths/weakening of the carbonate bonds, however this shift of v_1 is greater than those seen for all other Ln systems (Ln = Yb, Lu, Tm and Er). In comparison to the other $Ba_3LnO_5(CO_3)$ systems there are a lot more bands observed which may relate to the greater impurity levels in the sample.

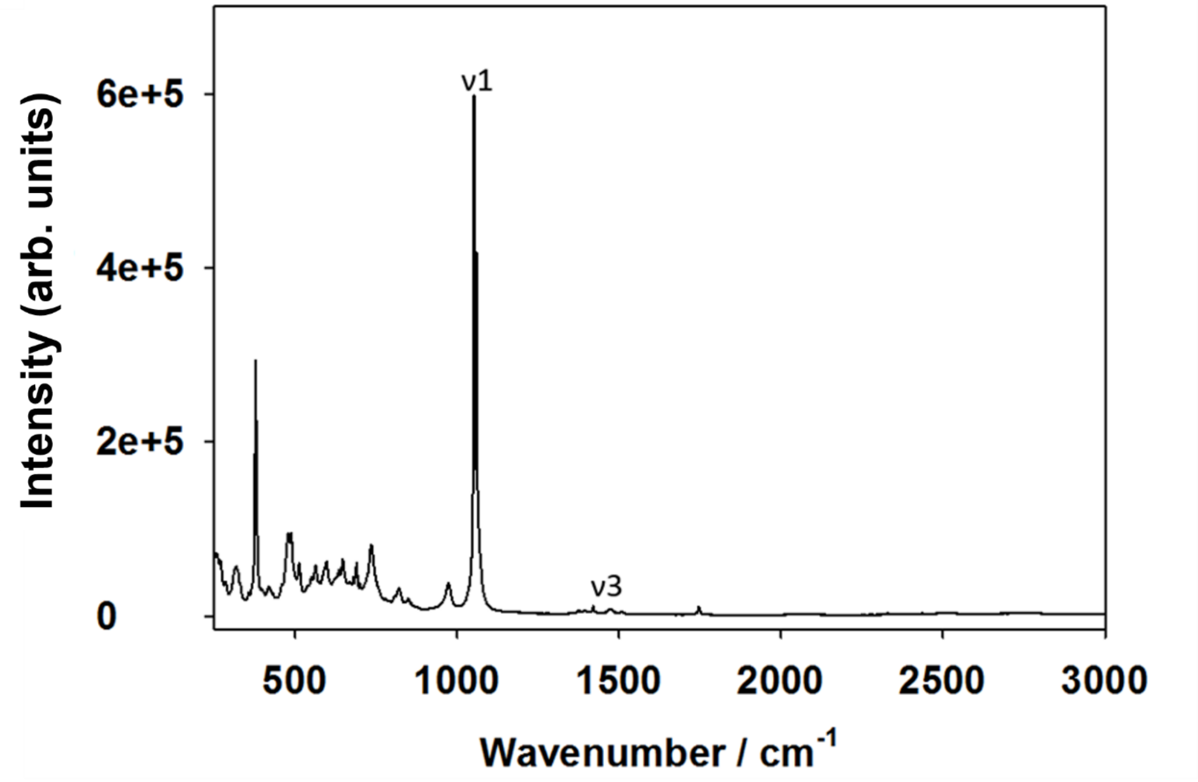

Figure 3.26 Raman spectroscopy data for $Ba_3Y_2O_5CO_3$ detailing specific Raman bands seen for carbonate vibrational modes

Table 3.21 Raman band wavenumbers for carbonate vibrational modes of $BaCO_3$ and $Ba_3Y_2O_5CO_3$

System	ν 1 / cm^{-1}	ν 3 / cm^{-1}	ν 4 / cm^{-1}
$BaCO_3$	1059.5	1420.2 1508.1	690.8 699.2
$Ba_3Y_2O_5CO_3$	1051.5	1393.5 1472.3	- -

3.3.1.8 Structural Trends

With a number of systems being synthesised, values were tabulated to determine any trends between structural parameters and the size of the six coordinate Ln^{3+} ionic species. Attempts to prepare similar samples for rare earths larger than Dy were unsuccessful forming $Ba_3Ln_4O_9$ instead and this suggests that Dy is the largest rare earth that can be accommodated in the structure. This is not that surprising given that the rare earth is occupying the perovskite B (small cation) site in this phase and so us likely to be less stable in this site as the size of the rare earth increases. The refined unit cell parameters for the $Ba_3Ln_2O_5CO_3$ systems are given in ***Table 3.22.***

Table 3.22 Unit Cell parameters for $Ba_3Ln_2O_5CO_3$ (Ln=Lu, Yb, Tm. Er, Y, Ho, Dy)

Formula	**Ionic Radii (VI Coord)[166]**	**Unit Cell Parameters**		**Unit Cell Volume**
		a	***c***	
$Ba_3Lu_2O_5CO_3$	0.8610 Å	4.3223(1)Å	11.8311(4)Å	221.034(14)Å^3
$Ba_3Yb_2O_5CO_3$	0.8680 Å	4.3258(2)Å	11.9036(5)Å	222.750(24) Å^3
$Ba_3Tm_2O_5CO_3$	0.8800 Å	4.3439(1)Å	11.8795(4)Å	224.157(18) Å^3
$Ba_3Er_2O_5CO_3$	0.8900 Å	4.3671(3) Å	11.8623(7) Å	226.237(42) Å^3
$Ba_3Y_2O_5CO_3$	0.9000 Å	4.3809(3) Å	11.8514(7) Å	227.458(40) Å^3
$Ba_3Ho_2O_5CO_3$	0.9010 Å	4.3813(2) Å	11.8871(4) Å	228.185(23) Å^3
$Ba_3Dy_2O_5CO_3$	0.9120 Å	4.3900(3) Å	11.9244(8) Å	229.810(39) Å^3

As expected, there is a positive correlation between an increasing unit cell volume with increasing ionic radii (***Figure 3.27***).

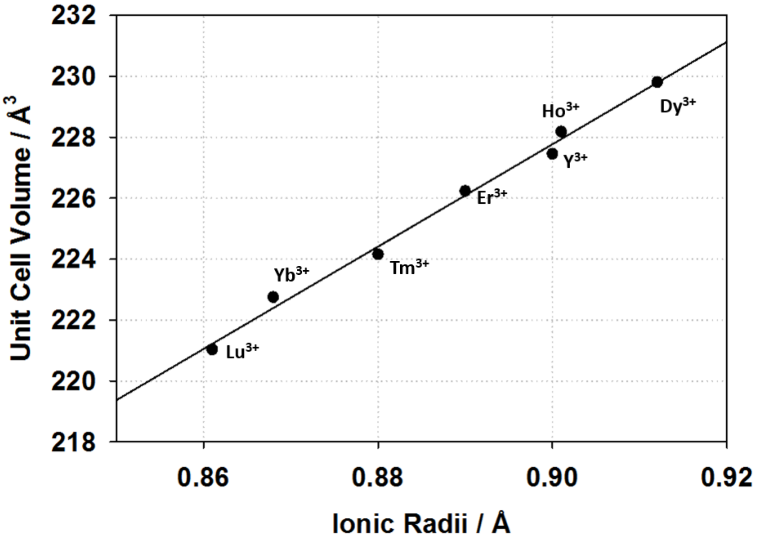

Figure 3.27 Variation in unit cell volume of $Ba_3Ln_2O_5CO_3$ with ionic radius

However, the variation in the individual cell parameters follow a less systematic trend. Unit cell parameter *a* shows a similar positive correlation with increasing ionic radii size (***Figure 3.28***).

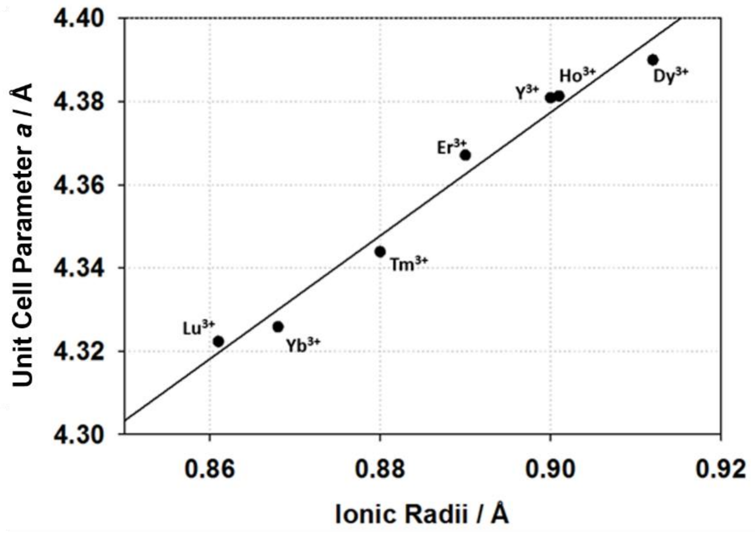

Figure 3.28 Variation in unit cell parameter a of $Ba_3Ln_2O_5CO_3$ with ionic radius

Unit cell parameter *c* appears to have no distinctive correlation across the lanthanide series (***Figure 3.29***). When comparing this data with that of bond distances for each system, there does appear to be a relationship seen between unit parameter *c* and the Ln1 – O4 bond length, with the exception that this value is smaller for Dy^{3+} than for Ho^{3+}. This same relationship is not seen for the Ln1 – O1 bond length values and suggests the variation in unit cell parameter *c* mostly reliant on the orientation of carbonate and hence Ln1 – O4 bond length.

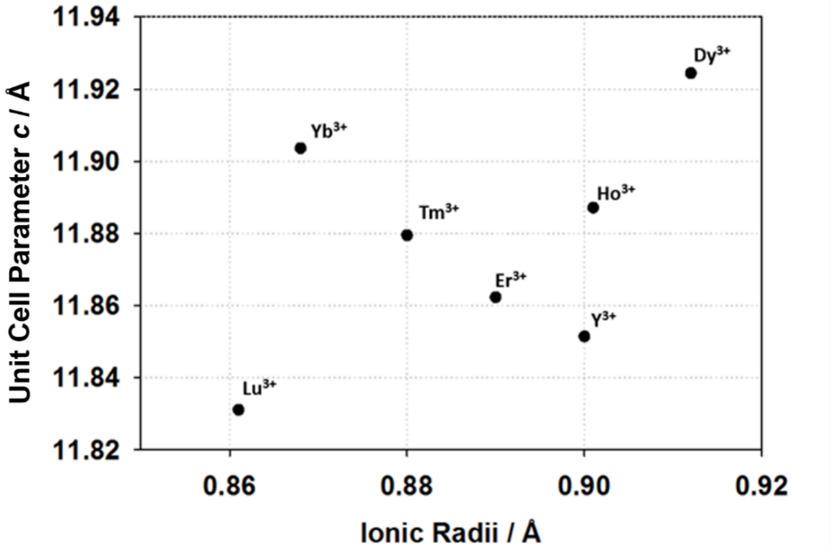

Figure 3.29 Variation in unit cell parameter c of $Ba_3Ln_2O_5CO_3$ with ionic radius

Other trends were also investigated. Investigation into the values of U_{iso} (***Table 3.23***) for each system found no obvious correlation between the increasing ionic radii of Ln and the value of U_{iso}. However, when only considering the lanthanide elements (Ln = Lu, Tm, Er, Ho, Dy) the value of the constrained oxygen U_{iso} finds a minimum with the Ln = Tm system before increasing as ionic radii increases. As the Ln = Yb starting model was used for refinements of the XRD data for these systems, the oxygen positions in the Ln = Tm system is most like that of the Ln = Yb model, whilst other systems show greater oxygen U_{iso} values supporting that orientation of carbonate in these systems differ to a greater extent.

Table 3.23 Comparison table of XRD data U_{iso} values with increasing ionic radius

	Lu	**Tm**	**Er**	**Y**	**Ho**	**Dy**
	(0.8610 Å)	**(0.8800 Å)**	**(0.8900 Å)**	**(0.9000 Å)**	**(0.9010 Å)**	**(0.9120 Å)**
Atom	**U_{iso}**	**U_{iso}**	**U_{iso}**	**U_{iso}**	**U_{iso}**	**U_{iso}**
C1	0.006(1)	0.008(1)	0.012(2)	0.005(3)	0.002(1)	0.004(2)
Ba1	0.015(1)	0.014(2)	0.016(2)	0.021(4)	0.012(2)	0.034(4)
Ba2	0.008(1)	0.014(1)	0.016(2)	0.014(3)	0.013(2)	0.014(3)
Ln1	0.006(1)	0.008(2)	0.012(2)	0.005(2)	0.002(1)	0.004(2)
O1	0.074(5)	0.037(5)	0.068(8)	0.053(10)	0.081(6)	0.105(14)
O2	0.074(5)	0.037(5)	0.068(8)	0.053(10)	0.081(6)	0.105(14)
O3	0.074(5)	0.037(5)	0.068(8)	0.053(10)	0.081(6)	0.105(14)

Comparing bond lengths of each system (***Figure*** showed no real correlation between the increasing ionic radii of Ln and most bond lengths associated to these systems. A positive correlation is only seen for the Ba1 – O2 bond lengths which increase with increasing ionic radii, but this is unreliable as these two positions are on set positions and would increase proportionally as the unit cell increases. When comparing the values of bonds associated with the O1 and O4 oxygen, there does not appear to be any correlation with bond length values, however, the error values of these increase with increasing ionic radii which provides further evidence for the possible differing orientations of the carbonate and tilting of the LnO_6 octahedra.

Table 3.24 Comparison table of structural bond lengths with increasing ionic radius

	Lu	**Tm**	**Er**	**Y**	**Ho**	**Dy**
	(0.8610 Å)	**(0.8800 Å)**	**(0.8900 Å)**	**(0.9000 Å)**	**(0.9010 Å)**	**(0.9120 Å)**
Bond.	**Length / Å**	**Length / Å**	**Length / Å**	**Length / Å**	**Length / Å**	**Length / Å**
C1 – O3	1.275(45)	1.286(52)	1.284(86)	1.275(105)	1.284(11)	1.273(118)
C1 – O4	1.307(18)	1.321(19)	1.296(26)	1.299(29)	1.293(46)	1.293(58)
Ba1 – O1	3.198(10)	3.256(12)	3.415(19)	3.206(21)	3.300(20)	3.366(36)
Ba1 – O2	3.057(1)	3.072(1)	3.088(1)	3.099(1)	3.098(1)	3.104(1)
Ba2 – O1	2.703(8)	2.680(9)	2.579(13)	2.758(18)	2.675(15)	2.656(27)
Ba2 – O3	2.931(5)	3.012(28)	2.989(14)	2.974(16)	2.944(9)	2.953(22)
Ba2 – O4	2.962(25)	2.808(18)	2.884(34)	2.938(56)	3.151(65)	3.039(114)
Dy1 – O1	2.179(1)	2.196(2)	2.242(6)	2.200(3)	2.221(4)	2.241(9)
Dy1 – O2	2.080(2)	2.101(3)	2.117(5)	2.138(8)	2.105(3)	2.099(3)
Dy1 – O4	2.658(13)	2.709(14)	2.664(15)	2.603(18)	2.693(32)	2.675(29)

A more detailed neutron study of each of these systems would be beneficial to provide more accurate structural trend investigations, providing further insight into the actual carbonate orientations within each system.

3.3.2 Attempted Synthesis of Sulphate Analogue System $Ba_3Yb_2O_5(SO_4)$ (X = S)

As CO_3^{2-} and SO_4^{2-} are isovalent, attempts were then made to replace CO_3^{2-} with SO_4^{2} using a reaction of $Ba_3Yb_2O_5CO_3$ with $(NH_4)_2SO_4$ to allow for sulphate exchange for carbonate. XRD patterns for this attempted oxyanion exchange are shown in ***Figure 3.30***.

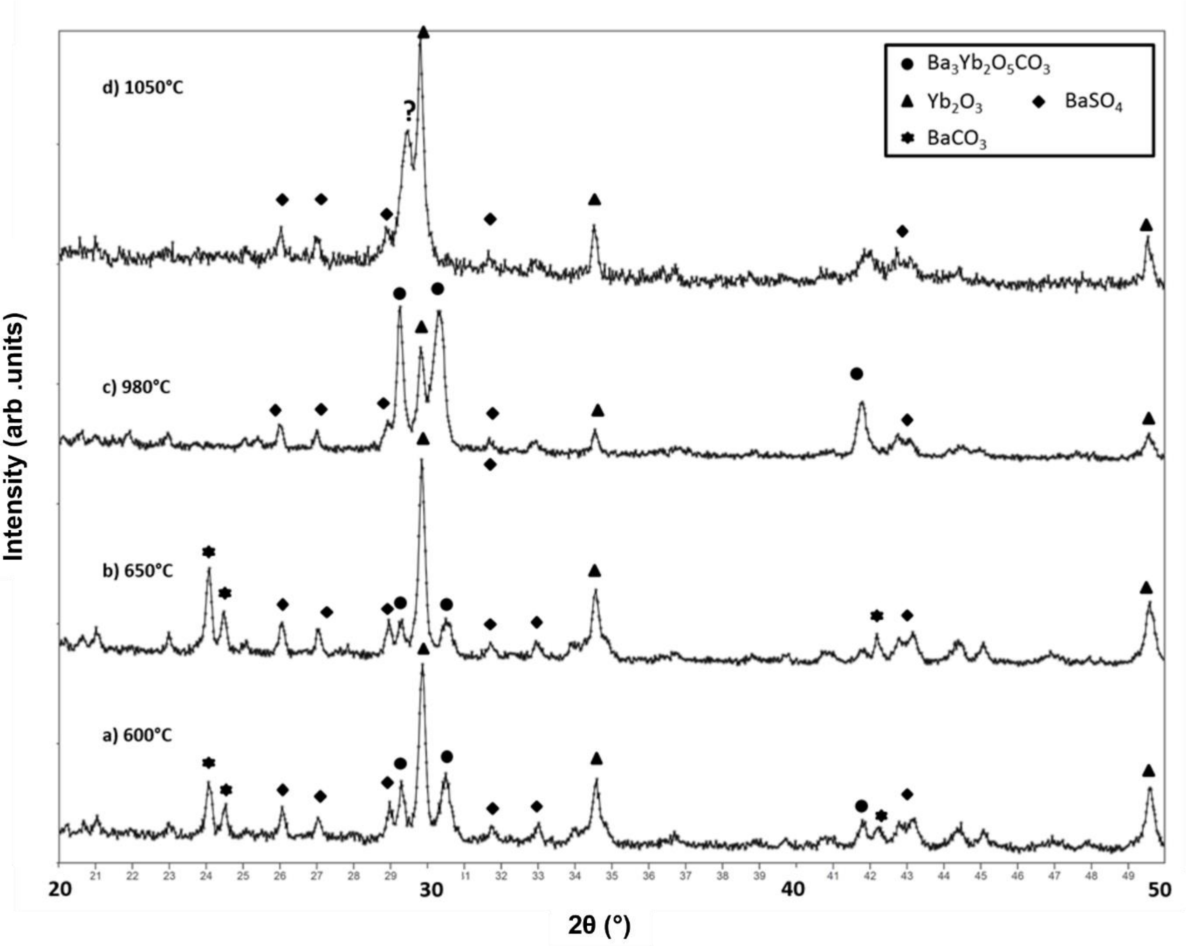

Figure 3.30 X-ray diffraction patterns for a 1:1 mixture of $Ba_3Yb_2O_5CO_3$: $(NH_4)_2SO_4$ heated at different temperatures

Like the borate attempt, initial heating of the reagents leads to a large loss of the $Ba_3Yb_2O_5CO_3$ structure as the increasing presence of Yb_2O_3, $BaCO_3$ and $BaSO_4$ occuring at 600°C and 650°C. At 980°C, the $Ba_3Yb_2O_5CO_3$ structure begins to return with the loss of $BaCO_3$, however it is apparent that sulphate does not appear to have been incorporated as shown from the constant appearance of $BaSO_4$. Increasing to 1050°C leads to full decomposition of the $Ba_3Yb_2O_5CO_3$ structure and the occurrence of a peak which is difficult to determine with certainty; this unidentifiable peak could be related to a sulphate containing system, although further work would be needed to confirm this. One thing to note is the lack of $Ba_3Yb_4O_9$ which has generally been seen for all carbonate systems so far at this temperature.

With the interesting formation of the unknown peak, a different approach was taken; attempting to synthesise the sulphate related phase from the beginning, adding $(NH_4)_2SO_4$ to $BaCO_3$ and Yb_2O_3 in the required ratios.

It was found by performing this synthesis that a compound with similar structure formed at 1150°C, however, its appearance suggests that the phase is significantly impure, with these impurities remaining after further heating. One reason for this was postulated that the complete replacement of CO_3^{2-} by SO_4^{2-} to nominally give $Ba_3Yb_2O_5SO_4$ would lend to a perovskite which may give strain issues with the maintenance of tetrahedral coordination for SO_4^{2-}, as this would require complex ordering of the orientation of SO_4^{2-} groups. To overcome this, ZnO was added as a starting reagent with the idea this would co-occupy the S position and reduce the overall oxygen content towards that of "O_8", as seen for the carbonate phase. XRD data for this study can be seen in ***Figure 3.31***.

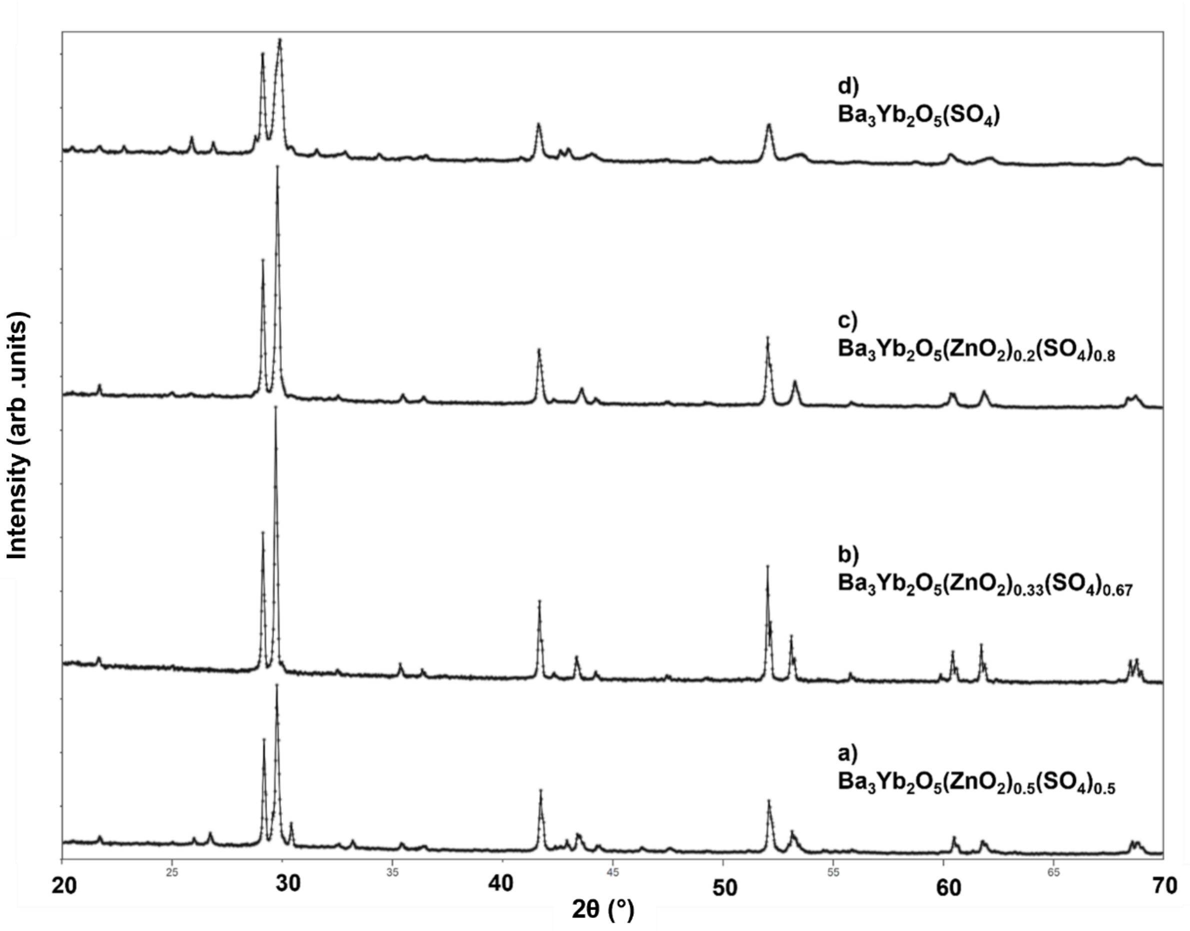

Figure 3.31 X-ray diffraction patterns of $Ba_3Yb_2O_5(ZnO_2)_x(SO_4)_{1-x}$ (x = 0.5, 0.33, 0.2, 0) at 1150°C

The addition of Zn to this structure clearly shows the reduced strain by the narrowing of the structural peaks, becoming the most crystalline for the $Ba_3Yb_2O_5(ZnO_2)_{0.33}(SO_4)_{0.67}$ system. On increasing the amount of Zn up to 0.33 the samples have the best purity, with larger impurity peaks being seen for the Zn 0.5 system.

The pattern seen for the $Ba_3Yb_2O_5(ZnO_2)_{0.33}(SO_4)_{0.67}$ system matches with the $Ba_3Yb_2O_5CO_3$ structure, but with an elongation of unit cell *c* parameter. This investigation has shown that a zinc doped sulphate analogue related to $Ba_3Yb_2O_5CO_3$ is possible and further investigation of this can be found in section 3.3.3.

3.3.3 $Ba_3Ln_2O_5(ZnO_2)_{0.33}(SO_4)_{0.67}$ (Ln = Yb, Tm, Er, Ho, Dy)

3.3.3.1 $Ba_3Yb_2O_5(ZnO_2)_{0.33}(SO_4)_{0.67}$ (Ln = Yb)

3.3.3.1.1 Powder X-Ray Diffraction

As previously mentioned, the successful synthesis of $Ba_3Yb_2O_5(ZnO_2)_{0.33}(SO_4)_{0.67}$ was performed and XRD data was recorded (***Figure 3.32***)

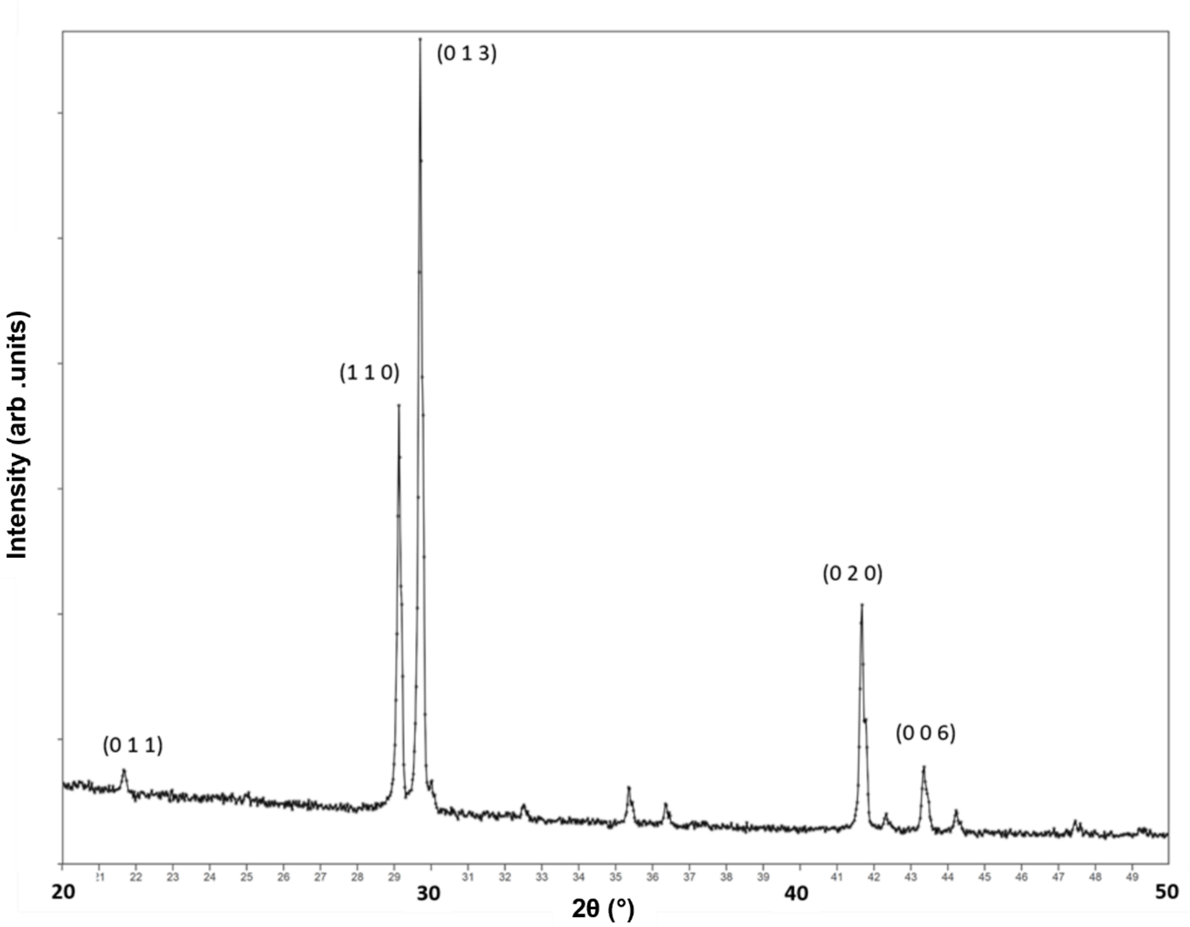

Figure 3.32 XRD pattern of $Ba_3Yb_2O_5(ZnO_2)_{0.33}(SO_4)_{0.67}$ synthesised at 1150°C detailing the main Miller Indices of the P4/mmm space group

The XRD pattern shows an elongation of the unit cell parameter *c* as illustrated by the (1 1 0) and (0 1 3) planes moving closer together. It is also important to notice the reduced intensity (0 1 1) and missing (0 1 2) peaks suggesting a loss of ordering within the system. These planes are represented in ***Figure 3.33*** and are seen the run through the modified C1 site which is now co-occupied with S/Zn in this system. Tetrahedral coordination of S/Zn means that O situated around these would have to orientate in a way that still satisfies the six coordination of Yb^{3+} (***Figure 3.34***).

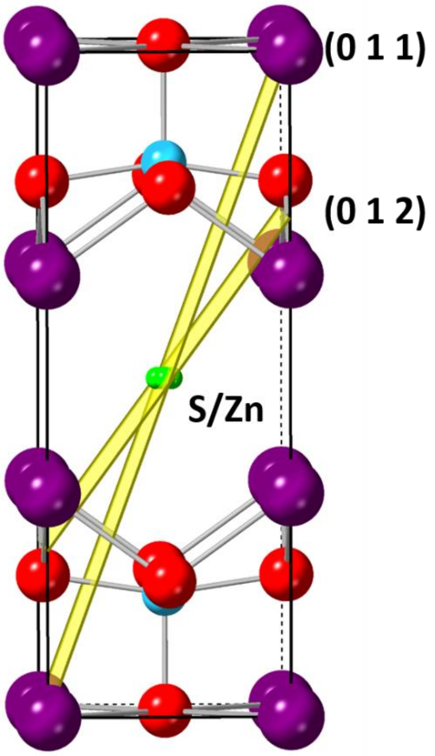

Figure 3.33 Suggested structure of $Ba_3Yb_2O_5(ZnO_2)_{0.33}(SO_4)_{0.67}$ *(with central oxygens not placed) using the P4/mmm space group showing the affected (0 1 1) and (0 1 2) planes*

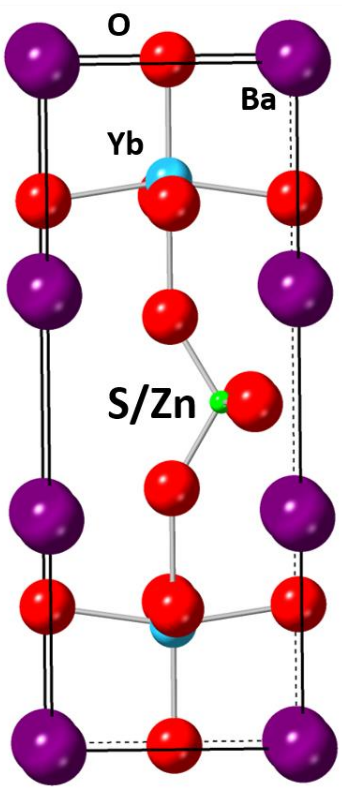

Figure 3.34 Predicted structure of $Ba_3Yb_2O_5(ZnO_2)_{0.33}(SO_4)_{0.677}$ using the P4/mmm space group showing SO_4 orientation

Rietveld refinement using the XRD data was attempted using the predicted $Ba_3Yb_2O_5(ZnO)_{0.33}(SO_4)_{0.67}$ structure. During the refinement process, it became evidently clear that this model would satisfactorily fit general unit cell parameters (***Table 3.25***)

Table 3.25 Unit cell parameter values of $Ba_3Yb_2O_5(ZnO_2)_{0.33}(SO_4)_{0.67}$ XRD data

Formula	**Unit Cell Parameters**		**Unit Cell Volume**
	a	***c***	
$Ba_3Yb_2O_5CO_3$	4.3258(2)Å	11.9036(5)Å	222.750(24) Å^3
$Ba_3Yb_2O_5(ZnO_2)_{0.33}(SO_4)_{0.67}$	4.3286(1)Å	12.5061(2)Å	234.321(6) Å^3

Difficulties were found including unstable U_{iso} values and unstable occupancy values of Yb, S and Zn. A more detailed neutron diffraction data set would be required to resolve this and provide a better structural solution, helping to determine if Zn/S may also be substituting onto the Yb1 site providing a partial mixed occupancy in all layers or if there is additional ordering of zinc and sulphur in these layers. Further detailed neutron data collection would also provide insight of oxygen positions and orientations. These issues are also found for all further refinements within section 3.3.3.

When comparing the two Ln = Yb systems, unit cell parameter *a* appears stable as cell parameter *c* increases. As Ln = Yb in both systems, the size of the lanthanide is constant and would not contribute to any increases seen in the unit cell values. When comparing the carbonate and sulphate systems, increases in the unit cell parameter *c* and unit cell volume can be attributed to six coordinate S^{6+} (0.12 Å) and six coordinate Zn^{2+} (0.60 Å) both having larger ionic radii than that of three coordinate C^{4+} (-0.08 Å).[166]

3.3.3.1.2 Raman Spectroscopy

A Raman spectroscopic study was used to confirm the presence of any sulphate in the system (***Figure 3.35***) and comparing to values of sulphate recorded in the same manner for reagent $(NH_4)_2SO_4$ and $BaSO_4$ which may form during the synthesis (***Table 3.26***).

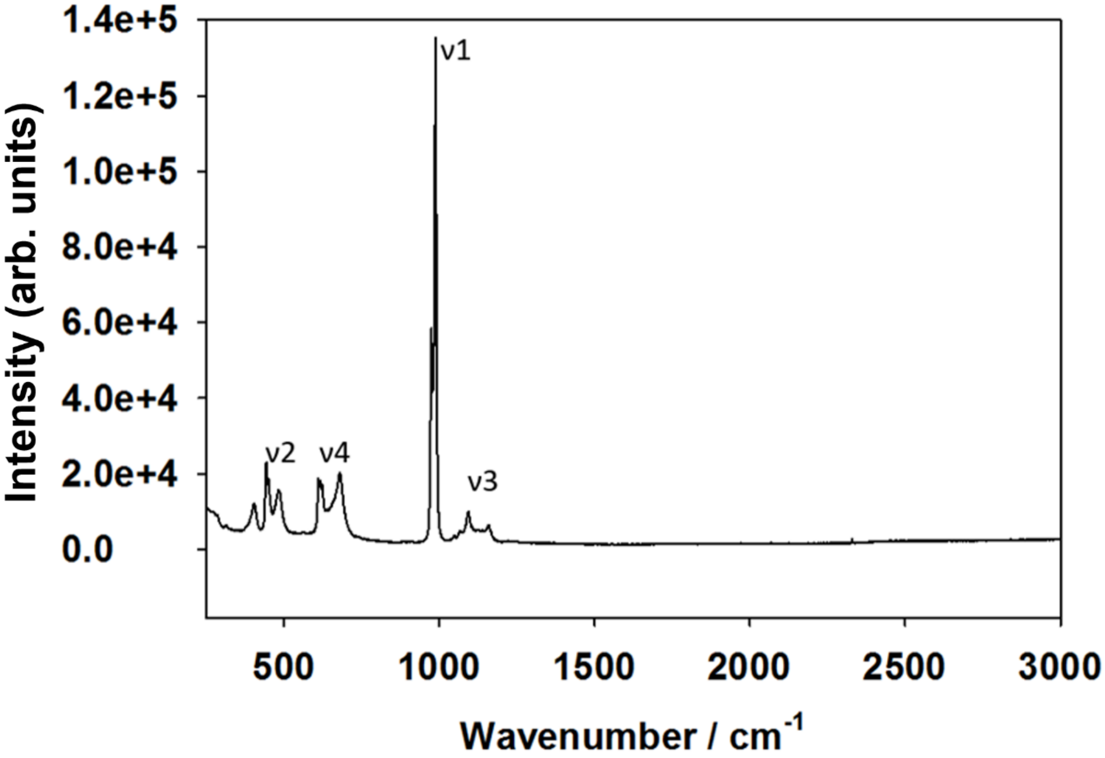

Figure 3.35 Raman spectroscopy data for $Ba_3Yb_2O_5(ZnO_2)_{0.33}(SO_4)_{0.67}$ detailing specific Raman bands seen for carbonate vibrational modes

Table 3.26 Raman band wavenumbers for carbonate vibrational modes of $(NH_4)_2SO_4$, $BaSO_4$ and $Ba_3Yb_2O_5(ZnO_2)_{0.33}(SO_4)_{0.67}$

System	ν 1 / $^{-1}$	v2 / cm^{-1}	ν 3 / $^{-1}$	ν 4 / $^{-1}$
$(NH_4)_2SO_4$	975.6	452.0	1090.4	615.1 624.7
$BaSO_4$	987.6	452.3 461.0	1138.9 1166.6	617.4 647.3
$Ba_3Yb_2O_5(ZnO_2)_{0.33}(SO_4)_{0.67}$	974.4 987.6	450.1 482.1	1093.2 1157.7	611.0 679.1

Raman data supports the inclusion of sulphate in the $Ba_3Yb_2O_5(ZnO_2)_{0.33}(SO_4)_{0.67}$ system with the appearance of the expected v_1 (symmetric stretch), v_2 (doubly degenerate bend), v_3 (triply degenerate asymmetric stretch) and v_4 (triply degenerate asymmetric bend) sulphate vibrational modes[168] with most bands recorded for these being shifted in wavenumbers in comparison to those seen in $(NH_4)_2SO_4$ or $BaSO_4$. This shift is important in providing evidence that sulphate is indeed a part of the $Ba_3Yb_2O_5(ZnO_2)_{0.33}(SO_4)_{0.67}$ structure. $Ba_3Yb_2O_5(ZnO_2)_{0.33}(SO_4)_{0.67}$ also appears to give rise to a second v_1 band which is similar to that of $BaSO_4$, when analysed in conjunction with the lack of $BaSO_4$ visualised in the XRD pattern for this system at 1150°C, this finding supports the idea that there may be more than one SO_4^{2-} environment in this structure.

3.3.3.2 $Ba_3Tm_2O_5(ZnO_2)_{0.33}(SO_4)_{0.67}$ (Ln = Tm)

3.3.3.2.1 Powder X-Ray Diffraction

After the successful synthesis of $Ba_3Yb_2O_5(ZnO_2)_{0.33}(SO_4)_{0.67}$, the same synthesis route was employed and $Ba_3Tm_2O_5(ZnO_2)_{0.33}(SO_4)_{0.67}$ was successfully synthesised (***Figure 3.36***). As before, the (0 1 1) and (0 1 2) crystalline plane peaks are clearly reduced in intensity.

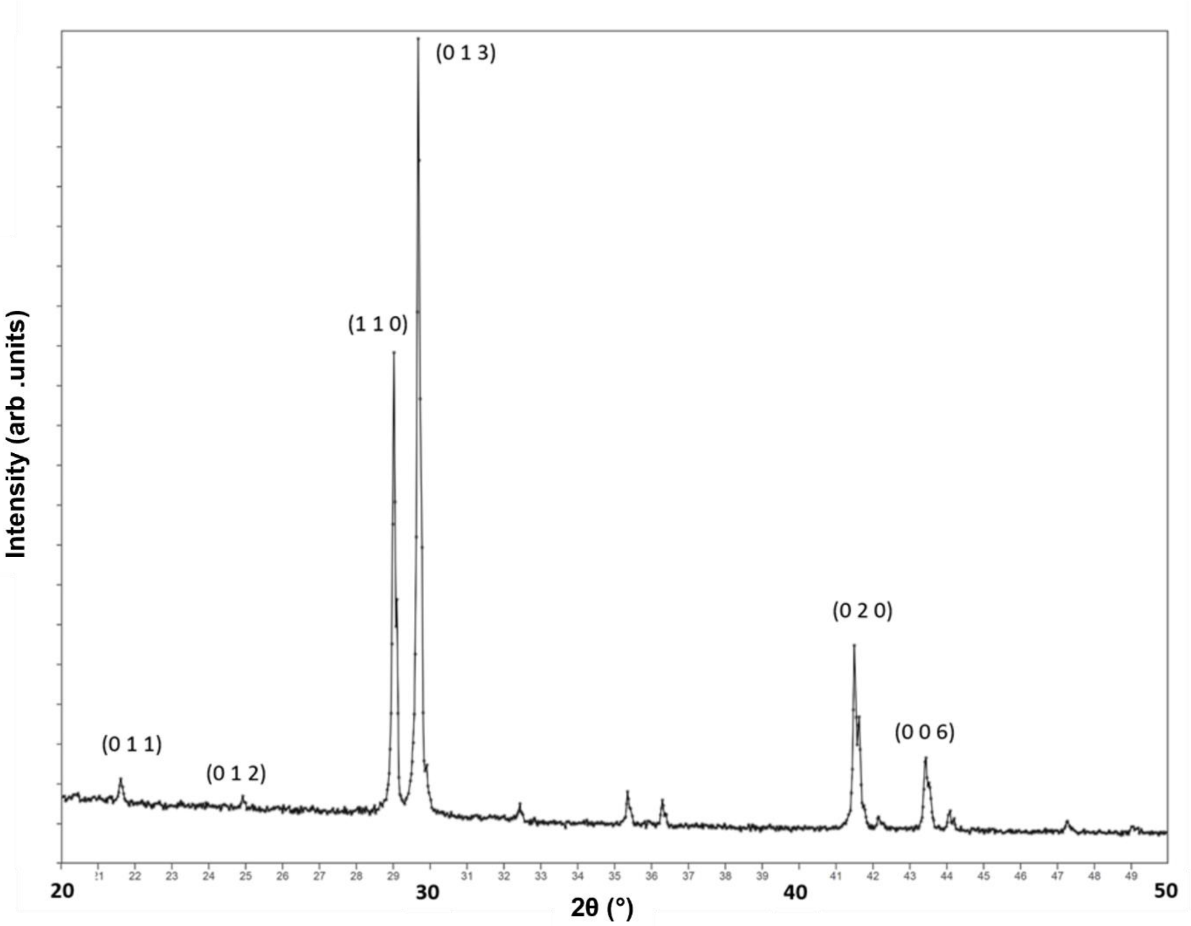

Figure 3.36 XRD pattern of $Ba_3Tm_2O_5(ZnO_2)_{0.33}(SO_4)_{0.67}$ synthesised at 1150°C detailing the main Miller Indices of the P4/mmm space group

Rietveld refinement of the structure using the XRD data was attempted using a modified version of the predicted $Ba_3Yb_2O_5(ZnO_2)_{0.33}(SO_4)_{0.67}$ structure, replacing Ln = Yb with Ln = Tm. Comparable unit cell parameters are given in ***Table 3.27***.

Table 3.27 Unit cell parameter values of $Ba_3Tm_2O_5(ZnO_2)_{0.33}(SO_4)_{0.67}$ XRD data

Formula	**Unit Cell Parameters**		**Unit Cell Volume**
	a	***c***	
$Ba_3Tm_2O_5CO_3$	4.3439(1)Å	11.8795(4)Å	224.157(18) Å^3
$Ba_3Tm_2O_5(ZnO_2)_{0.33}(SO_4)_{0.67}$	4.3464(1)Å	12.4885(2)Å	235.926(8) Å^3
$Ba_3Yb_2O_5(ZnO_2)_{0.33}(SO_4)_{0.67}$	4.3286(1)Å	12.5061(2)Å	234.321(6) Å^3

When comparing the unit cell parameters of the two Ln = Tm systems, unit cell parameter *a* appears stable as cell parameter *c* increases, as describe previously. The unit cell parameter *a* and unit cell volume of the Ln = Tm sulphate system is larger than those of the Ln = Yb system, which is attributed to the larger ionic radii of six coordinate Tm^{3+} (0.880 Å) in comparison to six coordinate Yb^{3+} (0.868 Å).[166] Additionally, the ionic radii of four coordinate S^{6+} and four coordinate Zn^{2+} are larger than that of three coordinate C^{4+}, which would also contribute to the increase in unit cell volume when comparing the carbonate and sulphate systems.[166]

3.3.3.2.2 Raman Spectroscopy

The Raman spectrum (***Figure 3.37***) supports the inclusion of sulphate in the $Ba_3Tm_2O_5(ZnO_2)_{0.33}(SO_4)_{0.67}$ system with wavenumber values determined shown in ***Table 3.28***.

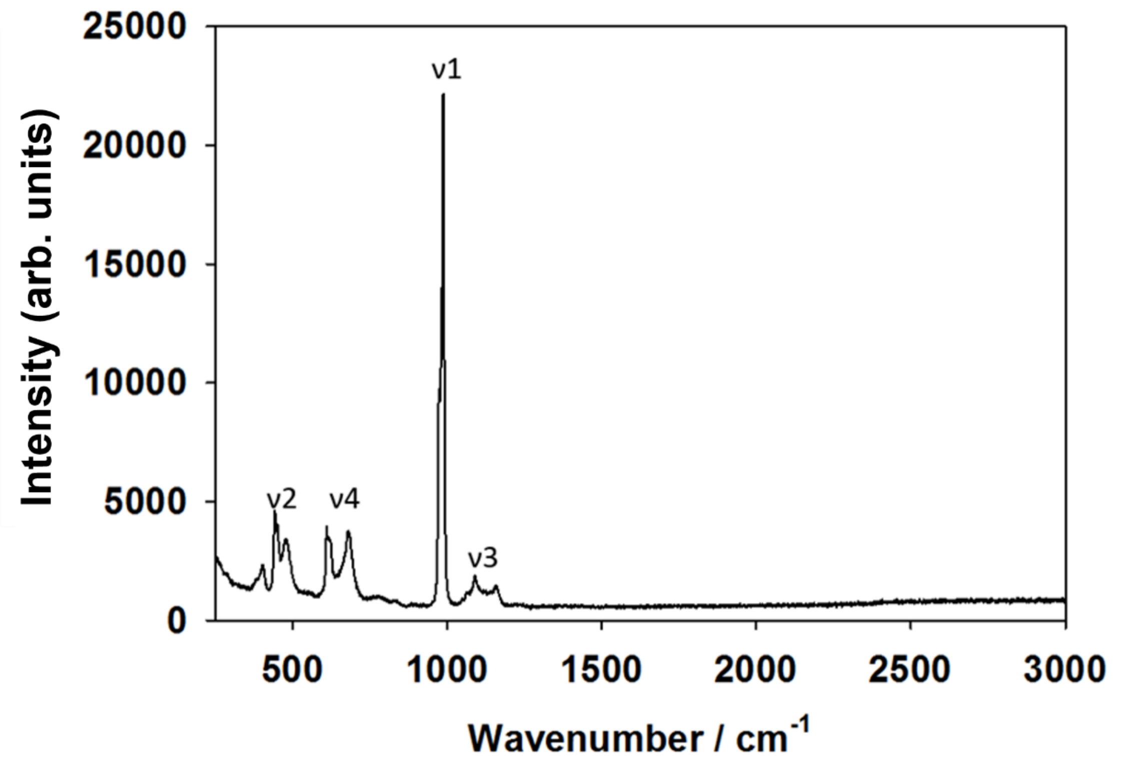

Figure 3.37 Raman spectroscopy data for $Ba_3Tm_2O_5(ZnO_2)_{0.33}(SO_4)_{0.67}$ detailing specific Raman bands seen for carbonate vibrational modes

Table 3.28 Raman band wavenumbers for carbonate vibrational modes of $(NH_4)_2SO_4$, $BaSO_4$ and $Ba_3Tm_2O_5(ZnO_2)_{0.33}(SO_4)_{0.67}$

System	**ν 1 /$^{-1}$**	**v2 / cm^{-1}**	**ν 3 /$^{-1}$**	**ν 4 /$^{-1}$**
$(NH_4)_2SO_4$	975.6	452.0	1090.4	615.1 624.7
$BaSO_4$	987.6	452.3 461.0	1138.9 1166.6	617.4 647.3
$Ba_3Tm_2O_5(ZnO_4)_{0.33}(SO_4)_{0.67}$	973.4 987.6	442.5 479.6	1093.2 1157.7	611.0 679.1

The Raman spectrum confirms appearance of the expected v_1 (symmetric stretch), v_2 (doubly degenerate bend), v_3 (triply degenerate asymmetric stretch) and v_4 (triply degenerate asymmetric bend) sulphate vibrational modes[168]. Most bands recorded for these are shifted in wavenumbers in comparison to those seen in $(NH_4)_2SO_4$ or $BaSO_4$.

$Ba_3Tm_2O_5(ZnO_2)_{0.33}(SO_4)_{0.67}$ also gives rise to a second v_1 band which is similar to that of $BaSO_4$, however, XRD data for this system shows no presence of $BaSO_4$ and so supports the idea of there being more than one SO_4^{2-} environment.

3.3.3.3 $Ba_3Er_2O_5(ZnO_2)_{0.33}(SO_4)_{0.67}$ (Ln = Er)

3.3.3.3.1 Powder X-Ray Diffraction

Utilising the same synthesis route, $Ba_3Er_2O_5(ZnO_2)_{0.33}(SO_4)_{0.67}$ was successfully synthesised (***Figure 3.38***) with the appearance of (0 1 1) and (0 1 2) crystalline plane peaks clearly reduced in intensity.

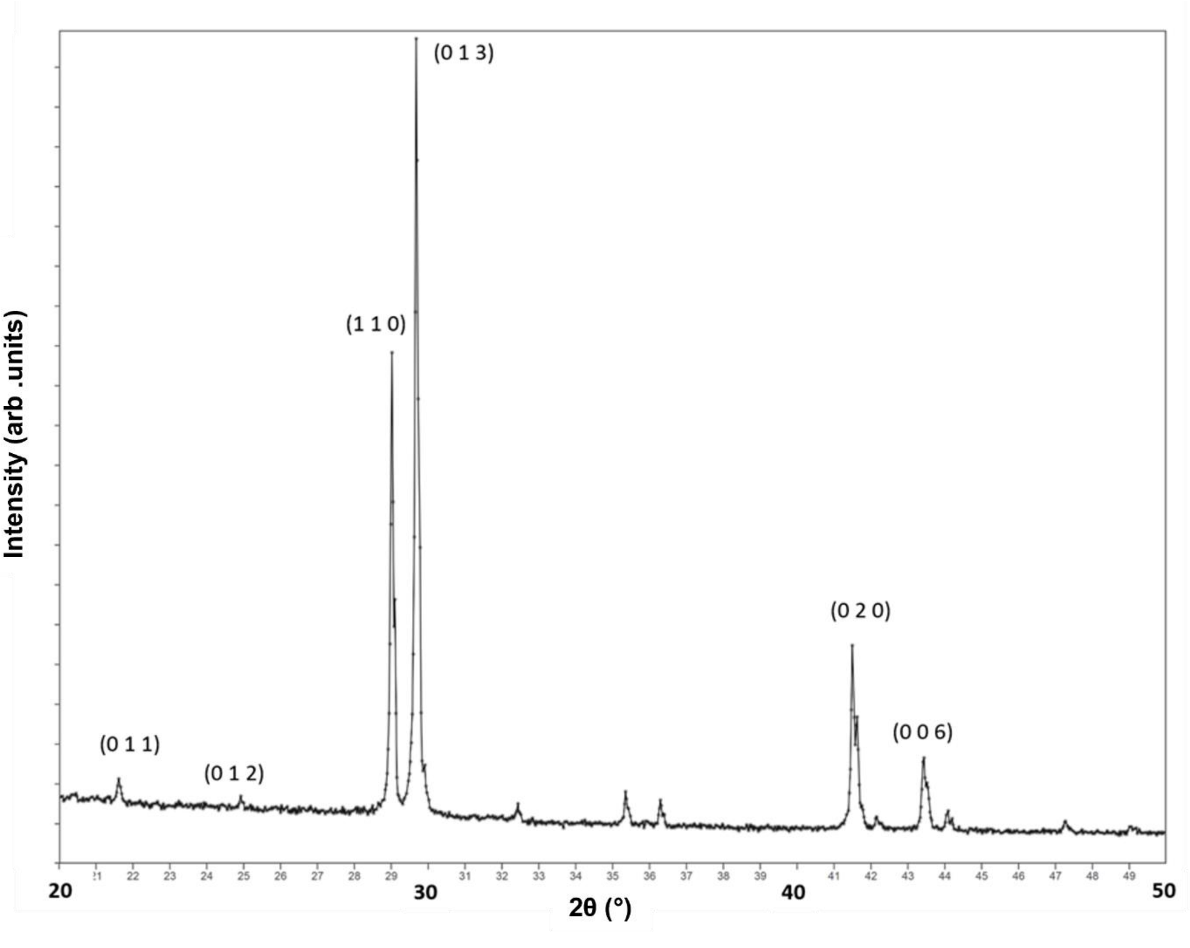

Figure 3.38 XRD pattern of $Ba_3Er_2O_5(ZnO_2)_{0.33}(SO_4)_{0.67}$ synthesised at 1150°C detailing the main Miller Indices of the P4/mmm space group

Rietveld refinement of the structure using XRD data was attempted using a modified version of the predicted $Ba_3Yb_2O_5(ZnO_2)_{0.33}(SO_4)_{0.67}$ structure, replacing Ln = Yb with Ln = Er and determined unit cell parameter are shown in ***Table 3.29***.

Table 3.29 Unit cell parameter values of $Ba_3Er_2O_5(ZnO_2)_{0.33}(SO_4)_{0.67}$ XRD data

Formula	**Unit Cell Parameters**		**Unit Cell Volume**
	a	***c***	
$Ba_3Er_2O_5CO_3$	4.3671(3)Å	11.8623(7)Å	226.237(42) Å^3
$Ba_3Er_2O_5(ZnO_2)_{0.33}(SO_4)_{0.67}$	4.3655(1)Å	12.4946(3)Å	238.115(6) Å^3
$Ba_3Yb_2O_5(ZnO_2)_{0.33}(SO_4)_{0.67}$	4.3286(1)Å	12.5061(2)Å	234.321(6) Å^3

When comparing the unit cell parameters of the two Ln = Er systems, unit cell parameter *a* appears stable as cell parameter *c* increases, as describe previously. Unit parameter *a* and unit cell volume of the Ln = Er sulphate system is larger than those of the Ln = Yb system, which is attributed to the greater ionic radii of six coordinate Er^{3+} (0.890 Å) in comparison to six coordinate Yb^{3+} (0.868 Å).[166] Additionally, the ionic radii of four coordinate S^{6+} and four coordinate Zn^{2+} (0.60 Å) are larger than that of three coordinated C^{4+}, which would also contribute to the increase unit cell volume.[166]

3.3.3.3.2 Raman Spectroscopy

As with its carbonate counterpart, it is difficult to determine any of the expected sulphate vibrational modes for this Er system (***Figure 3.39***) due to problems arising from the photoluminescence process of Er^{3+} explained in section 3.3.1.4.

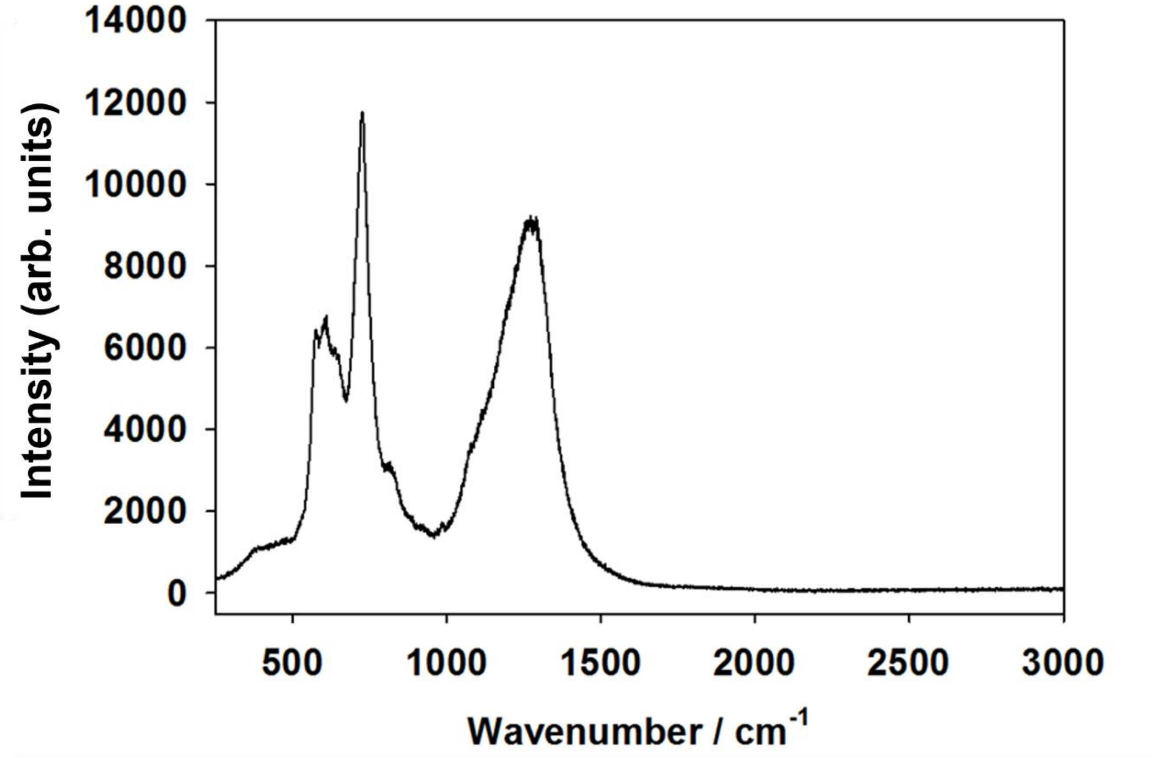

Figure 3.39 Raman spectroscopy data for $Ba_3Er_2O_5(ZnO_2)_{0.33}(SO_4)_{0.67}$ *detailing specific Raman bands seen for carbonate vibrational modes*

3.3.3.4 $Ba_3Ho_2O_5(ZnO_2)_{0.33}(SO_4)_{0.67}$ (Ln = Ho)

3.3.3.4.1 Powder X-Ray Diffraction

Utilising the same synthesis route, $Ba_3Ho_2O_5(ZnO_2)_{0.33}(SO_4)_{0.67}$ was also successfully synthesised (***Figure 3.40***) with the (0 1 1) reflection being greatly reduced in intensity and the (0 1 2) reflection not being seen at all. Unlike other samples in this series there was still a slight presence of $BaSO_4$, suggesting a short further heating would be required for this system.

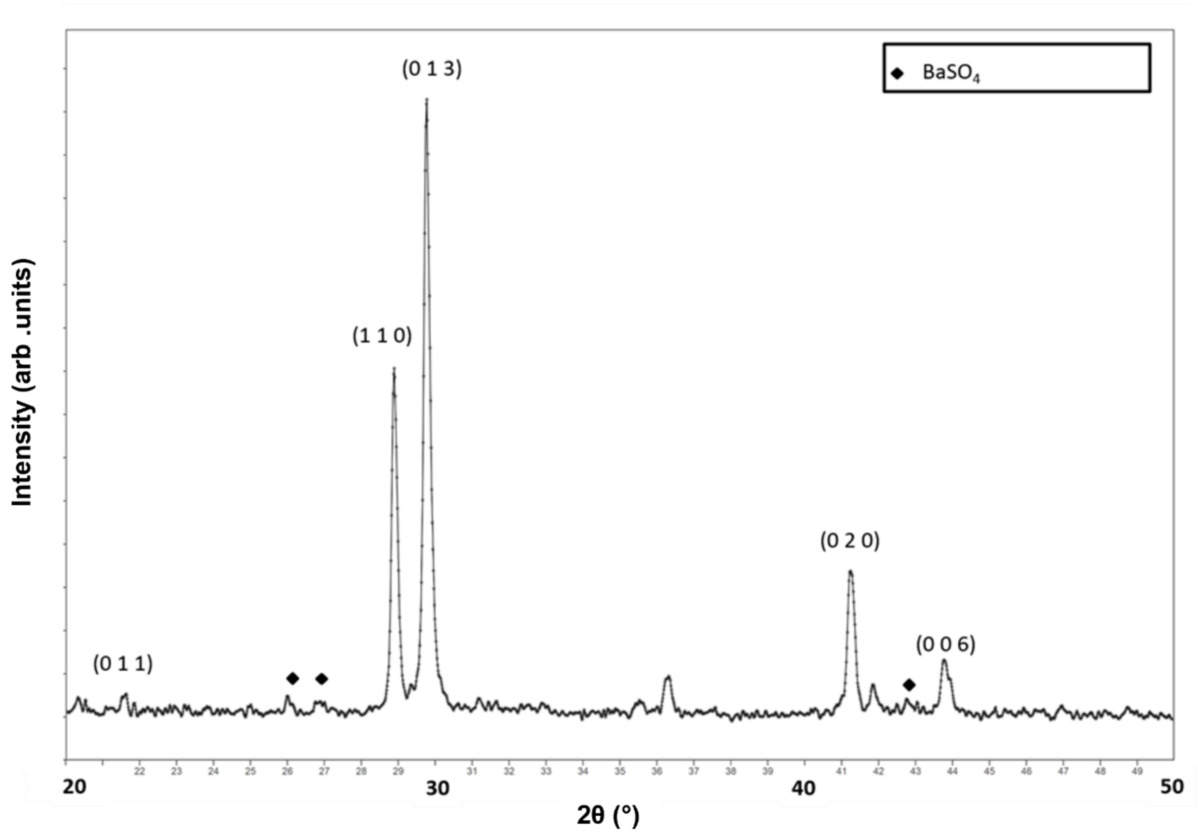

Figure 3.40 XRD pattern of $Ba_3Ho_2O_5(ZnO_2)_{0.33}(SO_4)_{0.67}$ synthesised at 1150°C detailing the main Miller Indices of the P4/mmm space group

Rietveld refinement of the structure using XRD data was attempted using a modified version of the predicted $Ba_3Yb_2O_5(ZnO_2)_{0.33}(SO_4)_{0.67}$ structure, replacing Ln = Yb with Ln = Ho where unit cell parameters are shown in ***Table 3.30***.

Table 3.30 Unit cell parameter values of $Ba_3Ho_2O_5(ZnO_2)_{0.33}(SO_4)_{0.67}$ XRD data

Formula	**Unit Cell Parameters**		**Unit Cell Volume**
	a	***c***	
$Ba_3Ho_2O_5CO_3$	4.3813(2)Å	11.8871(4)Å	228.185(23) Å^3
$Ba_3Ho_2O_5(ZnO_2)_{0.33}(SO_4)_{0.67}$	4.3892(1)Å	12.4512(4)Å	239.874(6) Å^3
$Ba_3Yb_2O_5(ZnO_2)_{0.33}(SO_4)_{0.67}$	4.3286(1)Å	12.5061(2)Å	234.321(6) Å^3

When comparing the unit cell parameters of the two Ln = Ho system, unit cell parameter *a* appears similar while cell parameter *c* increases, as described previously. Unit parameter *a* and the unit cell volume of the Ln = Ho sulphate system are larger than those of the Ln = Yb system, which is attributed to the greater ionic radii of six coordinate Ho^{3+} (0.901 Å) in comparison to six coordinate Yb^{3+} (0.868 Å).[166] Additionally, the ionic radii of four coordinate S^{6+} and four coordinate Zn^{2+} are larger than that of three coordinated C^{4+}, which would also contribute to the increase unit cell volume when comparing the carbonate and sulphate systems.[166]

3.3.3.4.2 Raman Spectroscopy

As with its carbonate counterpart, it is difficult to determine any of the expected sulphate vibrational modes for this Ho system other than the v_1 (symmetric stretch) due to problems arising from the photoluminescence process of Ho^{3+} (***Figure 3.41***). With the presence of $BaSO_4$ being detected in the XRD data, it is uncertain to say whether this v_1 vibrational mode is that seen from the expected $Ba_3Ho_2O_5(ZnO_2)_{0.33}(SO_4)_{0.67}$ system or leftover reagent $BaSO_4$ (***Table 3.31***).

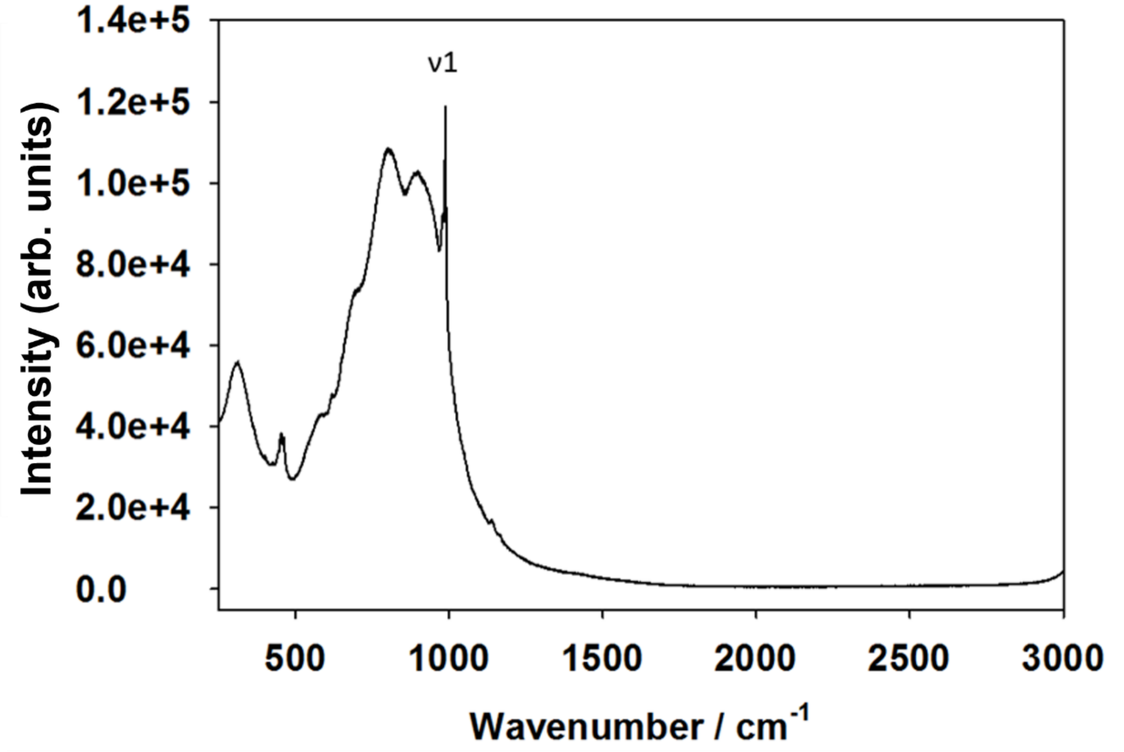

Figure 3.41 Raman spectroscopy data for $Ba_3Ho_2O_5(ZnO_2)_{0.33}(SO_4)_{0.67}$ detailing specific Raman bands seen for carbonate vibrational modes

Table 3.31 Raman band wavenumbers for carbonate vibrational modes of $(NH_4)_2SO_4$, $BaSO_4$ and $Ba_3Ho_2O_5(ZnO_2)_{0.33}(SO_4)_{0.67}$

System	**ν 1 /$^{-1}$**	**ν2 / cm^{-1}**	**ν 3 /$^{-1}$**	**ν 4 /$^{-1}$**
$(NH_4)_2SO_4$	975.6	452.0	1090.4	615.1 624.7
$BaSO_4$	987.6	452.3 461.0	1138.9 1166.6	617.4 647.3
$Ba_3Ho_2O_5(ZnO_2)_{0.33}(SO_4)_{0.67}$	- 987.6	- -	- -	- -

3.3.3.5 $Ba_3Dy_2O_5(ZnO_2)_{0.33}(SO_4)_{0.67}$ (Ln = Dy)

3.3.3.5.1 Powder X-Ray Diffraction

Utilising the same synthesis route, $Ba_3Dy_2O_5(ZnO_2)_{0.33}(SO_4)_{0.67}$ was also successfully synthesised (***Figure 3.42***) with the (0 1 1) reflection being greatly reduced in intensity and the (0 1 2) reflection not being seen at all. There also appears to be a slight presence of $BaSO_4$ and $Ba_3Dy_4O_9$ suggesting a longer heating time at slightly lower temperature could be required to improve purity.

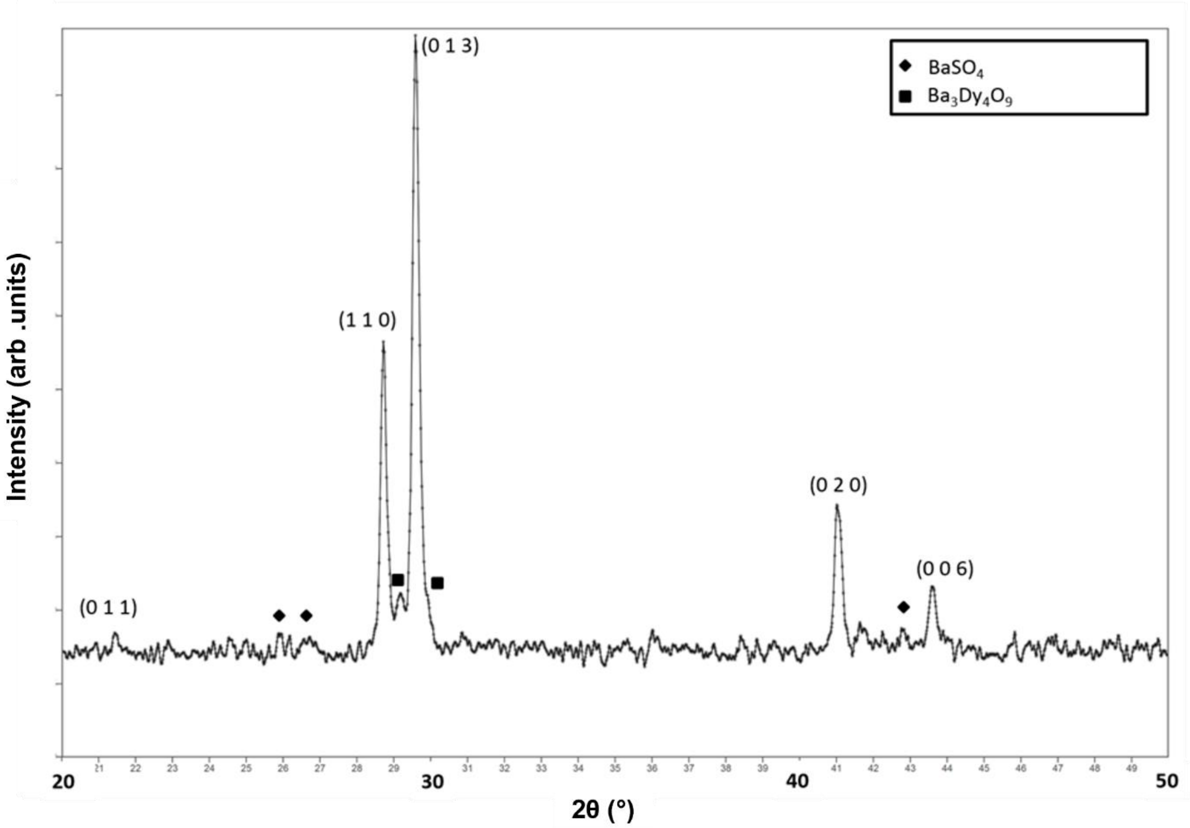

Figure 3.42 XRD pattern of $Ba_3Dy_2O_5(ZnO_2)_{0.33}(SO_4)_{0.67}$ synthesised at 1150°C detailing the main Miller Indices of the P4/mmm space group

Rietveld refinement of the structure using XRD data was attempted using a modified version of the predicted $Ba_3Yb_2O_5(ZnO_2)_{0.33}(SO_4)_{0.67}$ structure, replacing Ln = Yb with Ln = Dy where unit cell parameters are shown in ***Table 3.32***.

Table 3.32 Unit cell parameter values of $Ba_3Dy_2O_5(ZnO_2)_{0.33}(SO_4)_{0.67}$ XRD data

Formula	**Unit Cell Parameters**		**Unit Cell Volume**
	a	***c***	
$Ba_3Dy_2O_5CO_3$	4.3900(3)Å	11.9244(8)Å	229.810(39) Å^3
$Ba_3Dy_2O_5(ZnO_2)_{0.33}(SO_4)_{0.67}$	4.3953(1)Å	12.4583(2)Å	240.679(42) Å^3
$Ba_3Yb_2O_5(ZnO_2)_{0.33}(SO_4)_{0.67}$	4.3286(1)Å	12.5061(2)Å	234.321(6) Å^3

When comparing the unit cell parameters of the two Ln = Ho systems, unit cell parameter *a* appears relatively similar as cell parameter *c* increases, as describe previously. Unit parameter *a* and unit cell volume of the Ln = Dy sulphate system are larger than those of the Ln = Yb system, which is attributed to the greater ionic radii of six coordinate Dy^{3+} (0.912 Å) in comparison to six coordinated Yb^{3+} (0.868 Å).[166] Additionally, the ionic radii of four coordinate S^{6+} and four coordinate Zn^{2+} are larger than that of three coordinate C^{4+}, which would also contribute to the increase unit cell volume whilst also being responsible for the increasing unit cell parameter *c* when comparing carbonate and sulphate systems.[166]

3.3.3.5.2 Raman Spectroscopy

The Raman spectrum seen in ***Figure 3.43*** supports the inclusion of sulphate in the $Ba_3Dy_2O_5(ZnO_2)_{0.33}(SO_4)_{0.67}$ system with the appearance of the expected v_1 (symmetric stretch), v_2 (doubly degenerate bend), v_3 (triply degenerate asymmetric stretch) and v_4 (triply degenerate asymmetric bend) sulphate vibrational modes[168]. Most bands recorded for these are shifted in wavenumbers in comparison to those seen in $(NH_4)_2SO_4$ or $BaSO_4$ (***Table 3.33***). $Ba_3Tm_2O_5(ZnO_2)_{0.33}(SO_4)_{0.67}$ also gives rise to a second v_1 band which is similar to that of $BaSO_4$ and the other sulphate systems. The fact that there are many bands seen around the v_3 region make it is difficult to say with certainty which belong to this system. The presence of $BaSO_4$ in the XRD data means it is challenging to say whether this v_1 vibrational mode is that seen from the expected $Ba_3Dy_2O_5(ZnO_4)_{0.33}(SO_4)_{0.67}$ system or leftover reagent $BaSO_4$.

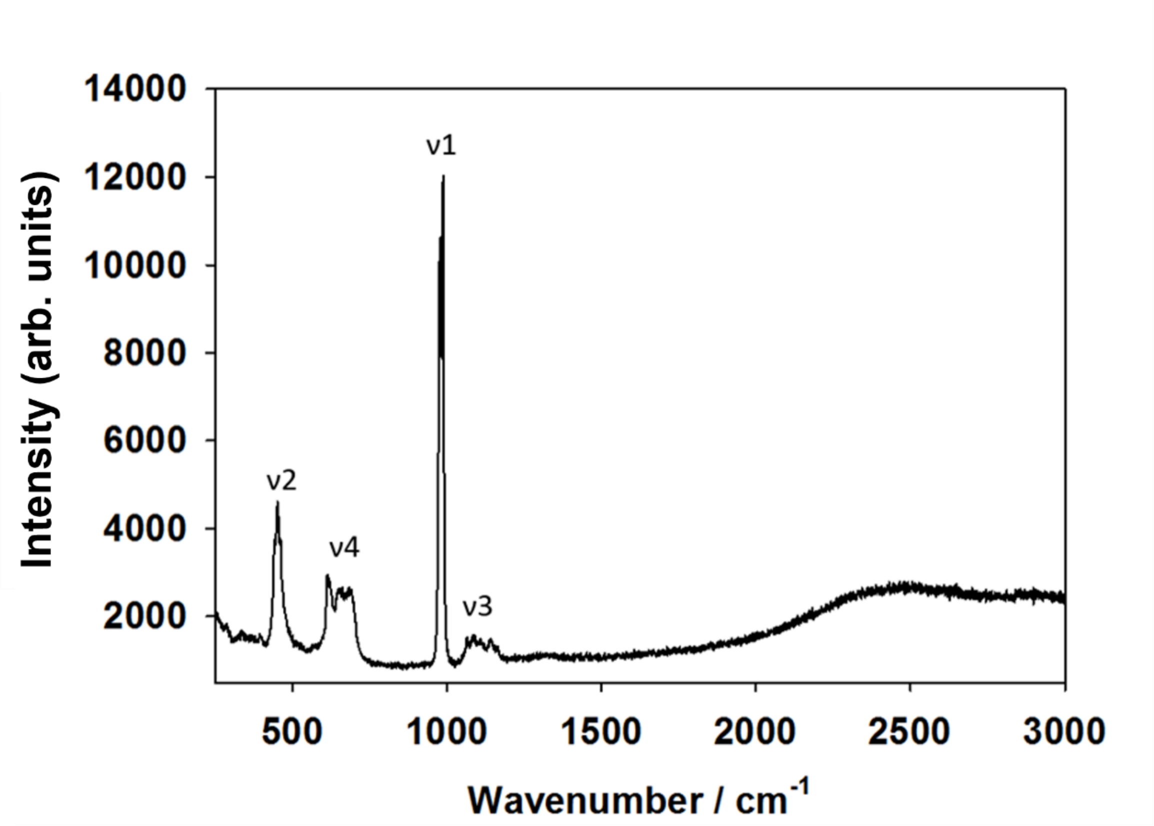

Figure 3.43 Raman spectroscopy data for $Ba_3Dy_2O_5(ZnO_4)_{0.33}(SO_4)_{0.67}$ detailing specific Raman bands seen for carbonate vibrational modes

Table 3.33 Raman band wavenumbers for carbonate vibrational modes of $(NH_4)_2SO_4$, $BaSO_4$ and $Ba_3Dy_2O_5(ZnO_4)_{0.33}(SO_4)_{0.67}$

System	ν 1 /$^{-1}$	ν2 / cm^{-1}	ν 3 /$^{-1}$	ν 4 /$^{-1}$
$(NH_4)_2SO_4$	975.6	452.0	1090.4	615.1 624.7
$BaSO_4$	987.6	452.3 461.0	1138.9 1166.6	617.4 647.3
$Ba_3Dy_2O_5(ZnO_4)_{0.33}(SO_4)_{0.67}$	978.8 987.9	452.2 -	- -	613.2 649.4 682.3

3.3.3.6 Structural Trend

With all systems in this section being synthesised using different lanthanides, values were tabulated (***Table 3.32***) to determine any trends between structural parameters and the size of the six coordinate Ln^{3+} ionic species.

Table 3.34 Unit Cell parameters for $Ba_3Ln_2O_5(ZnO_2)_{0.33}(SO_4)_{0.67}$ (Ln= Yb, Tm. Er, Ho, Dy)

Formula	Ionic Radii (VI Coord)[166] / Å	Unit Cell Parameters / Å		Unit Cell Volume / Å^3
		a	***c***	
$Ba_3Yb_2O_5(ZnO_2)_{0.33}(SO_4)_{0.67}$	0.8680	4.3286(1)	12.5061(2)	234.321(6)
$Ba_3Tm_2O_5(ZnO_2)_{0.33}(SO_4)_{0.67}$	0.8800	4.3464(1)	12.4885(4)	235.926(18)
$Ba_3Er_2O_5(ZnO_2)_{0.33}(SO_4)_{0.67}$	0.8900	4.3655(3)	12.4946(7)	238.115(42)
$Ba_3Ho_2O_5(ZnO_2)_{0.33}(SO_4)_{0.67}$	0.9010	4.3892(2)	12.4512(4)	239.874(23)
$Ba_3Dy_2O_5(ZnO_2)_{0.33}(SO_4)_{0.67}$	0.9120	4.3953(3)	12.4583(8)	240.679(39)

As expected, there is a positive correlation between an increasing unit cell volume with increasing ionic radii (***Figure 3.44***). Whilst unit cell parameter *a* shows a similar positive correlation with increasing ionic radii size (***Figure 3.45***), unit cell parameter *c* goes against these trends showing a general decrease with increasing ionic radii size (***Figure 3.46***). This negative correlation of unit cell parameter *c* is interesting and requires further study to clarify. A more detailed neutron diffraction study would be required to help understand and explain this.

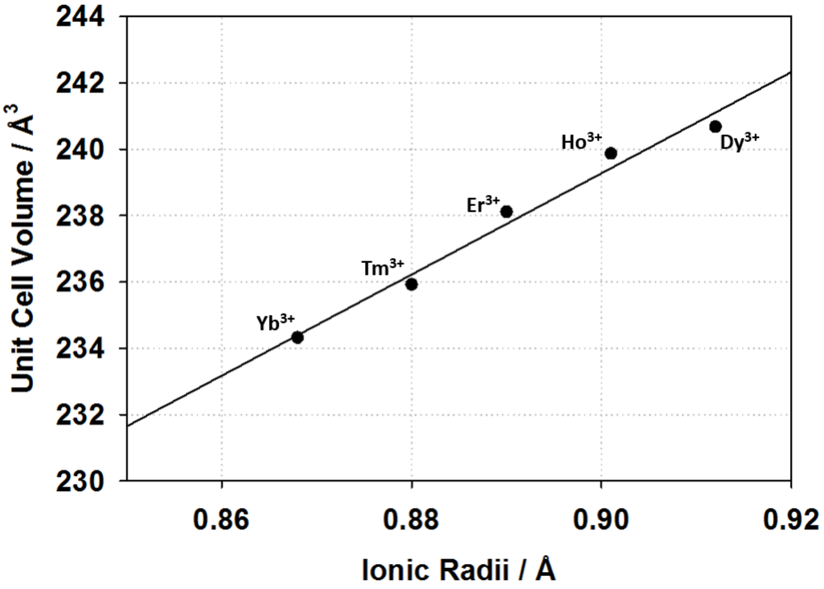

Figure 3.44 Variation in unit cell volume of $Ba_3Ln_2O_5(ZnO_2)_{0.33}(SO_4)_{0.67}$ *with ionic radius*

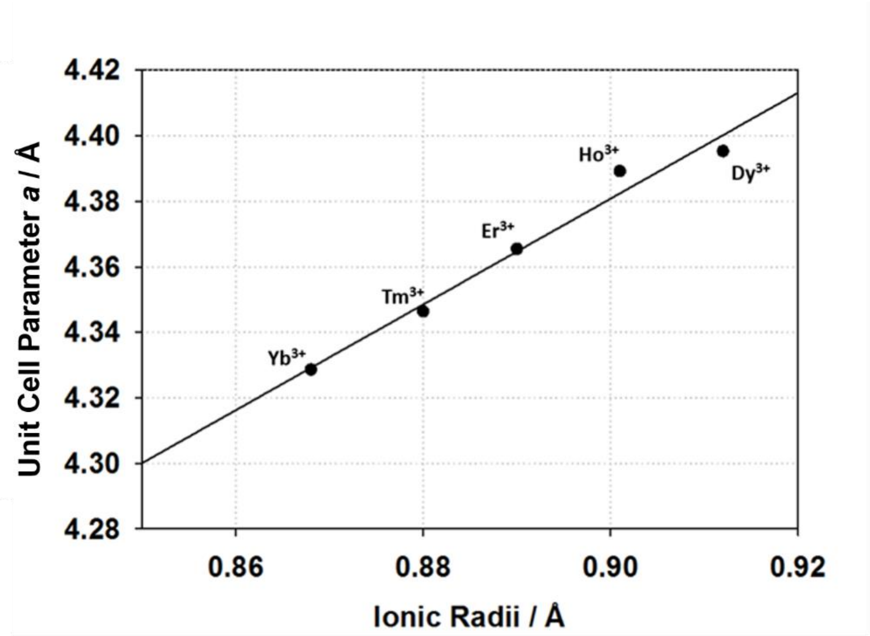

Figure 3.45 Variation in unit cell parameter a of $Ba_3Ln_2O_5(ZnO_2)_{0.33}(SO_4)_{0.67}$ with ionic radius

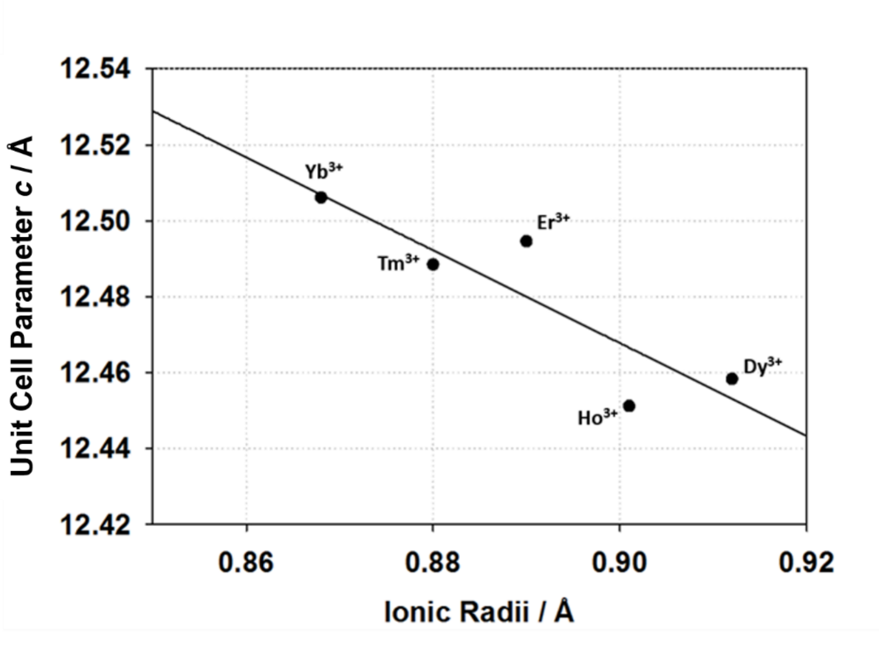

Figure 3.46 Variation in unit cell parameter c of $Ba_3Ln_2O_5(ZnO_2)_{0.33}(SO_4)_{0.67}$ with ionic radius

3.4 Conclusion

In this chapter, $Ba_3Ln_2O_5CO_3$ (Ln = Yb, Lu, Tm, Er, Ho, Dy, Y) phases were successfully synthesised and are shown to be new layered perovskites, with double Ln layers separated by carbonate layers. The determination of carbonate within the systems was supported through Raman spectroscopy which showed Raman band shifts to lower wavenumbers associated with carbonate vibrational modes, in comparison to $BaCO_3$. The magnitude of this shift generally increased as the size of Ln increased. Rietveld refinement of these systems showed the need for neutron diffraction for accurate structure determination due to the weak X-ray scattering factors of C and O which could have a variation of carbonate position and orientation on the central layer.

Whilst the formation of these systems is clear, signs of impurity phases indicate the difficulty involved with synthesising these systems in terms of avoiding carbonate loss through the synthesis techniques used. Attempted synthesis of more thermally stable oxyanion systems containing borate, sulphate and phosphate which are structurally similar to that of $Ba_3Yb_2O_5CO_3$ were mostly unsuccessful. However, a zinc stabilised sulphate system was obtained with the formula of $Ba_3Yb_2O_5(ZnO_2)_{0.33}(SO_4)_{0.67}$.

Isostructural systems for $Ba_3Ln_2O_5(ZnO_2)_{0.33}(SO_4)_{0.67}$ (Ln = Yb, Tm, Er, Ho, Dy) were successfully synthesised at 1150°C in air, appearing to be a much greater purity in comparison to their carbonate counterparts. The stabilisation provided by the zinc and sulphate in these systems can be seen by the reduced absence of $Ba_3Ln_4O_9$ which is normally the major product when heated at 1100°C in air for the carbonate systems. Raman spectroscopy studies supports that these systems show successful incorporation of sulphate into these systems, whilst the appearance of two v_1 bands confirms that sulphate is successfully incorporated, it also suggests there may be more than one sulphate environment in this structure however this second band may also indicate the presence of $BaSO_4$. Like the carbonate equivalent systems, neutron diffraction studies are required to determine exact oxygen orientations around the zinc and sulphur. These findings illustrate how the formation of the structure can be extended to other, more thermally stable oxyanions.

The work presented in this chapter is important as it highlights the need to consider the potential incorporation of carbonate in perovskite materials prepared at temperatures $\leq$1000°C, as many perovskite systems prepared at low temperature could possibly be incorporating carbonate, affecting the materials properties rather than simply previously considered morphological effects.

.

4. Investigation of the Possible Oxyanion Incorporation in $Ba_2Co_{1-x}O_{4-\delta}$ and $Ba_2Fe_{1-x}O_{4-\delta}$

4.1 Introduction

Development of new transition metal containing materials for use in solid oxide fuel cells (SOFCs) is being widely researched given the interest in such systems for more efficient electrical energy generation. SOFCs have wide applications from large scale use for power generation to small scale use for residential, industrial and transportation applications.[169] These fuel cells usually use an oxide-ion conducting ceramic material as the electrolyte. Fluorite based oxide ion conducting electrolytes have typically dominated, although there is also interest in perovskite-based proton conducting electrolytes, while perovskite-type mixed metal oxides have been studied as electrode materials due to their low cost, high catalytic activity and high thermal stability.[170]

Materials with general formula A_2BO_4 (A = alkali earth/rare earth, B = transition metal) can adopt either the K_2NiF_4[171] or β-K_2SO_4[172] structure – the latter observed for small cations capable of tetrahedral coordination. Recently $Ln_{1-x}Ba_{1+x}(Ga/Al)O_{4-x/2}$ (Ln = La, Pr, Nd) with the β-K_2SO_4 structure has been shown to have high levels of proton conductivity.[177-182] This raises the potential that transition metal containing materials with this structure-type may display mixed proton-electronic conductivity and so potentially be utilised as cathode materials for proton conducting ceramic fuel cells. In this respect, Ba_2CoO_4 is known to possess this structure.

The magnetic properties of Ba_2CoO_4 have attracted interest as an example of a structure containing Co(IV)O_4 units.[48, 183-187] An interesting aspect of Ba_2CoO_4 , is that two polymorphs are known, the first is orthorhombic β-K_2SO_4[48, 77] and the second is a monoclinic polymorph (β angle ≠ 90°) of this structure, as also adopted by β-Ca_2SiO_4[188] and Ba_2TiO_4.[121] During the course of the synthesis of Ba_2CoO_4 we discovered that the Co content appeared to be less than expected. Following on from this find, various $Ba_2Co_{1-x}O_y$ ($0 \leq x \leq 0.25$) systems were synthesised to determine the extent of Co deficiency before impurities became prevalent. Rietveld refinement studies of X-ray and neutron diffraction data helped to clarify the possibility of the incorporation of carbonate in place of the missing CoO_4 tetrahedral units.

This is interesting as there is growing evidence of the presence of carbonate in systems prepared via low temperature routes, such as the oxide carbonate composition $Y_3Al_3O_8CO_3$[189] which was previously thought to be $YAlO_3$, Ba_2TiO_4[190] has also been shown to contain carbonate and water, whilst more recently it was found that carbonate can be utilised to stabilise new perovskite phase $Ba_3Yb_2O_5CO_3$.[191]

In this chapter the synthesis and structural characterisation of these $Ba_2(CoO_4)_{1-x}(CO_3)_x$ ($0 \leq x \leq 0.20$) systems is investigated, highlighting through various studies that carbonate is readily accommodated to replace the Co deficiency. These investigations are then extended onto the possible carbonate and sulphate incorporation of the structurally related Fe systems; $Ba_2(FeO_4)_{1-x}(CO_3)_x$ (x = 0.10, 0.15, 0.20) and $Ba_2(FeO_4)_{1-x}(SO_4)_x$ (x = 0.10, 0.15, 0.20) respectively.

4.2 Experimental Procedure

A series of samples with the nominal compositions $Ba_2Co_{1-x}O_{4-\delta}$ ($0 \leq x \leq 0.25$) were prepared from the appropriate stoichiometric amounts of $BaCO_3$ (Alfa Aesar 99.8%) and Co_3O_4 (Alfa Aesar 99.7%). The intimately ground powders were heated at a rate of 10°C/min to 980°C where they were held for a combined 48 hours with two intermediate regrinds. The resultant powders were then reground and characterised.

A series of samples with the nominal compositions $Ba_2Fe_{1-x}O_{4-\delta}$ ($0 \leq x \leq 0.20$) were prepared similarly from the appropriate stoichiometric amounts of $BaCO_3$ (Alfa Aesar 99.8%) and Fe_2O_3 (Sigma-Aldrich ≥96.0%). The intimately ground powders were heated at a rate of 10°C/min to 980°C where they were held for a combined 24 hours with one intermediate regrind. The resultant powders were then reground and characterised.

A series of samples with the nominal compositions $Ba_2Fe_{1-x}S_xO_4$ ($0 \leq x \leq 0.20$) were prepared from the appropriate stoichiometric amounts of $BaCO_3$ (Alfa Aesar 99.8%), Fe_3O_4 (Sigma-Aldrich ≥96.0%) and $(NH_4)_2SO_4$ (ACS Reagent ≥99.0%). The intimately ground powders were heated at a rate of 10°C/min to 980°C where they were held for a combined 24 hours with one intermediate regrind. The resultant powders were then reground and characterised.

Powder X-ray diffraction (XRD) analysis of $Ba_2Co_{1-x}O_{4-\delta}$ systems were carried out using a PANalytical Empyrean X-Ray Diffractometer (Cu Kα radiation). Data collected were used to identify the phases present and determine the initial structure of the samples through Rietveld profile refinement.

Powder X-ray diffraction (XRD) analysis of $Ba_2Fe_{1-x}O_{4-\delta}$ and $Ba_2Fe_{1-x}S_xO_4$ systems were carried out using D2 Phaser X-Ray Diffractometer (Co Kα radiation). Data collected were used to identify the phases present and determine the initial structure of the samples through Rietveld profile refinement.

For detailed structural characterisation of $Ba_2Co_{1-x}O_{4-\delta}$ systems (x = 0, 0.10, 0.15), time of flight neutron powder diffraction (NPD) data sets were collected on the HRPD diffractometer at the ISIS neutron diffraction facility, Rutherford Appleton Laboratory. Structure refinements were performed using the GSAS II suite of programs.

Raman spectroscopy measurements of $Ba_2Co_{1-x}O_{4-\delta}$ systems were performed using a DILOR XY spectrometer with a CCD detector at the University of Zaragoza. Measurements were taken at room temperature using varying laser line power. In addition measurements were taken at constant laser line power at varying temperatures.

Raman spectroscopy measurements of the $Ba_2Fe_{1-x}O_{4-\delta}$ and $Ba_2Fe_{1-x}S_xO_4$ systems were performed using a Renishaw inVia Raman microscope using a 532 nm laser with 0.5% power.

Thermogravimetric analysis with mass spectroscopy (TGA-MS) data were collected on a Netsch TGA-MS using a temperature range of 40° - 1300°C at a rate of 10°C/min under a dry N_2 atmosphere.

4.3 Results and Discussion

4.3.1 Synthesis and Structural Characterisation of $Ba_2(CoO_4)_{1-x}(CO_3)_x$

4.3.1.1 Powder X-ray Diffraction

Ba_2CoO_4 has been reported to have two different polymorphs; the first is isostructural to the orthorhombic β-K_2SO_4 system (orthorhombic space Group – *Pnma*) and the second is isostructural to the monoclinic Ca_2SiO_4 system (Space Group – $P\ 1\ 2_1/n\ 1$).

The synthesis of this compound, Ba_2CoO_4 in air, proved to be very difficult with invariably small impurities observed. The phase purity was improved upon by introducing Co deficiency, and the synthesis of a series of $Ba_2Co_{1-x}O_y$ ($0<x\leq0.20$) samples showed distinct changes in the X-ray diffraction pattern, suggesting a change of cell symmetry from monoclinic to orthorhombic as the Co deficiency increased (***Figure 4.1***). Higher values of Co deficiency ($x>0.20$) led to the identification of impurities, typically $BaCO_3$.

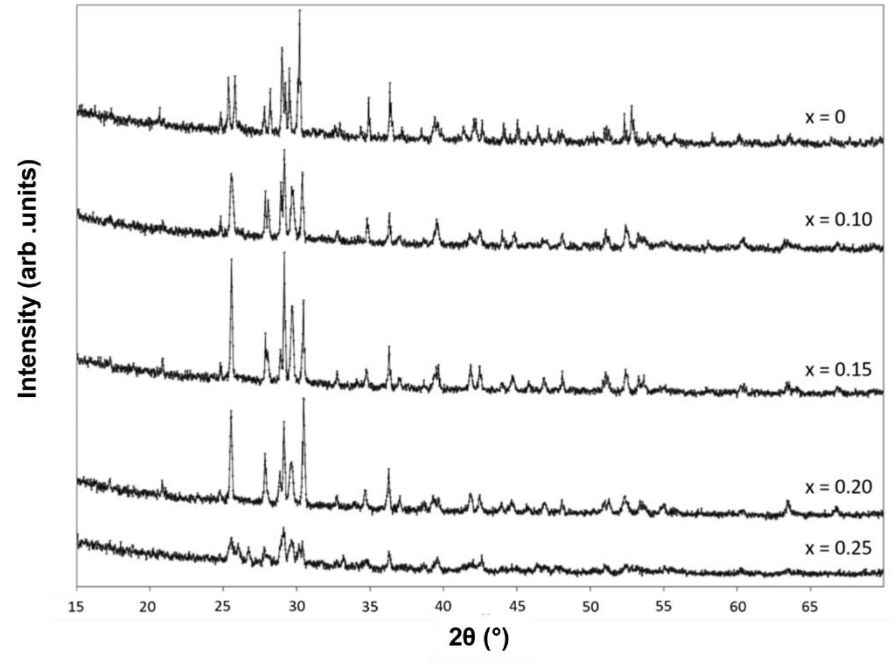

Figure 4.1 X-ray diffraction patterns for $Ba_2Co_{1-x}O_{4-\delta}$ *(* $0 < x \leq 0.25$*) systems synthesised at 980°C, showing changes in peak splitting for* $0 < x \leq 0.20$ *values.*

Additional synthesis attempts were performed with heat treatments above 1000°C. However, these higher temperature syntheses appeared to give rise to sample decomposition (***Figure 4.2***) and so all the synthesis temperatures were limited to 980°C.

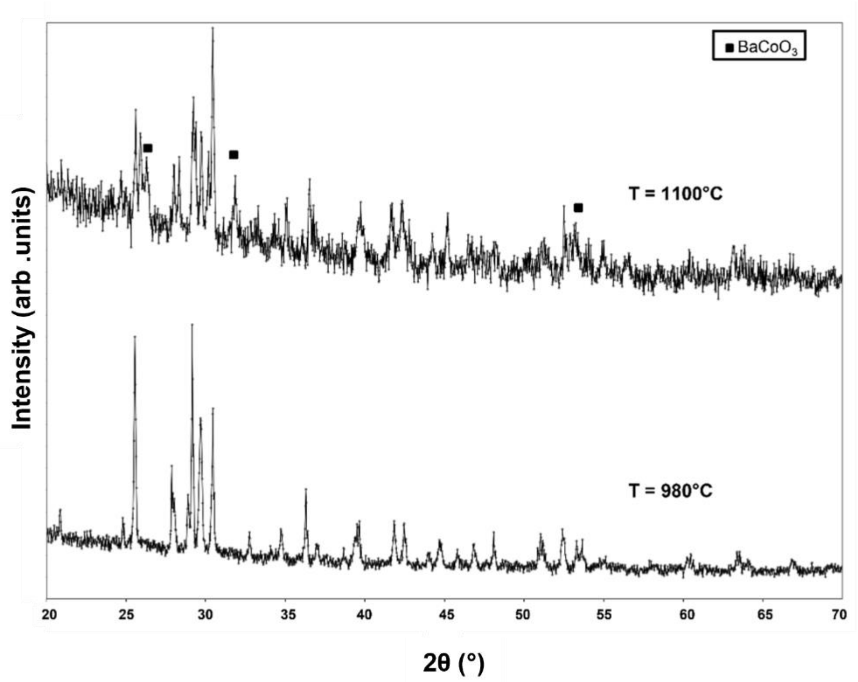

Figure 4.2 X-ray diffraction patterns for $Ba_2Co_{1-x}O_{4-ŭ}$ *(x = 0.15) system synthesised at 980°C and 1100°C, highlighting the appearance of impurity phases at the higher synthesis temperature.*

When heated to these higher synthesis temperatures, Co deficient samples begin to transition between the two polymorphs. With reference to the x = 0.15 sample, as the temperature is raised a change is seen from the orthorhombic phase to a phase more resembling that of the monoclinic phase with the additional presence of a $BaCoO_{3-y}$ impurity.

4.3.1.2 Rietveld Refinement using Neutron Diffraction Data

Initial structure refinements using the acquired neutron data, suggested an apparent Co deficiency. Improved fits in the refinements could be produced by balancing deficiencies of Co with the introduction of C as carbonate. Further structure refinement with this model of carbonate incorporation supported this methodology and was shown to provide great goodness of fits for the more deficient samples.

Thus, a model was proposed which employed the incorporation of CO_3^{2-} groups as a partial substitution for CoO_4^{4-} groups leading to predicted compositions of $Ba_2(CoO_4)_{1-x}(CO_3)_x$. Several approaches were applied to introduce the carbonate group, with the best fits for the Co deficient samples obtained through the placement of CO_3^{2-} group in the O1-O3-O4 tetrahedral face of the CoO_4^{2-} group (***Figure 4.3***).

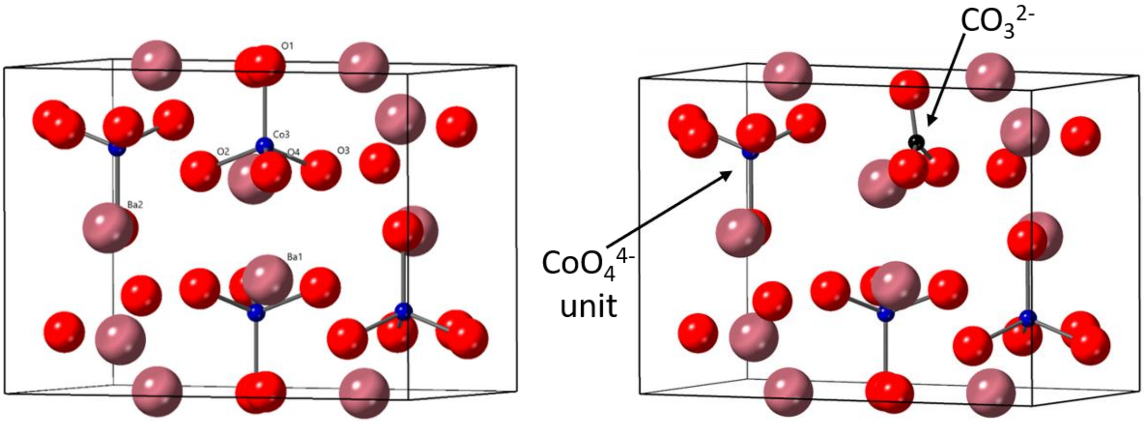

Figure 4.3 Structure showing monoclinic structure (P 1 2_1*/n* 1*) and the preferred position of* CO_3^{2-}

Neutron diffraction data was collected for the $Ba_2Co_{1-x}O_{4-\delta}$ ($0<x\leq0.15$) systemswhich was then refined. Refinement used two TOF data banks and the respective GOF values of the two models (carbonated/uncarbonated) are given in ***Table 4.1***. Unit cell parameters are given in ***Table 4.2***, while. The observed, calculated and difference profiles are shown in ***Figure 4.4***, ***Figure 4.5*** and ***Figure 4.6***.

Table 4.1 Rietveld Refinement Goodness of Fit (GOF) values for $Ba_2Co_{1-x}O_{4-\delta}$ *(* $0 < x \leq 0.15$*) systems with and without* CO_3^{2-} *included into the starting model.*

$Ba_2(CoO_4)_{1-x}(CO_3)_x$ (x =)	**GOF (no carbonate)**	**GOF (carbonate present)**
0.15	5.18	2.88
0.10	4.41	2.20
0.00	4.43	4.50

Table 4.2 Refined unit cell parameters for $Ba_2Co_{1-x}O_{4-\breve{u}}$ (0 < x Ò 0.15) in reference to their best fitted model (x = 0.15, 0.10 Ą CO_3^{2-} included; x = 0 Ą CO_3^{2-} excluded)

$Ba_2(CoO_4)_{1-x}(CO_3)_x$	**Unit Cell Parameter / Å**				
X	***a***	***b***	***c***	**β /**	**Volume / Å³**
0.15	5.871(1)	7.630(1)	10.501(1)	90.03(1)	470.427(17)
0.10	5.883(1)	7.629(1)	10.464(1)	90.50(1)	469.606(13)
0.00	5.915(1)	7.625(1)	10.419(1)	91.22(1)	469.826(15)

Increasing the value of x, and hence increasing incorporation of CO_3^{2-} a decrease in the monoclinic, β, angle is observed indicating a structural progression from monoclinic towards orthorhombic.

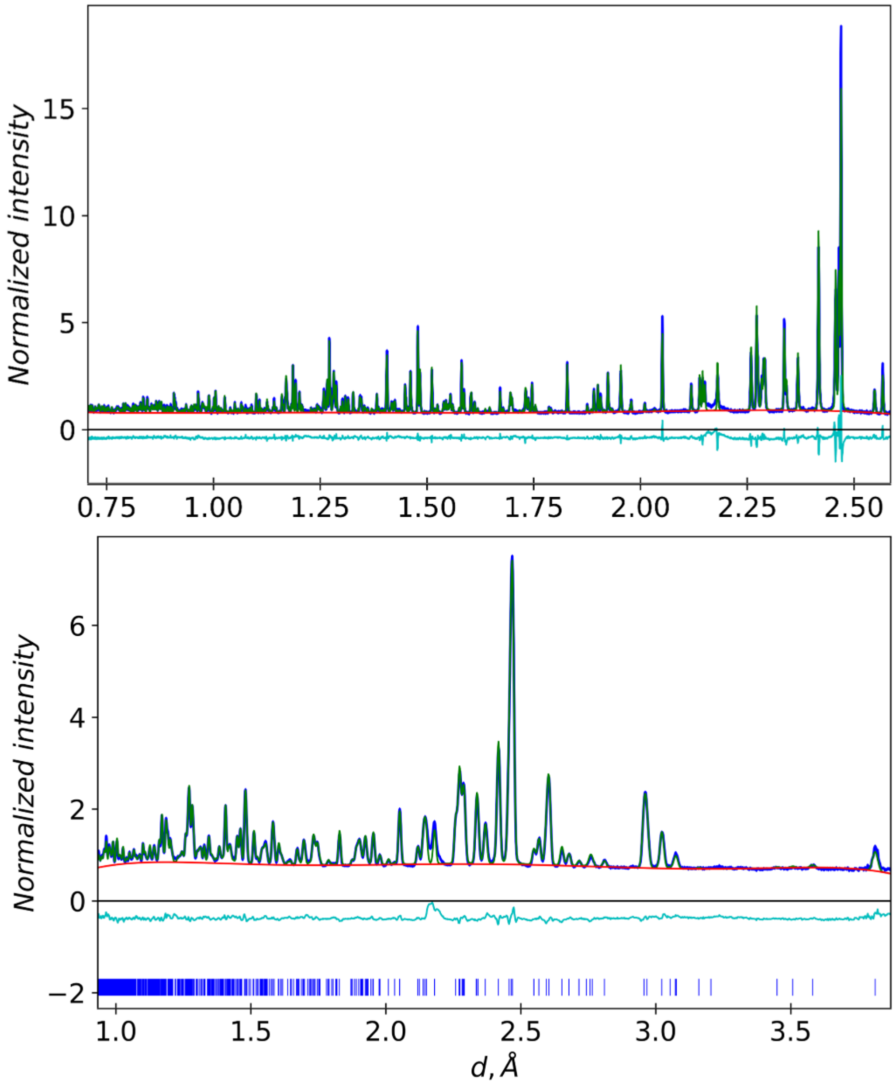

Figure 4.4 Observed, calculated and difference neutron diffraction profiles for Ba_2CoO_4 (Bank 1 top, Bank 2 bottom)
Space Group: $P12_1/n1$
GOF = 4.43

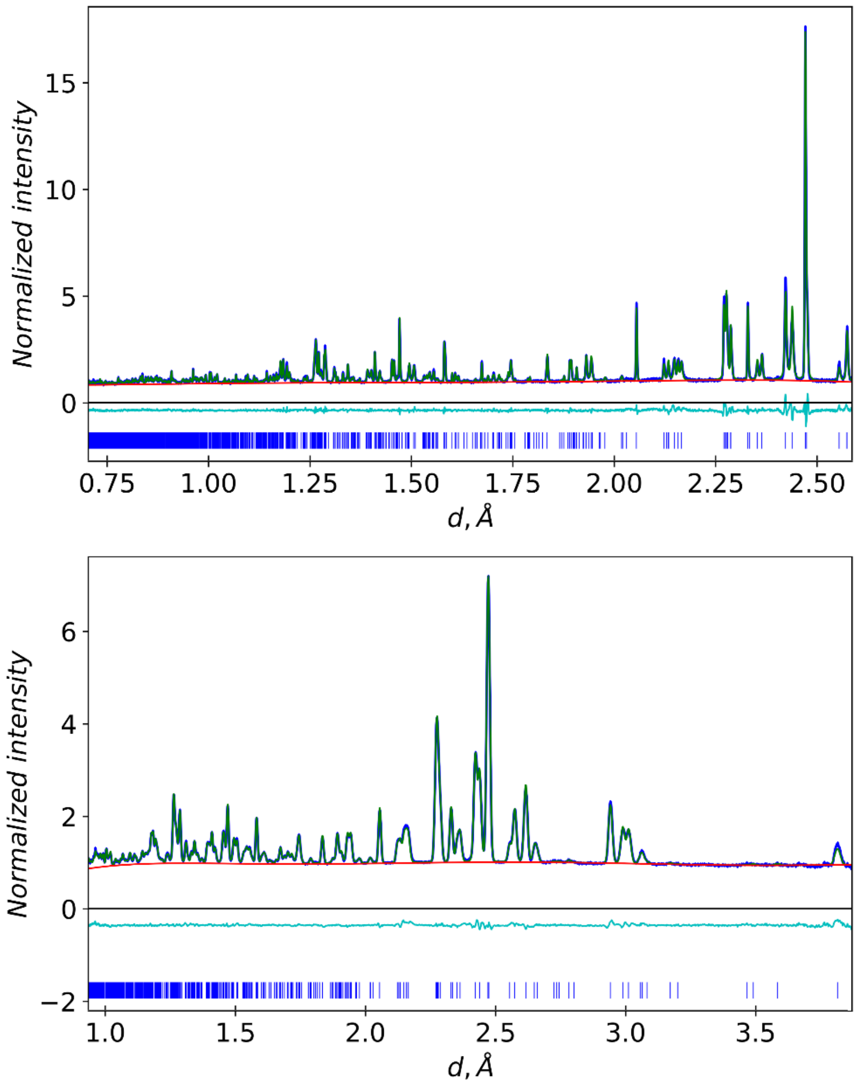

Figure 4.5 Observed, calculated and difference neutron diffraction profiles for $Ba_2(CoO_4)_{0.90}(CO_3)_{0.10}$ *(Bank 1 top, Bank 2 bottom)*
Space Group: $P12_1/n1$
GOF = 2.20

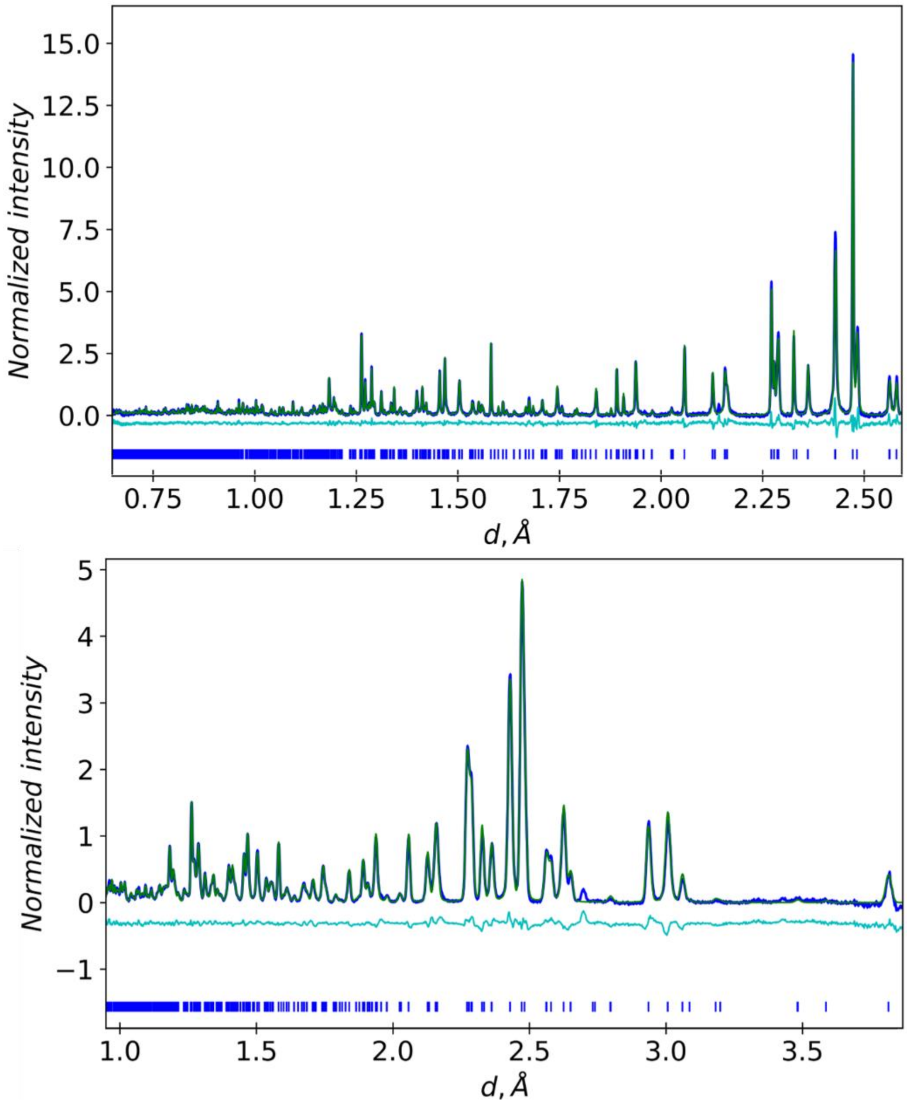

Figure 4.6 Observed, calculated and difference neutron diffraction profiles forBa$_2$(CoO$_4$)$_{0.85}$(CO$_3$)$_{0.15}$ (Bank 1 top, Bank 2 bottom)
Space Group: $P12_1/n1$
GOF = 2.88

The addition of CO_3^{2-} in place of the CoO_4 unit showed an improved fit for both the x = 0.10 and x = 0.15 systems helping to support the presence of carbonate in the sample. All refinements produced on the x = 0 system using the CO_3^{2-} substituted model, produced fits worse than that of the system with only Co^{4+} vacancies. In this x = 0 model, carbonate was introduced with a small fraction (0.01). The issue with this model for x = 0 is that any amount of carbonate of a cobalt site would lead to the creation more oxide vacancies than expected for a system assumed to have no cobalt vacancies. This suggests that there is no presence of carbonate within this system and so the uncarbonated model was used for the x = 0 system. The x = 0 system also appears to show somewhat of an impurity, upon investigation on what this impurity could be, it was found to be undeterminable.

The final refined structural information from the neutron refinements are given in ***Table 4.3***. Bond lengths determined from these refined structures are given in ***Table 4.4***, with bond angles associated with the CoO_4 tetrahedra in ***Table 4.5***.

Table 4.3 Refined structural data for $Ba_2(CoO_4)_{1-x}(CO_3)_x$ *(x = 0.15, 0.10, 0)*

Atom	**x**	**y**	**Z**	**Fraction**	**Wyckoff Position**	**U_{iso}/U11**	**U22**	**U33**
Ba1								
0.85	0.259(1)	0.354(1)	0.580(1)	1.000	4e	0.024(1)	-	-
0.90	0.257(1)	0.354(1)	0.580(1)	1.000	4e	0.018(1)	-	-
1.00	0.260(1)	0.351(1)	0.581(1)	1.000	4e	0.010 (1)	-	-
Ba2								
0.85	0.266(1)	0.003(1)	0.309(1)	1.000	4e	0.011(1)	-	-
0.90	0.256(1)	0.005(1)	0.310(1)	1.000	4e	0.010(1)	-	-
1.00	0.256(1)	0.008(1)	0.308(1)	1.000	4e	0.004(1)	-	-
Co1								
0.85	0.257(1)	0.776(1)	0.581(1)	0.857(3)	4e	0.006(1)	-	-
0.90	0.251(1)	0.777(1)	0.583(1)	0.939(5)	4e	0.010(1)	-	-
1.00	0.246(1)	0.774(1)	0.584(1)	1.000	4e	0.004(1)	-	-
O1								
0.85	0.265(1)	1.012(1)	0.579(1)	0.857(3)	4e	0.060(1)	0.001(1)	0.016(1)
0.90	0.255(1)	1.010(1)	0.581(1)	0.939(5)	4e	0.062(1)	0.009(1)	0.033(1)
1.00	0.257(1)	1.009(1)	0.584(1)	1.000	4e	0.044(2)	0.005(1)	0.032(2)
O2								
0.85	0.244(1)	0.680(1)	0.419(1)	0.857(3)	4e	0.026(1)	0.016(1)	0.008(1)

0.90	0.238(1)	0.682(1)	0.419(1)	0.939(5)	4e	0.035(1)	0.021(1)	0.014(1)
1.00	0.215(1)	0.686(1)	0.421(1)	1.000	4e	0.039(2)	0.006(1)	0.013(2)
O3								
0.85	0.492(1)	0.692(1)	0.643(1)	0.857(3)	4e	0.024(2)	0.035(2)	0.032(2)
0.90	0.500(1)	0.687(1)	0.644(1)	0.939(5)	4e	0.019(1)	0.030(1)	0.029(1)
1.00	0.502(1)	0.680(1)	0.642(1)	1.000	4e	0.010(2)	0.008(1)	0.028(2)
O4								
0.85	0.005(1)	0.694(1)	0.657(1)	0.857(3)	4e	0.006(2)	0.041(2)	0.050(2)
0.90	0.004(1)	0.694(1)	0.660(1)	0.939(5)	4e	0.025(1)	0.032(1)	0.036(1)
1.00	0.010(1)	0.699(1)	0.664(1)	1.000	4e	0.014(2)	0.037(2)	0.027(2)
C1								
0.85	0.291(1)	0.780(1)	0.654(1)	0.143(3)	4e	0.056(4)	-	-
0.90	0.279(1)	0.781(1)	0.657(1)	0.061(5)	4e	0.031(11)	-	-
1.00	-	-	-	-	-	-	-	-
O1a								
0.85	0.304(1)	0.951(1)	0.641(1)	0.143(3)	4e	0.046(2)	0.017(1)	0.007(1)
0.90	0.305(1)	0.945(1)	0.639(1)	0.061(5)	4e	0.086(3)	0.072(3)	0.021(2)
1.00	-	-	-	-	-	-	-	-
O3a								
0.85	0.473(1)	0.693(1)	0.678(1)	0.143(3)	4e	0.046(2)	0.017(1)	0.007(1)
0.90	0.450(1)	0.685(1)	0.687(1)	0.061(5)	4e	0.086(3)	0.072(3)	0.021(2)
1.00	-	-	-	-	-	-	-	-
O4a								
0.85	0.095(1)	0.695(1)	0.662(1)	0.143(3)	4e	0.046(2)	0.017(1)	0.007(1)
0.90	0.081(1)	0.711(1)	0.645(1)	0.061(5)	4e	0.086(3)	0.072(3)	0.021(2)
1.00	-	-	-	-	-	-	-	-

Constraints: Anisotropic parameters (U) O1a=O3a=O4a
Fraction Co1+C1=1, Co1=O1=O2=O3=O4, C1=O1a=O3a=O4a

Table 4.4 Bond lengths determined from refined structures of $Ba_2(Co_4)_{1-x}(CO_3)_x$

Bond	System	Bond Length (Å)	Bond	System	Bond Length (Å)
C1 – O1a	0.85	1.315(9)	**Ba2 – O2**	0.85	2.725(10)
	0.90	1.280(8)		0.90	2.725(10)
	1.00	-		1.00	2.746(5)
C1 – O3a	0.85	1.285(10)	**Ba2 – O3**	0.85	2.775(8)
	0.90	1.281(9)		0.90	2.714(7)
	1.00	-		1.00	2.680(5)
C1 – O4a	0.85	1.325(10)	**Ba2 – O4**	0.85	2.576(8)
	0.90	1.280(9)		0.90	2.639(8)
	1.00	-		1.00	2.662(5)
Ba1 – O1	0.85	2.609(8)	**Ba2 – O1a**	0.85	2.605(10)
	0.90	2.619(8)		0.90	2.776(12)
	1.00	2.609(4)		1.00	-
Ba1 – O2	0.85	2.932(10)	**Ba2 – O3a**	0.85	2.661(9)
	0.90	3.018(8)		0.90	2.632(10)
	1.00	2.825(5)		1.00	-
Ba1 – O3	0.85	2.784(8)	**Ba2 – O4a**	0.85	2.897(11)
	0.90	2.778(9)		0.90	3.188(12)
	1.00	2.747(5)		1.00	-
Ba1 – O4	0.85	2.922(8)	**Co1 – O1**	0.85	1.800(10)
	0.90	2.956(7)		0.90	1.782(10)
	1.00	3.001(5)		1.00	1.769(10)
Ba1 – O1a	0.85	3.041(11)	**Co1 – O2**	0.85	1.856(12)
	0.90	3.084(11)		0.90	1.861(11)
	1.00	-		1.00	1.833(8)
Ba1 – O3a	0.85	3.051(9)	**Co1 – O3**	0.85	1.653(9)
	0.90	2.790(10)		0.90	1.740(9)
	1.00	-		1.00	1.799(8)
Ba1 – O4a	0.85	2.905(11)	**Co1 – O4**	0.85	1.842(11)
	0.90	2.779(11)		0.90	1.780(10)
	1.00	-		1.00	1.744(8)
Ba2 – O1	0.85	2.833(8)			
	0.90	2.833(6)			
	1.00	2.878(4)			

Table 4.5 CoO_4 Tetrahedra angles from refined structures of $Ba_2(Co_4)_{1-x}(CO_3)_x$

Associated Bond	Angle (°)	Angle (°)	Angle (°)
O1 - Co1 - O2	112.412	112.246	112.588
O1 - Co1 - O3	111.694	112.956	111.892
O1 - Co1 - O4	111.843	111.756	111.523
O2 - Co1 - O3	102.517	102.29	104.02
O2 - Co1 - O4	105.25	104.406	103.166
O3 - Co1 - O4	112.605	112.5	113.124

Investigation into the structure of these systems had a primary focus on the changes to the CoO_4 tetrahedra as this allowed for the analysis of all three systems. Both Co1 – O1 and Co1 – O4 showed a positive correlation between bond length and increasing value of x, whilst the Co1 – O3 bond length showed a negative correlation decreasing with an increasing value of x. The bond length of Co1 – O2 shows an increase from x = 0 to x = 0.10, however, the bond lengths of x = 0.10 and x =0.15 appear similar. The reverse effect of these relationships can also be seen in the majority of the associated Ba1 and Ba2 bonds, except for those related to the O1 atom.

Carbonate units have a rigid trigonal planar geometry which does not allow for much distortion and is therefore required to be in a favourable orientation. This is evident when comparing the bond lengths of Ba1 and Ba2 bonds to carbonate associated oxygen atom sites (O1a, O3a, O4a), with that of the cobalt tetrahedra oxygen (O1, O3, O4). Bond lengths of Ba1 – O1a and Ba1 – O3a are greater than that of Ba1 – O1 and Ba1 – O3, whilst Ba1 – O4a is short than that of Ba1 – O4. The reverse of this can be seen for the Ba2 oxygens, which demonstrates that the rigid carbonate structure orientates in a manner where O4a is closest to the Ba1 atom site and O1a and O3a are closest to Ba2.

With an ideal tetrahedral angle being 109.5°, deviation from this shows distortion of the tetrahedra. Changes in these angles as x varies show how the cobalt tetrahedra continues to distort in a way to help stabilise the changing structure.

An important factor that must also not be ignored is that the partial reduction of Co^{4+} to Co^{3+} as the value of x increases. Whilst Co^{4+} has 4-coordinate tetrahedral geometry, Co^{3+} prefers a 6-coordinate octahedral geometry, this change in geometry would affect bond lengths and bond angles.

4.3.1.3 Effect of synthesis conditions: Synthesis Under a Dry O_2 Atmosphere

In an attempt to make the x = 0 sample without impurity, synthesis under a dry O_2 atmosphere was employed to ensure complete oxidation of the cobalt source reagent, which begins with a mixture of Co^{2+}/Co^{3+}, to the highest oxidation state of Co^{4+} which is assumed for a pure Ba_2CoO_4 system. To compare the effect of the synthesis atmosphere the x = 0.15 variation was also studied in this fashion. Initially, samples were heated to 980°C at a rate of 10°C/min for 48 hours in O_2 with two intermediate regrinds. Under the conditions specified both x = 0.15 samples showed somewhat similar XRD patterns (***Figure 4.7***).

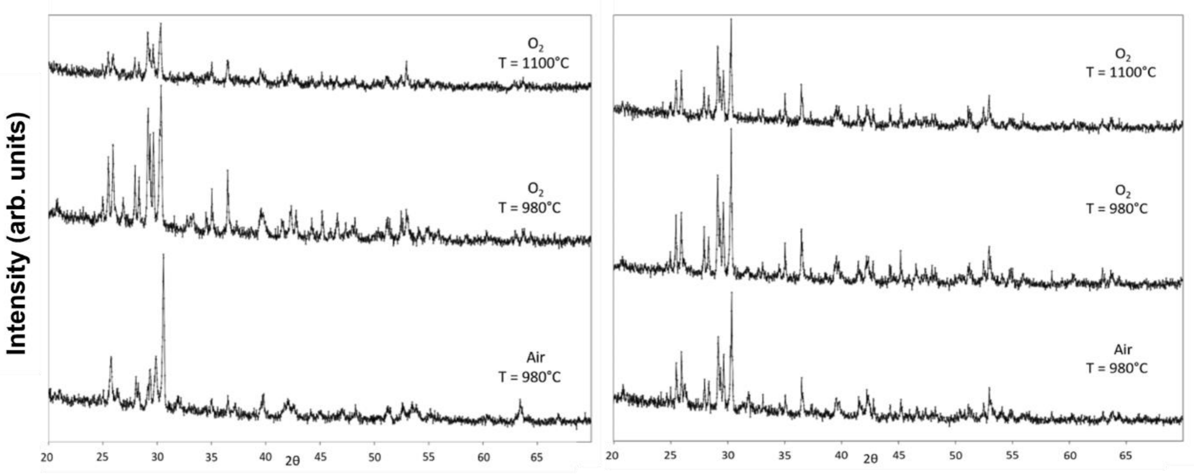

Figure 4.7 XRD Patterns of $Ba_2Co_{1-x}O_{4-\breve{u}}$ when synthesised in O_2 (x = 0.15 left, x = 0.00 right)

When synthesised under an O_2 atmosphere it is quite clear that both form the monoclinic polymorph providing support that the full oxidation of cobalt has occurred. The monoclinic structure remained at the higher temperature of 1100°C. This study clarifies that synthesis in air and the requirement of Co^{3+} to be present in order to balance the oxygen deficiency created by the accommodation of CO_3^{2-} in place of CoO_4^{4-}.

4.3.1.4 Thermal Stability Studies

Throughout the synthesis of these systems, there was great difficulty in producing pure samples. To provide some information on this, thermal stability studies were performed on the sample in the range $0 \leq x \leq 0.20$. In each case the samples were studied under the following conditions: (a) original samples (b) heated to 980°C and held for 30 minutes then quenched to room temperature, (c) heated to 980°C and held for 30 minutes then furnace slow cooled at a rate of 1°C/min to room temperature, (d) heated 400°C for 12 hours and left to furnace cool to room temperature. (***Figure 4.8***)

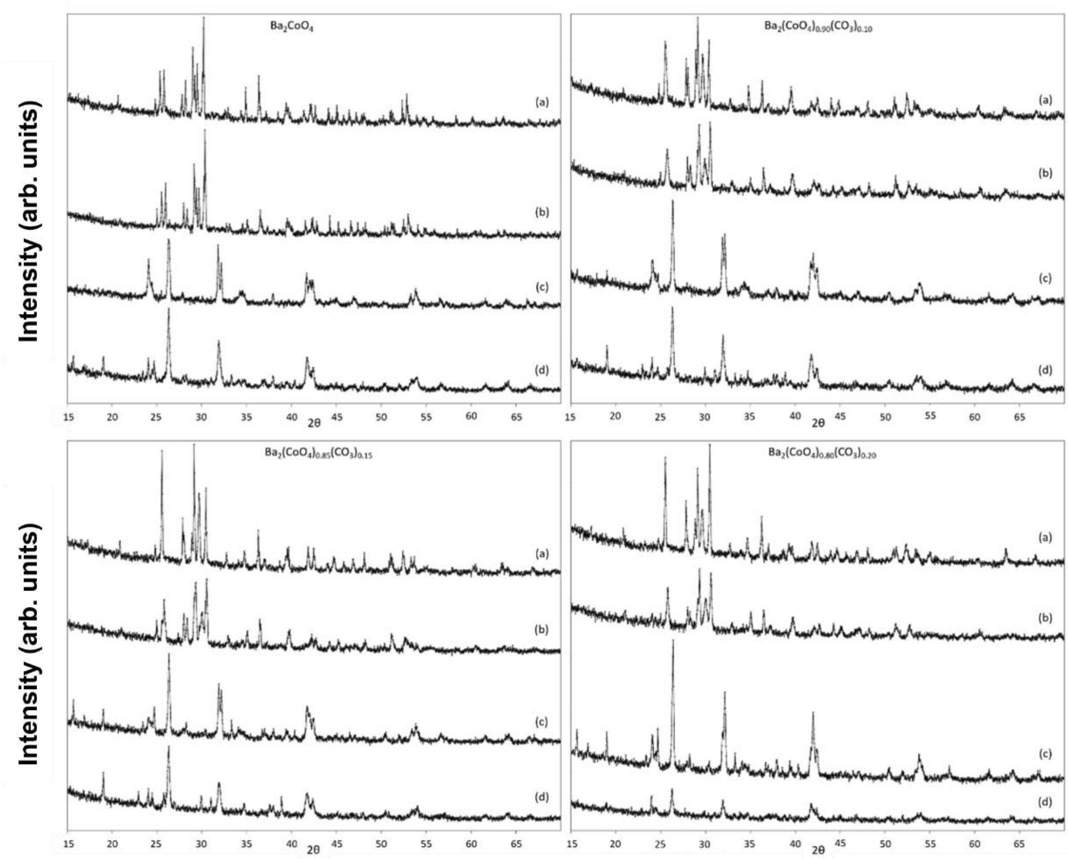

Figure 4.8 Thermal Stability XRD Patterns of $Ba_2Co_{1-x}O_{4-ŭ}$ (0 < x 2̀0) 0. showing that the systems are not stable upon slow cooling or being subsequently heated at lower than the synthesis temperature;
x = 0 (top left), 0.10 (top right), 0.15 (bottom left), 0.20 (bottom right)

Using the conditions specified in (b) there are slight changes seen in the structural profiles of the samples showing some stability under these conditions. One change that is seen is a splitting of a peak 2θ~28 for x = 0.15 and x = 0.20; this splitting can be typically seen in the x = 0.10 and x = 0 and could be attributed to a change in the β angle. Conditions (c) and (d) showed a decomposition from the original systems to a mixture of products which include $BaCO_3$, $Ba_3Co_2O_6(CO_3)_{0.6}$ as well as another unidentified system. Quenching and faster cooling rates favour the formation of the intended systems.

To further understand the processes happening, a variable temperature XRD study (***Figure 4.9***) was also undertaken.

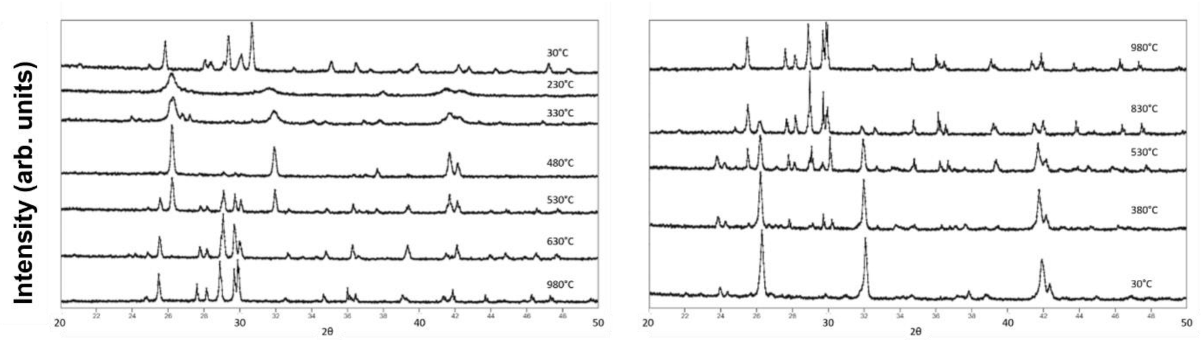

Figure 4.9 Variable Temperature XRD Patterns of $Ba_2(CoO_4)_{0.80}(CO_3)_{0.20}$*; heating (left), cooling (right)*

Data were collected for $Ba_2(CoO_4)_{0.8}(CO_3)_{0.2}$ at set points and shows the systems to be thermally unstable above 150°C decomposing to $BaCO_3$ and the barium cobalt oxycarbonate ($Ba_3Co_2O_6(CO_3)_{0.6}$)[192] with the $BaCO_3$ disappearing as temperature increases. Above 500°C, the appearance of the expected high temperature variation of the structure is noted with all traces of $Ba_3Co_2O_6(CO_3)_{0.6}$ gone from 630°C leaving only the high temperature $Ba_2(CoO_4)_{0.8}(CO_3)_{0.2}$ being seen. Upon cooling back to room temperature, with data again being recorded at set points, the sample does not retain to the original $Ba_2(CoO_4)_{0.8}(CO_3)_{0.2}$ structure composition under these conditions, degrading back into a mixture of $BaCO_3$ and $Ba_3Co_2O_6(CO_3)_{0.6}$. This can be correlated with the slow rate of cooling of the equipment.

4.3.1.5 Thermogravimetric and Mass Spectrometry

TGA-MS was used to confirm the existence of carbonate within the $Ba_2(CoO_4)_{1-x}(CO_3)_x$ systems (x = 0.10, 0.15, 0.20) with expected mass percentage losses of CO_2 being calculated and then compared to the values extracted from the TGA-MS data given below in ***Figure 4.10***.

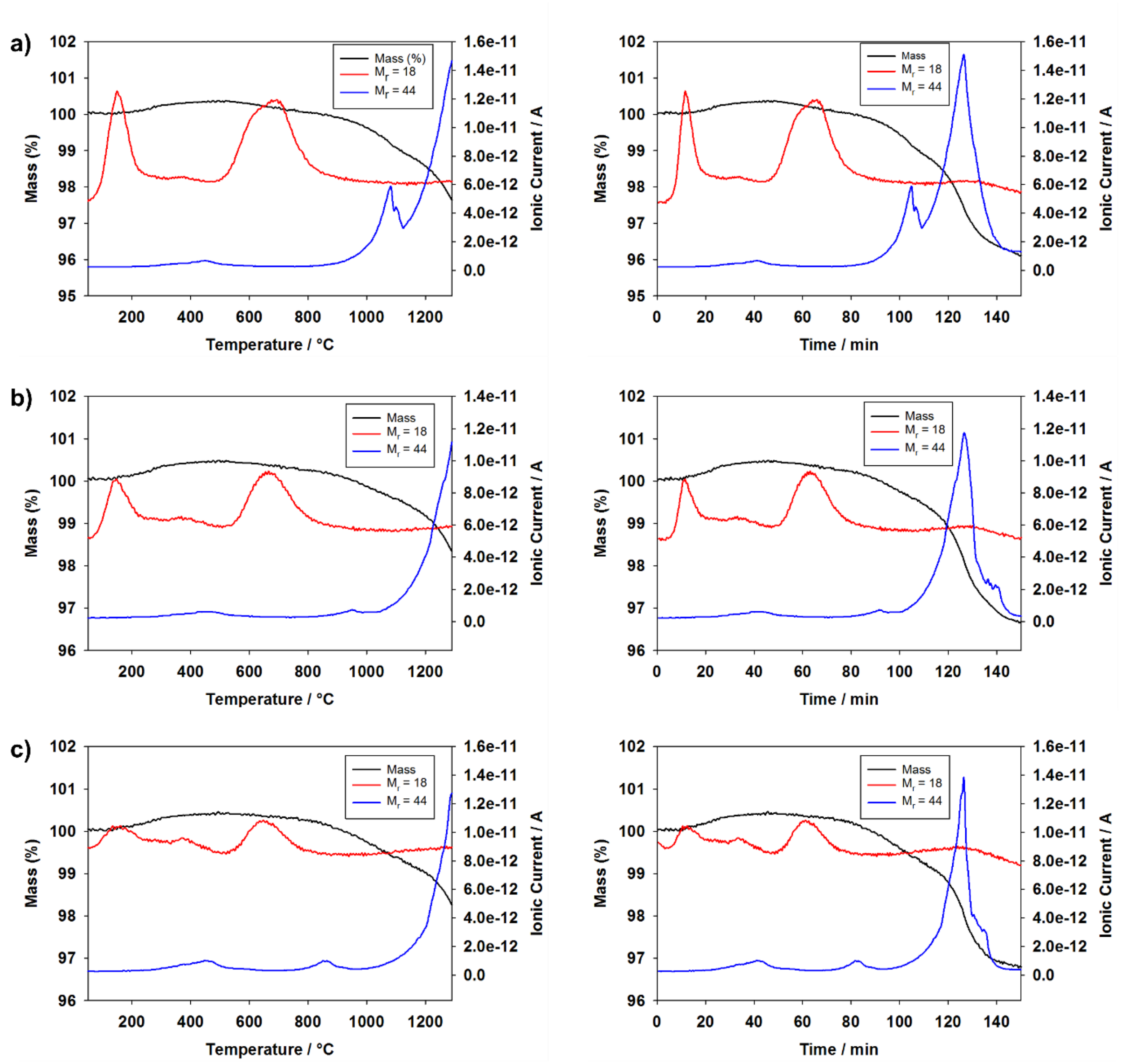

Figure 4.10 TGA-MS profiles for the $Ba_2(CoO_4)_{1-x}(CO_3)_x$ systems (a) x = 0.20, b) x = 0.15, c) x = 0.10) showing water and CO_2 losses over time with increasing temperature.

An interesting unexpected observation was water loss. When comparing these profiles, water appears to be lost in three separate stages: ~100 - 200°C, ~350 - 450°C and ~550 - 750°C which correlates with the significant structural changes presented in the VT-XRD study. These results suggest that water may be helping to stabilise these systems somewhat at lower temperatures, but with all water removed by the synthesis temperature it is not key in the formation of the carbonate containing compound at these temperatures. CO_2 can also be seen to be lost from the systems, notably with losses beginning at around synthesis temperature, increasing in loss as the temperature increases. Another CO_2 loss can be seen at much earlier temperature (~350 - 500°C) which coincides with the disappearance of $BaCO_3$ upon heating. Again, comparing with the VT-XRD data no $BaCO_3$ remains at the synthesis temperature and therefore any carbonate loss can be assumed to be from the high temperature $Ba_2(CoO_4)_{1-x}(CO_3)_x$ structures.

Comparing expected vs calculated losses of carbonate from the systems showed in each case there is a much greater mass (%) reduction: x = 0.20 (expected mass (%) loss due to CO_2 = 2.29%, calculated mass (%) loss due to CO_2 = 3.89%), x = 0.15 (expected mass (%) loss due to CO_2 = 1.70%, calculated mass (%) loss due to CO_2 = 3.34%), x = 0.10 (expected mass (%) loss due to CO_2 = 1.12%, calculated mass (%) loss due to CO_2 = 3.21%). These greater mass (%) losses could suggest a greater amount of carbonate incorporation than expected, the presence of some unreacted $BaCO_3$, and/or O_2 losses at these temperatures which could add to the mass loss but was not considered during the running of the experiment.

4.3.1.6 Raman spectroscopy

Raman spectra were recorded for all values of x (***Figure 4.11***), with the key observations being a large band at ~700 cm^{-1} with two smaller bands ~310 – 350 cm^{-1}. Changes in the spectra as the value of x increases include the broadening of bands previously mentioned as well as the disappearance of some additional smaller bands, most predominantly seen for the x = 0 system. These alterations in the spectra can be attributed to the monoclinic structure appearing to become more orthorhombic like.

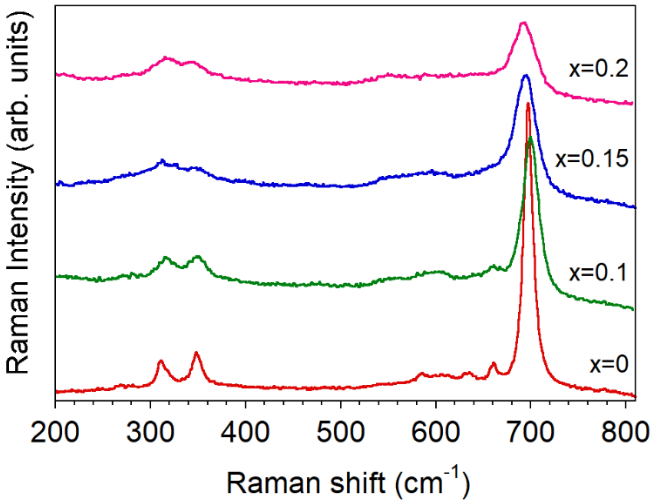

Figure 4.11 Raman data profiles of $Ba_2(CoO_4)_{1-x}(CO_3)_x$

Through examination of extended spectra it became apparent at 10 mW laser power there was little to no sign of the carbonate Raman bands expected and so further studies were implemented by increasing the laser power. As the power increased, the original bands disappeared and the formation of two broad bands at ~ 600 cm^{-1} and ~ 350 cm^{-1} is seen (***Figure 4.12***). This change is attributed to the degradation of the samples through laser damage as these compounds have a high optical absorption in the visible range. The same degradation was also seen whilst increasing the temperature at the fixed 10 mW laser power (***Figure 4.13***).

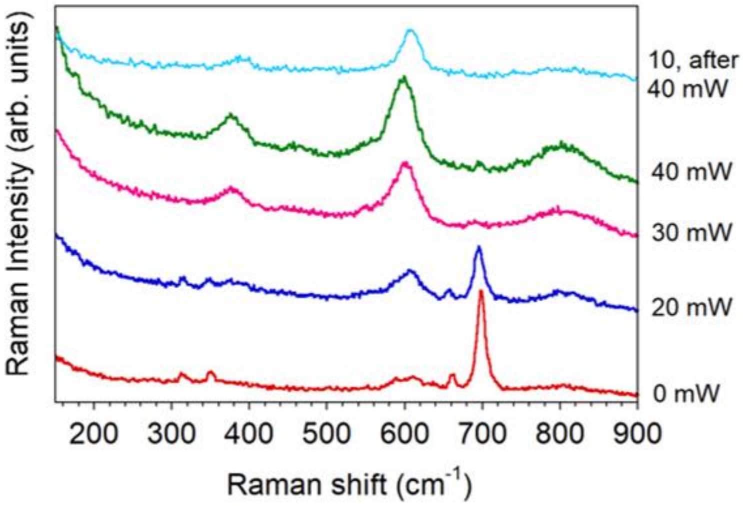

Figure 4.12 Raman data profiles of $Ba_2(CoO_4)_{0.9}(CO_3)_{0.1}$ showing band changes upon increasing laser line power.

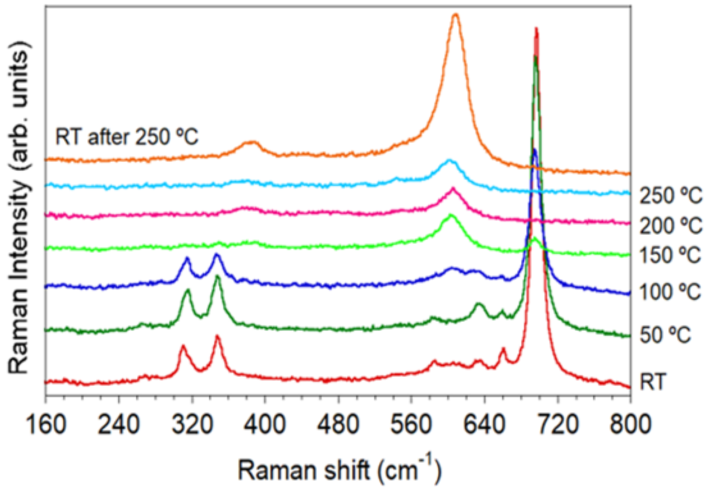

Figure 4.13 Raman data profiles of $Ba_2(CoO_4)_{0.9}(CO_3)_{0.1}$ showing band changes upon increasing temperature whilst at the same laser line power.

From the combined findings of the variable temperature XRD and temperature Raman studies, $Ba_3Co_2O_6(CO_3)_{0.6}$ was synthesised using a combination of known routes to compare with the original Raman spectra[192-193]. Comparisons of the spectra show that the degradation seen during earlier Raman studies was in fact leading to the formation of $Ba_3Co_2O_6(CO_3)_{0.6}$ (***Figure 4.14***). Interestingly, despite being known as a carbonate containing compound; extended Raman spectra showed very weak or even undetectable signs of a carbonate stretching band.

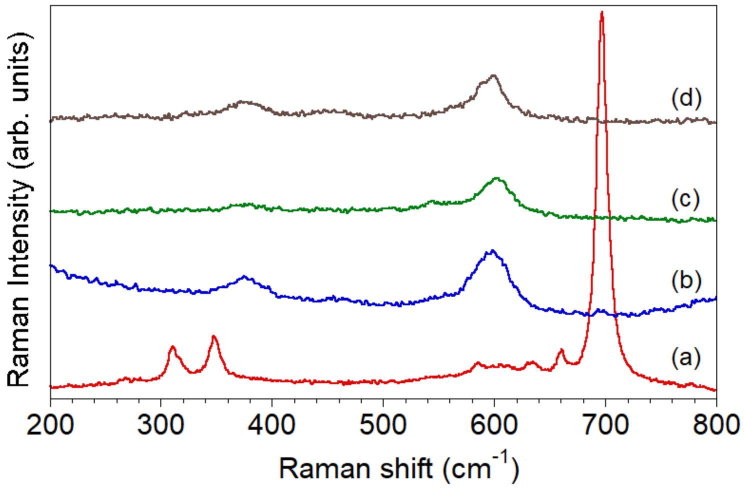

Figure 4.14 Raman data profiles of $Ba_2(CoO_4)_{0.9}(CO_3)_{0.1}$ *showing band changes seen is due to the degradation of the* $Ba_2(CoO_4)_{0.9}(CO_3)_{0.1}$ *structure to* $Ba_3Co_2O_6(CO_3)_{0.6}$. *(a) Room Temperature, b) 40mW laser line power, c) 250°C, d)* $Ba_3Co_2O_6(CO_3)_{0.6}$*)*

4.3.2 Synthesis and Structural Characterisation of $Ba_2(FeO_4)_{1-x}(CO_3)_x$

4.3.2.1 Powder X-Ray Diffraction

Similar studies were also performed for the related Ba_2FeO_4 system as this is also known to adopt the monoclinic β-Ca_2SiO_4 structure. As before, varying amounts of Fe deficiency were attempted and a series was produced for $Ba_2(FeO_4)_{1-x}(CO_3)_x$ ($0 \leq x \leq 0.20$) and XRD data patterns were recorded (***Figure 4.15***).

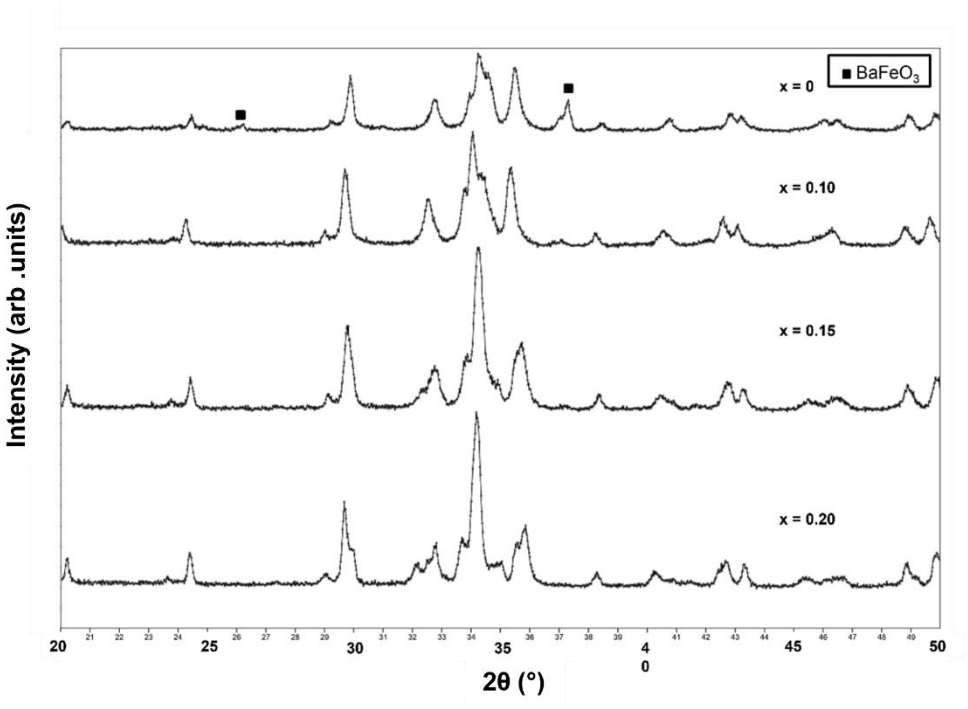

Figure 4.15 X-ray diffraction patterns for $Ba_2Fe_{1-x}O_{4-\delta}$ *(0 < x ≤ 0.2) systems synthesised at 980°C, showing slight changes in structure.*

Unlike its Co counterpart, the x = 0 system begins as the orthorhombic like phase, with increasing amounts of Fe deficiency leading to the appearance of the monoclinic structure. This change in structure can be seen mostly for the x = 0.20 system, with the most obvious splitting of peaks seen at the 2θ = 29°, 32 - 33° and 36°. Initial structural determination gave the unit cell parameters reported in ***Table 4.6***.

Table 4.6 Refined unit cell parameters for $Ba_2Fe_{1-x}O_{4-ŭ}$ (0 < x Ò 0.20) when synthesised under normal conditions (x = 0.20, 0.15, 0.10 Ą CO_3^{2-} included; x = 0 Ą CO_3^{2-} excluded)

$Ba_2(FeO_4)_{1-x}(CO_3)_x$	**Unit Cell Parameter / Å**				
X	***a***	***b***	***c***	**β / °**	**Volume / Å^3**
0.20	5.848(1)	7.604(2)	10.741(3)	89.89(4)	477.493(246)
0.15	5.870(1)	7.598(1)	10.690(2)	90.14(3)	476.803(227)
0.10	5.900(1)	7.605(1)	10.578(2)	90.23(1)	474.649(196)
0.00	5.901(2)	7.604(1)	10.581(2)	90.19(1)	474.779(206)

Similar to the trend seen with the unit cell parameters for the Co based system, there appears to be an increase in the overall volume of the unit cell as the amount of Fe deficiency increases. Whilst this would not be expected from the substitution of the C for Fe (has C has a smaller ionic radii) the unit cell expansion for these systems can be a consequence of the increase in ionic size from Fe^{4+} to Fe^{3+} which is required to compensate the overall charge in the system due to oxide vacancies introduced from the CO_3^{2-} incorporation in place of FeO_4^{4-}. Another possibility could be the incorporation of moisture which may reduce some FeO_4^{4-} (Fe^{4+}) to $FeO_3(OH)^{4-}$ (Fe^{3+}).

4.3.2.2 Thermal Stability Studies

As for the Co based systems, an investigation to determine the effect of cooling rate upon the formation of these systems was undertaken. During this investigation, synthesised samples of the $Ba_2(FeO_4)_{1-x}(CO_3)_x$ systems ($0 \leq x \leq 0.20$) were subjected to a heat treatment at 980°C for 30mins before being quenched (***Figure 4.16***) or slow-cooled at 1°C/min (***Figure 4.17***).

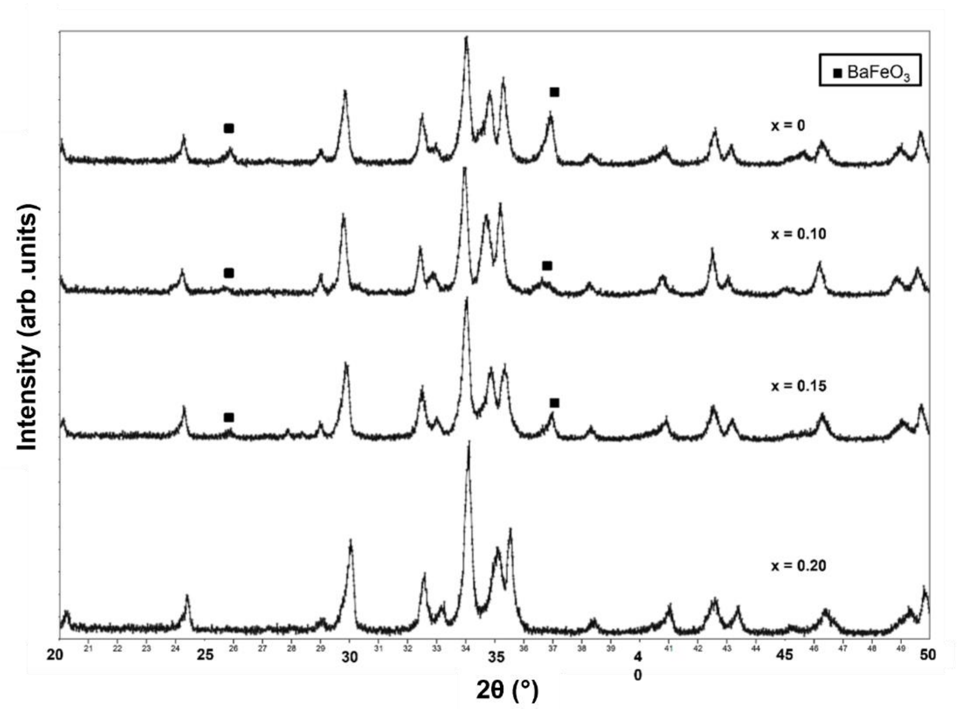

Figure 4.16 X-ray diffraction patterns for $Ba_2Fe_{1-x}O_{4-ŭ}$ (0 < x Ò 0.2) systems synthesised at 980°C and then quenched to room temperature, showing a more crystalline and defined structure.

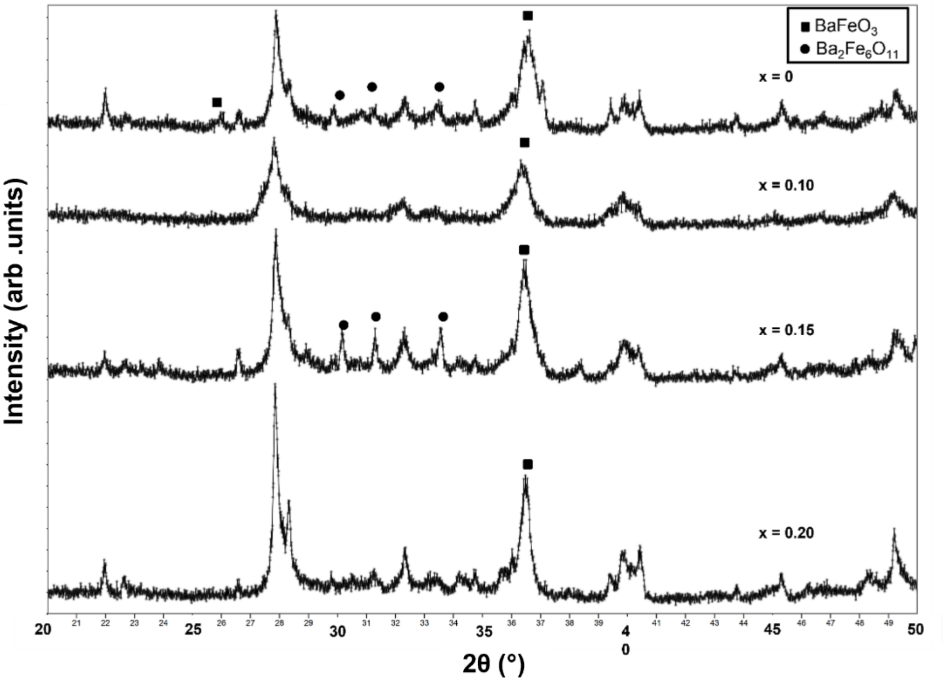

Figure 4.17 X-ray diffraction patterns for $Ba_2Fe_{1-x}O_{4-ŭ}$ ($0 < x \le 0.2$) systems synthesised at 980°C and then slow cooled (1°C / min) to room temperature, showing loss of the $Ba_2Fe_{1-x}O_{4-ŭ}$ structure.

When the samples were quenched, XRD patterns showed greater definition between individual peaks and similar splitting can be seen with the peak originally between 2θ = 32-33°, which was notable in the Co systems also. All patterns for these Fe systems look relatively similar, however what is apparent is the greater formation of the $BaFeO_{3-y}$ impurity within the XRD data for all samples except x = 0.20. Slow cooling the samples leads to the degradation of these systems with each XRD pattern consisting mostly of $BaCO_3$ and $BaFeO_{3-y}$. Whilst the $Ba_2Fe_6O_{11}$ structure may be present in all samples it is most prominent in the x = 0, 0.15 systems.

Continuing on from this, VT-XRD data were recorded to evaluate the stability of the $Ba_2(FeO_4)_{1-x}(CO_3)_x$ systems upon heating and provide additional insight into the intermediate products. XRD data were recorded at set intervals upon heating of the sample, the results for the x = 0.20 system can be seen below in ***Figure 4.18*** showing the most significant changes.

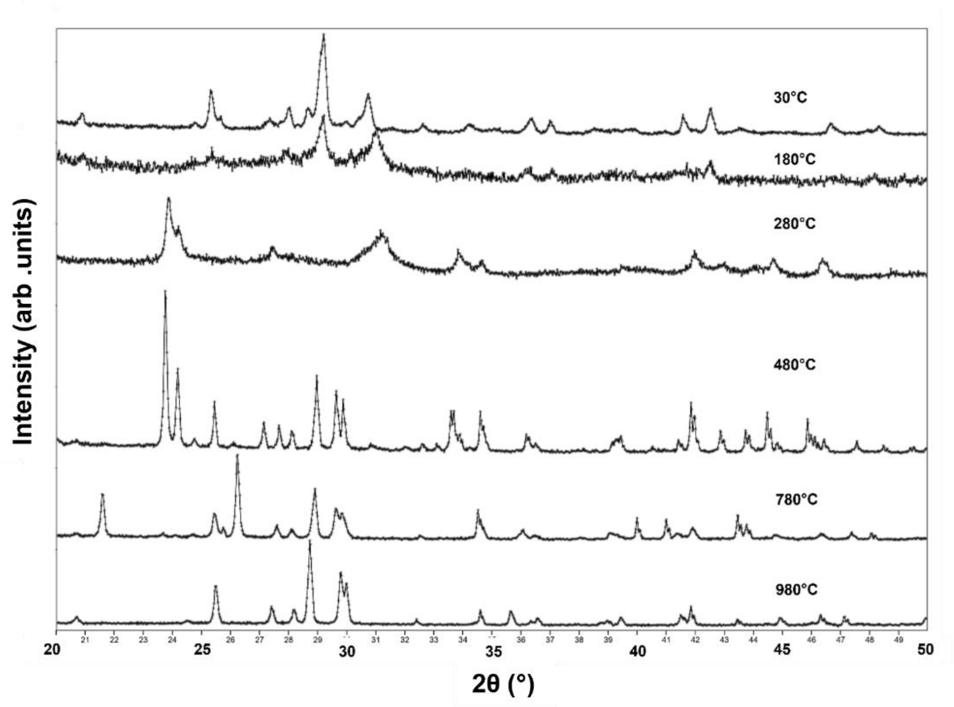

Figure 4.18 Variable Temperature XRD Patterns of $Ba_2(FeO_4)_{0.80}(CO_3)_{0.20}$*, showing the stages of degradation and reformation of the expected structure upon heating.*

Upon heating the x = 0.20 sample to 180°C, the last remnant of the original structure is seen as the sample decomposes above this temperature to $BaCO_3$ and $BaFeO_{3-y}$ which can be seen at 280°C. As the temperature increases to 480°C $BaCO_3$ becomes more crystalline and the high temperature $Ba_2(FeO_4)_{0.8}(CO_3)_{0.2}$ structure has begun reforming. No significant changes are then seen until a temperature of 780°C is recorded, and the $BaCO_3$ has now transitioned from the normal *Pmnc* space group to the high temperature *R*3*mh* space group phase which is characterised by the large peaks present at 2θ = 21.5 and 26°. As the original synthesis temperature is reached, only the high temperature $Ba_2(FeO_4)_{0.8}(CO_3)_{0.2}$ structure is observed. Cooling of the samples leads only $BaCO_3$ and $BaFeO_{3-y}$ forming attributed to the slow cooling process.

4.3.2.3 Thermogravimetric and Mass Spectrometry

TGA-MS was used to determine the existence of CO_3^{2-} within the $Ba_2(FeO_4)_{1-x}(CO_3)_x$ systems (x = 0.10, 0.15, 0.20) with expected mass percentage losses of CO_2 being calculated and then compared to the values extracted from the TGA-MS data, given below in ***Figure 4.19***.

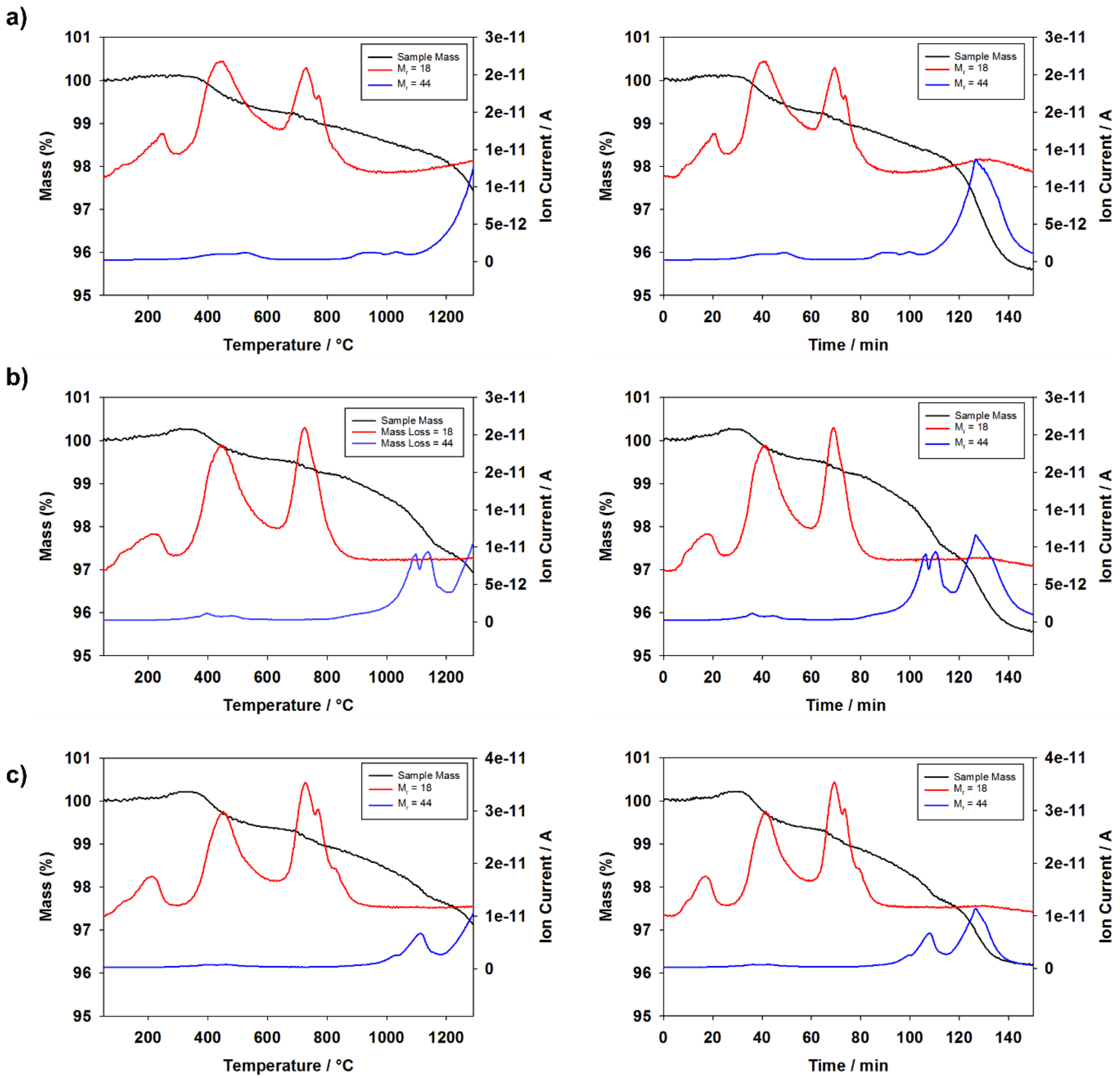

Figure 4.19 TGA-MS profiles for the $Ba_2(FeO_4)_{1-x}(CO_3)_x$ systems (a) x = 0.20, b) x = 0.15, c) x = 0.10) showing water and CO_2 losses over time with increasing temperature.

As for the Co based systems, water also appears to be present which is lost on heating. When comparing these profiles, water appears to be lost in three separate stages which correlates with the significant structural changes presented in the VT-XRD study. These results suggest that, as for the Co based systems, water may be helping to stabilise these systems somewhat at lower temperatures, but with all water removed by the synthesis temperature it is not key in the formation of the structure at these temperatures. Carbonate can also be seen to be lost from the systems, with losses beginning at around synthesis temperature, increasing in loss as the temperature increases. As before, comparing with the VT-XRD data no $BaCO_3$ remains at this temperature and therefore any carbonate loss can be assumed to be from the high temperature $Ba_2(FeO_4)_{1-x}(CO_3)_x$ structures.

Comparing expected vs calculated losses of carbonate from the systems showed in each case there is a much greater mass (%) reduction: x = 0.20 (expected mass (%) loss due to CO_2 = 2.30%, calculated mass (%) loss due to CO_2 = 3.27%), x = 0.15 (expected mass (%) loss due to CO_2 = 1.71%, calculated mass (%) loss due to CO_2 = 3.53%), x = 0.10 (expected mass (%) loss due to CO_2 = 1.13%, calculated mass (%) loss due to CO_2 = 2.52%). These greater mass (%) losses could suggest a greater amount of carbonate incorporation than expected, the possible presence of unreacted $BaCO_3$, and/or O_2 losses at these temperatures, which could add to the mass loss but was not considered during the running of the experiment. Mass losses were calculated at a point after the first loss of water is seen, this first water mass loss is assumed to be from surface moisture with subsequent mass losses being seen above the expected the expected temperature for this and may be suggesting the incorporation of water into the systems

4.3.2.4 Raman Spectroscopy

With the expectation for these systems to contain carbonate, Raman spectroscopy measurements were performed. As previously described, the main hope was to be able to determine the presence of carbonate through the appearance of the v_1 symmetric stretch vibrational mode of the carbonate which can be seen at ~1059.6 cm^{-1} in room temperature $BaCO_3$ with any shifting of this being attributed to successful incorporation. The more highly deficient Fe systems (x = 0.15, 0.20) were the focus of this investigation, and Raman spectra for these shown in ***Figure 4.20*** and ***Figure 4.21*** respectively.

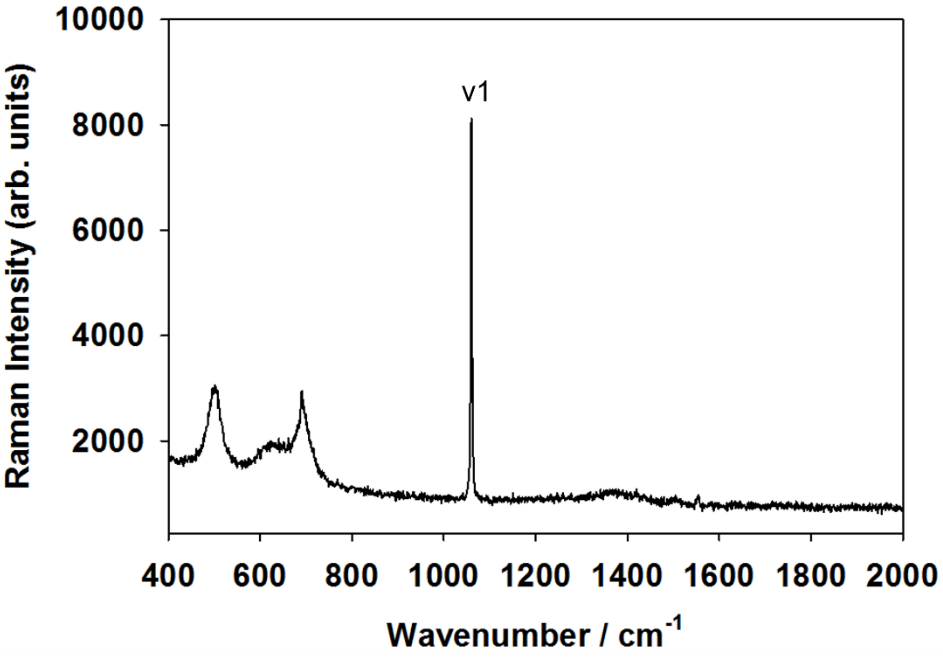

Figure 4.20 Raman profile for $Ba_2(FeO_4)_{0.8}(CO_3)_{0.2}$ drawing attention to the CO_3^{2-} v_1 symmetric stretch band

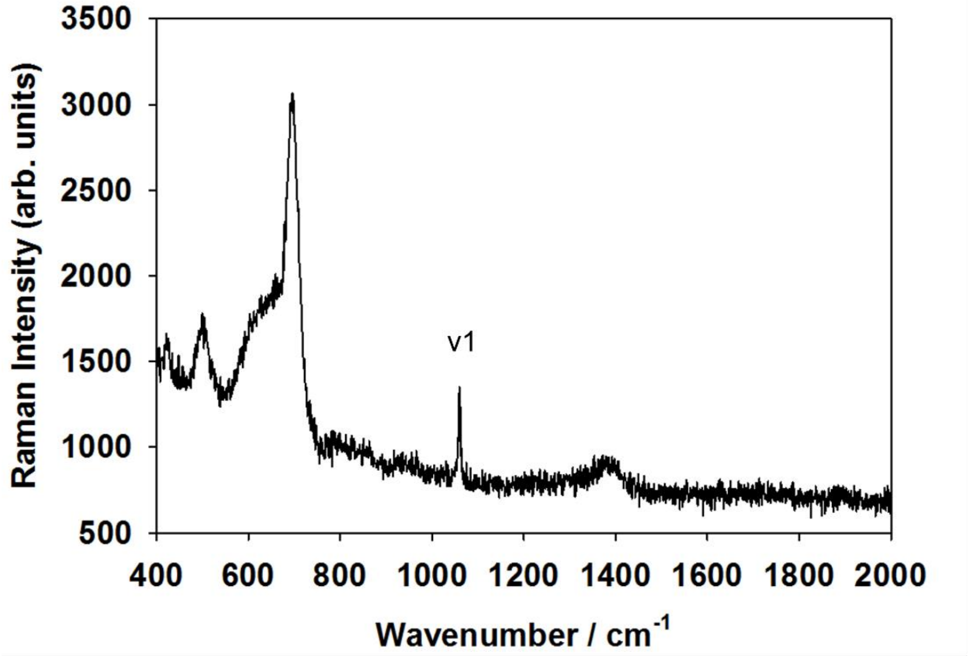

Figure 4.21 Raman profile for $Ba_2(FeO_4)_{0.85}(CO_3)_{0.15}$ *drawing attention to the* CO_3^{2-} v_1 *symmetric stretch band*

In both cases of these systems the v_1 symmetrical stretching band of carbonate is seen, however neither the v_3 nor v_4 vibrational modes are observed. When comparing the values of the v_1 bands to that of $BaCO_3$ (1059.53 cm^{-1}), both are very similar to this value; x = 0.15 (1059.35 cm^{-1}), x = 0.20 (1060.35 cm^{-1}), and due to the stability of these systems it cannot be clearly determined whether the carbonate detected is due to successful incorporation, the presence of unreacted $BaCO_3$ or the degradation of the systems. A broad band seen just below 1400 cm^{-1} is characteristic of a v_3 symmetric bending mode of water and suggests this is present within the samples, consistent with the TGA studies.

4.3.2.5 Infra-red Spectroscopy

Fourier transformed infra-red (FT-IR) spectroscopy was also performed on the $Ba_2(FeO_4)_{1-x}(CO_3)_x$ systems, to again try and provide evidence for the incorporation of carbonate. All data are compared to that of $BaCO_3$, with the primary focus on determining the v_3 vibrational mode band first as this is the most intense. FT-IR recorded spectra are shown in ***Figure 4.22***.

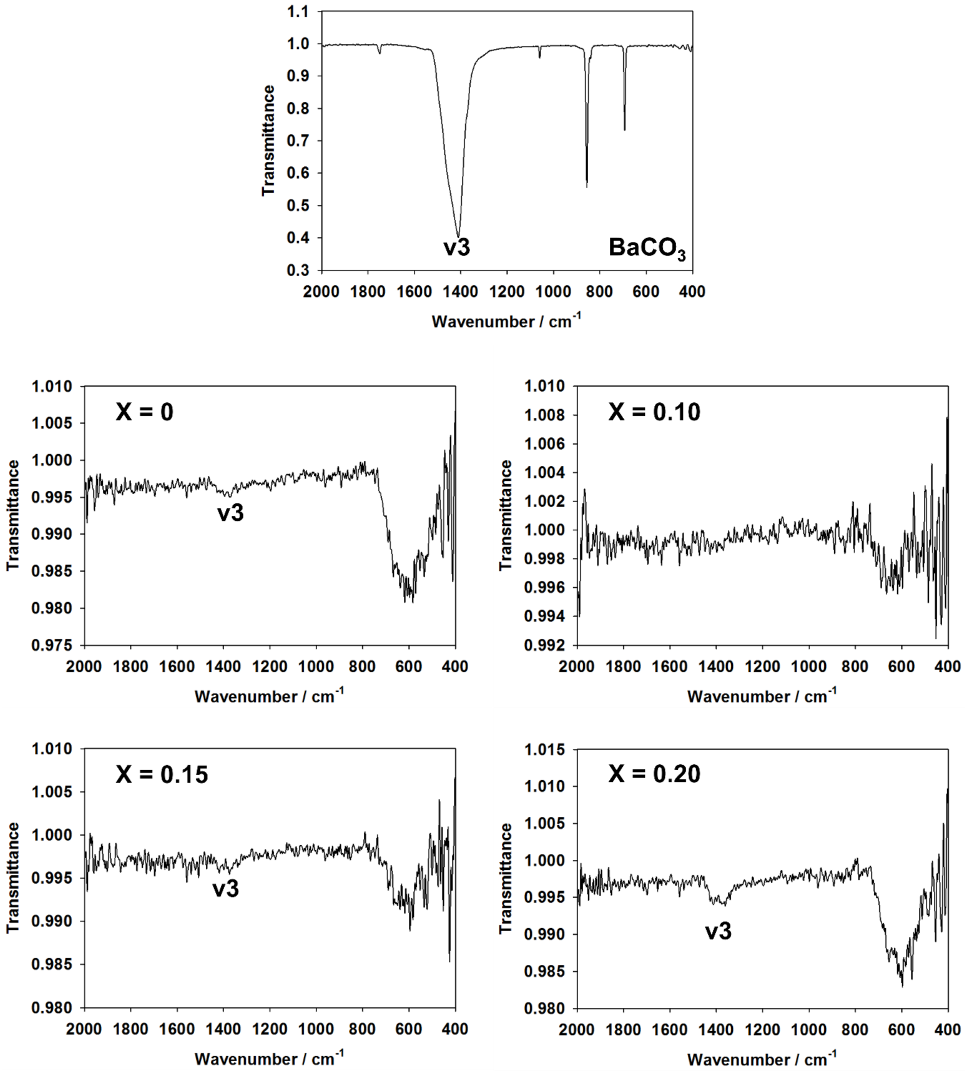

Figure 4.22 FT-IR spectra of $BaCO_3$ and $Ba_2(FeO_4)_{1-x}(CO_3)_x$ systems highlighting the possible appearance of the v_3 doubly degenerate asymmetric carbonate stretching mode

In almost all cases for the $Ba_2(FeO_4)_{1-x}(CO_3)_x$ systems (except the x = 0.10 sample) a very small signal could be seen. The signal detected could quite possibly be the v_3 doubly degenerate asymmetric stretching mode most prominent in the $BaCO_3$ profile. When discussing the $Ba_2(FeO_4)_{1-x}(CO_3)_x$ systems, it appears most prominent for the x = 0.20 system as expected, however, the strength and position of these signals make it incredibly difficult to determine whether the CO_3^{2-} detected is from incorporation into the structure or unreacted $BaCO_3$.

4.3.2.6 Rietveld Refinement using XRD Data

Unfortunately, no neutron diffraction data were recorded for these systems and so assessment of possible carbonate incorporation was based on less reliable XRD data. Refinement fits are presented in ***Figure 4.23 ï 4.26*** with structural information and unit cell parameters given in ***Table 4.7*** and ***Table 4.8*** respectively.

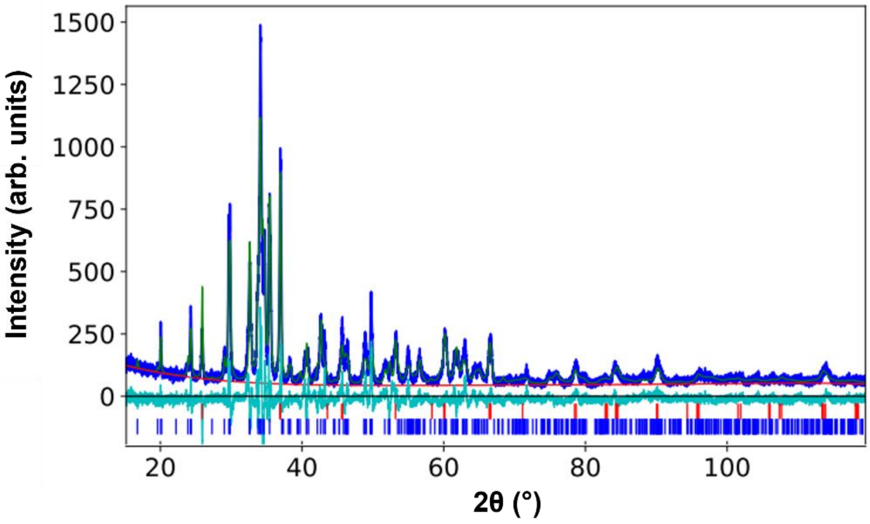

Figure 4.23 Observed, calculated and difference profiles of Ba_2FeO_4 XRD data
Space Group: $P12_1/n1$
(top = $BaFeO_3$ (17wt%), bottom = Ba_2FeO_4 (83wt%))
GOF = 1.56

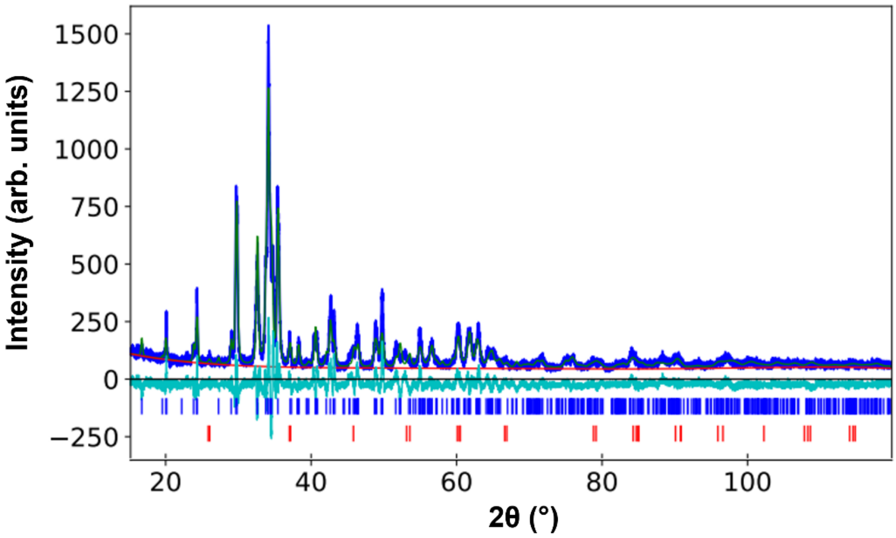

Figure 4.24 Observed, calculated and difference profiles of $Ba_2(FeO_4)_{0.90}(CO_3)_{0.10}$ XRD data
Space Group: $P12_1/n1$
(top = $BaFeO_3$ (3wt%), bottom = Ba_2FeO_4 (97wt%))
GOF = 1.21

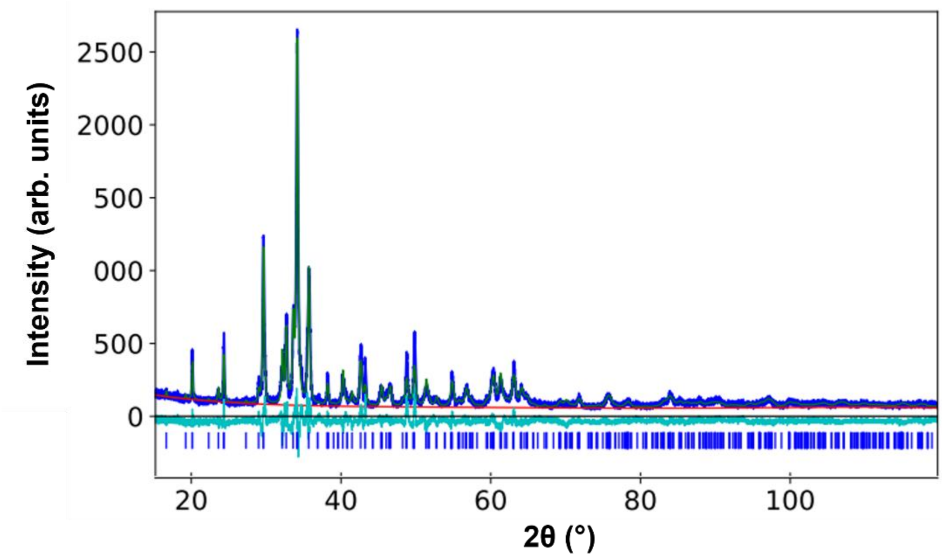

Figure 4.25 Observed, calculated and difference profiles of $Ba_2(FeO_4)_{0.85}(CO_3)_{0.15}$ XRD data
Space Group: $P\ 12_1/n1$
GOF = 1.17

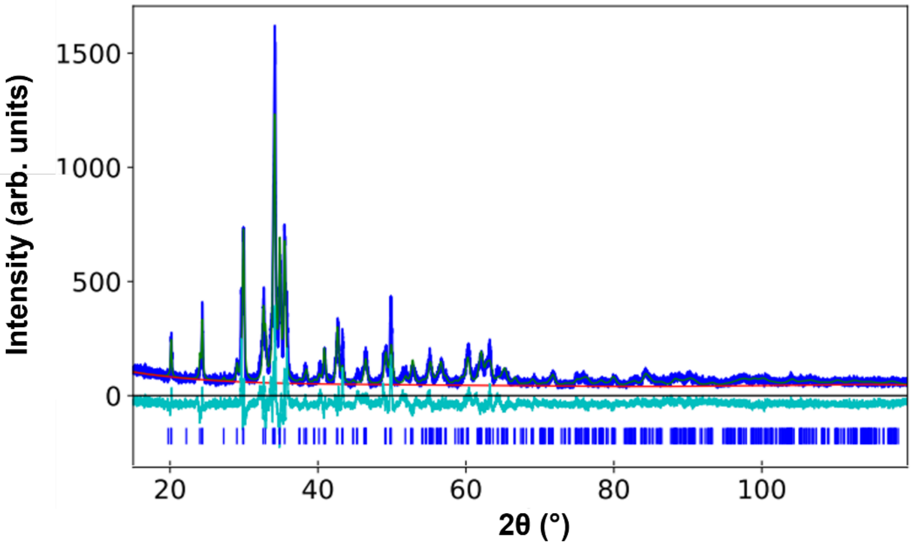

Figure 4.26 Observed, calculated and difference profiles of $Ba_2(FeO_4)_{0.80}(CO_3)_{0.20}$ *XRD data*
Space Group: $P12_1/n1$
GOF = 1.20

Table 4.7 Refined structural data for $Ba_2(FeO_4)_{1-x}(CO_3)_x$ $(0 < x \leq 0.20)$ *which excludes* CO_3^{2-} *due to XRD limitations*

Atom	**x**	**y**	**Z**	**Fraction**	**Wyckoff Position**	$\mathbf{U_{iso}}$
Ba1						
0.80	0.762(4)	0.839(1)	0.083(1)	1.000	4e	0.029(4)
0.85	0.757(3)	0.840(1)	0.083(1)	1.000	4e	0.027(4)
0.90	0.760(3)	0.842(1)	0.083(1)	1.000	4e	0.026(4)
1.00	0.756(6)	0.843(2)	0.083(1)	1.000	4e	0.042(8)
Ba2						
0.80	0.252(3)	0.503(1)	0.197(1)	1.000	4e	0.029(4)
0.85	0.246(4)	0.503(1)	0.195(1)	1.000	4e	0.027(4)
0.90	0.256(3)	0.501(1)	0.197(1)	1.000	4e	0.026(4)
1.00	0.258(5)	0.503(1)	0.196(1)	1.000	4e	0.042(8)
Fe1						
0.80	0.802(6)	0.271(2)	0.084(2)	0.925(22)	4e	0.029(4)
0.85	0.782(8)	0.275(2)	0.085(2)	0.940(19)	4e	0.027(4)

0.90	0.783(8)	0.278(2)	0.087(2)	0.954(19)	4e	0.026(4)
1.00	0.784(13)	0.280(3)	0.082(3)	1.020(29)	4e	0.042(8)
O1						
0.80	0.863(8)	0.503(3)	0.085(5)	1.000	4e	0.117(14)
0.85	0.842(9)	0.506(3)	0.075(4)	1.000	4e	0.071(13)
0.90	0.814(11)	0.512(3)	0.095(4)	1.000	4e	0.065(13)
1.00	0.777(22)	0.515(4)	0.063(6)	1.000	4e	0.039(15)
O2						
0.80	0.545(10)	0.230(7)	0.174(6)	1.000	4e	0.117(14)
0.85	0.54591)	0.239(6)	0.191(4)	1.000	4e	0.071(13)
0.90	0.560(9)	0.213(7)	0.194(4)	1.000	4e	0.065(13)
1.00	0.580(11)	0.215(8)	0.199(4)	1.000	4e	0.039(15)
O3						
0.80	1.036(10)	0.154(7)	0.157(6)	1.000	4e	0.117(14)
0.85	1.028(10)	0.165(6)	0.148(4)	1.000	4e	0.071(13)
0.90	1.045(9)	0.176(7)	0.135(5)	1.000	4e	0.065(13)
1.00	1.065(11)	0.212(10)	0.135(6)	1.000	4e	0.039(15)
O4						
0.80	0.766(14)	0.197(5)	-0.079(3)	1.000	4e	0.117(14)
0.85	0.720(13)	0.189(5)	-0.072(3)	1.000	4e	0.071(13)
0.90	0.717(12)	0.210(5)	-0.075(3)	1.000	4e	0.065(13)
1.00	0.721(16)	0.177(6)	-0.069(4)	1.000	4e	0.039(15)

Constraints: Isotropic thermal parameters (U) O1=O2=O3=O4; Ba1=Ba2=Fe1

Table 4.8 Refined unit cell parameters for quenched $Ba_2(FeO_4)_{1-x}(CO_3)_x$ $(0 < x \leq 0.20)$

$Ba_2(FeO_4)_{1-x}(CO_3)_x$	**Unit Cell Parameter / Å**				
X	***a***	***b***	***c***	**β /**	**Volume / Å^3**
0.20	5.898(1)	7.640(2)	10.359(3)	90.11(1)	466.806(152)
0.15	5.907(1)	7.631(1)	10.375(1)	90.10(1)	467.634(141)
0.10	5.915(1)	7.619(1)	10.389(1)	90.08(2)	468.210(166)
0.00	5.911(1)	7.620(2)	10.413(2)	90.07(4)	469.030(271)

During the refinement process it became clear that each $Ba_2(FeO_4)_{1-x}(CO_3)_x$ system also included varying amounts of $BaFeO_3$ impurity which decreased with increasing values of x (x = 0 (17%), x = 0.10 (3%), x = 0.15 (0%), x = 0.20 (0%)).

Refinement of the Fe occupancies showed a value of 1 for the x=0 sample, as expected, with the occupancy decreasing with increasing Fe content (x>0), consistent with either the presence of Fe vacancies or carbonate groups in place of Fe.

When the data for the quenched samples is compared to the unit cell parameters of samples which have been cooled regularly, it is clear that the quenched samples have smaller unit cells. However, a difference is that the unit cell volume of the quenched samples decreases upon the increasing amount of Fe deficiency. This would be expected with the incorporation of CO_3^{2-} on the FeO_4^{4-} site as the ionic radii of C^{4+} is much smaller than that of Fe^{3+}/Fe^{4+} . These findings suggest that the expansion of unit cell volume upon increasing Fe deficiency of the regularly cooled samples is most likely due to the incorporation of water as well as CO_3^{2-}.

4.3.3 Investigation into possible Sulphate Incorporation of $Ba_2Fe_{1-x}O_{4-\delta}$

4.3.3.1 Powder X-Ray Diffraction

After showing how CO_3^{2-} could be incorporated into the $Ba_2(CoO_4)_{1-x}(CO_3)_x$ and $Ba_2(FeO_4)_{1-x}(CO_3)_x$ systems, an attempt was made to incorporate SO_4^{2-} instead, as this oxyanion has the same ionic charge, and is generally more thermally stable in structures than carbonate. SO_4^{2-} is tetrahedral in shape, just like the FeO_4^{4-} substituent, and so has the potential to stabilise the structure more readily, as the oxygen ion vacancies introduced in the CO_3^{2-}incorporated structure would no longer be produced. For these systems, it was found that higher temperatures could be employed for the synthesis, due to the greater thermal stability: these $Ba_2(FeO_4)_{1-x}(SO_4)_x$ systems ($x = 0.10, 0.15, 0.20$) were synthesised at 1100°C with the resulting XRD patterns shown in ***Figure 4.27***.

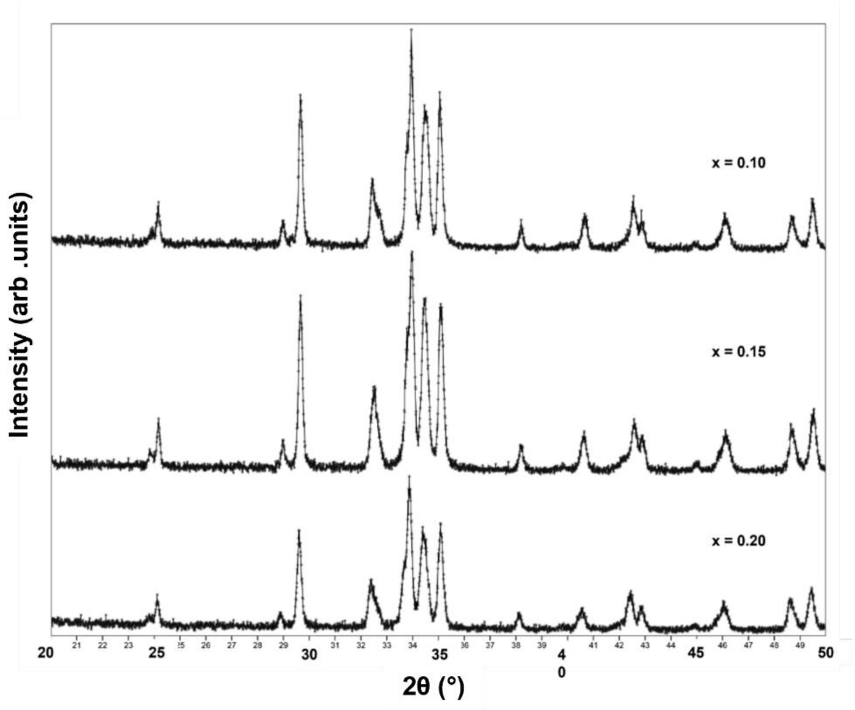

Figure 4.27 X-ray diffraction patterns for $Ba_2(FeO_4)_{1-x}(SO_4)_x$ *(0.10< x Ò20).systems synthesised at 1100°C and then furnaced cooled to room temperature, showing no apparent impurities.*

Synthesis at 1100°C leads to the formation of a crystalline structure pattern resembling that of the quenched $Ba_2(FeO_4)_{1-x}(CO_3)_x$ systems, with the main difference being the coalescence of the two peaks at 2θ = 32 and 33. The coalescence of these peaks may be brought about by several reasons: the slower rate of cooling (furnace cooling) implemented to these systems, changes in the structural parameters (β-angle) of the systems as well as any preferred orientation of the sulphate anions. No apparent impurities are detected within these systems.

4.3.3.2 Raman Spectroscopy

A Raman spectroscopy investigation was undertaken for the $Ba_2(FeO_4)_{1-x}(SO_4)_x$ (x = 0.20) system to try to provide evidence for the presence of SO_4^{2-}. The Raman spectrum for this system is shown in ***Figure 4.28***.

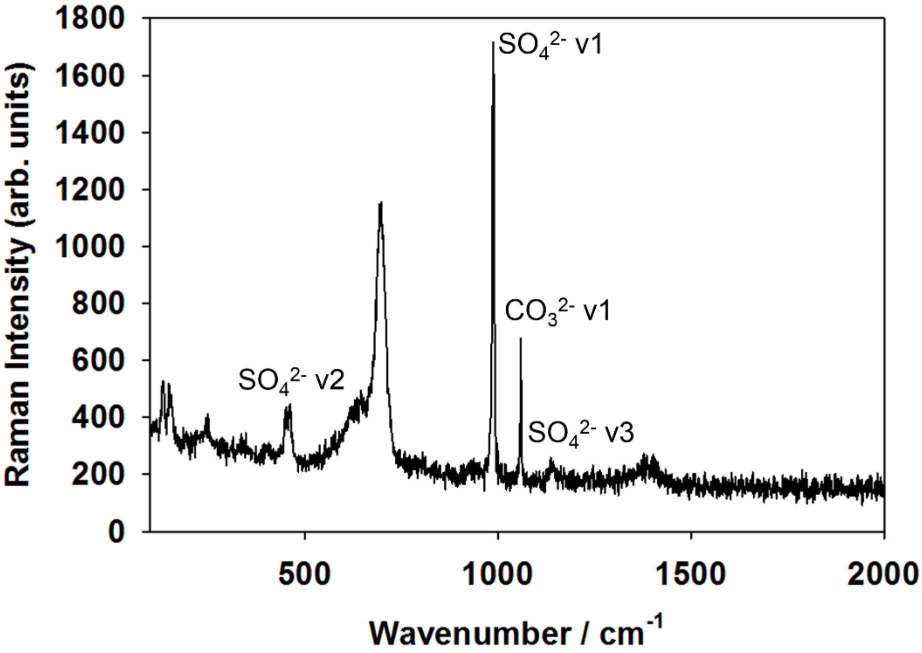

Figure 4.28 Raman spectrum for $Ba_2(FeO_4)_{0.8}(SO_4)_{0.2}$: bands attributed to SO_4^{2-} and CO_3^{2-} are labelled.

The spectrum for the x = 0.20 system shows the presence of bands attributed to SO_4^{2-} v_1 (symmetric stretch), v_2 (doubly degenerate bend) and v_3 (triply degenerate asymmetric stretch) modes. A broad band seen just below 1400 cm^{-1} is characteristic of a v_3 symmetric bending mode of water and suggests this is present within the samples, however, whether this is surface moisture or a part of the structure is yet to be determined. Interestingly, despite being heated at 1100°C, a v_1 (symmetric stretch) is also present, attributed to CO_3^{2-} suggesting this may also be incorporated into the structure.

4.3.3.3 Rietveld Refinements using XRD Data

Rietveld refinements were performed using the XRD data for these $Ba_2(FeO_4)_{1-x}(SO_4)_x$ samples and refinement fits are presented in ***Figures 4.29 - 4.31*** with refined structural information and unit cell parameters given in ***Table 4.9*** and ***Table 4.10*** respectively. During this refinement, it is assumed that Fe/S share the occupancy of the same site and were therefore made equivalent during this process. U_{iso} values were constrained as equivalent for all cations and anions respectively.

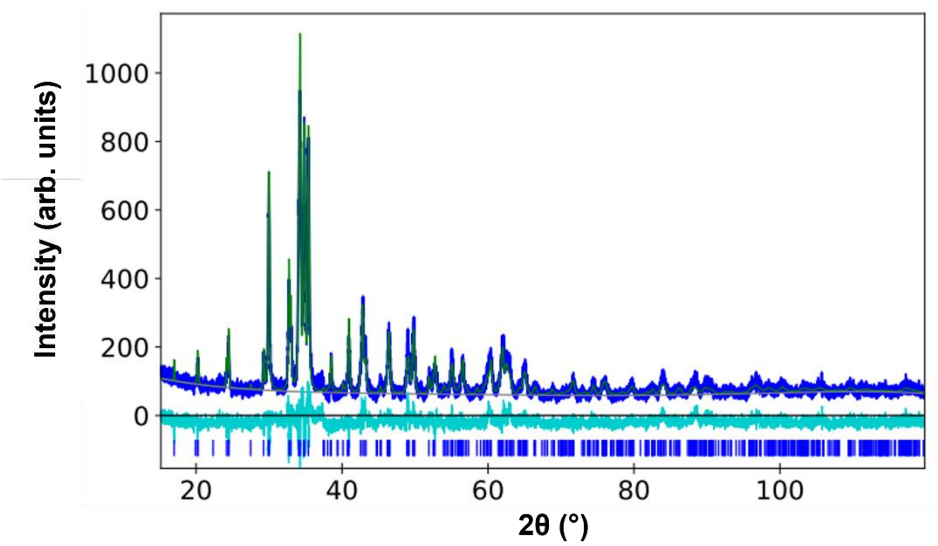

Figure 4.29 Observed, calculated and difference XRD profiles of quenched $Ba_2(FeO_4)_{0.90}(SO_4)_{0.10}$
Space Group: P 1 2_1/*n* 1
GOF = 1.19

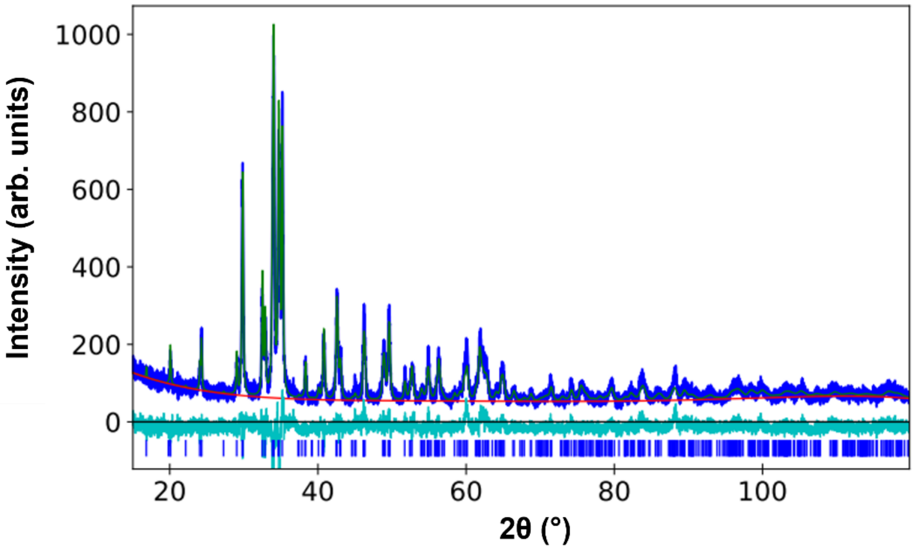

Figure 4.30 Observed, calculated and difference XRD profiles of quenched $Ba_2(FeO_4)_{0.85}(SO_4)_{0.15}$
Space Group: $P\ 1\ 2_1/n\ 1$
GOF = 1.18

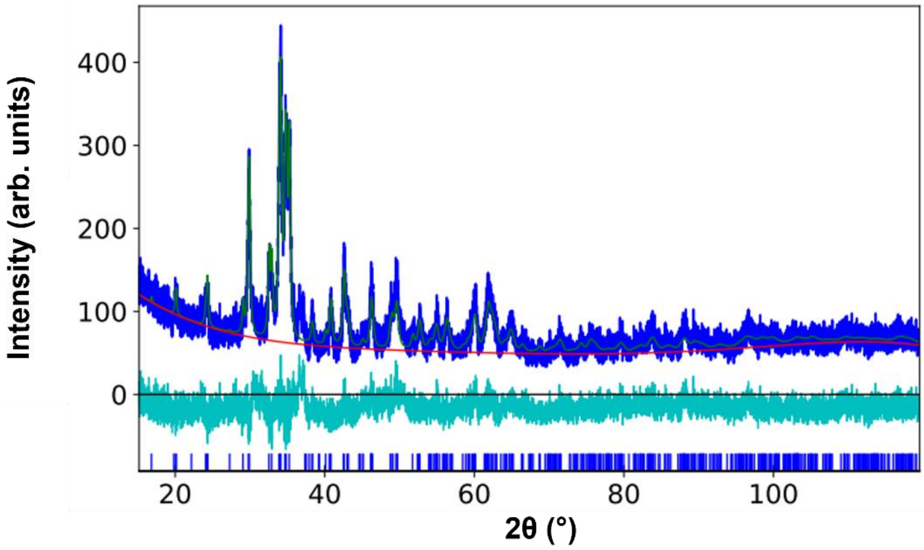

Figure 4.31 Observed, calculated and difference XRD profiles of quenched $Ba_2(FeO_4)_{0.80}(SO_4)_{0.20}$
Space Group: $P\ 1\ 2_1/n\ 1$
GOF = 1.20

Table 4.9 Refined structural parameters for $Ba_2(FeO_4)_{1-x}(SO_4)_x$ *(0.10< x Ò20).*

Atom	x	y	Z	Fraction	Wyckoff Position	U_{iso}
Ba1						
0.80	0.744(3)	0.840(1)	0.083(1)	1.000	4e	0.009(2)
0.85	0.749(2)	0.839(1)	0.082(1)	1.000	4e	0.028(2)
0.90	0.749(2)	0.842(1)	0.082(1)	1.000	4e	0.040(2)
Ba2						
0.80	0.239(2)	0.497(1)	0.196(1)	1.000	4e	0.009(2)
0.85	0.242(2)	0.496(1)	0.195(1)	1.000	4e	0.028(2)
0.90	0.243(2)	0.497(1)	0.196(1)	1.000	4e	0.040(2)
Fe1						
0.80	0.720(6)	0.278(3)	0.075(2)	0.800	4e	0.009(2)
0.85	0.714(4)	0.268(2)	0.068(2)	0.850	4e	0.028(2)
0.90	0.713(4)	0.276(2)	0.077(2)	0.900	4e	0.040(2)
S1						
0.80	0.720(6)	0.278(3)	0.075(2)	0.200	4e	0.009(2)
0.85	0.714(4)	0.268(2)	0.068(2)	0.150	4e	0.028(2)
0.90	0.713(4)	0.713(4)	0.077(2)	0.100	4e	0.040(2)
O1						
0.80	0.815(7)	0.485(1)	0.091(1)	1.000	4e	0.007(9)
0.85	0.773(9)	0.444(5)	0.103(2)	1.000	4e	0.011(8)
0.90	0.808(8)	0.467(6)	0.085(3)	1.000	4e	0.060(9)
O2						
0.80	0.547(8)	0.228(7)	0.179(1)	1.000	4e	0.007(9)
0.85	0.527(6)	0.225(5)	0.180(4)	1.000	4e	0.011(8)
0.90	0.523(7)	0.221(7)	0.184(4)	1.000	4e	0.060(9)
O3						
0.80	1.060(7)	0.137(9)	0.144(5)	1.000	4e	0.007(9)
0.85	1.033(6)	0.118(6)	0.141(4)	1.000	4e	0.011(8)
0.90	1.032(7)	0.141(8)	0.150(4)	1.000	4e	0.060(9)
O4						
0.80	0.773(13)	0.195(5)	-0.043(4)	1.000	4e	0.007(9)
0.85	0.794(10)	0.191(4)	-0.059(3)	1.000	4e	0.011(8)
0.90	0.768(12)	0.181(6)	-0.051(4)	1.000	4e	0.060(9)

Constraints: Isotropic thermal parameters (U) O1=O2=O3=O4; Ba1=Ba2=Fe1=S1
Atomic Position Fe1(x)=S1(x), Fe1(y)=S1(y), Fe1(z)=S1(z)

Table 4.10 Refined unit cell parameters for $Ba_2(FeO_4)_{1-x}(SO_4)_x$ (0.10< x Ò20).

$Ba_2(FeO_4)_{1-x}(CO_3)_x$	**Unit Cell Parameter / Å**				
X	***a***	***b***	***c***	**β / °**	**Volume / Å^3**
0.20	5.934(1)	7.627(1)	10.528(1)	90.17(1)	476.495(32)
0.15	5.936(1)	7.607(1)	10.525(1)	90.13(1)	475.305(102)
0.10	5.939(1)	7.606(1)	10.503(1)	90.16(1)	474.426(25)

Good fits were obatined for all systems when refined using a modified Ba_2FeO_4 structural model with all samples proving to be phase-pure. Analysis of the structural data shows that values determined for the oxygen atoms have the greatest errors in these systems, which can be related to the fact that they are the lightest of the atoms, as well as due to variations in oxygen position due to the presence of both FeO_4^{4-} and SO_4^{2-}, with the former bond length of Fe-O expected to be greater than the latter. The disadvantages of XRD accurately locating the positions of lighter atoms, means that neutron diffraction data is required to determine oxygen positions more accurately.

Increasing incorporation of the tetrahedral SO_4^{2-} may potentially be expected to have less effect on the overall structure as the incorporation of CO_3^{2-}, as this no longer introduces oxygen vacancies, with the incorporated sulphate group potentially keeping the same orientation as the replaced tetrahedral FeO_4^{4-}. The effect of this can be seen with the similar β angle values, however an increasing unit cell volume is shown with greater Fe deficiency. This volume increase could be attributed to changes in Fe oxidation state with the increase in ionic radii of Fe^{4+} to Fe^{3+} and/or incorporation of water into the systems outweighing the effect of replacing the larger ionic radii

Fe^{3+}/Fe^{4+} with a much small ionic radii S^{6+}. Mössbauer spectroscopy studies are planned to examine the changes in Fe oxidation state in detail.

Whilst analysing the quenched analogues of the $Ba_2(FeO_4)_{1-x}(SO_4)_x$ systems, it is clear that the coalescence of the peaks (2θ = 32 - 33°) is a permanent feature of these structures, and so the effect of furnace cooling or quenching of the sample has little to no effect on the structure. Therefore it can be determined that this coalescence is most likely due to the change in the β-angles of the structures, whilst these are similar between the sulphate systems, the β-angles are greater than that seen in the carbonate equivalents, these changes may be due to the orientation of sulphate anions in the systems.

4.4 Conclusions

The results in this chapter have shown how carbonate can be readily introduced into Co deficient $Ba_2(CoO_4)_{1-x}(CO_3)_x$ systems where a structural change is seen from monoclinic to more orthorhombic like. Rietveld refinements using ND data, along with TGA-MS data, provide evidence to support that carbonate is found in the systems whilst Raman and thermal stability studies showed significant changes depending on the heating conditions, helping to increase our understanding of the systems stability. This presence of carbonate provides further support for the importance of considering the possibility of carbonate incorporated in other systems prepared by low temperature synthesis routes (<1000°C). Investigations into these systems also suggest that water may also play a strong role in the stabilisation of the structure closer to room temperature but not in the overall formation.

Similar findings were also seen when extending investigations into the $Ba_2(FeO_4)_{1-x}(CO_3)_3$ ($0<x\leq0.20$) systems leading to the similar overall conclusions as outlined above. Further structural characterisation would be required in the form of Neutron diffraction data acquisition to help determine accurate positions for the CO_3^{2-} in these Fe systems.

The work has been extended to show that sulphate can also be incorporated into such systems, with these $Ba_2(FeO_4)_{1-x}(SO_4)_3$ ($0.10<x\leq0.20$) materials showing improved thermal stability, and so proving easier to synthesise consistently. Rietveld refinement using XRD data provided support that sulphate was incorporated into the system. Raman spectra also supports the conclusion that SO_4^{2-} has been successfully incorporated, however, also appears to show the presence of both water and CO_3^{2-}. Whether these are incorporated into the main structure or captured upon cooling is yet to be determined, and further studies, such as VT-XRD and TGA-MS, could help solve this matter. Neutron diffraction data would also help to provide a more accurate and detailed structure.

5. Investigation of the $Sr_{4-x}Ba_xNa_{1-y}Li_y(BO_3)_3$ series and Possible Isostructural Systems[251]

5.1 Introduction

In 2005, Wu et al. reported the structural determination of the novel cubic borates $Ba_4Na(BO_3)_3$, $Sr_4Na(BO_3)_3$ and $Sr_4Li(BO_3)_3$.[194] These systems were shown to be isostructural, with the cubic space group $Ia\bar{3}d$, and with the structure being fundamentally described as consisting of isolated planar $(BO_3)^{3-}$ units distributed perpendicularly to each other in three directions coordinating to Na/Li, with the Sr/Ba located in the cavities of the framework. It was during this study that the $Sr_{4-x}Ba_xNa(BO_3)_3$ complete ($0 \leq x \leq 4$) solid solution was also produced showing the expected linear increase in unit cell parameters with increasing Ba content. Since this report there have been several studies regarding borates with this structure, all of which have primarily focused on expanding this previous work to study the photoluminescence of the solid solution series. Thus, many different dopants have been introduced to investigate the effect on these properties, such as Eu^{3+}, Ce^{3+}, Sm^{3+}, Dy^{3+} and also Pb^{2+}.[194-199]

Given the observation of the ability to accommodate trigonal planar oxyanions, such as carbonate, in materials with the β-K_2SO_4 structure, we initially investigated whether the isovalent substitution of PO_4^{3-} by BO_3^{3-} was possible in $NaBaPO_4$ with a view to possibly preparing a new electrolyte capable of proton conduction ($NaBa(PO_4)_{1-x}(BO_3)_x$ Ą $NaBa(PO_4)_{1-x}(BO_4H_2)_x$ after hydration). Unfortunately the results showed limited solubility of borate in the structure, but the work did raise an interesting observation. Significantly, the above $Ba_4Na(BO_3)_3$ phase was the main impurity and the similarity of the X-ray diffraction (XRD) pattern of this phase to that of perovskites was noted (***Figure 5.1***). In particular, the main peaks can be related to a simple (a = 3.954 Å) perovskite sub cell unit, with the additional weaker reflections related to the expanded cell, which takes into account the ordering of the Na and borate groups.

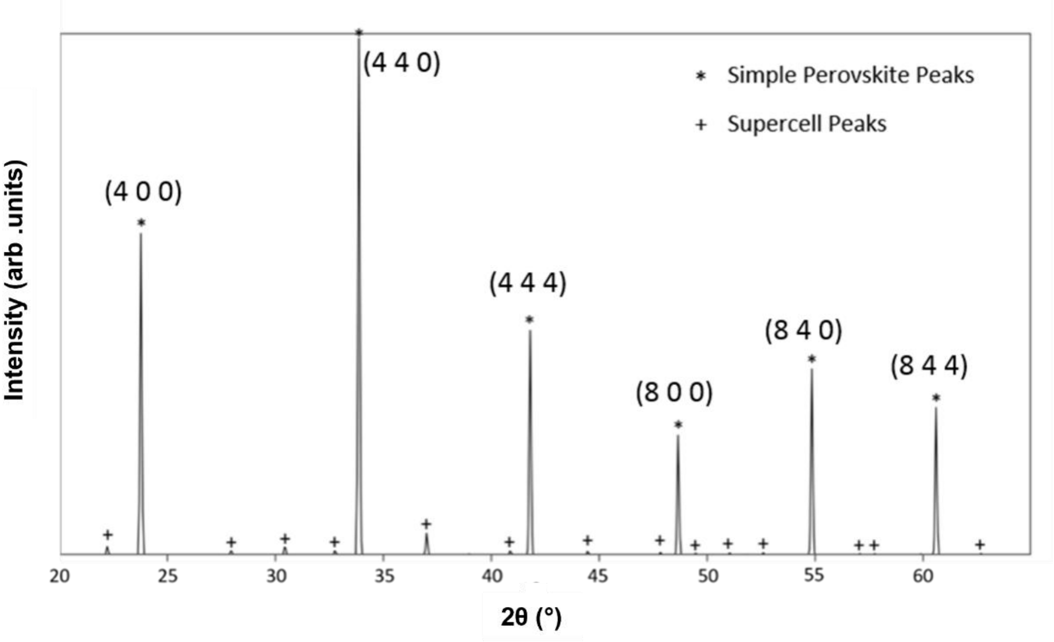

Figure 5.1 $Ba_4Na(BO_3)_3$ X-ray Diffraction Pattern from CIF file reported by Wu et al. highlighting the simple cubic perovskite peaks, as well as the weaker supercell peaks associated with the ordering of Na and B on the small cation sites[1]

This relationship to the perovskite structure has not previously been noted in the prior work on these systems: in terms of the perovskite-type structural description, they can be classed as a 1:3 ordered small cation (Na, B) site system, with the oxygen atoms on the borate group orientated such that the Na coordination is octahedral (***Figure 5.2***).

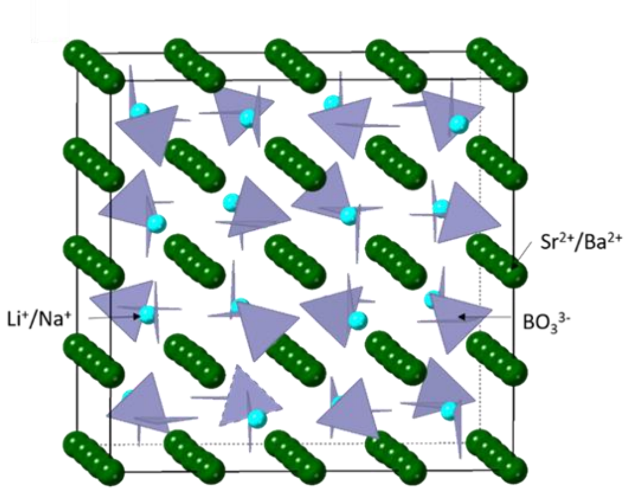

Figure 5.2 Structure of $Sr_{4-x}Ba_xNa_{1-y}Li_y(BO_3)_3$ (Space Group: $Ia\bar{3}d$). The structure is essentially a 1:3 ordered small perovskite cation (Na/Li, B) site system, with the oxygen atoms on the borate group orientated such that the Na/Li coordination is octahedral.

On a larger scale the $Ba_4Na(BO_3)_3$ system has cation ordering with features of both perovskite systems $Ba_4LiBi_3O_{12}$ [200] and $Ba_4LiSb_3O_{12}$ [201] in which lithium orders on the same face of the perovskite in the former and opposite corners in the latter (***Figure 5.3*** highlights these relationships, and the overall structural relationship to the perovskite structure).

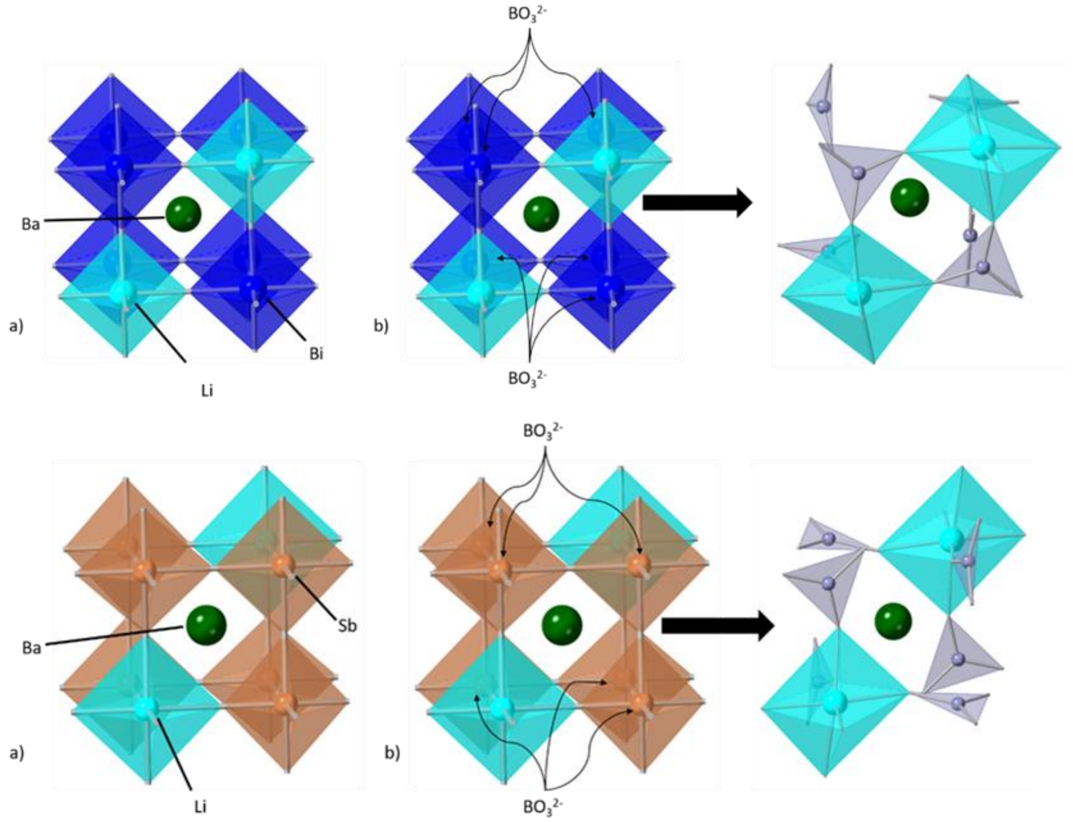

Figure 5.3 (a) 1:3 Li:Bi ordering in $Ba_4LiBi_3O_{12}$ and the relation between $Ba_4LiBi_3O_{12}$ and $Ba_4Na(BO_3)_3$ where the Bi octahedra are replaced by trigonal planar BO_3^{3-} (b) 1:3 Li:Sb ordering in $Ba_4LiSb_3O_{12}$ and the relation between $Ba_4LiSb_3O_{12}$ and $Ba_4Na(BO_3)_3$ where the Sb octahedra are replaced by trigonal planar BO_3^{3-}. In the extended structure of $Ba_4Na(BO_3)_3$ there are both these ordering features.

While borate containing perovskites are known, previously the borate content have been significantly lower (maximum 50% substitution on the small cation site, as shown by $LaBaCuO_2BO_3$),[202-208] and moreover these $Sr_{4-x}Ba_xNa(BO_3)_3$ systems represent the only examples, where all the oxygen atoms are associated with the borate groups. In the same way as Brownmillerite ($Ca_2(Fe/Al)_2O_5$) can be classed as an oxygen vacancy ordered perovskite, leading to alternate layers of octahedra and tetrahedra, these systems can similarly be classed as oxygen vacancy ordered perovskites with the vacancies around the boron and where the coordination preference of boron means that three vacant sites are favoured to give trigonal planar coordination, while the alkali metal maintains octahedral coordination.

By looking at the simple perovskite, browmillerite and the $Sr_{4-x}Ba_x(Na/Li)(BO_3)_3$ systems in terms of a generalised formula ABO_{3-x}, they show an increase in the number of oxygen vacancies across the series; ideal perovskite ABO_3 (x=0), browmillerite $ABO_{2.5}$ (x=0.5), $Sr_{4-x}Ba_x(Na/Li)(BO_3)_3$ systems $ABO_{2.25}$ (x=0.75). ***Figure 5.4*** provides a visual representation of the difference in a single layer of all three types of systems, emphasising how the latter two structure can be seen as oxygen deficient when compared to the archetypal perovskite structure.

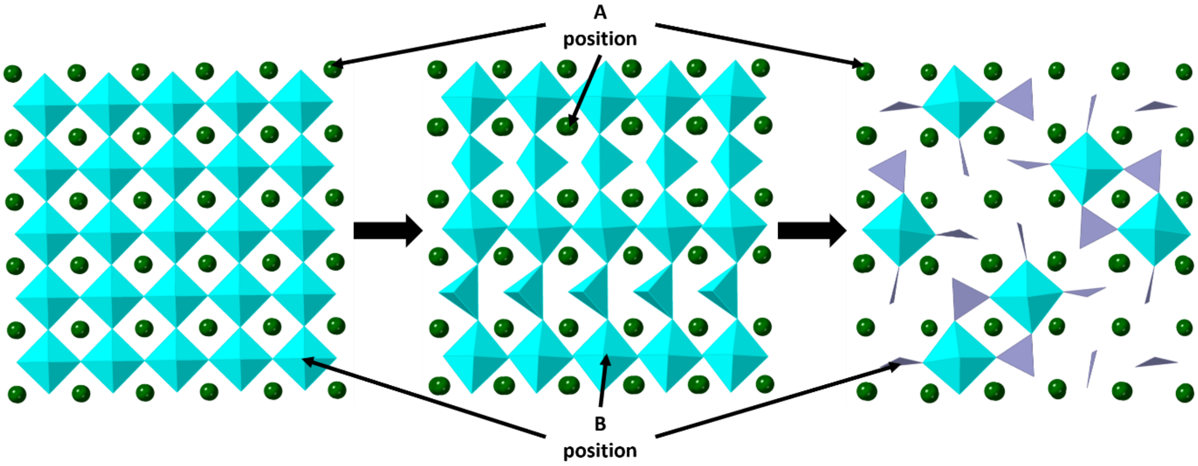

Figure 5.4 Visual comparison of increasing oxygen vacancies, and how they are arranged, from simple perovskite (left) to a brownmillerite structure (middle) to finally the $Sr_{4-x}Ba_x(Na/Li)(BO_3)_3$ (right)

In the $Sr_{4-x}Ba_x(Na/Li)(BO_3)_3$ systems, the orientational order of these borate groups is likely key to their formation by ensuring that the Na is octahedrally coordinated. Such orientational ordering has also been shown to play a vital role in the formation of other perovskite like structures e.g. organic link perovskites such as $[C(NH_2)_3]Cu_xM_{1-x}(HCOO)_3$ (M = Mn, Zn, Mg)[209-210] where formate bridges order in a way that tilts the corner octahedral B sites providing the oxygen required to stabilise the [$C(NH_2)_3$] in the A site and thus stabilising the overall perovskite structure.

With research into oxyanion doped perovskite type materials attracting increasing attention[143 -150, 154-158] we have investigated these $Ba_4Na(BO_3)_3$, $Sr_4Na(BO_3)_3$ and $Sr_4Li(BO_3)_3$ systems further, examining whether other compositions were possible. In this respect, whilst much work has been done with regards to the $Sr_{4-x}Ba_xNa(BO_3)_3$ series, there is a lack of studies on a solid solution pertaining to the substitution of Na^+ with Li^+.

In this chapter, extended studies on these systems are discussed, reporting on the successful synthesis of a new solid solution series $Sr_{4-x}Ba_xNa_{1-y}Li_y(BO_3)_3$. Also reported is an investigation into the possibility of synthesising related systems including the $Sr_{4-x}Ca_xLi(BO_3)_3$ series, with this latter work leading to the discovery of a new ordered variant of these materials.

5.2 Experimental Procedure

$BaCO_3$ (Alfa Aesar 99.8%), Li_2CO_3 (Alfa Aesar 99%), H_3BO_3 (Alfa Aesar 99.8%), $SrCO_3$ (Sigma-Aldrich 99.9%) and Na_2CO_3 (VWR Chemicals BDH® 99.9%) were used to prepare the series $Sr_{4-x}Ba_xNa_{1-y}Li_y(BO_3)_3$ (x = 0, 1, 2, 3, 4 y = 0, 0.5, 1). For each composition, stoichiometric ratios of reagents were intimately ground and heated in air for 12hrs at 800°C - 900°C. The subsequent mixtures were then reground and heated again at the same temperature for 12hrs. This same method was also used in the preparation of the $Sr_{4-x}Ca_xLi(BO_3)_3$ series of samples utilising $CaCO_3$ (Alfa Aesar 99.95%).

Powder X-ray diffraction (XRD) analysis were carried out using the PANalytical Empyrean (Cu Kα radiation) diffractometer. This was used for initial phase analysis as well as to determine the structure of the samples through Rietveld profile refinement using the GSAS-II computer programme.[164]

5.3 Results and Discussion

5.3.1 $Sr_{4-x}Ba_xNa(BO_3)_3$, $Sr_{4-x}Ba_xLi(BO_3)_3$ (x = 0, 1, 2, 3, 4)

Initially the $Sr_{4-x}Ba_xNa(BO_3)_3$ and $Sr_{4-x}Ba_xLi(BO_3)_3$ series were synthesised through solid state reaction, as outlined in the experimental section, and XRD data are shown in ***Figure 5.5*** and ***Figure 5.6*** respectively.

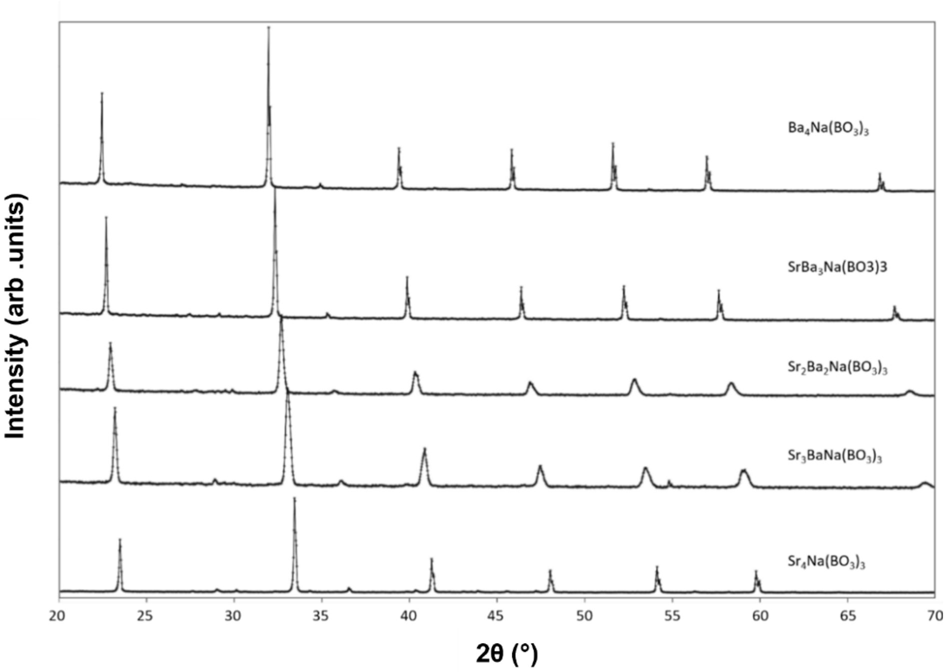

Figure 5.5 X-Ray Diffraction Data of $Sr_{4-x}Ba_xNa(BO_3)_3$ (x =0, 1, 2, 3, 4.) showing a complete solid solution series

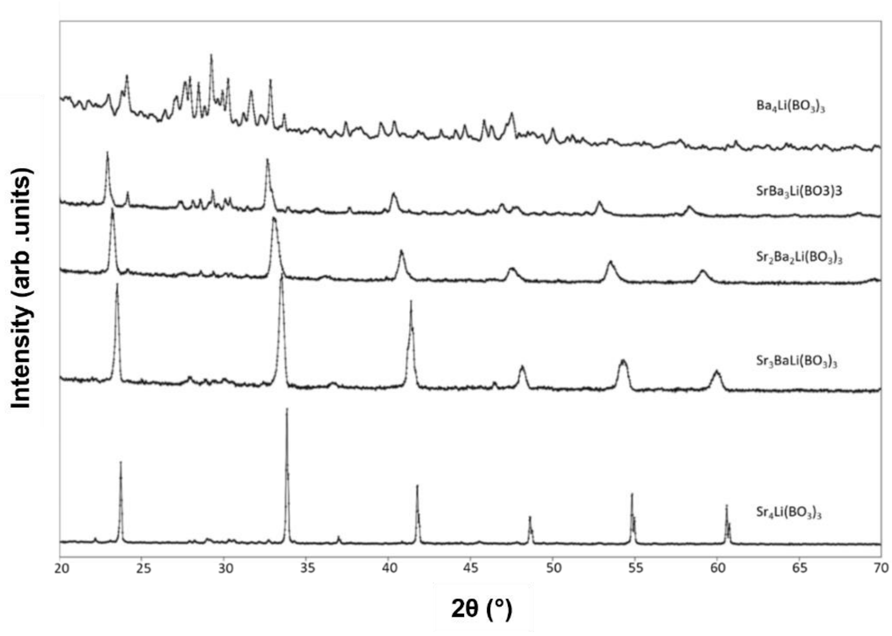

Figure 5.6 X-Ray Diffraction Data of $Sr_{4-x}Ba_xLi(BO_3)_3$ *(x =0, 1, 2, 3, 4.), showing the appearance of increasing amounts of impurities as x increases*

In agreement with prior studies by Wu et al, XRD studies indicated a complete solid solution series was observed for $Sr_{4-x}Ba_xNa(BO_3)_3$, however, attempts to prepare a similar series for $Sr_{4-x}Ba_xLi(BO_3)_3$ were less successful. In this case, significant impurities ($BaLi(BO_3)$ and $Ba_3(BO_3)_2$) were observed as the value of x increases, indicating a lower ability to accommodate Ba into the Li based perovskite related structure which is most likely related to the smaller size of Li.

5.3.2 $Sr_{4-x}Ba_xNa_{1-y}Li_y(BO_3)_3$ (x = 0, 1, 2, 3, 4)(y = 0.5, 0.75)

In order to investigate whether co-doping with Na would allow the complete Ba/Sr solid solution series to be achieved, the series $Sr_{4-x}Ba_xNa_{0.5}Li_{0.5}(BO_3)_3$ was first examined. The outcome of this investigation is the successful stabilisation of the perovskite like structure containing a mixture of both Na^+ and Li^+ in a 1:1 ratio for the full Ba/Sr range (***Figure 5.7***)

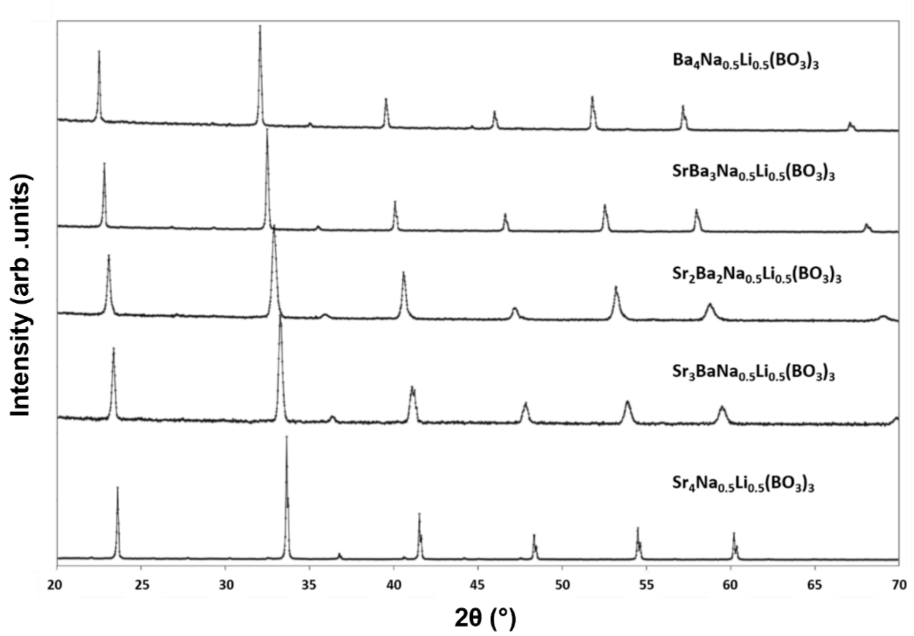

Figure 5.7 X-Ray Diffraction Data of $Sr_{4-x}Ba_xNa_{0.5}Li_{0.5}(BO_3)_3$ (x = 0, 1, 2, 3, 4), showing the formation of a complete solid solution series.

XRD patterns observed for x = 1, 2, 3 systems appear to show asymmetric broadening of peaks, the origin of which may be associated with a number of factors; (1) it may indicate some inhomogeneity/difference in local cation ordering in the Ba/Sr distribution throughout the sample; (2) the broadening may be indicative of a miscibility gap in this intermediate range, which would mean that each XRD pattern could instead be a combination of 2 or more different compositions. This broadening was also seen for the $Sr_{4-x}Ba_xNa(BO_3)_3$ and $Sr_{4-x}Ba_xLi(BO_3)_3$ series of samples, and while visible in the previous literature on these systems, it was not discussed further.[194] Attempts were made to fit the data to two closely related perovskite phases, and while a small improvement in the fit was obtained, the use of two phases was still not adequate to accurately model the peak broadening.

The higher Li content series, $Sr_{4-x}Ba_xNa_{0.25}Li_{0.75}(BO_3)_3$ (x = 0, 1, 2, 3, 4) was also examined (***Figure 5.8***) to see if the Li content could be increased and still obtain a complete solid solution series. However, for the x = 4 and x =3 systems, increasing amounts of impurities such as $BaLi(BO_3)_3$ were also obtained in this case.

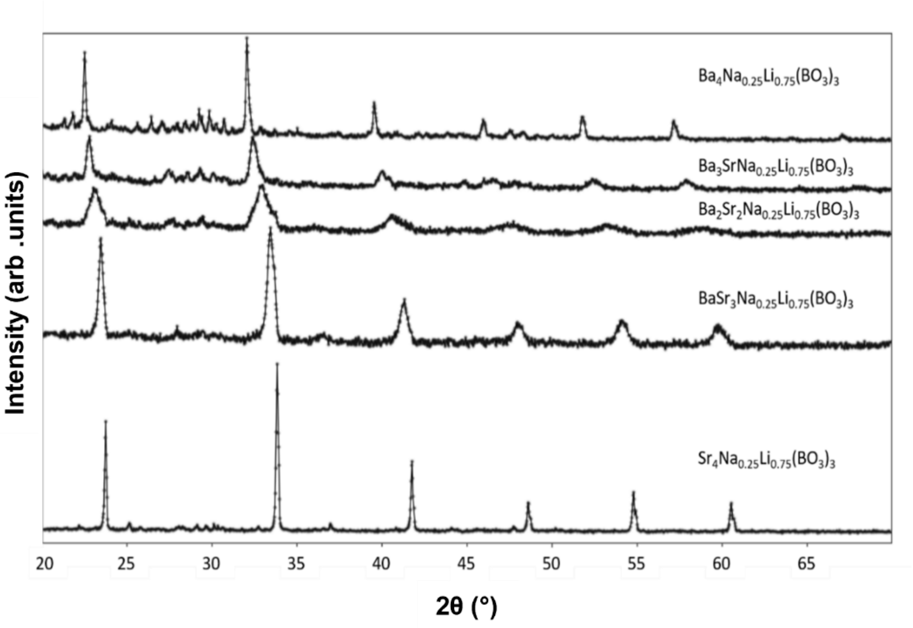

Figure 5.8 X-ray Diffraction data of $Sr_{4-x}Ba_xNa_{0.25}Li_{0.75}(BO_3)_3$ (x = 0, 1, 2, 3, 4), showing unsuccessful formation of a complete solid solution series without significant impurity

5.3.3 Structural Characterisation of the $Sr_{4-x}Ba_xNa_{0.5}Li_{0.5}(BO_3)_3$ series

5.3.3.1 $Ba_4Na_{0.5}Li_{0.5}(BO_3)_3$

5.3.3.1.1 Powder X-Ray Diffraction

The complete solid solution seris $Sr_{4-x}Ba_xNa_{0.5}Li_{0.5}(BO_3)_3$ was successfully synthesised through standard solid state synthesis as previously described. The XRD data for the x=4 sample can be seen in ***Figure 5.9***.

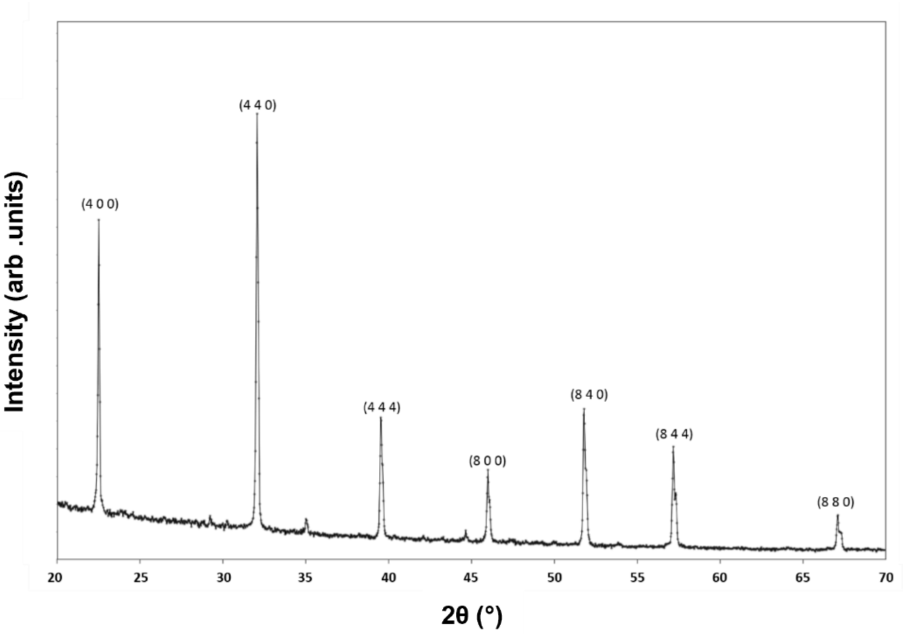

Figure 5.9 X-ray diffraction data for $Ba_4Na_{0.5}Li_{0.5}(BO_3)_3$

5.3.3.1.2 Rietveld Refinement using XRD Diffraction Data

Structure determination using Rietveld refinement was then performed for the $Sr_{4-x}Ba_xNa_{0.5}Li_{0.5}(BO_3)_3$ series beginning with the x = 4 phase. In each refinement it was assumed that a single phase was present. The starting model for this structure refinement employed that determined by Wu et al.[194] with the refined structural data of $Ba_4Na(BO_3)_3$ shown in ***Table 5.1*** and ***Table 5.2*****.**

Table 5.1 Structural information for $Ba_4Na(BO_3)_3$

Atom	Wyckoff Position	x	y	z	Fraction	U_{iso}
Ba1	16b	0	0	0	1.000	0.002(1)
Ba2	48f	0	0.25	-0.002(1)	1.000	0.002(1)
Na	16b	0.125	0.125	0.125	1.000	0.002(1)
B	48g	0.104(1)	0.354(1)	0.125	1.000	0.002(1)
O1	96h	0.127(2)	0.271(1)	0.135(4)	1.000	0.016(10)
O2	48g	0.164(1)	0.414(1)	0.125	1.000	0.016(10)

($Ia\bar{3}d$ Unit Cell Parameter *a* = 15.8177(2) Å, Volume = 3957.56(13)$Å^3$)

Table 5.2 Selected interatomic distances of $Ba_4Na(BO_3)_3$

Bond	Bond Length / Å	Bond	Bond Length / Å
Ba1 – O1	2.734(17)	**Na – O1**	2.338(11)
Ba2 – O1	2.793(16)	**B – O1**	1.402(34)
Ba2– O2	2.625(12)	**B – O2**	1.399(35)

Appropriate values of Sr on the Ba sites and Li on the Na site was employed for subsequent refinements of the $Sr_{4-x}Ba_xNa_{0.5}Li_{0.5}(BO_3)_3$ series. For Li/Na, there is only a single site in the structure, while there are two possible sites for Sr/Ba allowing for the possibility that there may be a preferential site substitution. In order to investigate this in the structure refinement, two models were initially trialled: (1) ordering of Sr/Ba, (2) random substitution of Sr/Ba. From these refinements, all samples appeared to favour a random distribution on the Ba/Sr sites.

As XRD analysis is not the most suitable for the determination of lighter elements positions and their atomic displacement parameters, certain constraints were introduced during the refinement process. This included fixing the Li/Na site coordinates and introducing constrained generalised U_{iso} for all cations and anions respectively; sample displacement and microstrain were also refined. For mixed Li/Na systems, the Ba1 16b sites were shifted slightly to a 32e Wyckoff position to compensate for any structural variation caused by the Na/Li substitution. The Rietveld refinement fit for $Ba_4Na_{0.5}Li_{0.5}(BO_3)_3$ can be seen in ***Figure 5.10*** with structural data shown in ***Table 5.3*** and ***Table 5.4***.

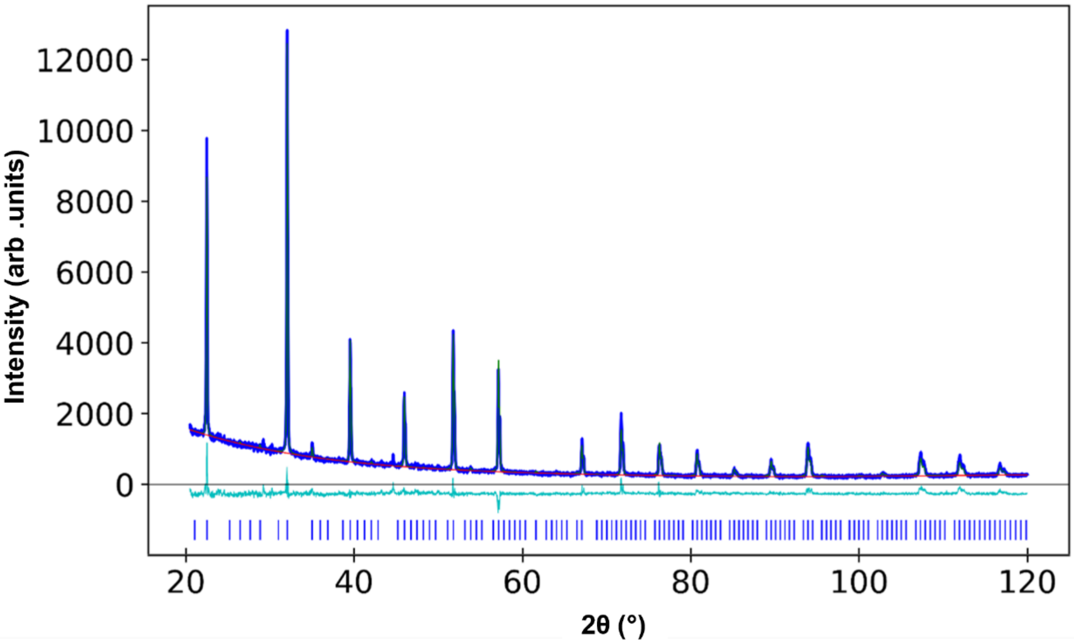

Figure 5.10 Observed, calculated and difference x-ray diffraction profiles for $Ba_4Na_{0.5}Li_{0.5}(BO_3)_3$
(Tick marks ï $Ba_4Na_{0.5}Li_{0.5}(BO_3)_3$)

Table 5.3 Structural information for $Ba_4Na_{0.5}Li_{0.5}(BO_3)_3$

Atom	**x**	**y**	**z**	**Site Occupancy**	**Wyckoff Position**	**U_{iso}**
Ba1	-0.003(3)	-0.003(3)	-0.003(3)	0.500	32e	0.014 (1)
Ba2	0.0	0.25	-0.005(1)	1.000	48f	0.014 (1)
Li	0.125	0.125	0.125	0.500	16b	0.014 (1)
Na	0.125	0.125	0.125	0.500	16b	0.014 (1)
B	0.105(1)	0.355(1)	0.125	1.000	48f	0.014 (1)
O1	0.122(1)	0.276(1)	0.161(2)	1.000	96h	0.141(23)
O2	0.168(1)	0.418(1)	0.125	1.000	48f	0.141(23)

R_{wp} = 4.59% GOF = 1.75 ($Ia\bar{3}d$ a = 15.7756(5) Å, Volume = 3926.07(36) Å^3)

Table 5.4 Selected interatomic distances of $Ba_4Na_{0.5}Li_{0.5}(BO_3)_3$

Bond	**Bond Length / Å**	**Bond**	**Bond Length / Å**
Ba1 – O1	2.728(1)	**Li/Na – O1**	2.334(1)
Ba2 – O1	2.789(1)	**B – O1**	1.400(1)
Ba2– O2	2.625(1)	**B – O2**	1.394(1)

Values given in show that allowing the Ba1 atomic site to shift from the 16b Wyckoff position to a 32e position leads to negligible shift, whilst large U_{iso} and error values of the O1 and O2 sites suggest variations in borate orientations within this system. Both unit cell parameter *a* and consequently the unit cell volume has decreased in size in comparison to the $Ba_4Na(BO_3)_3$ system, which is expected due to the smaller atomic radii of 6 coordinate Li^+ (0.76 Å) in comparison to 6 coordinate Na^+ (1.02 Å).[166] The determined bond lengths are similar to that of the $Ba_4Na(BO_3)_3$ system showing that the refinement of the XRD data leads to bond length values somewhat dependant on the Ba^{2+} sites. More accurate positions for the Li/B/O sites, and hence relevant bond lengths, could be determined using neutron diffraction data acquisition which would help clarify changes in the borate orientation and the possibility of any octahedral tilting of NaO_6/LiO_6.

5.3.3.1.3 Raman Spectroscopy

Raman data ***(Figure 5.11)*** confirms the presence of borate in the $Ba_4Na_{0.5}Li_{0.5}(BO_3)_3$ system with the appearance of the expected v_1 (symmetric stretch), v_3 (doubly degenerate asymmetric stretch) and v_4 (doubly degenerate asymmetric bend) BO_3^{3-} vibrational modes[211] with the bands recorded for these being shifted in comparison to those seen in H_3BO_3 (***Table 5.5***).

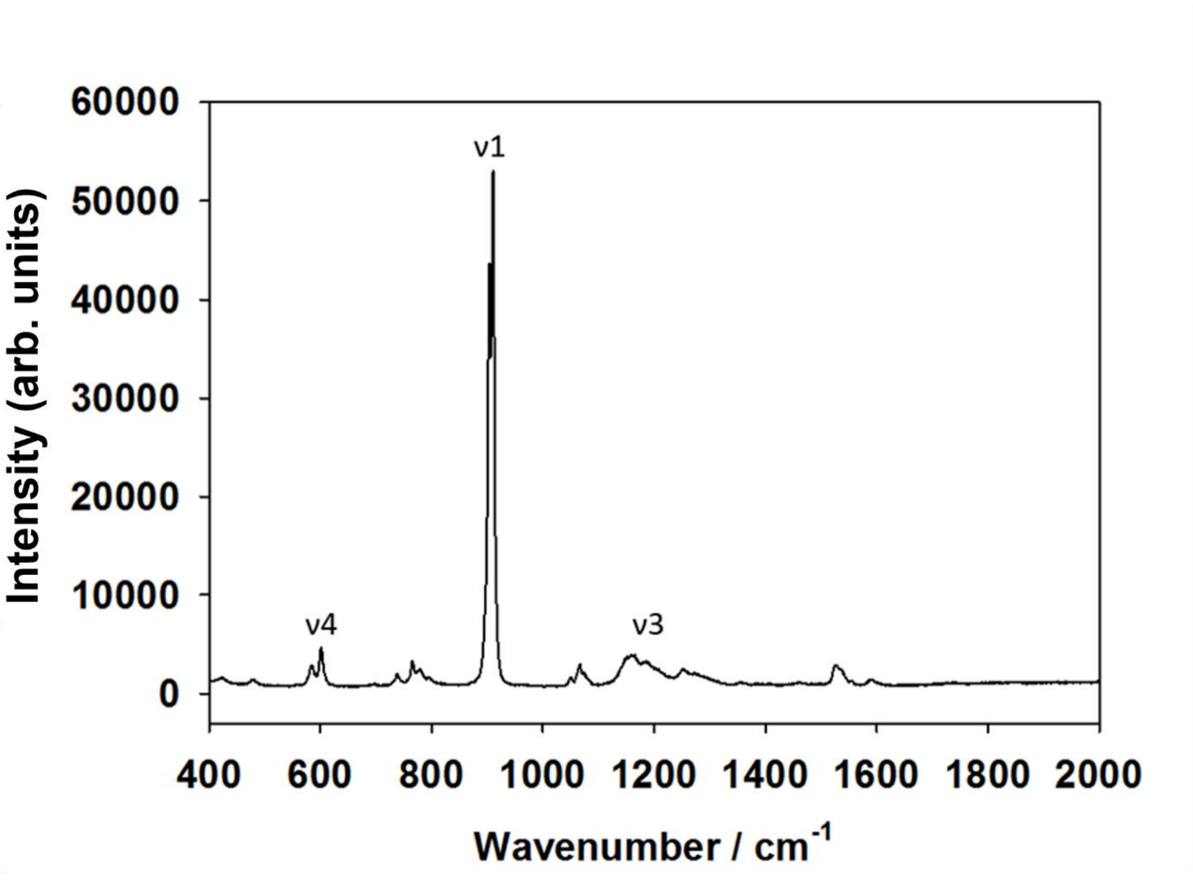

Figure 5.11 Raman spectroscopy data for $Ba_4Na_{0.5}Li_{0.5}(BO_3)_3$ detailing specific Raman bands seen for BO_3^{3-} vibrational modes

Table 5.5 Raman band wavenumbers for BO_3^{3-} vibrational modes of H_3BO_3 and $Ba_4Na_{0.5}Li_{0.5}(BO_3)_3$

System	ν 1 /$^{-1}$	ν 3 /$^{-1}$ cm	ν 4 /$^{-1}$
H_3BO_3	881.67	1168.06	500.09
$Ba_4Na_{0.5}Li_{0.5}(BO_3)_3$	903.25 910.43 939.08	1136.38 – 1272.95	583.18 601.40

Three distinctive v_1 BO_3^{3-} Raman bands can be determined from these data suggesting three different environments for the BO_3^{3-} groups, with each borate group directly connected to two octahedral NaO_6/LiO_6 the three possible environments are: Na^+:Na^+, Na^+:Li^+ or Li^+:Li^+. Borate is known for forming larger borate complexes each with their own specific Raman bands, some of these can be seen in this Raman spectra. Bands seen 421.52 cm^{-1}, 477.26 cm^{-1} and 1066.56 cm^{-1} can be attributed to diborate groups and the band ranges seen at 736.96 – 794.56 cm^{-1} and 1525.12 – 1589.12 cm^{-1} can be attributed to metaborate chains.[212] The presence of these extra Raman bands could suggest localised distortions in the overall structure or maybe from unidentified borate glass impurities.

5.3.3.2 $SrBa_3Na_{0.5}Li_{0.5}(BO_3)_3$

5.3.3.2.1 Rietveld Refinement using XRD Data

The Rietveld refinement of the structure using XRD data for the $SrBa_3Na_{0.5}Li_{0.5}(BO_3)_3$ system can be seen in ***Figure 5.12***, with structural data shown in ***Table 5.6*** and ***Table 5.7***.

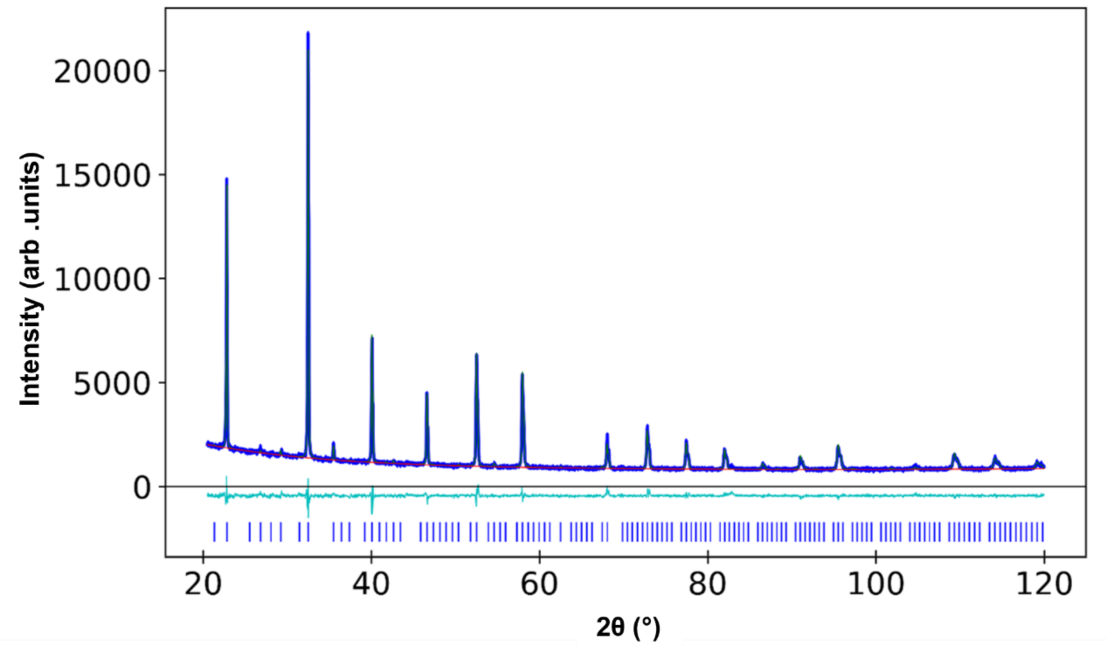

Figure 5.12 Observed, calculated and difference x-ray diffraction profiles for $SrBa_3Na_{0.5}Li_{0.5}(BO_3)_3$
(Lower tick marks ï $SrBa_3Na_{0.5}Li_{0.5}(BO_3)_3$*)*

Table 5.6 Structural information for $SrBa_3Na_{0.5}Li_{0.5}(BO_3)_3$

Atom	**x**	**y**	**z**	**Site Occupancy**	**Wyckoff Position**	**U_{iso}**
Ba1	-0.008(2)	-0.008(2)	-0.008(2)	0.750	32e	0.008(1)
Sr1	-0.008(2)	-0.008(2)	-0.008(2)	0.250	32e	0.008(1)
Ba2	0.0	0.25	-0.004(1)	0.750	48f	0.008(1)
Sr2	0.0	0.25	-0.004(1)	0.250	48f	0.008(1)
Li	0.125	0.125	0.125	0.500	16b	0.008(1)
Na	0.125	0.125	0.125	0.500	16b	0.008(1)
B	0.101(1)	0.351(1)	0.125	1.000	48f	0.008(1)
O1	0.121(1)	0.268(1)	0.151(2)	1.000	96h	0.095(13)
O2	0.164(1)	0.414(1)	0.125	1.000	48f	0.095(13)

R_{wp} = 4.41% GOF = 1.50 ($Ia\bar{3}d$ a = 15.5724(4) Å, Volume = 3776.29(27) Å^3)

Table 5.7 Selected interatomic distances of $SrBa_3Na_{0.5}Li_{0.5}(BO_3)_3$

Bond	**Bond Length / Å**	**Bond**	**Bond Length / Å**
Sr1/Ba1 – O1	2.693(1)	**Li/Na – O1**	2.304(1)
Sr2/Ba2 – O1	2.752(1)	**B – O1**	1.382(1)
Sr2/Ba2– O2	2.584(1)	**B – O2**	1.376(1)

Values given show that the observed shift of the Ba1/Sr1 from 16b Wyckoff position to a 32e position was small, whilst U_{iso} and relevant error values of the O1 and O2 sites suggest variations in borate orientations within this system. Both unit cell parameter *a* and subsequently the unit cell volume has decreased greatly in size when compared to the $Ba_4Na(BO_3)_3$ and $Ba_4Na_{0.5}Li_{0.5}(BO_3)_3$ systems, which is expected due to the substitution of the smaller atomic radii of 8 coordinate Sr^{2+} (1.26 Å) when compared to that of 8 coordinate Ba^{2+} (1.42 Å) and also the previously mention atomic radii of 6 coordinate Li^+ (0.76 Å) being smaller in size in comparison to 6 coordinate Na^+ (1.02 Å).[166] Bond lengths are shorter than those for the $Ba_4Na(BO_3)_3$ and $Ba_4Na_{0.5}Li_{0.5}(BO_3)_3$ systems emphasising the main dependency on the Ba^{2+}/Sr^{2+} sites. Again, a more accurate structural analysis could be produced through the collection of neutron diffraction data.

5.3.3.2.2 Raman Spectroscopy

Figure 5.13 reports the presence of borate in the $SrBa_3Na_{0.5}Li_{0.5}(BO_3)_3$ system with the appearance of the expected v_1, v_3 and v_4 BO_3^{3-} vibrational modes[211] with the bands recorded for these being shifted in comparison to those seen in H_3BO_3 (***Table 5.8***).

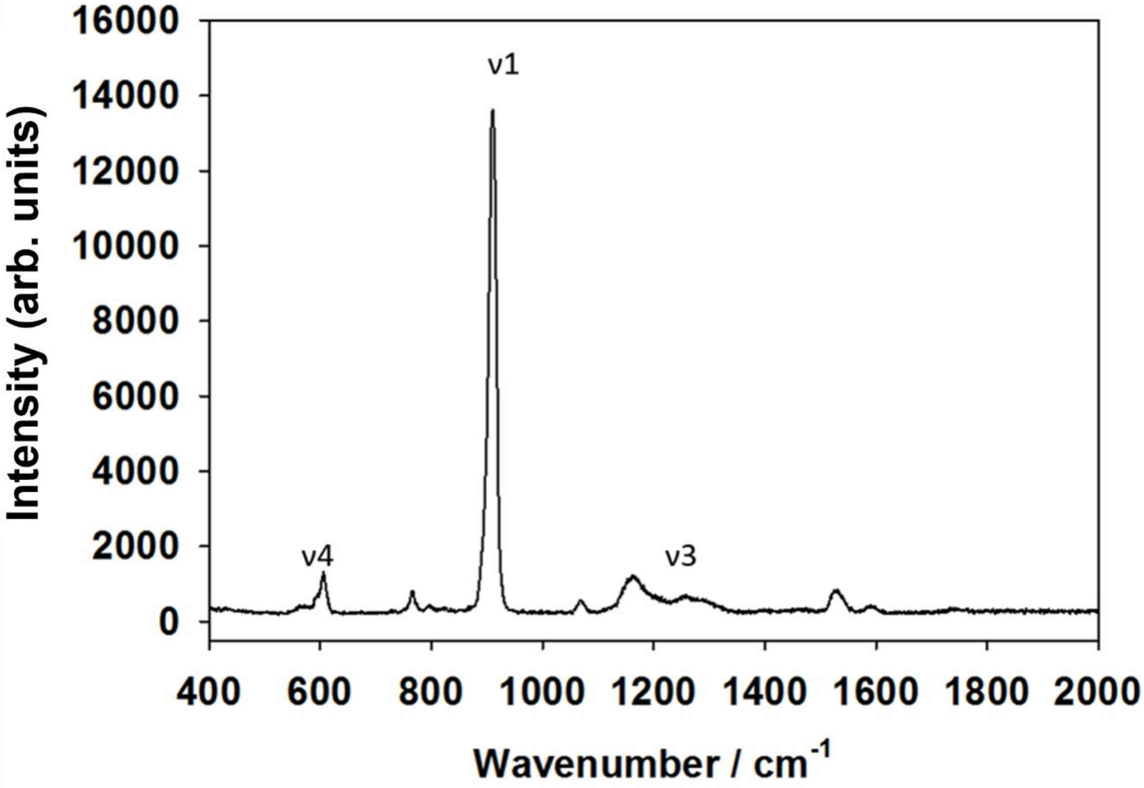

Figure 5.13 Raman spectroscopy data for $SrBa_3Na_{0.5}Li_{0.5}(BO_3)_3$ detailing specific Raman bands seen for BO_3^{3-} vibrational modes

Table 5.8 Raman band wavenumbers for BO_3^{3-} vibrational modes of H_3BO_3 and $SrBa_3Na_{0.5}Li_{0.5}(BO_3)_3$

System	**ν 1 /$^{-1}$**	**ν 3 /$^{-1}$ cm**	**ν 4 /$^{-1}$**
H_3BO_3	881.67	1168.06	500.09
$SrBa_3Na_{0.5}Li_{0.5}(BO_3)_3$	909.41	1151.24– 1353.21	562.76 605.68

The Raman spectrum for this system only shows one BO_3^{3-} v_1 vibration, this is most likely due to overlapping of multiple bands resulting from the random Ba^{2+}/Sr^{2+} substitution, as this likely leads to many more BO_3^{3-} environments, giving the appearance of one large band rather than the three seen for $Ba_4Na_{0.5}Li_{0.5}(BO_3)_3$. The Bands seen 1067.56 cm^{-1} can be attributed to diborate groups and the band ranges seen at 766.48 – 797.80 cm^{-1} and 1531.51 – 1590.20 cm^{-1} can be attributed to metaborate chains. [212] The presence of these extra Raman bands could suggest localised distortions in the overall structure or maybe from unidentified borate glass impurities.

5.3.3.3 $Sr_2Ba_2Na_{0.5}Li_{0.5}(BO_3)_3$

5.3.3.3.1 Rietveld Refinement using XRD Data

The Rietveld refinement of the structure using XRD data for the $Sr_2Ba_2Na_{0.5}Li_{0.5}(BO_3)_3$ system can be seen in ***Figure 5.14***, with structural data shown in ***Table 5.9*** and ***Table 5.10***.

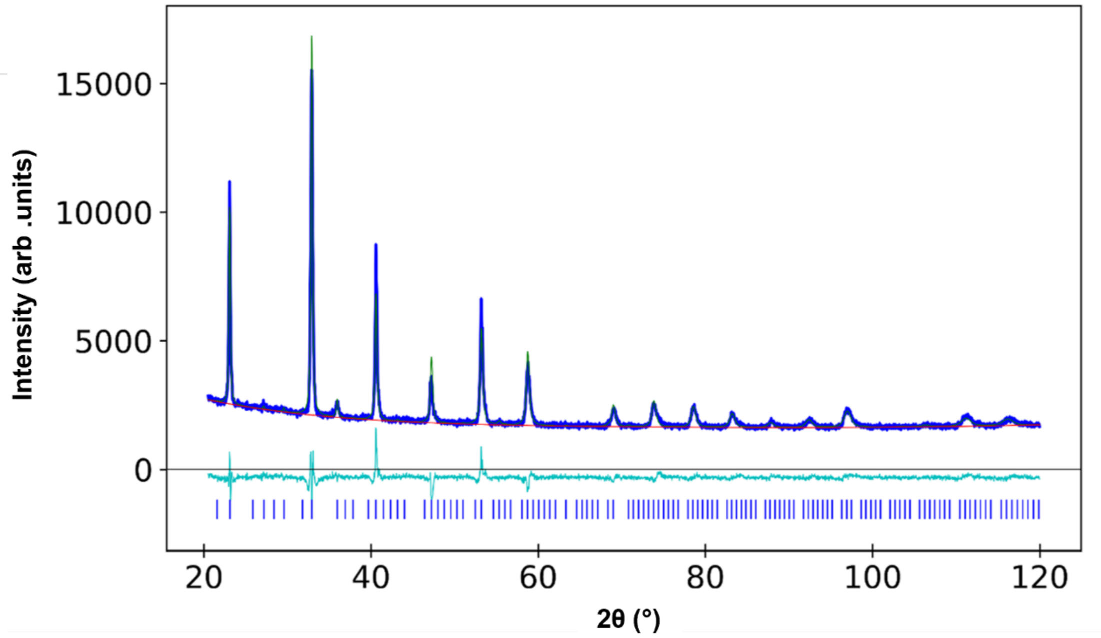

*Figure 5.14 Observed, calculated and difference x-ray diffraction profiles for $Sr_2Ba_2Na_{0.5}Li_{0.5}(BO_3)_3$
(Tick marks ï $Sr_2Ba_2Na_{0.5}Li_{0.5}(BO_3)_3$)*

Table 5.9 Structural information for $Sr_2Ba_2Na_{0.5}Li_{0.5}(BO_3)_3$

Atom	**x**	**y**	**z**	**Fraction**	**Wyckoff Position**	**U_{iso}**
Ba1	0.002(7)	0.002(7)	0.002(7)	0.500	32e	0.012(1)
Sr1	0.002(7)	0.002(7)	0.002(7)	0.500	32e	0.012(1)
Ba2	0.0	0.25	-0.001(1)	0.500	48f	0.012(1)
Sr2	0.0	0.25	-0.001(1)	0.500	48f	0.012(1)
Li	0.125	0.125	0.125	0.500	16b	0.012(1)
Na	0.125	0.125	0.125	0.500	16b	0.012(1)
B	0.110(1)	0.360(1)	0.125	1.000	48f	0.012(1)
O1	0.130(1)	0.278(1)	0.149(1)	1.000	96h	0.063(4)
O2	0.179(1)	0.429(1)	0.125	1.000	48f	0.063(4)

$R_{wp} = 4.60\%$ GOF = 2.07 ($Ia\bar{3}d$ $a = 15.4185(8)$ Å, Volume = 3665.46(54) $Å^3$)

Table 5.10 Selected interatomic distances of $Sr_2Ba_2Na_{0.5}Li_{0.5}(BO_3)_3$

Bond	**Bond Length / Å**	**Bond**	**Bond Length / Å**
Sr1/Ba1 – O1	2.609(1)	**Li/Na – O1**	2.256(1)
Sr2/Ba2 – O1	2.691(1)	**B – O1**	1.396(1)
Sr2/Ba2– O2	2.500(1)	**B – O2**	1.486(1)

Shifting of the Ba1 atomic site was negligible, with U_{iso} and relevant error values of the O1 and O2 sites becoming more stable suggesting a good insight that borate orientations within this system are similar to that of the starting model. Both unit cell parameter *a* and unit cell volume has decreased greatly in size when compared to the $Ba_4Na(BO_3)_3$ and $SrBa_3Na_{0.5}Li_{0.5}(BO_3)_3$ systems, which is expected due to the increased amount of Sr^{2+} when compared to Ba^{2+} and the previously mentioned Na^+/Li^+ substitution. Most bond lengths are shorter than that of the $Ba_4Na(BO_3)_3$ and

$SrBa_3Na_{0.5}Li_{0.5}(BO_3)_3$ with exception of the B – O bond lengths which could be attributed to the difficulty in determination of the B/O positions through refinement of XRD data. A more detailed and accurate structural analysis could be produced through the refinement of neutron diffraction data.

Peak broadening described earlier is prominently seen for the x = 2 and x =3 systems. As specified, an attempt to produce refinement using more than one sized system was trialled but ultimately was not fully successful. Transmission electron spectroscopy (TEM) would be required to help determine if these are made from more than one system or suffer from significant inhomogeneity.

5.3.3.3.2 Raman Spectroscopy

Raman data (***Figure 5.15***) details the presence of borate in the $Sr_2Ba_2Na_{0.5}Li_{0.5}(BO_3)_3$ system with the appearance of the expected v_1, v_3 and v_4 BO_3^{3-} vibrational modes[211] with the bands recorded for these being shifted in comparison to those seen in H_3BO_3 (***Table 5.11***).

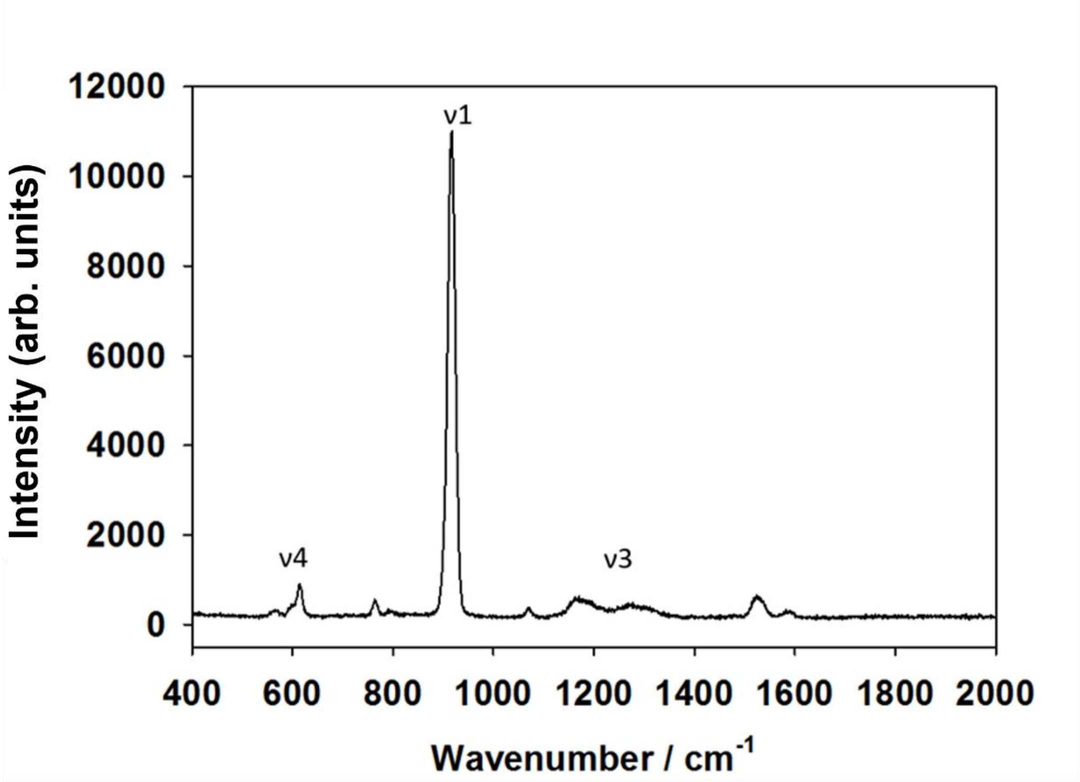

Figure 5.15 Raman spectroscopy data for $Sr_2Ba_2Na_{0.5}Li_{0.5}(BO_3)_3$ detailing specific Raman bands seen for BO_3^{3-} vibrational modes

Table 5.11 Raman band wavenumbers for BO_3^{3-} vibrational modes of H_3BO_3 and $Sr_2Ba_2Na_{0.5}Li_{0.5}(BO_3)_3$

System	**ν 1 /$^{-1}$**	**ν 3 /$^{-1}$ c m**	**ν 4 /$^{-1}$**
H_3BO_3	881.67	1168.06	500.09
$Sr_2Ba_2Na_{0.5}Li_{0.5}(BO_3)_3$	915.55	1136.37– 1321.41	564.91 614.23

The Raman spectrum for this system only shows one BO_3^{3-} v_1 vibration, this is most likely due to overlapping mentioned previously. The Bands seen 1068.56 cm^{-1} can be attributed to diborate groups and the band ranges seen at 764.80 – 792.96 cm^{-1} and 1527.04 – 1589.76 cm^{-1} can be attributed to metaborate chains. [212] The presence of these extra Raman bands could suggest localised distortions in the overall structure or maybe from unknown borate glass impurities.

5.3.3.4 $Sr_3BaNa_{0.5}Li_{0.5}(BO_3)_3$

5.3.3.4.1 Rietveld Refinement using XRD Data

The Rietveld refinement of the structure using XRD data for the $Sr_2Ba2Na_{0.5}Li_{0.5}(BO_3)_3$ system can be seen in ***Figure 5.16***, with structural data shown in ***Table 5.12*** and ***Table 5.13***.

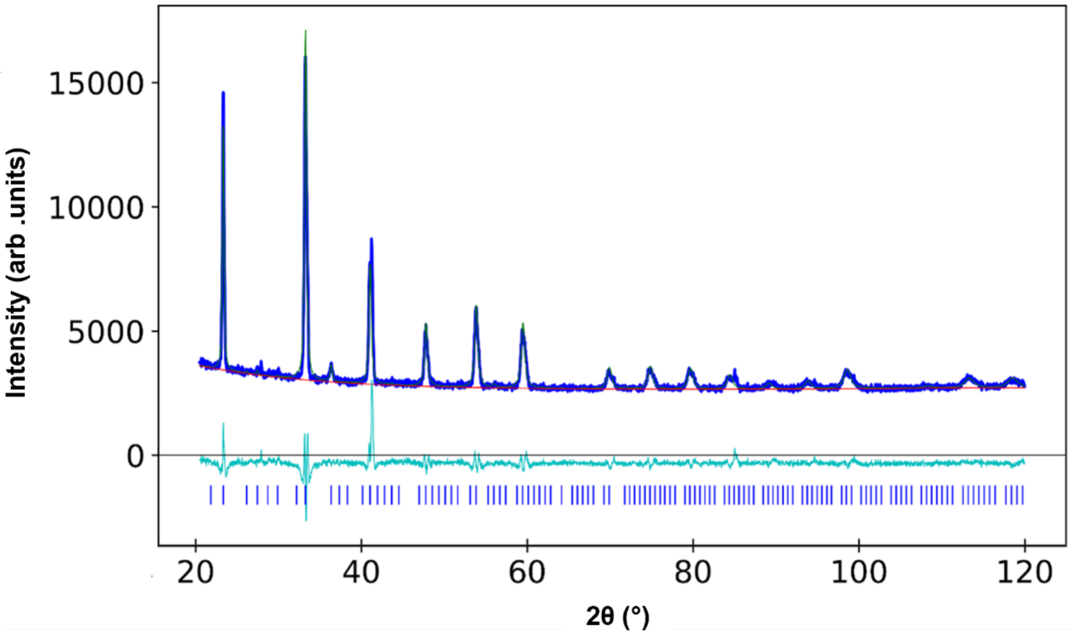

Figure 5.16 Observed, calculated and difference x-ray diffraction profiles for $Sr_3BaNa_{0.5}Li_{0.5}(BO_3)_3$
(Tick marks ï $Sr_3BaNa_{0.5}Li_{0.5}(BO_3)_3$)

Table 5.12 Structural information for $Sr_3BaNa_{0.5}Li_{0.5}(BO_3)_3$

Atom	**x**	**y**	**z**	**Fraction**	**Wyckoff Position**	**U_{iso}**
Ba1	0.007(4)	0.007(4)	0.007(4)	0.250	32e	0.004(2)
Sr1	0.007(4)	0.007(4)	0.007(4)	0.750	32e	0.004(2)
Ba2	0.0	0.25	-0.003(1)	0.250	48f	0.004(2)
Sr2	0.0	0.25	-0.003(1)	0.750	48f	0.004(2)
Li	0.125	0.125	0.125	0.500	16b	0.004(2)
Na	0.125	0.125	0.125	0.500	16b	0.004(2)
B	0.107(1)	0.357(1)	0.125	1.000	48f	0.004(2)
O1	0.128(1)	0.269(1)	0.145(2)	1.000	96h	0.012(7)
O2	0.178(1)	0.428(1)	0.125	1.000	48f	0.012(7)

R_{wp} = 4.81% GOF = 2.66 ($Ia\bar{3}d$ a = 15.2134(6) Å, Volume = 3521.10(41) Å^3)

Table 5.13 Selected interatomic distances of $Sr_3BaNa_{0.5}Li_{0.5}(BO_3)_3$

Bond	**Bond Length / Å**	**Bond**	**Bond Length / Å**
Sr1/Ba1 – O1	2.581(1)	**Li/Na – O1**	2.232(1)
Sr2/Ba2 – O1	2.666(1)	**B – O1**	1.381(1)
Sr2/Ba2– O2	2.485(1)	**B – O2**	1.470(1)

Shifting of the Ba1 atomic site was negligible, with U_{iso} and relevant error values of the O1 and O2 sites becoming more stable suggesting a good insight that borate orientations within this system are similar to that of the starting model. Both unit cell parameter *a* and unit cell volume has decreased greatly in size when compared to the $Ba_4Na(BO_3)_3$ and $Sr_2Ba_2Na_{0.5}Li_{0.5}(BO_3)_3$ systems, which is expected due to the reduced amount of Sr^{2+}/Ba^{2+} substitution and the previously mentioned Na^+/Li^+ substitution. Most bond lengths are shorter than that of the $Ba_4Na(BO_3)_3$ and

$Sr_2Ba_2Na_{0.5}Li_{0.5}(BO_3)_3$ with exception of the B – O bond lengths which could be attributed to the difficulty in determination of the B/O positions through refinement of XRD data. A more detailed and accurate structural analysis could be produced through the refinement of neutron diffraction data.

5.3.3.4.2 Raman Spectroscopy

Raman data (***Figure 5.17***) details the presence of borate in the $Sr_3BaNa_{0.5}Li_{0.5}(BO_3)_3$ system with the appearance of the expected v_1, v_3 and v_4 BO_3^{3-} vibrational modes[211] with the bands recorded for these being shifted in comparison to those seen in H_3BO_3 (***Table 5.14***).

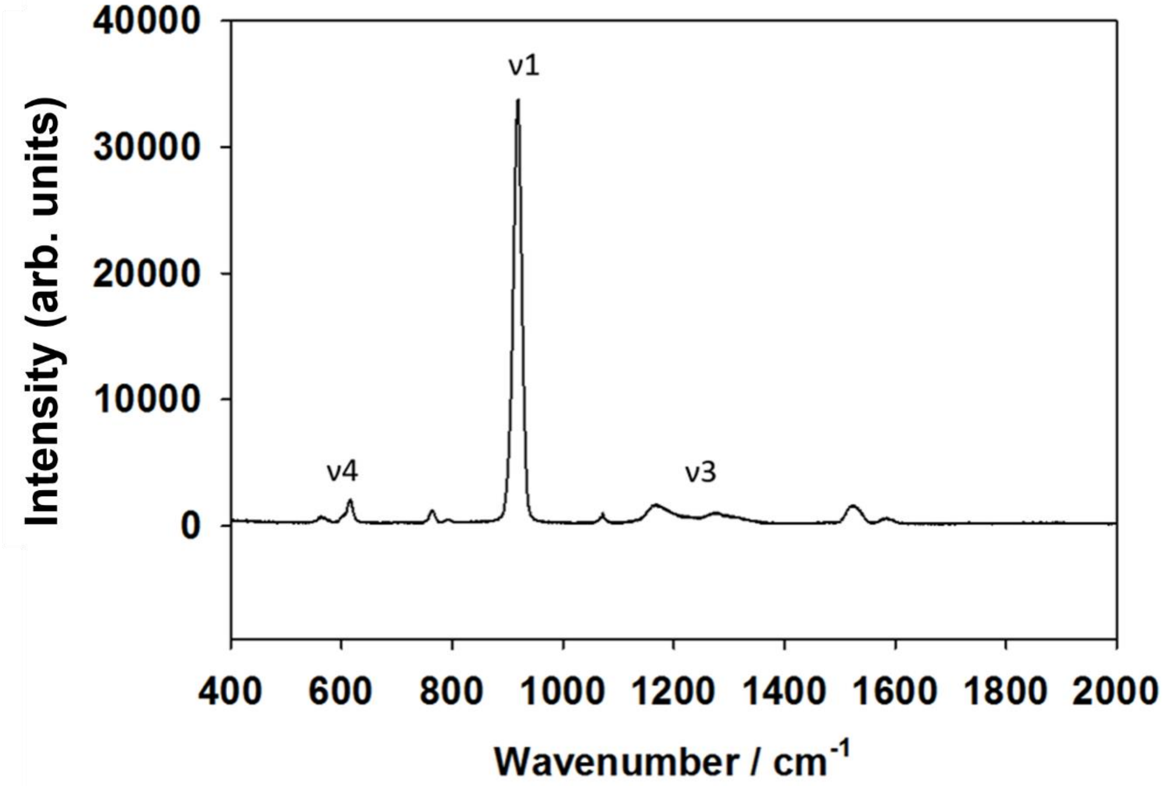

Figure 5.17 Raman spectroscopy data for $Sr_3BaNa_{0.5}Li_{0.5}(BO_3)_3$ detailing specific Raman bands seen for BO_3^{3-} vibrational modes

Table 5.14 Raman band wavenumbers for BO_3^{3-} vibrational modes of H_3BO_3 and $Sr_3BaNa_{0.5}Li_{0.5}(BO_3)_3$

System	ν 1 /$^{-1}$	ν 3 /$^{-1}$ cm	ν 4 /$^{-1}$
H_3BO_3	881.67	1168.06	500.09
$Sr_3BaNa_{0.5}Li_{0.5}(BO_3)_3$	918.63	1139.35– 1328.17	562.76 615.30

The Raman spectrum for this system only shows one BO_3^{3-} v_1 vibration, this is most likely due to overlapping of the multiple bands as mentioned previously. The Bands seen 1072.64 cm^{-1} can be attributed to diborate groups and the band ranges seen at 764.39 – 792.59 cm^{-1} and 1524.02 – 1584.64 cm^{-1} can be attributed to metaborate chains.[212] The presence of these extra Raman bands could suggest localised distortions in the overall structure or maybe from unknown borate glass impurities.

5.3.3.5 $Sr_4Na_{0.5}Li_{0.5}(BO_3)_3$

5.3.3.5.1 Rietveld Refinement using XRD Data

The Rietveld refinement of the structure using XRD data for the $Sr_2Ba2Na_{0.5}Li_{0.5}(BO_3)_3$ system can be seen in ***Figure 5.18***, with structural data shown in ***Table 5.15*** and ***Table 5.16***.

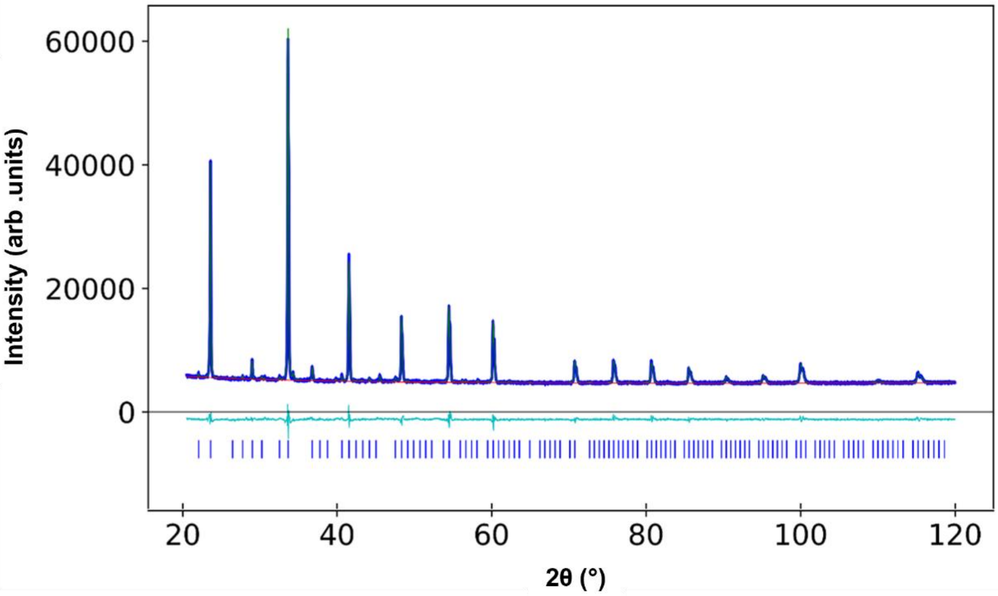

Figure 5.18 Observed, calculated and difference x-ray diffraction profiles for $Sr_4Na_{0.5}Li_{0.5}(BO_3)_3$
(Tick marks ï $Sr_4Na_{0.5}Li_{0.5}(BO_3)_3$*)*

Table 5.15 Structural information for $Sr_4Na_{0.5}Li_{0.5}(BO_3)_3$

Atom	**x**	**y**	**z**	**Fraction**	**Wyckoff Position**	**U_{iso}**
Sr1	-0.001(4)	-0.001(4)	-0.001(4)	0.500	32e	0.010(1)
Sr2	0	0.25	0.003(1)	1.000	48f	0.010(1)
Li	0.125	0.125	0.125	0.500	16b	0.010(1)
Na	0.125	0.125	0.125	0.500	16b	0.010(1)
B	0.109(1)	0.359(1)	0.125	1.000	48f	0.010(1)
O1	0.133(1)	0.270(1)	0.130(1)	1.000	96h	0.002(2)
O2	0.178(1)	0.428(1)	0.125	1.000	48f	0.002(2)

R_{wp} = 2.45% GOF = 1.79 ($Ia\bar{3}d$ a = 15.0292(4) Å, Volume = 3394.73(25) Å^3)

Table 5.16 Selected interatomic distances of $Sr_4Na_{0.5}Li_{0.5}(BO_3)_3$

Bond	Bond Length / Å	Bond	Bond Length / Å
Sr1/Ba1 – O1	2.552(1)	**Li/Na – O1**	2.207(1)
Sr2/Ba2 – O1	2.635(1)	**B – O1**	1.365(1)
Sr2/Ba2– O2	2.457(1)	**B – O2**	1.453(1)

Shifting of the Ba1 atomic site was negligible, with U_{iso} and relevant error values of the O1 and O2 sites becoming smaller than expected suggesting an issue in the determination of borate orientations within this system when compared to that of the starting model. Unit cell parameter *a* and unit cell volume of the system has decreased greatly in size when compared to the $Ba_4Na(BO_3)_3$ and $Sr_3BaNa_{0.5}Li_{0.5}(BO_3)_3$ systems, which is expected due to the reducing amount of Sr^{2+}/Ba^{2+} substitution and the previously mentioned Na^+/Li^+ substitution. Most bond lengths are shorter than that of the $Ba_4Na(BO_3)_3$ and $Sr_3BaNa_{0.5}Li_{0.5}(BO_3)_3$ with exception of the B – O bond lengths which could be attributed to the difficulty in determination of the B/O positions through refinement of XRD data. A more detailed and accurate structural analysis could be produced through the refinement of neutron diffraction data.

5.3.3.5.2 Raman Spectroscopy

Raman data (***Figure 5.19***) details the presence of borate in the $Sr_4Na_{0.5}Li_{0.5}(BO_3)_3$ system with the appearance of the expected v_1, v_3 and v_4 BO_3^{3-} vibrational modes[211] with the bands recorded for these being shifted in comparison to those seen in H_3BO_3 (***Table 5.17***).

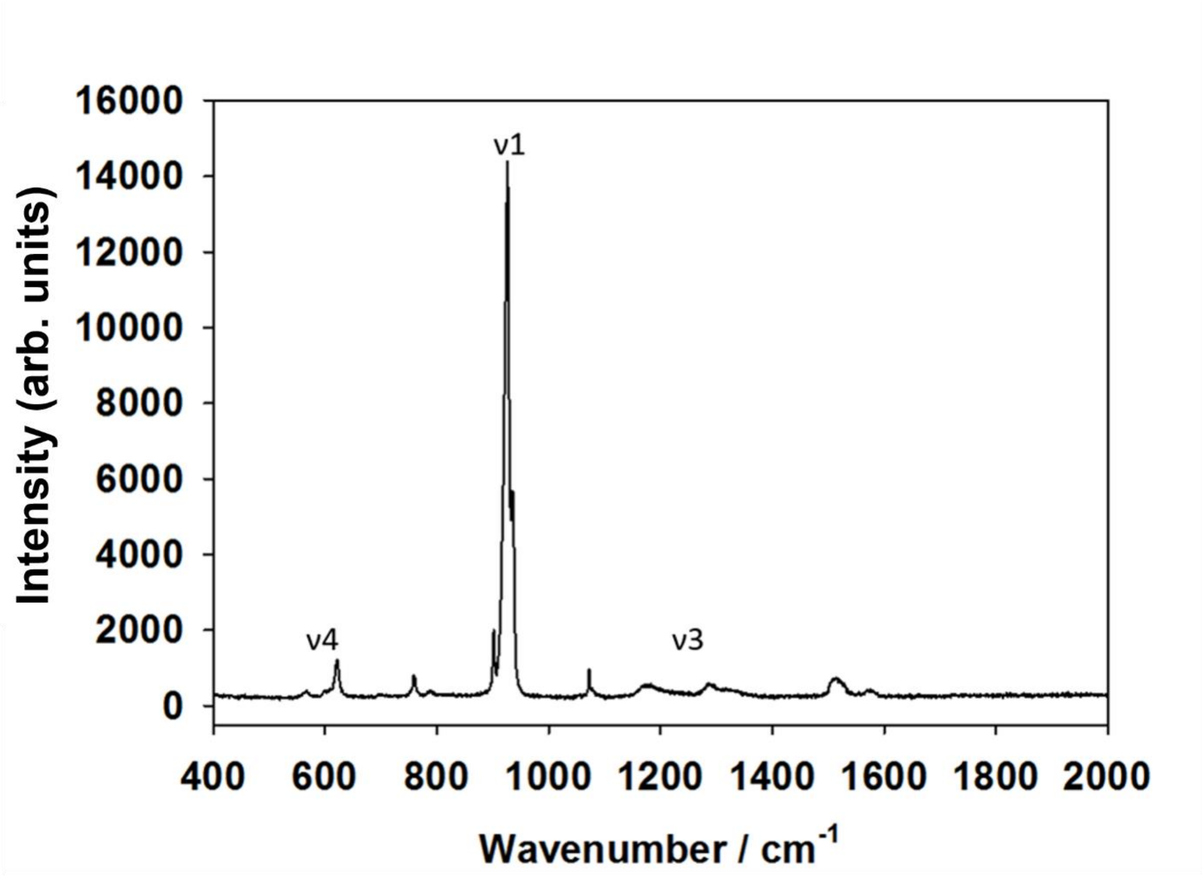

Figure 5.19 Raman spectroscopy data for $Sr_4Na_{0.5}Li_{0.5}(BO_3)_3$ detailing specific Raman bands seen for BO_3^{3-} vibrational modes

Table 5.17 Raman band wavenumbers for BO_3^{3-} vibrational modes of H_3BO_3 and $Sr_4Na_{0.5}Li_{0.5}(BO_3)_3$

System	ν 1 /$^{-1}$	ν 3 /$^{-1}$ cm	ν 4 /$^{-1}$
H_3BO_3	881.67	1168.06	500.09
$Sr_4Na_{0.5}Li_{0.5}(BO_3)_3$	902.23 925.79 934.99	1151.24– 1353.21	567.07 621.71

There are 3 distinctive borate v_1 bands suggesting three different BO_3^{3-} environments as previously mentioned when describing the Raman spectrum of $Ba_4Na_{0.5}Li_{0.5}(BO_3)_3$. The Bands seen 1072.57 cm^{-1} can be attributed to diborate groups and the band ranges seen at 759.15 – 788.42 cm^{-1} and 1515.02 – 1570.70 cm^{-1} can be attributed to metaborate chains.[212] The presence of these extra Raman bands could suggest localised distortions in the overall structure or maybe from unknown borate glass impurities.

5.3.3.6 Overall comparison of $Sr_{4-x}Ba_xNa_{1-y}Li_y(BO_3)_3$ systems

Refined unit cell parameters for the $Sr_{4-x}Ba_xNa_{1-y}Li_y(BO_3)_3$ series (x = 0, 1, 2, 3, 4)(y = 0, 0.5, 1) are given in ***Table 5.18.*** Larger errors seen for $SrBa_3Li(BO_3)_3$, $Sr_2Ba_2Li(BO_3)_3$ and $Sr_3BaLi(BO_3)_3$ samples can be attributed to the peak broadening.

Table 5.18 Refined cell parameters for $Sr_{4-x}Ba_xNa_{1-y}Li_y(BO_3)_3$

System	Unit Cell Parameter *a* / Å	Unit Cell Volume / Å^3
$Ba_4Na(BO_3)_3$	15.818(2)	3957.56(13)
$Ba_4Li_{0.5}Na_{0.5}(BO_3)_3$	15.776(1)	3926.10(4)
$SrBa_3Na(BO_3)_3$	15.647(2)	3830.45(12)
$SrBa_3Li_{0.5}Na_{0.5}(BO_3)_3$	15.572(4)	3776.29(27)
$SrBa_3Li(BO_3)_3$	15.499(20)	3722.85(192)
$Sr_2Ba_2Na(BO_3)_3$	15.480(7)	3709.23(51)
$Sr_2Ba_2Li_{0.5}Na_{0.5}(BO_3)_3$	15.419(8)	3665.46(54)
$Sr_2Ba_2Li(BO_3)_3$	15.301(17)	3581.89(117)
$Sr_3BaNa(BO_3)_3$	15.307(4)	3586.72(27)
$Sr_3BaLi_{0.5}Na_{0.5}(BO_3)_3$	15.213(6)	3521.10(41)
$Sr_3BaLi(BO_3)_3$	15.117(12)	3454.62(115)
$Sr_4Na(BO_3)_3$	15.142(1)	3471.56(8)
$Sr_4Li_{0.5}Na_{0.5}(BO_3)_3$	15.029(4)	3394.73(25)
$Sr_4Li(BO_3)_3$	14.958(1)	3346.73(7)

The unit cell volume was plotted against the value of x for each $Sr_{4-x}Ba_xNa_{1-y}Li_y(BO_3)_3$ series to visualise any correlation (***Figure 5.20***).

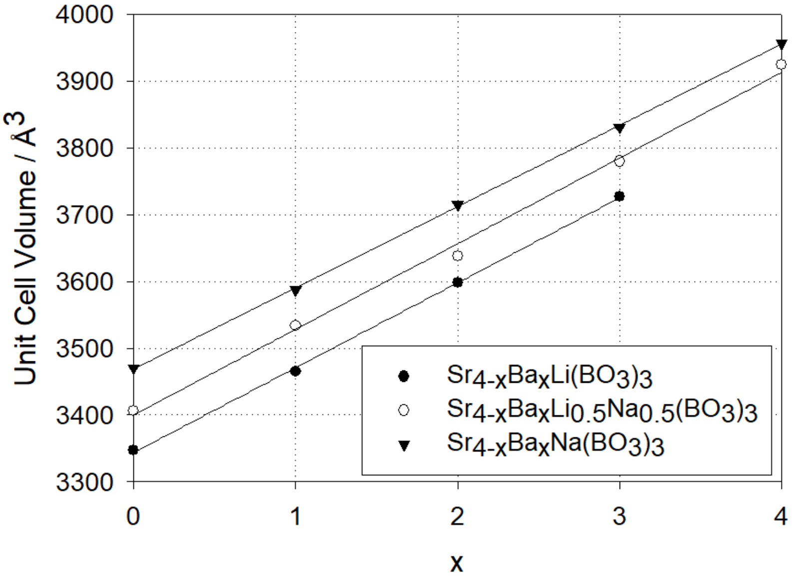

Figure 5.20 Variation in cell volume with Ba^{2+} content for $Sr_{4-x}Ba_x(Na/Li)(BO_3)_3$ (Error bars not included due to errors being smaller than the size of the data markers (the values of the errors are given in Table 18)

As expected, there is a positive linear correlation between increasing values of x and increases in the volume of the unit cell for all series which is due to the increasing amounts of the larger Ba^{2+} being introduced in place of the smaller Sr^{2+}.

5.3.4 Investigation into the potential to form isostructural $Sr_4Ca_xNa_{1-y}Li_{1-y}(BO_3)_3$

In an attempt to extend work on these ordered borate systems, a similar substitution method was utilised to synthesise isostructural Sr/Ca systems ($Sr_{4-x}Ca_xLi(BO_3)_3$ (x = 0, 1, 2, 3, 4) and $Sr_{4-x}Ca_xNa(BO_3)_3$ (x = 0, 1, 2, 3, 4).

5.3.4.1 $Sr_{4-x}Ca_xLi(BO_3)_3$

The $Sr_{4-x}Ca_xLi(BO_3)_3$ (x = 0, 1, 2, 3, 4) series was attempted and XRD data of the products was acquired (***Figure 5.21***).

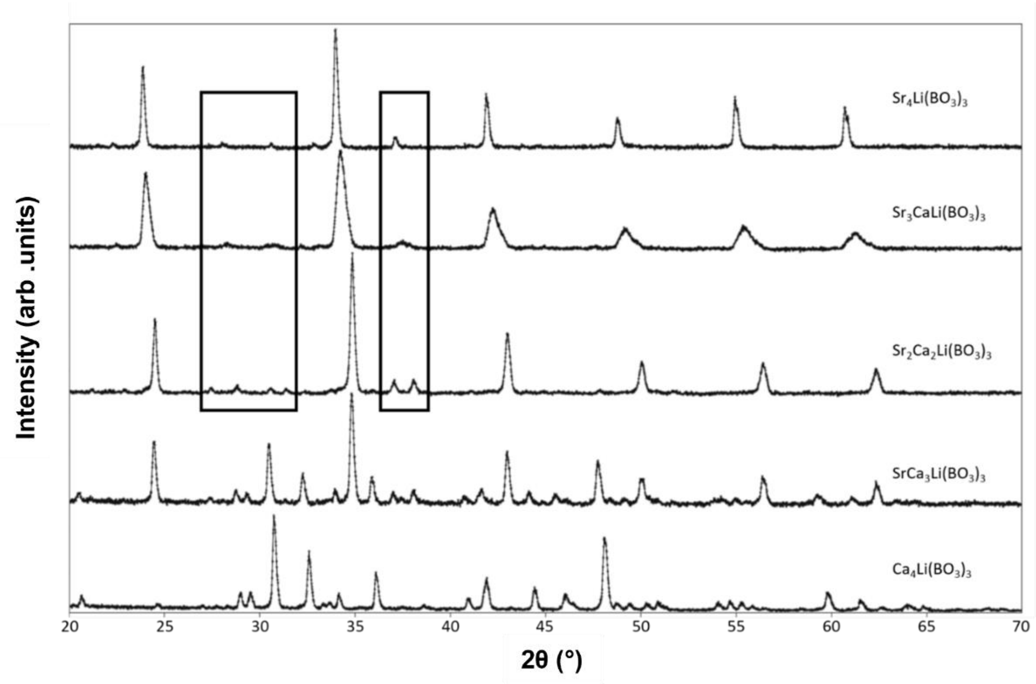

Figure 5.21 X-ray Diffraction Data of $Sr_{4-x}Ca_xLi(BO_3)_3$ (x = 0, 1, 2, 3, 4) showing successful substitution of Ca for xÒ2, wit regions where the main extra superstructure peaks are observed.

In the case of the $Sr_{4-x}Ca_xLi(BO_3)_3$ series of samples, significant impurities ($CaLiBO_3$ and $Ca_3(BO_3)_2$) were observed for x>2**,** with no sign of the perovskite-type phase for x=4. The lower Ca content samples (x≤2), however, showed the successful synthesis of the perovskite-type phase. For x=0, 1, the XRD patterns obtained were similar, with the expected peak shift to higher 2θ (smaller unit cell) on Ca incorporation. However, anisotropic broadening of these peaks was observed as for the Ba/Sr systems, which may indicate some inhomogeneity/difference in local cation ordering accompanying the substitution of Sr^{2+} by the smaller Ca^{2+} or indicate a miscibility gap as discussed earlier. Most interesting is the XRD pattern obtained for the x = 2 sample

($Sr_2Ca_2Li(BO_3)_3$) which does not suffer from this peak broadening suggesting a more ordered structure, but also shows the appearance of extra weak peaks. As these could not be assigned to potential impurities, we examined the possibility that these extra weak peaks could be related to Sr/Ca cation ordering given that there is an equal amount of both for this particular system, which will discussed later.

5.3.4.2 $Sr_{4-x}Ca_xNa(BO_3)_3$

While successful partial incorporation of Ca was observed for the series, $Sr_{4-x}Ca_xLi(BO_3)_3$, XRD data for the $Sr_{4-x}Ca_xNa(BO_3)_3$ series suggested negligible incorporation of Ca (***Figure 5.22***).

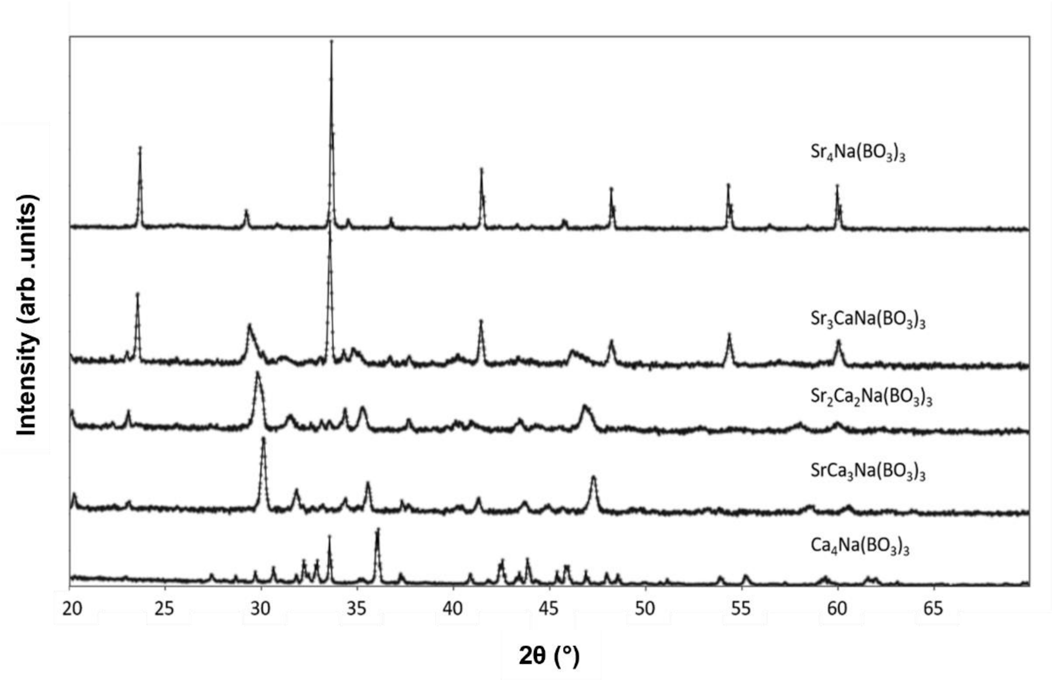

Figure 5.22 X-ray Diffraction Data of $Sr_{4-x}Ca_xNa(BO_3)_3$ (x = 0, 1, 2, 3, 4) showing unsuccessful substitution of Ca

Whilst the formation of the expected perovskite related phase was observed for x = 1, significant $Sr_3(BO_3)_2$/$Ca_3(BO_3)_2$ impurity was observed and there was no peak shift seen suggesting formation of undoped $Sr_4Na(BO_3)_3$.For the x = 2 sample, these impurities become more prominent, and the perovskite phase is no longer seen. Increasing to x = 3 makes a more crystalline $Sr_3(BO_3)_2$/$Ca_3(BO_3)_2$ phase with the maximum substitution value x = 4 forming the know $Ca_4Na(BO_3)_3$ phase crystallising in the space group *Ama*2.

5.3.4.3 $Sr_{4-x}Ca_xNa_{0.5}Li_{0.5}(BO_3)_3$

As for the initial investigation surrounding the $Sr_{4-x}Ba_xNa(BO_3)_3$ and $Sr_{4-x}Ba_xLi(BO_3)_3$ series, it was investigated whether a 1:1 Na^+:Li^+ mixture would be able to stabilise the perovskite like structure for $Sr_{4-x}Ca_xNa_{0.5}Li_{0.5}(BO_3)_3$ (***Figure 5.23***).

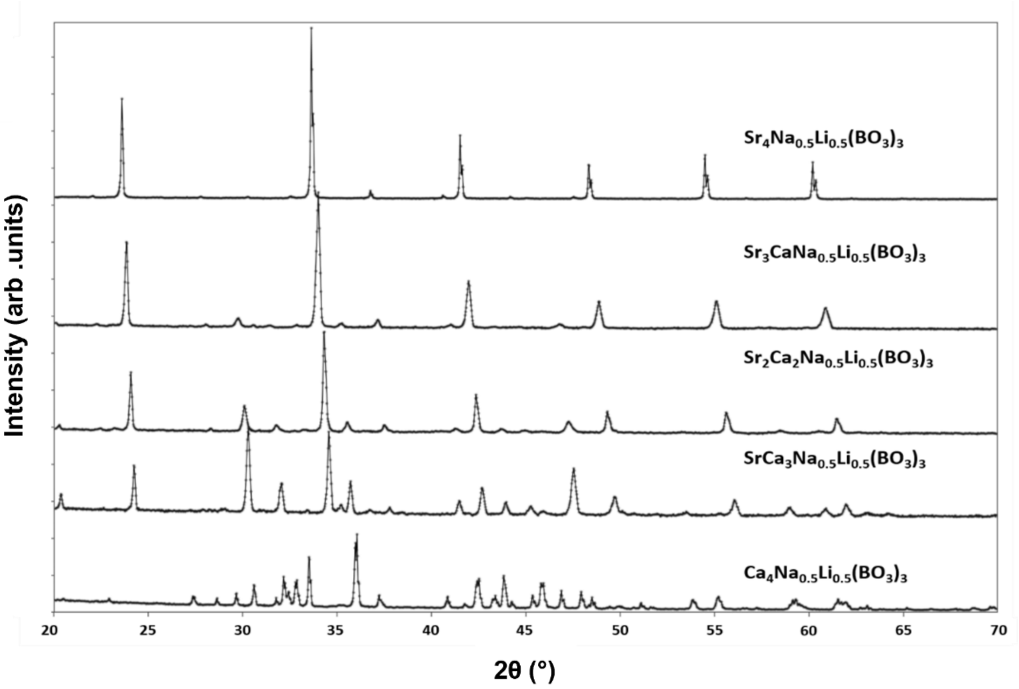

Figure 5.23 X-ray Diffraction Data of $Sr_{4-x}Ca_xNa_{0.5}Li_{0.5}(BO_3)_3$ (x = 0, 1, 2, 3, 4) showing the potentially unsuccessful substitution of Ca

However, even for low Ca levels, x = 1, impurities begin to appear which can be attributed to that of a $Sr_3(BO_3)_2$/$Ca_3(BO_3)_2$ mixed system, and these impurities become more prominent as the value of x increases. Impurity peaks up to x = 3 also show a shift to higher 2θ as the mixed systems weighs more towards the $Ca_3(BO_3)_2$ system.

Unlike the $Sr_{4-x}Ca_xNa(BO_3)_3$ series, the perovskite type structure is seen in samples with x up to x = 3, however, such phases are impure. Also, when comparing cell parameters, those seen for the perovskite phase in the x =3 sample are quite similar to those seen for the $Sr_2Ca_2Li(BO_3)_3$ phase. For the highest value of x = 4 the only phase clearly seen is one like that of the already mentioned $Ca_4Na(BO_3)_3$ phase.

5.3.5 Structural Characterisation of the $Sr_2Ca_2Li(BO_3)_3$

5.3.5.1 Powder X-Ray Diffraction

With the x=2, $Sr_{4-x}Ca_xLi(BO_3)_3$ phase showing extra weak peaks suggesting additional ordering effect, a structural investigation and analysis was performed. The XRD pattern for the synthesised $Sr_2Ca_2Li(BO_3)_3$ system can be seen in ***Figure 5.24***. This system was formed through the solid state synthesis route.

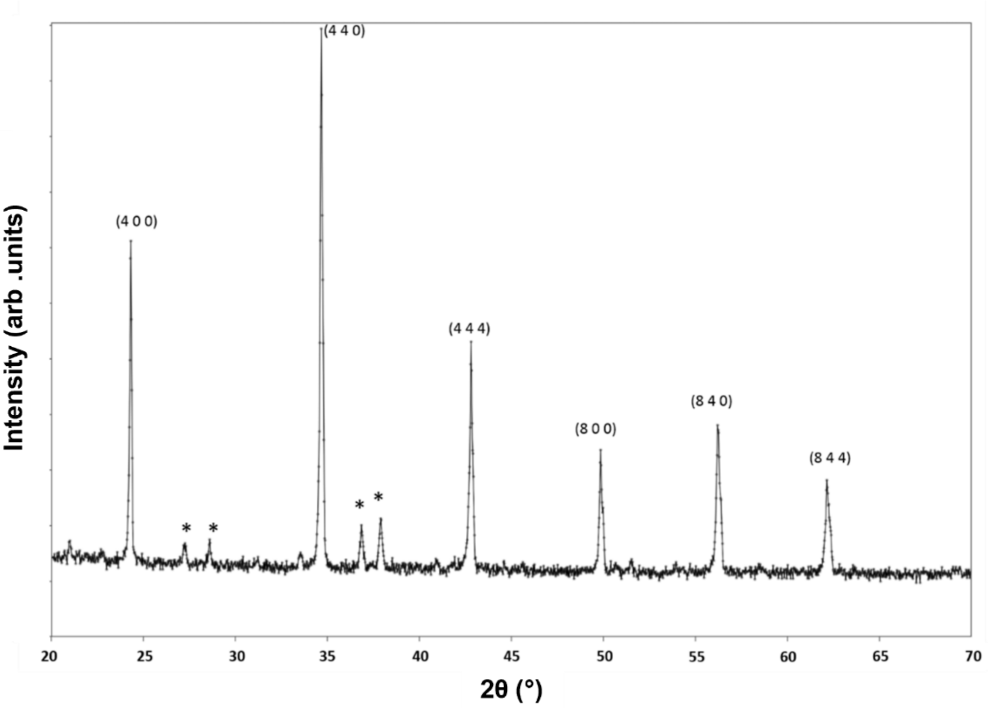

Figure 5.24 X-ray diffraction data for $Sr_2Ca_2Li(BO_3)_3$

5.3.5.2 Rietveld Refinement using XRD data

Possible Ca/Sr ordering models were examined to account for the extra weak peaks for the $Sr_2Ca_2Li(BO_3)_3$ sample, and through this investigation, it was found that the structure was best represented using the space group $Ia\bar{3}$ instead of $Ia\bar{3}d$ previously employed. The adoption of space group $Ia\bar{3}$ removes the *d* glide plane leading to a structure with four distinct Sr^{2+}/Ca^{2+} atom positions. These extra atom positions are pivotal in determining the correct ordering of the Sr^{2+}/Ca^{2+} and it was found that the ordering results in columns and rows of Ca^{2+} in each direction. The BO_3^{3-} and Li^+ ordering remains the same, with the orientation of the borate groups ensuring octahedral coordination for Li. (***Figure 5.25***)

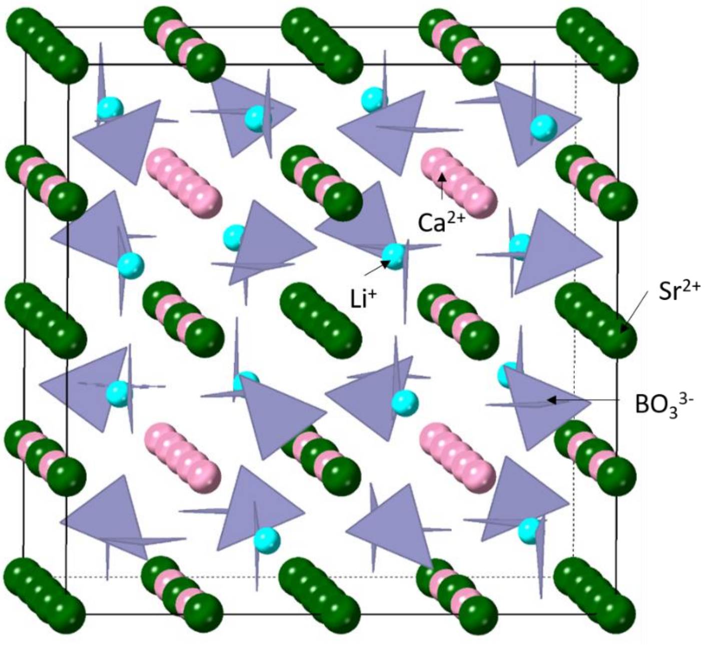

Figure 5.25 Structure of $Sr_2Ca_2Li(BO_3)_3$ illustrating the ordering of Ca and Sr Space Group: $Ia\bar{3}$

Due to fact that X-ray diffraction is not ideal for the determination of lighter elements, certain constraints and restraints were incorporated. This included fixing the Li site coordinates, a constrained generalised U_{iso} for all cations and anions respectively and constraining the fraction of the shared site to be equal to 1 (Ca2 + Sr3 = 1.00). Rietveld refinement of this structure using XRD data can be seen in ***Figure 5.26***, with the final structural information being given in ***Table 5.19***.

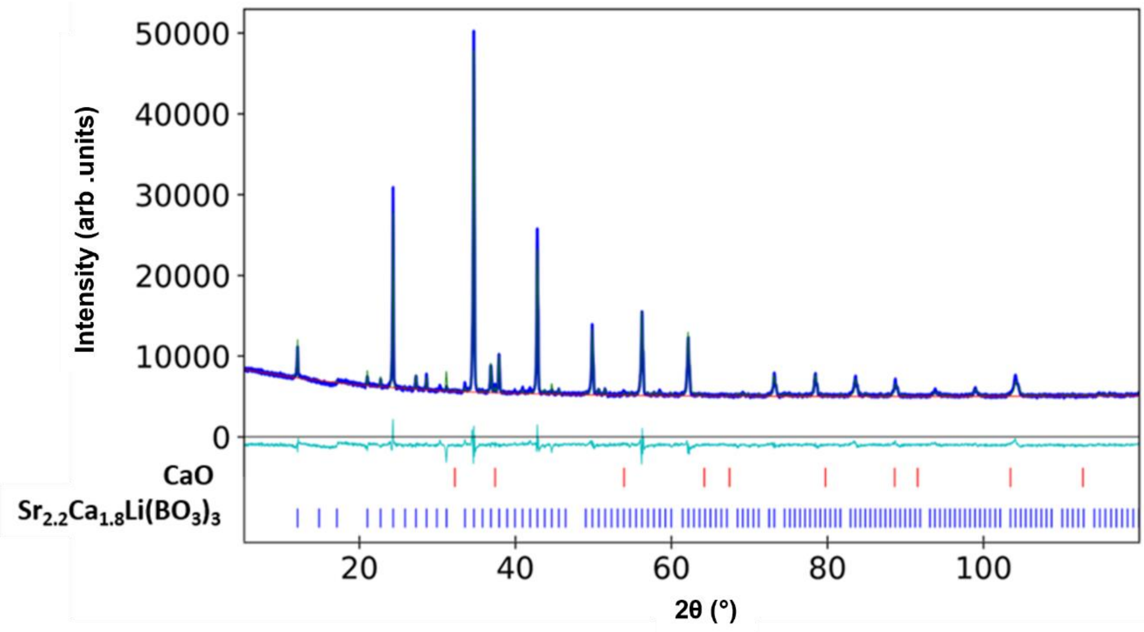

Figure 5.26 Observed, calculated and difference profiles for $Sr_{2.2}Ca_{1.8}Li(BO_3)_3$
Space Group : $Ia\bar{3}$
(top = CaO (1wt%), bottom = $Sr_{2.2}Ca_{1.8}Li(BO_3)_3$ *(99wt%))*
G.O.F = 2.41

Table 5.19 Structural information for $Sr_{2.2}Ca_{1.8}Li(BO_3)_3$

Atom	**x**	**y**	**z**	**Fraction**	**Wyckoff Position**	U_{iso}
Sr1	0	0	0.0000	1.000	8a	0.011(1)
Sr2	0	0.25	-0.011(1)	1.000	24d	0.011(1)
Sr3	0	0.25	0.245(2)	0.128(10)	24d	0.011(1)
Ca1	0.25	0.25	0.25	1.000	8b	0.011(1)
Ca2	0	0.25	0.245(2)	0.872(10)	24d	0.011(1)
Li	0.125	0.125	0.125	1.000	16c	0.011(1)

B	0.107(1)	0.361(1)	0.111(1)	1.000	48e	0.011(1)
O1	0.151(1)	0.276(1)	0.112(2)	1.000	48e	0.026(4)
O2	0.160(1)	0.443(1)	0.094(2)	1.000	48e	0.026(4)
O3	0.0124(8)	0.364(1)	0.132(1)	1.000	48e	0.026(4)

R_{wp} = 3.13% GOF = 2.41 ($Ia\bar{3}d$ a = 14.619(1) Å, Volume = 3124.32(11) Å^3)

The postulated structure was used for the Rietveld refinement of the $Sr_2Ca_2Li(BO_3)_3$ system providing a good fit (GOF : 2.41) to the data. However, during the refinement process there were still some peak intensity discrepancies**,** and so the occupancies of the Ca/Sr sites were allowed to vary. This subsequent refinement showed that one of the Ca sites had a higher value than expected, suggesting that there was some Sr present on this site. Thus, while there is Ca/Sr ordering, the composition was slightly Sr rich, with the refinement indicating a formula of $Sr_{2.2}Ca_{1.8}Li(BO_3)_3$, although there still appears to be some mismatch in peak intensities. The mismatch of peak intensity of the larger peaks may be partly attributed to constraints applied during the refinement process of the XRD data, whilst smaller peaks would be a combination of this and slight variations in the BO_3^{3-} orientations; as these peaks are very sensitive to slight changes in these. A more detailed neutron diffraction pattern would be useful in both of these instances allowing for an in depth analysis and so determine more accurate BO_3^{3-} orientations and individual atomic displacement parameters. The difference between the refined composition and expected composition can be explained by the presence of a slight CaO impurity (~1%).

5.3.5.3 Raman Spectroscopy Characterisation

The Raman spectrum for $Sr_{2.2}Ca_{1.8}Li(BO_3)_3$ (***Figure 5.27***) is similar to those seen for the $Sr_{4-x}Ba_xNa_{0.5}Li_{0.5}(BO_3)_3$ series,. The expected v_1, v_3 and v_4 vibrational modes of

BO_3^{3-} are seen[211] with the bands recorded for these being shifted in comparison to those seen in H_3BO_3 (***Table 5.20***).

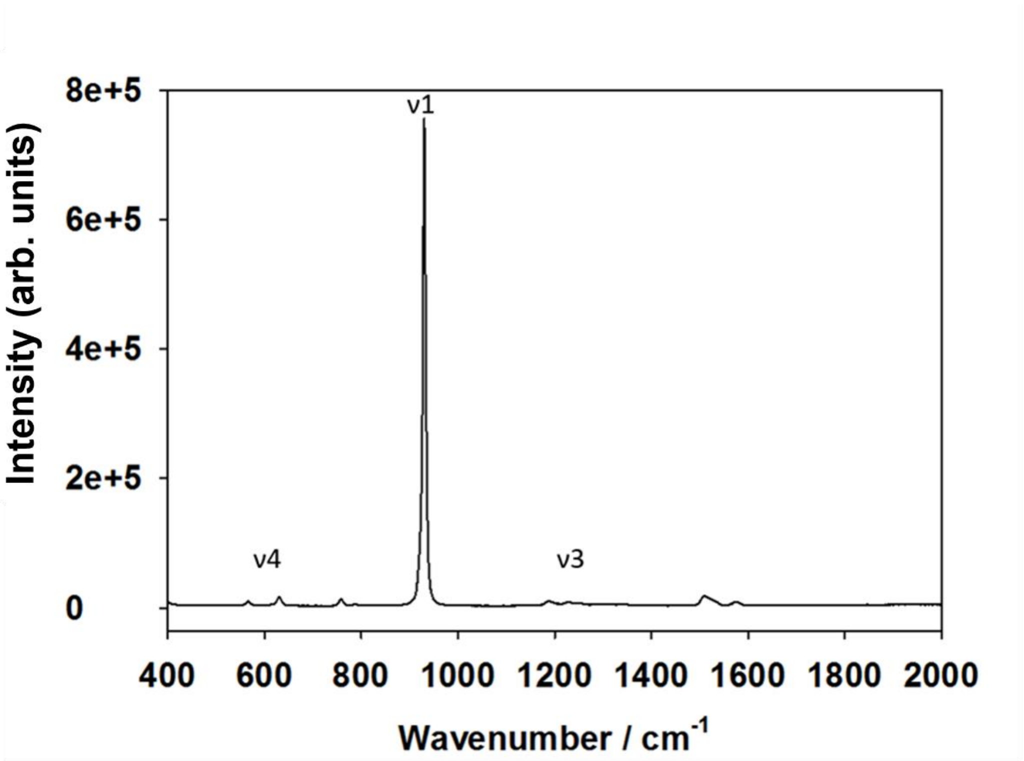

Figure 5.27 Raman spectroscopy data for $Sr_{2.2}Ca_{1.8}Li(BO_3)_3$ detailing specific Raman bands seen for BO_3^{3-} vibrational modes

Table 5.20 Raman band wavenumbers for BO_3^{3-} vibrational modes of H_3BO_3 and $Sr_{2.2}Ca_{1.8}Li(BO_3)_3$

System	**ν 1 /$^{-1}$**	**ν 3 /$^{-1}$ c m**	**ν 4 /$^{-1}$**
H_3BO_3	881.67	1168.06	500.09
$Sr_{2.2}Ca_{1.8}$ $Na_{0.5}Li_{0.5}(BO_3)_3$	930.21	1173.11– 1355.08	566.67 629.80

For this system only one BO_3^{3-} v_1 is seen, which has a greater sharpness compared to the mixed strontium/barium-sodium/lithium systems and can be correlated to the fact that LiO_6 octahedra are the only ones present in this system, and so each borate environment is expected to be equal (surrounded by 4 Sr^{2+}, 4 Ca^{2+} and 2 Li^{+}). Band ranges seen at 758.60 – 786.80 cm^{-1} and 1509.78 – 1576.05 cm^{-1} can be attributed to metaborate chains.[212] There is no sign of Raman bands seen attributed to diborate groups. The presence of these extra Raman bands could suggest localised distortions in the overall structure or maybe from unidentified borate glass impurities.

5.4 Conclusions

In this chapter it has been illustrated for the first time how the previously reported $Sr_{4-x}Ba_xNa(BO_3)_3$ series[194] can be described in terms of a perovskite type structure with ordering of Na and B on the smaller cation sites. Extended work in this area has shown the synthesis of a new solid solution series, $Sr_{4-x}Ba_xNa_{1-y}Li_y(BO_3)_3$ (y = 0.5).

In addition we show for the first time that Ca can be partially substituted onto the Sr site in $Sr_4Li(BO_3)_3$, with evidence that Sr/Ca ordering occurs for the composition $Sr_{2.2}Ca_{1.8}Li(BO_3)_3$ lowering the symmetry from $Ia\bar{3}d$ to $Ia\bar{3}$, but a more in depth structural analysis through neutron diffraction will allow for the determination of exact positions of lighter elements (Li, B, O).

These systems therefore add a further dimension to the wide range of materials which adopt a perovskite-type structure, where both systems can be seen as effectively heavily oxygen deficient compared to the archetypical perovskite through ordered oxygen vacancies, whilst all oxygen atoms are associated with the borate groups, thus resembling organic linker perovskites, such as $[C(NH_2)_3]Cu_xM_{1-x}(HCOO)_3$ (M = Mn, Zn, Mg).[209-210]

6. Further Investigations into the Possible Carbonate Incorporation of other materials

6.1 Introduction

As already outlined in the chapter 1, the incorporation of carbonate$^-$ has been seen in a range of materials such as: $Sr_2CuO_2CO_3$[89-91], $Ba_4YCu_{2+x}O_y(CO_3)_z$[95-98], $YBa_2Cu_3O_{7-x}$[109-110], $Ba_2Sc_{2-x}C_xO_{5+x/2}$[112-116], $Sr_4Fe_{3-x}(CO_3)_xO_{10-4x}$[213-220] and Hydroxyapatite structures[206-210]. Carbonate has also been shown to be incorporated into the $Ba_3Ln_2O_5CO_3$[191] and $Ba_2Co_{1-x}O_{4-\delta}$ presented in previous chapters. Throughout my studies many different systems were examined for possible carbonate incorporation.

Results presented in this chapter are just a few of these extra investigations. These include investigations to determine any possible stabilisation of low temperature phase transitions of anatase TiO_2 and the various phases of Nb_2O_5 through carbonate incorporation. Also reported is an investigation of the oxide ion conducting system $La_2Mo_2O_9$ to determine whether carbonate could be incorporated in place of tetrahedral Mo sites through a citrate Sol-Gel method, with the aim to try to stabilise its $P\,2_1\,3$ space group structure.

6.2 Experimental Procedure

Anatase study: Anatase (TiO_2, (Sigma-Aldrich 99.7%)) was heated at temperatures ranging from 200-1100°C at a heating rate of 10°C/min for 12hrs. Further investigations included the separate washing of anatase TiO_2 with 1M H_3NO_3 (Fischer) and 1M H_2SO_4 (Fischer) to remove any carbonate before heating at the determined transition temperature. Longer term washing experiments were also performed with the anatase soaked for 12hrs in solutions of 1M H_2SO_4 and Water whilst being stirred, which were then filtered dried and heated at the determined transition temperature. All resultant powder samples were reground and characterised.

Nb_2O_5 study: the low temperature (T) form of Nb_2O_5 (Sigma-Aldrich 99.99%) was used for all experiments. Powder samples were heated at varying temperatures (350-1000°C) at a heating rate of 10°C / min to observed the different phase transitions. The resultant powders were reground and characterised

$La_2Mo_2O_9$ study: A series of $La_2Mo_{2-x}O_{9-\delta}$ samples were prepared using the citrate Sol-Gel method. $La(NO_3)_3 \cdot xH_2O$ (Sigma-Aldrich 99.9%) and $(NH_4)_6Mo_7O_{24} \cdot 4H_2O$ (ACS Reagent 99.98%) were dissolved in water along with citric acid (Alfa Aesar ≥99%). Once sufficiently mixed, ethylene glycol (Fischer BioReagents™) was added whilst continuously stirring and heating the sample until a gel is formed. After an initial heat treatment at 500°C to burn off the organic component, the samples were then heated to 800°C at a rate of 10°C / min for 24hrs in air with an intermediate regrind. The resultant powders were also reground and characterised.

All Powder X-ray diffraction (XRD) analysis within this chapter were carried out using a PANalytical Empyrean X-Ray Diffractometer (Cu Kα radiation). Data were used to identify the phase and determine unit cell parameters, specifically for the $La_2Mo_{2-x}O_{9-\delta}$ series to assess possible carbonate incorporation.

Raman measurements of TiO_2 and the $La_2Mo_{2-x}O_{9-\delta}$ series of systems were performed using a Renishaw inVia Raman microscope using a 633 nm laser with 1% power, and 532 nm laser with 5% power respectively.

Thermogravimetric analysis with mass spectroscopy (TGA-MS) data were collected on a Netsch TGA-MS thermal analyser using an overall temperature range of 40° - 1300°C at a rate of 10°C/min under a dry N_2 atmosphere.

6.3 Results

6.3.1 Investigation of the Anatase to Rutile Phase Transition

6.3.1.1 Synthesis and XRD data analysis

Anatase TiO_2 is known to begin transitioning irreversibly into rutile phase at ~600°C[222-224] but this transition has also been reported to occur anywhere between 400-1200°C[225-231] As this transition is reported to generally occur at lower temperatures (600°C) an investigation was undertaken to determine if it is possible that CO_3^{2-} may be present which may help stabilise the anatase structure.

Anatase was heated at various temperatures to determine this anatase Ą rutile transition with XRD data recorded and patterns presented in ***Figure 6.1***.

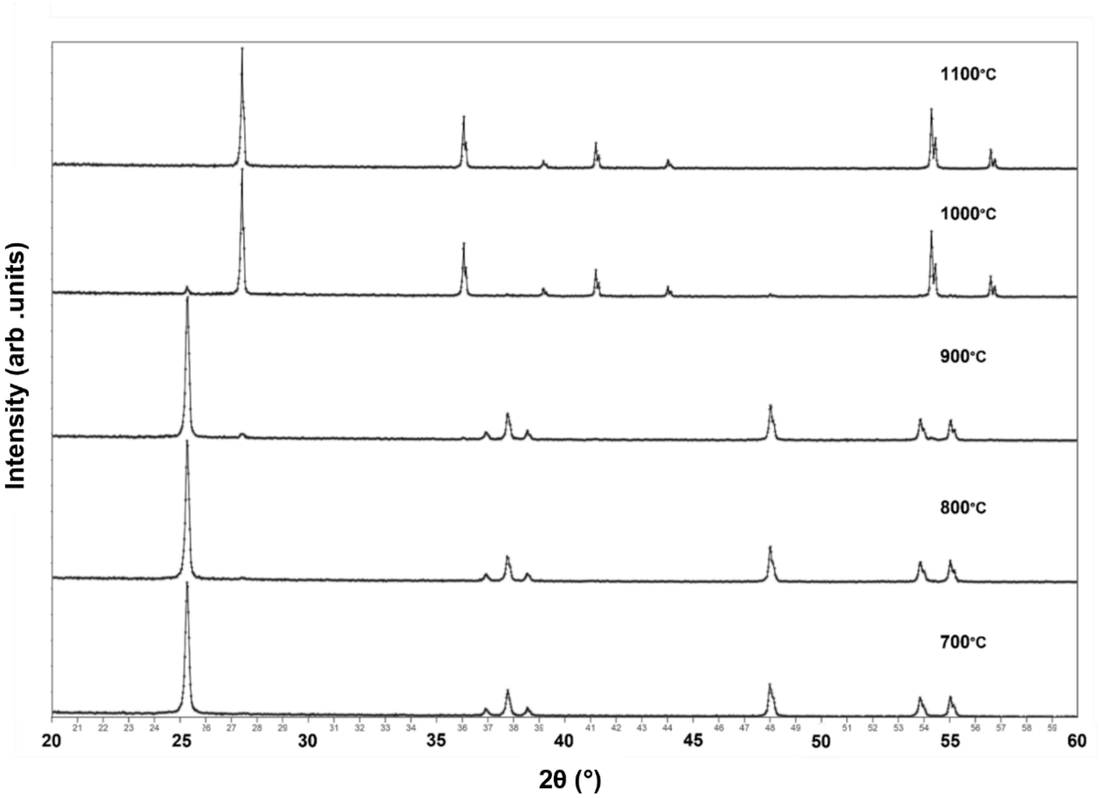

Figure 6.1 XRD patterns for Titanium(IV) oxide heated at increasing temperatures showing a major anatase Ą rutile phase transition between 900-1000°C.

This particular TiO_2 anatase reagent (Sigma Aldrich) appears to be stable up to 800°C with anatase being the only phase seen up to this temperature. At 900°C a small peak appears at ~27.5 2θ which can be attributed to the beginning of the anatase Ą rutile phase transformation. Increasing the heating temperature to 1000°C, leads to almost all anatase structured TiO_2 to have transformed to the rutile phase. When heated at 1100°C the full anatase Ą rutile coversion has occurred.

6.3.1.2 TGA-MS Study

To determine whether CO_3^{2-} may be incorporated into the anatase structure, a TGA-MS investigation was performed with data recorded between a 50-1000°C temperature range (***Figure 6.2***) for a fresh sample of anatase reagent.

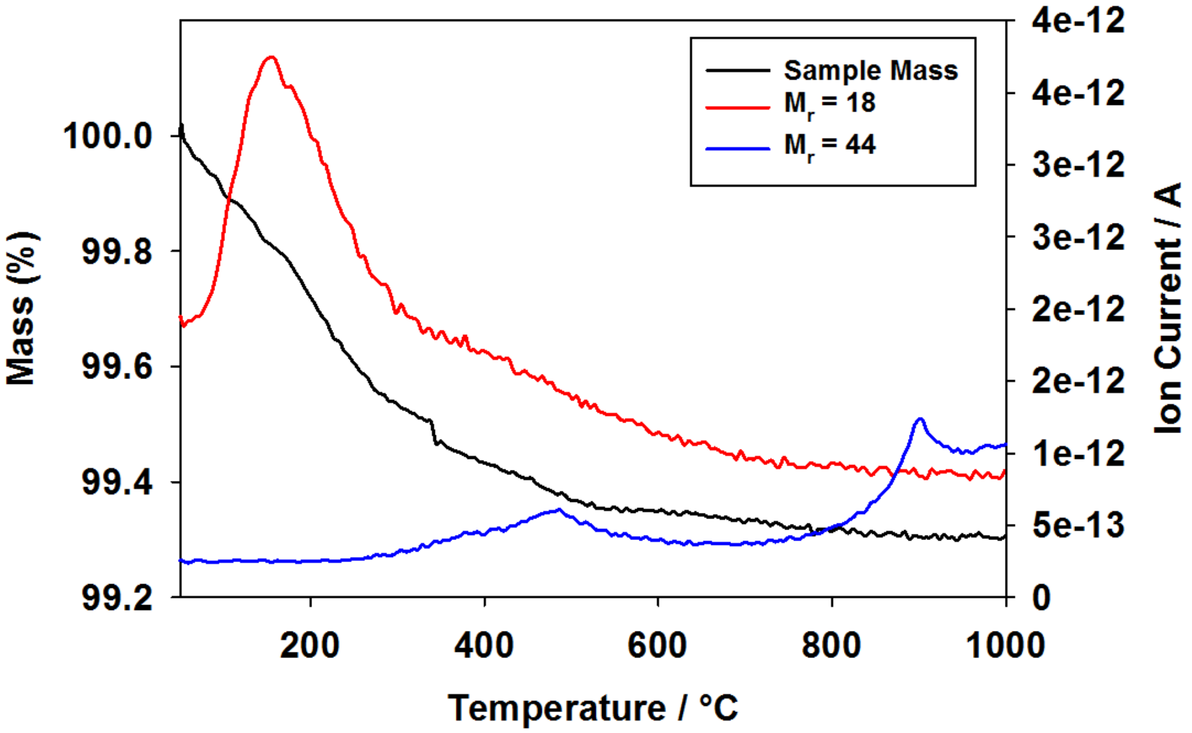

Figure 6.2 TGA-MS data for Titanium(IV) oxide showing water (Mr = 18) and CO2 (Mr = 44) losses, with CO2 loss is detected at phase transition temperatures.

Initial sample mass loss can be attributed to the loss of surface moisture, CO_2 appears to be released from the structure in two main ranges: 300-600°C and above 800°C. It is the latter range which is of interest as the CO_2 loss at these temperatures coincides with the anatase Ą rutile phase change of this sample. During this range of temperatures, the overall mass loss of the sample is only small, suggesting that although CO_3^{2-} may be present in the sample it is in very small amounts.

6.3.1.3 Raman Vibrational Spectroscopy Study

Continuing attempts to confirm the presence of CO_3^{2-} within the anatase structure, a Raman spectroscopy study was undertaken for TiO_2 samples heated at different temperatures (***Figure 6.3***).

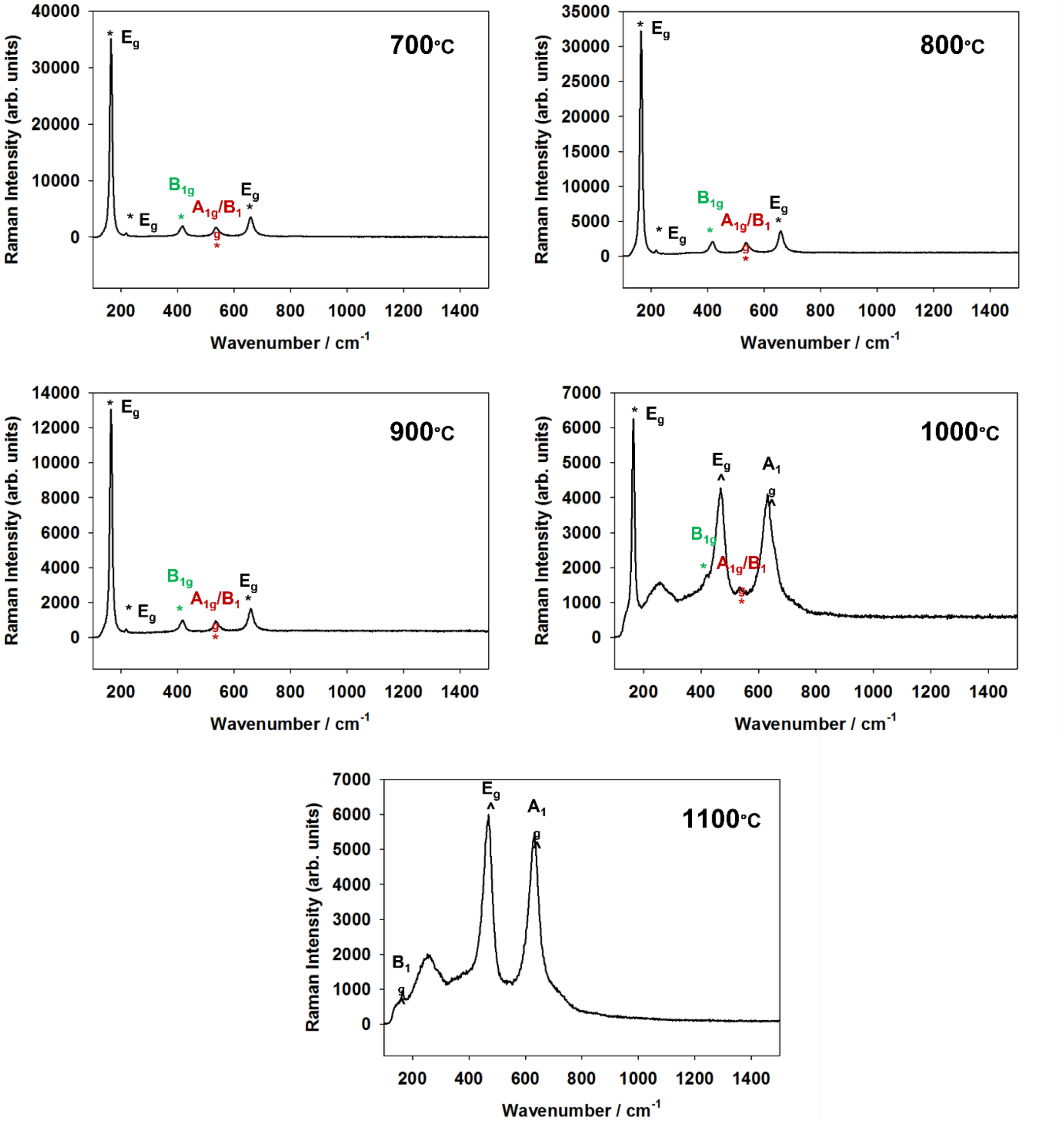

Figure 6.3 Raman spectra for Anatase reagent upon heating to different temperatures, illustrating vibrational modes associated with the anatase (*) and rutile (^) phases.

Using group theory, the anatase structure is characterized by the D_{4h} symmetry group and has six Raman active modes. These Raman active modes can be seen labelled in the spectra for the samples heated at 700°C, 800°C and 900°C, where in each case these bands are recorded at the same values (164 cm^{-1}, 218 cm^{-1}, 418 cm^{-1}, 536 cm^{-1}

and 659 cm^{-1}). From the XRD patterns, it would be expected to begin seeing vibrational bands for the rutile phase when the sample was heated to 900°C, however this does not seem to be case. Instead, bands associated with the Raman active modes of rutile become visible and prominent for the sample heated at 1000°C. Rutile can be characterized also by the D_{4h} symmetry group, however, only has four Raman active modes. As the sample heated at 1000°C is mixture of the anatase and rutile structures, Raman active modes of both can be determined. Those associated with anatase can be seen at the same values as previously mentioned (164 cm^{-1}, 418 cm^{-1}, 536 cm^{-1}), whilst those associated with rutile can be seen at 469 cm^{-1} and 631 cm^{-1}. The large band seen at 253 cm^{-1} is attributed to second order Raman scattering. The sample heated at 1100°C is expected to be purely rutile and Raman bands for this structure are seen at 163 cm^{-1}, 469 cm^{-1}, 631 cm^{-1}, again, with a large band due to second order Raman scattering.

For every heated sample, the Raman spectrum lacked the appearance of any vibrational modes associated with CO_3^{2-} (including focussed Raman studies on the 1000-1200 cm^{-1} region), providing no conclusive support that CO_3^{2-} is incorporated in the anatase structure. However, the lack of CO_3^{2-} bands could be due to the small amounts incorporated, such that it is not detectable through these investigation parameters.

6.3.1.4 Acid Stability Study

As carbonate materials react with acids liberating CO_2, the anatase reagent TiO_2 was initially washed with 1M solutions of HNO_3 and H_2SO_4 before being dried at 60°C and then heated at 900°C for 12hrs. XRD data were then recorded with patterns of the acid washed samples being compared with that of the normally heated sample (***Figure 6.4***)

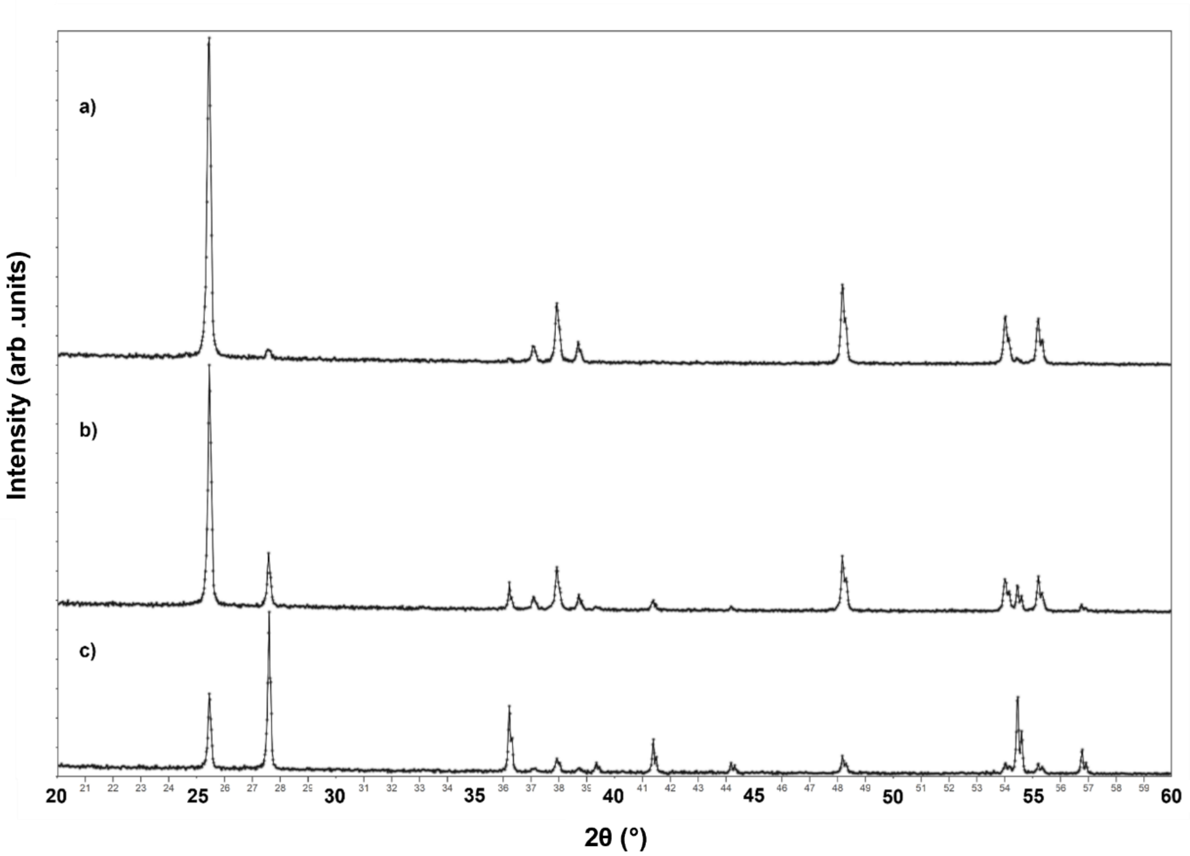

Figure 6.4 XRD patterns for anatase heated at 900°C
a) Reagent reference b) Washed with 1M HNO_3 *c) Washed with 1M* H_2SO_4

Use of acid washes results in more favourable formation of the rutile phase upon heating to 900°C. Of the two, washing with 1M H_2SO_4 shows the greatest conversion of anatase to rutile and so, further investigation was performed by soaking/stirring a sample of anatase overnight before the drying/heating processes. As a reference, a sample of anatase was also soaked/stirred in water overnight before the drying/heating processes. XRD data were recorded and are shown in ***Figure 6.5***.

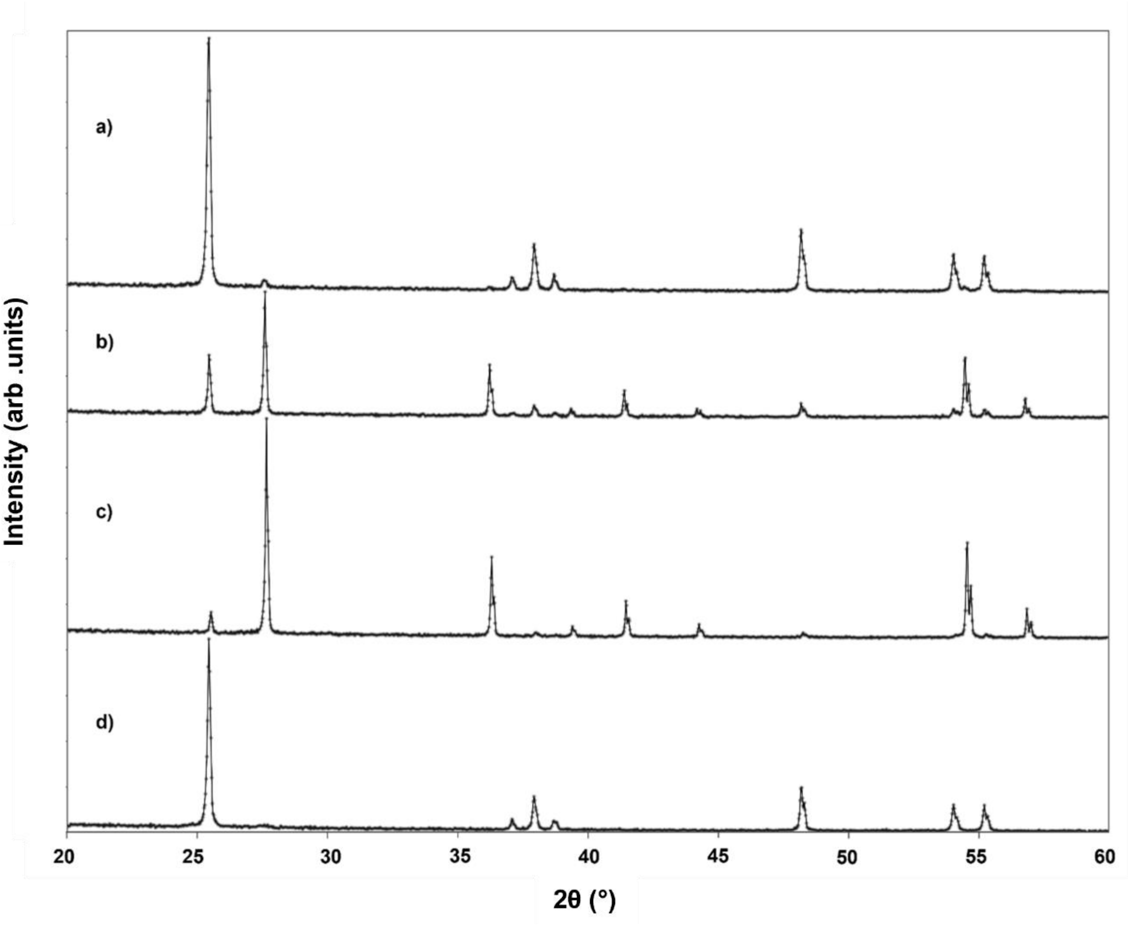

Figure 6.5 XRD patterns for anatase heated at 900°C
a) Reagent reference b) Washed with 1M H_2SO_4
c) Soaked for 12hrs in 1M H_2SO_4 d) Soaked for 24hrs in Water

Although the main focus is on the effect of the acid on the phase transition, it appears soaking the sample in water somewhat stabilises the anatase structure of this sample with less rutile phase being seen. Looking at the data, it is quite apparent that soaking the TiO_2 in 1M H_2SO_4 greatly favours the anatase → rutile transformation. Whilst this may provide some evidence to support the incorporation of CO_3^{2-} into the anatase structure, another theory suggested is that this favourable transition is brought about by the decomposition of a titanium oxysulphate intermediate. To determine if this indeed is the case, after initially drying the sample soaked in acid, XRD data were recorded (***Figure 6.6***)

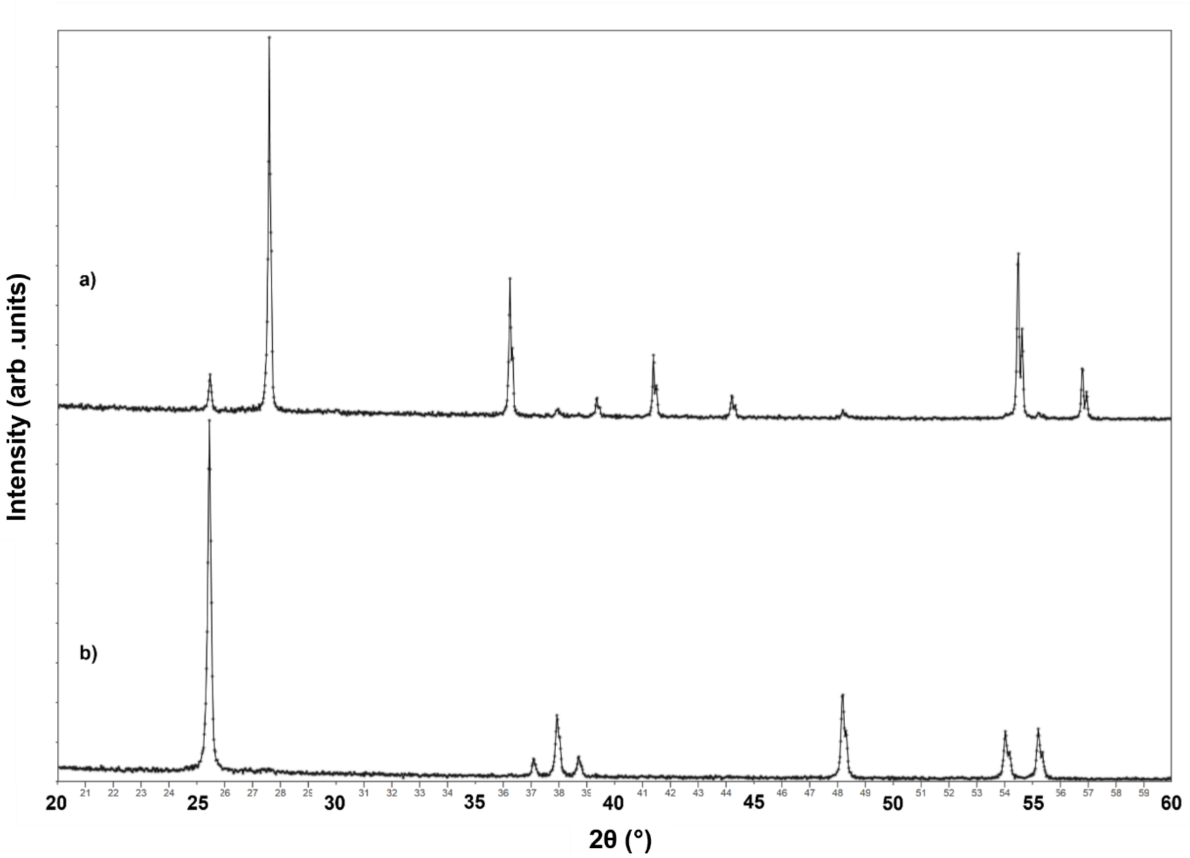

Figure 6.6 XRD patterns for anatase soaked in 1M H_2SO_4 for 12hrs
a) After 900°C heating b) Before 900°C heating, dried at 60°C for 12hrs

Drying the sample at 60°C shows that the anatase TiO_2 structure remains after being soaked in 1M H_2SO_4, meaning no major titanium oxysulphate intermediate is formed. However, this does not mean that sulphate may not be incorporated into the anatase structure.

Further investigation into this is required including Raman spectroscopy of the dried acid-soaked sample to determine any possible SO_4^{2-} incorporation of the anatase TiO_2 as well as XPS analysis to help understand any surface effects this acid soaking has upon the system, which may contribute to favouring the anatase Ą rutile transition.

6.3.2 Low Temperature Polymorph Transitions of Nb_2O_5

6.3.2.1 Synthesis and XRD data analysis

Since Nb_2O_5 was first studied, many investigations have shown that this system is known to have many different polymorphs.[232-234] With transitions noted at lower temperatures, a short investigation was implemented to determine whether CO_3^{2-} may play a role in the stabilisation of these lower temperature structures. Samples of Nb_2O_5 reagent (Sigma Aldrich) are heated to temperatures at which each polymorph is known under normal atmospheric conditions: TT–Nb_2O_5 (350°C), T-Nb_2O_5 (600°C), B-Nb_2O_5 (800°C), H-Nb_2O_5 (1000°C). Respective XRD data patterns for each temperature can be seen in ***Figure 6.7***.

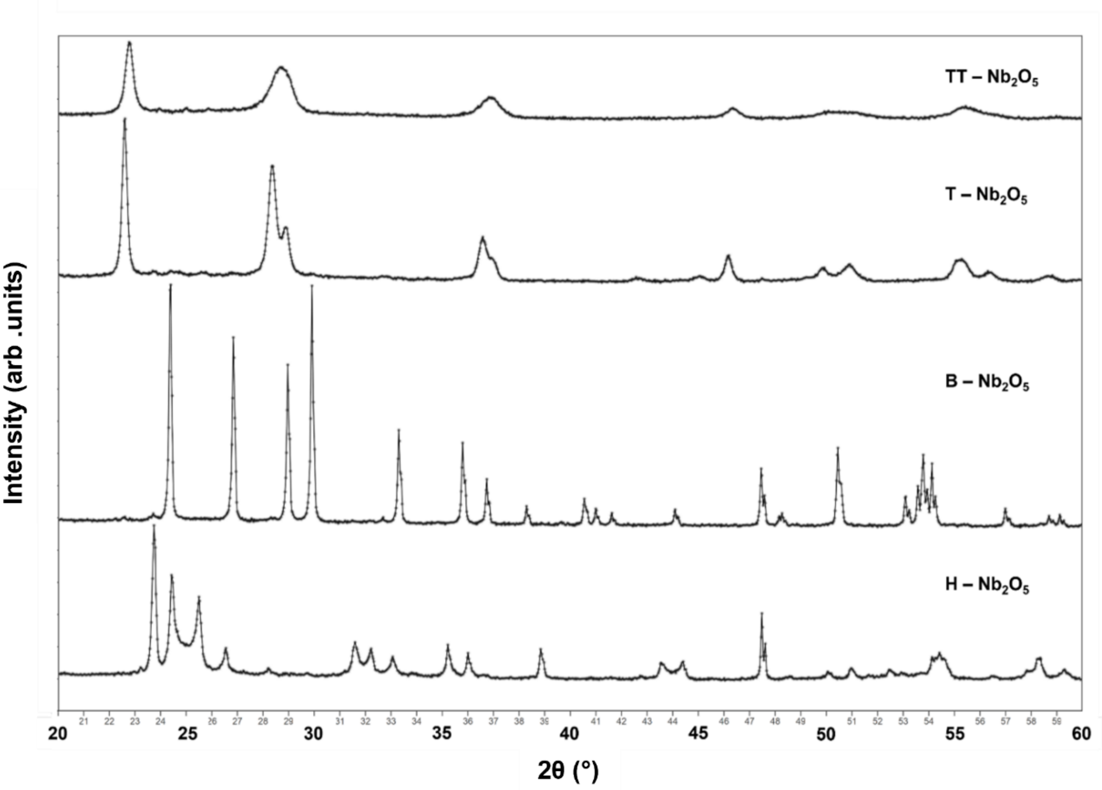

Figure 6.7 XRD patterns of Nb_2O_5 heated at various temperatures to form multiple polymorphs (TTï Nb_2O_5 (350°C), T-Nb_2O_5 (600°C), B-Nb_2O_5 (800°C), H-Nb_2O_5 (1000°C))

At 350°C, TT-Nb_2O_5 crystallises in a pseudohexagonal structure with the *P*6/*mmm* space group[233], with heating to 600°C leading to the formation of the T-Nb_2O_5 polymorph which is orthorhombic and has the *Pbam* space group.[233] The B-Nb_2O_5 polymorph is present when the sample is heated to 800°C[234], this polymorph is a tetragonal phase crystallising in the *I*4/*mmm* space group. Finally, when heated to 1000°C the H-Nb_2O_5 polymorph is seen[232], which is monoclinic (*P*12/*m*1 space group).

6.3.2.2 TGA-MS Study

Due to their low synthesis temperatures, a short TGA-MS study focussed on the TT-Nb_2O_5 and T-Nb_2O_5 polymorphs where both samples are heated to 1000°C to determine any possible CO_3^{2-} loss that may be stabilising these structures. Results from this investigation are shown in ***Figure 6.8***.

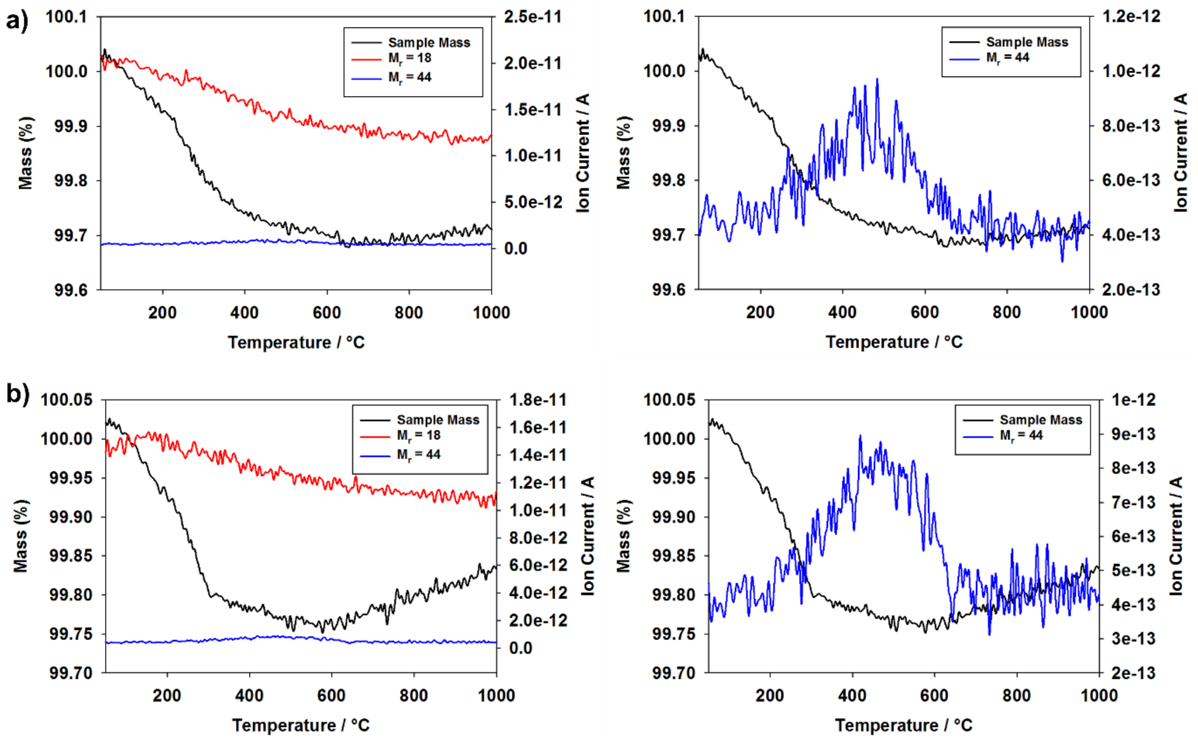

Figure 6.8 TGA-MS data for a) TT-Nb_2O_5 and b) T-Nb_2O_5 showing water (M_r = 18) and CO_2 (M_r = 44) losses (left), and focussed CO_2 losses (right).

On initial inspection of the TGA-MS results, there does appear to be a small mass loss with both starting polymorphs at lower temperatures which can be attributed to the loss of surface moisture. Closer inspection of the M_r = 44 MS lines shows a very small loss of CO_2 at temperatures ranging from 200-600°C which may provide support for the idea that small amounts of CO_3^{2-} may be incorporated into the lower temperature polymorphs of Nb_2O_5 providing some sort of stabilisation. This temperature range coincides with the transition from the pseudohexagonal TT-Nb_2O_5 to the orthorhombic T-Nb_2O_5 phase. No other CO_2 losses are recorded at higher transition temperatures suggesting that structural changes seen from T-Nb_2O_5 Ą B-Nb_2O_5 and B-Nb_2O_5 Ą H-Nb_2O_5 are not related to any possible CO_3^{2-} incorporation. Further investigation into these polymorphs is required with a focus on the TT-Nb_2O_5 Ą T-Nb_2O_5 transition.

6.3.3 Investigation into the stabilisation of $La_2Mo_{2-x}O_{9-\delta}$ by possible CO_3^{2-} incorporation

6.3.3.1 Synthesis and XRD data analysis

The $La_2Mo_2O_9$ system adopts a structure with the $P2_13$ space group and consists of one La^{3+} site, one Mo^{6+} site and three O^{2-} sites. Of these three O^{2-} site, two are known to be only partially occupied. These partial occupancies mean that Mo^{6+} has a general coordination 4.5 and so sits as a tetrahedral MoO_4 unit, with La^{3+} having a coordination of 10 forming a large polyhedral unit.[235] The general structure for $La_2Mo_2O_9$ is shown in ***Figure 6.9***, where only the tetrahedral MoO_4 bonds are kept for clarity.

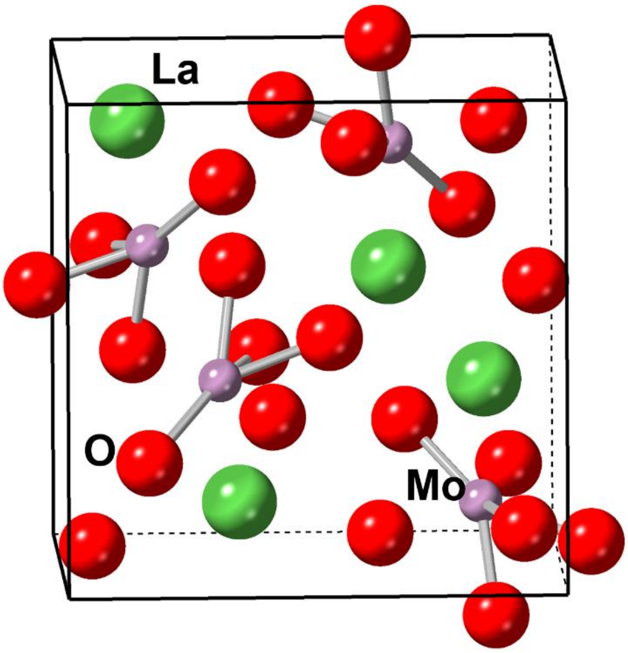

Figure 6.9 Structure of $La_2Mo_2O_9$ using the $P\ 2_1\ 3$ space group drawing attention to the MoO_4 tetrahedral units.

The idea behind this investigation is to determine whether lowering the Mo content would allow the incorporation of CO_3^{2-} onto the newly vacant MoO_4 tetrahedral sites using a citrate Sol-Gel synthesis technique.

A series of $La_2Mo_{2-x}O_{9-\delta}$ (x = 0, 0.10, 0.20, 0.30) systems were synthesised using a citrate Sol-Gel method, where samples were heated to 800°C for 24hrs with an intermediate regrind after 12hrs. The products were then analysed through XRD with their respective patterns are shown in ***Figure 6.10*****.**

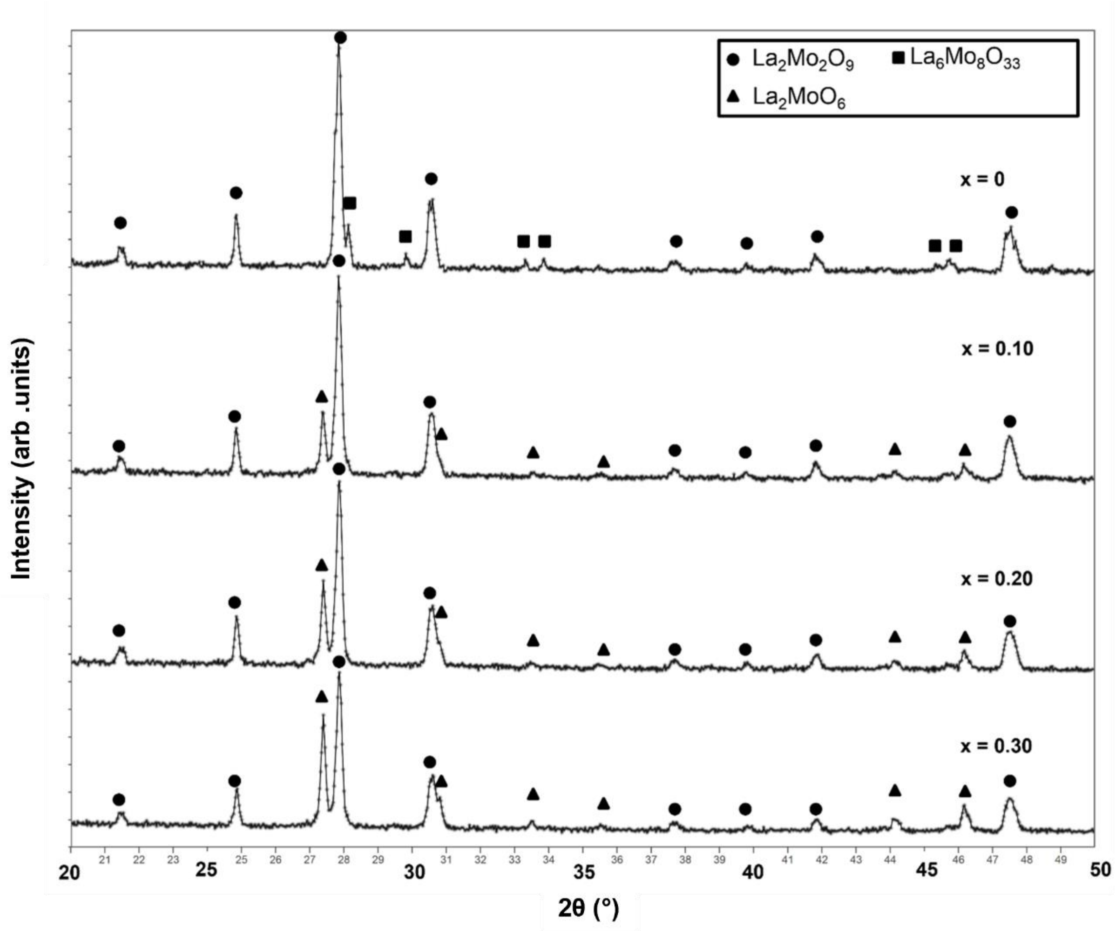

Figure 6.10 XRD patterns for the $La_2Mo_{2-x}O_{9-ŭ}$ (x = 0, 0.10, 0.20, 0.30) systems showing the formation of impurities on increasing Mo deficiency.

Using the Sol-gel synthesis route, the x = 0 system would be expected to be pure, however the existence of the impurity phase $La_6Mo_8O_{33}$ (14 wt%), suggested a greater excess amount of $La(NO_3)_3{\cdot}6H_2O$ is required for this method of synthesis (this may be related to the La reagent having a higher water content than expected). Upon increasing the value of x, the formation of the La_2MoO_6 impurity becomes apparent, with a larger wt% of this impurity being seen as x increases (x = 0.10 Ą 10 wt% La_2MoO_6, x = 0.20 Ą 19 wt% La_2MoO_6, x = 0.30 Ą 28 wt% La_2MoO_6). Despite the initial results suggesting that the $La_2Mo_{2-x}O_{9-\delta}$ structure had not successfully incorporate CO_3^{2-} into its structure, unit cell parameters were determined through initial refinements of the $La_2Mo_2O_9$ system (with each respective impurity included) and are shown in ***Table 6.1***.

Table 6.1 Unit cell parameters of the $La_2Mo_{2-x}O_{9-\text{ŭ}}$ (x = 0, 0.10, 0.20, 0.30) systems.

$La_2Mo_{2-x}O_{9-\delta}$	**Unit Cell Parameter / Å**	**Volume / $Å^3$**
X	***a***	
0.00	7.151(1)	365.751(40)
0.10	7.152(1)	365.807(37)
0.20	7.152(1)	365.764(35)
0.30	7.151(1)	365.710(37)

These show negligible change in cell parameters, supporting the original conclusion that no incorporation of CO_3^{2-} had occured. Instead any amount of Mo deficiency leads to the formation of the La_2MoO_6 impurity.

6.3.3.2 Raman Vibrational Spectroscopy Study

To confirm that there was no presence of carbonate in any of the impure $La_2Mo_{2-x}O_{9-\delta}$ systems, Raman spectroscopy data were collected. The spectra are shown in ***Figure 6.11***.

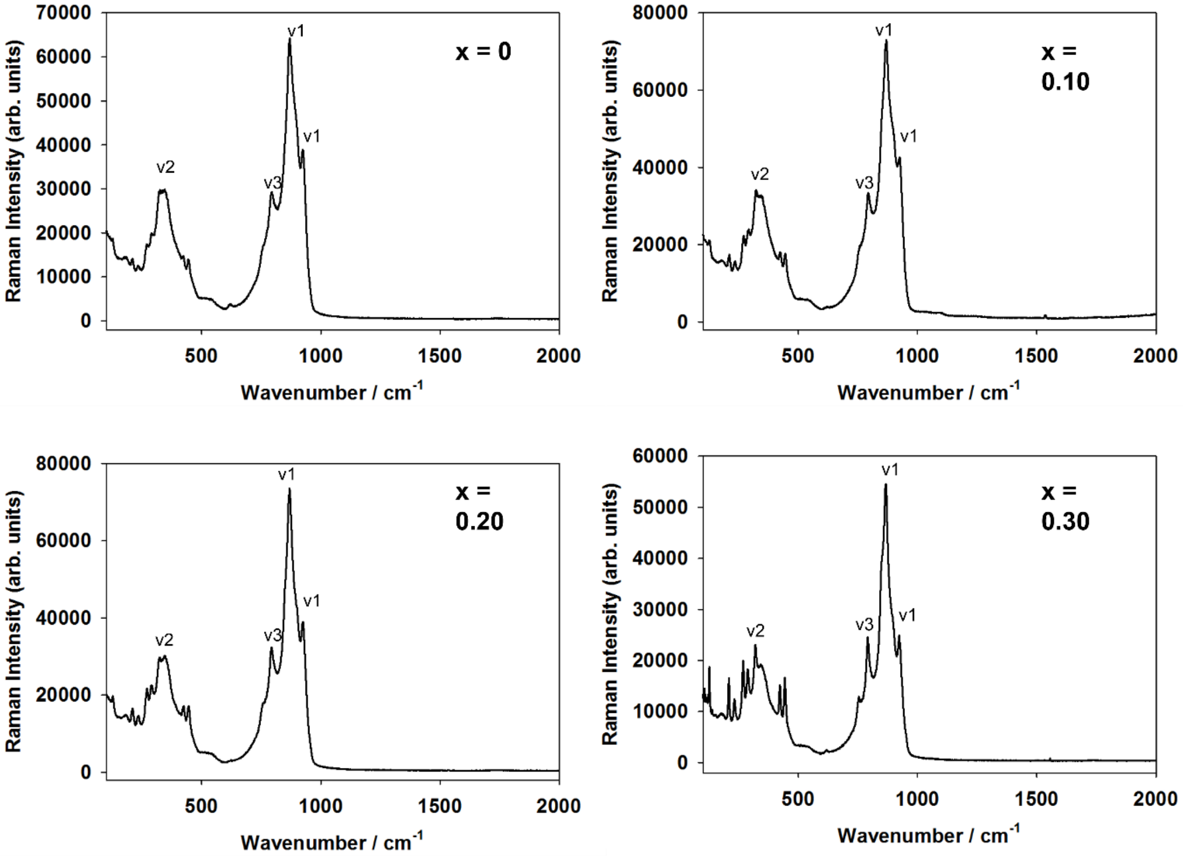

Figure 6.11 Raman spectra for the $La_2Mo_{2-x}O_{9-\breve{u}}$ series showing no signs of CO_3^{2-} and MoO_4 vibrational modes labelled.

Inspection of each Raman spectrum shows a distinct absence of any expected Raman active vibrational modes associated with the presence of CO_3^{2-}, supporting the inability to incorporate CO_3^{2-} into the $La_2Mo_{2-x}O_{9-\delta}$ systems. Significant Raman bands detected can be attributed to tetrahedral MoO_4 Raman active vibrational modes. In each spectrum, two bands seen at ~870 cm^{-1} and ~920 cm^{-1} are due to the v_1 mode (symmetric stretch) of the MoO_4 tetrahedral unit, a band seen at ~790 cm^{-1} is due to the v_3 mode (asymmetric stretch) of the MoO_4 tetrahedral unit, and the most prominent band determined at ~340 cm^{-1} is assigned to the v_2 mode (bending) of the MoO_4 tetrahedral unit.[236-238]

6.4 Conclusions

Whilst these are just a few of the other systems investigated for the incorporation of CO_3^{2-}, it is important to note the possibility that this incorporation may be present in reagent materials, however in small amounts. TGA-MS of anatase shows CO_2 loss at temperatures this specific reagent undergoes the anatase Ą rutile phase transition. However no Raman modes due to carbonate were visible. The same CO_2 mass loss can also be noted for the Nb_2O_5 pseudohexagonal Ą orthorhombic phase transition. Results suggested that attempts to incorporate carbonate into $La_2Mo_2O_9$ were unsuccessful, with increasing formation of La_2MoO_6 impurity seen in XRD data for the $La_2Mo_{2-x}O_{9-\delta}$ series, coupled with the lack CO_3^{2-} Raman modes.

Acid washing studies of the anatase TiO_2 shows that this treatment helps to favour the anatase Ą rutile transition at lower temperature. While this may be a possible sign of the removal of CO_3^{2-} from the structure, it must be noted that other trace metals in the reagent which could also be stabilising the anatase structure may be washed away during this investigation. Further studies are required to confirm the presence of carbonate in these materials.

7. Conclusions and Further Work

7.1 Conclusions

The work presented in this thesis has shown the successful incorporation of carbonate into several systems, new and already known, with the aim of assessing the potential that carbonate may play an important role in the stabilisation of lower temperature phases of certain oxide reagents.

A new layered perovskite $Ba_3Yb_2O_5CO_3$ system was discovered through solid state synthesis when heated in air at 1000°C, with Raman spectroscopy confirming the successful incorporation of carbonate into this structure. Rietveld refinement using neutron diffraction data acquired for this system provides an accurate determination of this structure which could then be extended to various other rare earths ($Ba_3Ln_2O_5CO_3$) which were obtained either under normal conditions (Ln = Lu, Tm) or under a dry N_2 atmosphere (Ln = Er, Ho, Dy, Y). The rate of carbonate loss plays a pivotal role in the formation of these structures with reaction under a dry N_2 atmosphere reducing this rate making synthesis of these systems much more reliable.

Being more thermally stable, the sulphate equivalent phases $Ba_3Ln_2O_5(ZnO_2)_{0.33}(SO_4)_{0.67}$ (Ln = Yb, Tm, Er, Ho, Dy) systems were also discovered through solid state synthesis in air at 1150°C. The addition of zinc oxide is required to relieve strain brought about by the additional oxygen provided by the tetrahedral sulphate, which is believed to be due to it providing oxygen vacancies within the structure so the sulphate can be accommodated unhindered.

Carbonate was confirmed to be present in cobalt deficient $Ba_2(CoO_4)_{1-x}(CO_3)_x$ systems where a structural progression is seen from monoclinic to orthorhombic-like. Rietveld refinement using neutron diffraction, along with TGA-MS data provide evidence to support that carbonate can be readily introduced into these systems whilst Raman spectroscopy and thermal stability studies allowed increased understanding of these systems stabilities. Such additional studies noted evidence for the incorporation of water which may also play a pivotal role in the stabilisation of the cobalt deficient structures.

Investigations into the iron deficient $Ba_2(FeO_4)_{1-x}(CO_3)_x$ systems led to similar conclusions to those for the cobalt deficient systems, but more detailed neutron diffraction studies are still required for this system. By again synthesising a more thermally stable sulphate equivalent of the iron deficient systems $Ba_2(FeO_4)_{1-x}(SO_4)_x$, Raman spectroscopy and Rietveld refinement of XRD data confirmed that sulphate can be readily incorporated into these systems.

The borate $Sr_{4-x}Ba_xNa_{1-y}Li_y(BO_3)_3$ series was synthesised showing that lithium could be successfully substituted in amounts where $y \leq 0.5$. Furthermore, for the first time these systems were shown to have perovskite-like superstructure for all values of x. Higher amounts of lithium substitution ($y = 0.75, 1$) are seen to destabilise this structure due to the increase in cation size differences.

Whilst investigating potential systems isostructural to that of $Sr_{4-x}Ba_xNa_{1-y}Li_y(BO_3)_3$, a newly discovered related strontium/calcium system ($Sr_{2.2}Ca_{1.8}Li(BO_3)_3$) was found. Unlike its strontium/barium counterpart which has random distribution of the large cations, Rietveld refinement shows that this strontium/calcium system has ordering in a way that the calcium forms columns and rows throughout the structure.

Various initial investigations have shown how carbonate could potentially be an important factor in the stabilisation of low temperature phases of some oxide reagent materials (TiO_2, Nb_2O_5). TGA-MS studies indicate the loss of carbon dioxide (and hence the presence of carbonate) at temperatures where low temperature phase transitions are seen. Further work is however needed on these systems to conclusively evaluate the importance of this carbonate.

The focus of this thesis is to show how carbonate can be readily incorporated into new and known materials. The findings presented in this work provide evidence in support of carbonate incorporation in a range of materials, although difficulty is seen in controlling the amount of carbonate incorporation involved when heated in air. Therefore great care must be taken (especially regarding solid state synthesis) when attempting synthesis in air at temperatures ≤1000°C as carbonate could very well be present. Therefore appropriate analytical techniques such as Raman spectroscopy, IR spectroscopy and TGA-MS should be routinely employed and used in conjunction with structural characterisation for a complete and accurate understanding of any oxide material synthesised under regular conditions.

Some of systems described in this work may hold potential for further studies as investigation for the applicability of solid-state electrolytes. Whilst the carbonate systems ($Ba_3Ln_2O_5CO_3$, $Ba_2(CoO_4)_{1-x}(CO_3)_x$, $Ba_2(FeO_4)_{1-x}(CO_3)_x$) systems would be unsuitable for this application due to low degradation temperature the sulphate equivalents may be of some interest. Due to the yet unknown orientation of sulphate in the $Ba_3Ln_2O_5(ZnO_2)_{0.33}(SO_4)_{0.67}$ systems, these may be of interest of an oxide ion conducting electrolyte, with oxygen vacancies on the central layer of this system and improved thermal stability this may be something that may want to be investigated. In the same respect, the $Ba_2(FeO_4)_{1-x}(SO_4)_x$ may also be of interest as use of an oxide ion conductor. As mentioned, the $Ba_2(FeO_4)_{1-x}(SO_4)_x$ systems may also be incorporating water, it is this possibility that may also warrant an investigation into the proton conduction of these systems. Due to having highly ordered structures of $Sr_{4-x}Ba_xNa_{0.5}Li_{0.5}(BO_3)_3$ systems, these would be unsuitable for oxide ion conductivity investigations.

7.2 Further Work

Lanthanide materials are well known for their luminescent properties mostly through an upconversion process.[239-244] It would be interesting to perform luminescence studies upon the $Ba_3Yb_2O_5CO_3$ system by the substitution of small amount of Erbium for Ytterbium.

To accurately determine the structure of the $Ba_3Ln_2O_5(ZnO_2)_{0.33}(SO_4)_{0.67}$, neutron diffraction data are required to determine accurate oxygen orientations around the zinc and sulphur and help to distinguish if each layer is now shared between Ln/Zn/S. The luminescence study could also be implemented for the ytterbium system as previously described. Investigation into oxide ion conductivity of these systems could be attempted to determine any potential.

Further structural characterisation is required for the iron deficient $Ba_2(FeO_4)_{1-x}(CO_3)_x$ systems. Acquisition of neutron diffraction data will help determine accurate positions for the carbonate atoms in these iron systems, whilst also helping to clarify any partial occupancies of carbon/iron sharing similar sites as with the cobalt deficient systems. Similarly Mössbauer spectroscopy studies would allow greater information about the Fe oxidation state and environment.

Regarding the sulphate incorporated iron deficient $Ba_2(FeO_4)_{1-x}(SO_4)_x$ systems, further studies, such as VT-XRD and TGA-MS, could help provide insight into the formation of these systems as well as clarify the existence of any water and carbonate present in the structure. The acquisition of neutron diffraction data and Fe Mössbauer spectroscopy data would also help to provide a more accurate and detailed structure. Investigation into oxide ion and proton conductivity of these systems could be attempted to determine any potential.

Given the prior interest in the luminescent properties of lanthanide doped $Sr_{4-x}Ba_xNa(BO_3)_3$[245-250] , these systems warrant further investigation in this respect, particularly for the $Sr_{2.2}Ca_{1.8}Li(BO_3)_3$ system, which offers an interesting potential avenue to tuning properties by virtue of the two distinct alkaline earth sites.

With the potential that carbonate is present and helping to stabilise low temperature phases of some reagent oxide materials, a larger scale investigation is required, studying oxide reagents from various manufacturers paying close attention to methods used in the manufacturing processes. TGA-MS of differing oxide reagents with low temperature phase transitions, could help provide a relationship between the incorporation of small amounts of carbonate and an increased stability of these low temperature phases.

Publications List

J. Deakin, I. Trussov, A. Gibbs, E. Kendrick, P. R. Slater, *Carbonate: an alternative dopant to stabilize new perovskite phases; Synthesis and structure of* $Ba_3Yb_2O_5CO_3$ *and related isostructural phases* $Ba_3Ln_2O_5CO_3$ *(Ln=Y, Dy, Ho, Er, Tm and Lu),* Dalton Trans., 2018, **47**, 12901.

J. Deakin, P. R. Slater, *Synthesis and structure of the perovskite related* $Sr_{4-x}Ba_xNa_{1-y}Li_y(BO_3)_3$ *solid solution series and the related a site cation ordered* $(Sr/Ca)_4Li(BO_3)_3$ *system*, Journal of Solid State Chemistry, 2021, **294**, 121870.

S. W. Thomas, M. S. James, M. P. Stockham, J. Deakin, A Jarvis, P. R. Slater, *Synthesis of Borate Doped La 10 Ge 6 O 27 : Confirming the Presence of a Secondary Conducting Pathway*, ECS Meeting Abstracts, MA2021-03, **1**, 292.

J. Deakin, J.M. Porras-Vazquez, M.L. Sanjuán, A. Orera, P.R. Slater, *Synthesis and Structural Characterisation of* $Ba_2Co_{1-x}Oy$ *Phases: The Incorporation of Carbonate*. In Preparation

J. Deakin, P. R. Slater, *Synthesis and structure of the Zinc stabilised layered perovskite systems* $Ba_3Ln_2O_5(ZnO_2)_{0.33}(SO_4)_{0.67}$ *(Ln = Yb, Tm, Er, Ho, Dy)*. In Preparation

References

[1] Faraday and Schöebein, The Letters of Faraday and Schöenbein, Universidad de California, 1899.

[2] E. I. Ortiz, A. L. Reyes-Hernandez and R. A-Febo, I.E.E.E., 2007.

[3] J. M. Andujar and F. Segura, Renewable and Sustainable Energy Reviews, 2009, 13, 2309.

[4] Boudghene Stambouli and E. Traversa, Renewable and Sustainable Energy Reviews, 2002, 6, 433.

[5] J. Appleby, Journal of Power Sources, 1990, 29, 3.

[6] J. H. Lee, S. T. Baek, H. J. Jung, H. H. Kang, J. M. Chung and I. Y. Suh, International Conference of Electrical Machines and Systems, 2007, 1, 354.

[7] Khaligh, A. M. Rahimi, L. Young-Joo, C. Jian, A. Emadi, S. D. Andrews, C. Robinson and C. Finnerty, I.E.E.E. Transactions of Vehicular Technology, 2007, 56, 3709.

[8] M. Vasallo and J. M. Anduja, I.E.E.E. Transactions on Industrial Electronics, 2009.

[9] F. Segura, E. Durán and J. M. Andujar, Journal of Power Sources, 2008, 193, 276.

[10] U.S. Department of Energy, Fuel Cell Hand Book (7th Edition), 2000.

[11] M. Farooque and H. C. Maru, I.E.E.E. Proceedings, 2001, 89, 1819.

[12] M. W. Ellis, M. R. Von Spakovsky and D. J. Nelson, I.E.E.E. Proceedings, 2001, 89, 1808.

[13] L. Dick, Fuel Cells Compendium, 2005, 147.

[14] J. B. O'Sullivan, I.E.E.E. Proceedings, 1999, 568.

[15] Kirubakaran, J. Shailendra and R. K. Nema, Renewable and Sustainable Energy Reviews, 2009, 13, 2430.

[16] J. Pan, S. Lu, Y. Li, A. Huang, L. Zhuang and J. Lu, Advanced Functional Materials, 2009, 20, 312.

[17] J. P. P. Huijsmans, F. P. F. van Berkel and G. M. Christie, Journal of Power Sources, 1998, 71, 107.

[18] K. E. Swider-Lyons, R.T. Carlin, R. L. Rosenfeld and R. J. Nawak, Workshop on Autonomous Underwater Vehicle Proceedings, 2002, 61.

[19] M. W. Davidson and G. F. Lofgren, Journal of Geographical Education, 1991, 39, 403.

[20] N. P. Brandon, S. Skinner and B. C. H. Steele, Annual Review of Materials Research, 2003, 33, 183.

[21] L. L. Hench, D. E. Clark and A. B. Harker, Journal of Materials Science, 1986, 21, 1457.

[22] W. Piekarczyk, W. Weppner and A. Rabenau, Materials Research Bulletin, 1978, 13, 1077.

[23] J. L. Garcia-Munoz, J. Rodriquezcarvajal, P. Lacorre and J. B. Torrance, Physical Review B, 1992, 46, 4414.

[24] C. Li, K. C. K. Soh and P. Wu, Journal of Alloys and Compounds, 2004, 372, 40.

[25] M. T. Weller, Oxford Chemistry Primers, 1994.

[26] S. Svarcova, K. Wiik, J. Tolchard, H. J. M. Bouwmeester and T. Grande, Solid State Ionics, 2008, 178, 1787.

[27] C. J. Howard, B. J. Kennedy and B. C. Chakoumakos, Journal of Physics, 2000, 12, 349.

[28] S. Sasaki, C. T. Prewitt, J. D. Bass and W. A. Schulze, Acta Crystallographica Section C, 1987, 43, 1668.

[29] P. Coppens and M. Eibschutz, Acta Crystallographica, 1965, 19, 524.

[30] A .M. Glazer, Acta Crystallographica, 1972, 28, 3384.

[31] O. Muller and R. Roy, Crystal Chemistry of Non-Metallic Materials, 1974.

[32] C. J. Howard and B. J. Kennedy, Journal of Physics, 1999, 11, 3229.

[33] T. Hashimoto, N. Tsuzuki, A. Kishi, K. Takagi, K. Tsuda, M. Tanaka, K. Oikawa, T. Kamiyama, K. Yoshida, H. Tagawa and M. Dokiya, Solid State Ionics, 2000, 132, 181.

[34] J. Lander, Acta Crystallographica, 1951, 4, 148.

[35] S. Geller and P. Romo, Acta Crystallographica, 1967, 124, 136.

[36] H. Iwahara, T. Yajima, T. Hibino, K. Ozaki and H. Suzuki, Solid State Ionics, 1993, 61, 65.

[37] S. A. Speakman, J. W. Richardson, B. J. Mitchell and S. T. Misture, Solid State Ionics, 2002, 149, 247.

[38] J. F. Shin, A. Orera, D. C. Apperley and P. R. Slater, Journal of Materials Chemistry, 2010, 874.

[39] J. B. Goodenough, J. E. Ruizdiaz and Y. S. Zhen, Solid State Ionics, 1990, 44, 21.

[40] S. N. Ruddlesden and P. Popper, Acta Crystallogr., 1957, 10, 538.

[41] S. N. Ruddlesden and P. Popper, Acta Crystallogr., 1958, 11, 54.

[42] B. V. Beznosikov and K. S. Aleksandrov, Crystallogr. Rep., 2000, 45, 792.

[43] X. Xu, Y. Pan, Y. Zhong, R. Ran, Z. Shao, Mater. Horiz., 2020, 7, 2519

[44] X. L. Wang, H. Sakurai, E. Takayama-Muromachi, J. Appl. Phys., 2005, 97, 10M519

[45] H. J. Mattausch, H. K. Müller-Buschbaum, Z. Anorg. Allg. Chem., 1971, 386

[46] J. R. Gunter, G. B. Jameson, Acta Crystallogr., Sect. C: Cryst. Struct. Commun., 1984, 40, 207

[47] J. B. Goodenough, Nature, 2000, 404, 821

[48] P.R. Slater, J. E. H. Sansom, J. R. Tolchard, The Chemical Record, 2004, 4, 6, 373

[49] N. Agmon, Chemical Physical Letter, 1995, 244, 456.

[50] S. Q. Hui, J. Roller, S. Yick, X. Zhang, C. Deces-Petit, Y. S. Xie, R. Maric and D. Ghosh, Journal of Power Sources, 2007, 172, 493.

[51] W. Smith, F. W. Meszaros and C. D. Amata, Journal of the American Chemical Society, 1966, 49, 240.

[52] L. D. Burke, H. Rickert and R. Steiner, Journal of Physical Chemistry, 1971, 74, 146.

[53] T. I. Politova and J. T. S. Irvine, Solid State Ionics, 2004, 168, 153.

[54] K. Kitazawa and R. L. Coble, Journal of the American Chemical Society, 1974, 57, 360.

[55] Tarancon, S. J. Skinner, R. J. Chater, F. Hernandez-Ramirez and J. A. Kilner, Journal of Materials Chemistry, 2007, 17, 3175.

[56] P. Plonczak, M. Gazda, B. Kusz and P. Jasinski, Journal of Power Sources, 2008, 181, 1.

[57] Y. Shimakawa, Inorganic Chemistry, 2008, 47, 8562.

[58] L. Qiu, T. Ichikawa, A. Hirano, N. Imanishi and Y. Takeda, Solid State Ionics, 2003, 158, 55.

[59] J. Tulloch and S. W. Donne, Journal of Power Sources, 2009, 188, 359.

[60] K. Zheng, B. C. H. Steele, M. Sahibzada and I. S. Metcalfe, Solid State Ionics, 1996, 86, 1241.

[61] K. Zheng, B. C. H. Steele, M. Sahibzada and I. S. Metcalfe, A. Rudkin, Catalysis Today, 1997, 38, 459.

[62] K. Q. Huang, M. Feng, J. B. Goodenough and M. Schmerling, Journal of Electrochemical Society, 1996, 143, 3630.

[63] J. M. Ralph, A. C. Schoeler and M. Krumpelt, Journal of Material Science, 2001, 36, 1161.

[64] H. Yokokawa, N. Sakai, T. Horita, K. Yamaji, M. E. Brito and H. Kishimoto, Journal of Alloys and Compounds, 2008, 452, 41.

[65] Mai, V. A. C. Haanappel, S. Uhlenbruck, F. Tietz and D. Stover, Solid State Ionics, 2005, 176, 1341.

[66] S. Yamaguchi and N. Yamada, Solid State Ionics, 2003, 162, 23.

[67] M. Y. Wang and L. G. Qiu, Chinese Journal of Chemical Physics, 2008, 21, 286.

[68] N. V. Sharova and V. P. Gorelov, Russian Journal of Electrochemistry, 2005, 41, 1001.

[69] E. Gorbova, V. Maragou, D. Medvedev, A. Demin and P. Tsiakaras, Journal of Power Sources, 2008, 181, 207.

[70] N. Maffei, L. Pelletier, J. P. Charland and A. McFarlan, Journal of Power Sources, 2006, 162, 165.

[71] C. Chen and G. L. Ma, Journal of Alloys and Compounds, 2009, 485, 69.

[72] N. I. Matskevich and T. A. Wolf, Journal of Chemical Thermodynamics, 2010, 42, 228.

[73] W. B. Wang, J. W. Liu, Y. D. Li, H. T. Wang, F. Zhang and G. L. Ma, Solid State Ionics, 2010, 181, 667.

[74] M. Y. Wang, L. G. Qiu and G. L. Ma, Chinese Journal of Chemistry, 2007, 25, 1273.

[75] J. L. Yin, X. W. Wang, J. H. Xu, H. T. Wang, F. Zhang and G. L. Ma, Solid State Ionics, 2011, 185, 6.

[76] L. G. Qiu and M. Y. Wang, Chinese Journal of Chemical Physics, 2010, 23, 707.

[77] N. I. Matskevich, T. Wolf, M. Y. Matskevich and T. I. Chupakhina, European Journal of Inorganic Chemistry, 2009, 1477.

[78] F. Giannici, A. Longo, A. Balerna, K. D. Kreuer and A. Martorana, Chemistry Materials., 2007, 19, 5714.

[79] Radojkovic, M. Zunic, S. M. Savic, G. Brankovic and Z. Brankovic, Ceramics International, 2013, 39, 307.

[80] R. Chen, M. Greenblatt, L. A. Bendersky, Chem. Mater., 2001, 13, 11, 4094

[81] Jarvis, F. J. Berry, J. F. Marco, M. Sanchez-Arenillas, G. Cibin, O. Clemens, P. R. Slater, J. Solid State Chem., 2020, 287, 121372

[82] Greaves and P. R. Slater, Physica C, 1991, 175, 172.

[83] Greaves and P. R. Slater, Journal of Material Chemistry, 1991, 1, 17.

[84] P. R. Slater, C. Greaves, M. Slaski and C. M. Muirhead, Physica C, 1993, 208, 193.

[85] Y. Miyazaki, H. Yamane, N. Ohnishi, T. Kajitani, K. Hiraga, Y. Morii, S. Funahashi and T. Hirai, Physica C, 1992, 198, 7.

[86] Maignan, M. Hervieu, C. Michel and B. Raveau, Physica C, 1993, 208, 116.

[87] K. Kinoshita and T. Yamada, Nature, 1992, 357, 313.

[88] H. G. Vonschnering, L. Walz, M. Schwarz, W. Becker, M. Hartweg, T. Popp, P. Hettich, P. Muller and G. Kampf, Angewandte Chemie International Edition in English, 1988, 27, 574.

[89] T. G. N. Babu, D. J. Fish and C. Greaves, Journal of Materials Chemistry, 1991, 1, 677.

[90] C. A. Hancock, J. M. Porras-Vazquez, P. J. Keenan and P. R. Slater, Dalton Transactions, 2015, 44, 10559

[91] M. G. Francesconi and C. Greaves, Superconductor Science and Technology, 1997, 10, A29.

[92] M. Uehara, H. Nakata and J. Akimitsu, Physica C, 1993, 216, 453.

[93] D. M. Deleeuw, C. Mutsaers, C. Langereis, H. C. A. Smoorenburg and P. J. Rommers, Physica C, 1988, 152, 39.

[94] M. Kikuchi, E. Ohshima, M. Kikuchi, T. Atou and Y. Syono, Physica C, 1994, 232, 263.

[95] Y. Miyazaki, H. Yamane, T. Kajitani, N. Kobayashi, K. Hirage, Y. Morii, S. Finahashi and T. Hirai, Physica C, 1994, 230, 89.

[96] J. Akimitsu, M. Uehara, M. Ogawa, H. Nakata, Y. Miyazaki, H. Yamane, T. Hirai, K. Kinoshita and Y. Matsui, Physica C, 1992, 201, 320.

[97] B. Domenges, M. Hervieu and B. Raveau, Physica C, 1995, 207, 65.

[98] N. Ohnishi, Y. Miyazaki, H. Yamane, T. Kajitani, T. Hirai and K. Hiraga, Physica C, 1995, 207, 175.

[99] T. Den, T. Kobayashi and J. Akimitsu, Physica C, 1993, 208, 351.

[100] J. F. Shin, L. Hussey, A. Orera and P. R. Slater, Chemical Communications, 2010, 46, 4613.

[101] J. F. Shin, D. C. Apperley and P. R. Slater, Chemistry of Materials, 2010, 22, 5945.

[102] G. B. Zhang and D. M. Smyth, Solid State Ionics, 1995, 82, 153.

[103] T. Schober, J. Friedrich and F. Krug, Solid State Ionics, 1997, 99, 9.

[104] T. Q. Ta, T. Tsuji and Y. Yamamura, Journal of Alloys and Compounds, 2006, 253, 408.

[105] T. Schober, Solid State Ionics, 1998, 1, 109.

[106] V. Jayaraman, A. Magrez, M. Caldes, O. Joubert, M. Ganne, Y. Piffard and L. Brohan, Solid State Ionics, 2004, 17, 170.

[107] Rolle, R. N. Vannier, N. V. Giridharan and F. Abraham, Solid State Ionics, 2005, 176, 2095.

[108] K. Kakinuma, H. Yamamura, H. Haneda and T. Atake, Solid State Ionics, 2001, 140, 301.

[109] H. Yamamura, Y. Yamada, T. Mori and T. Atake, Solid State Ionics, 1998, 108, 377.

[110] M. Aoki, Y. M. Chiang, I. Kosacki, I. J. R. Lee, H. Tuller and Y. P. Liu, Journal of American Ceramic Society, 1996, 79, 1169.

[111] S. P. S. Badwal, F. T. Ciacchi, S. Rajendran and J. Drennan, Solid State Ionics, 1998, 109, 167.

[112] C. C. Appel and N. Bonanos, Journal of the European Ceramic Society, 1999, 19, 847.

[113] J. F. Shin, K. Joubel, D. C. Apperley and P. R. Slater, Dalton Transactions, 2012, 41, 261.

[114] A. D. Smith, J. F. Shin and P. R. Slater, Journal of Solid State Chemistry, 2013, 198, 247.

[115] V. Caignaert, B. Domenges and B. Raveau, Journal of Solid State Chemistry, 1995, 120, 279.

[116] D. Pelloquin, M. Hervieu, C. Michel, N. Nguyen and B. Raveau, Journal of Solid State Chemistry, 1997, 134, 395.

[117] Y. Breard, C. Michel, M. Hervieu and B. Raveau, Journal of Materials Chemistry, 2000, 10, 1043.

[118] Y. Breard, C. Michel, M. Hervieu, N. Nguyen, A. Ducouret, V. Hardy, A. Maignan, B. Raveau, F. Bouree and G. Andre, Chemistry of Materials, 2004, 16, 2895.

[119] B. Raveau, M. Hervieu, D. Pelloquin, C. Michel and R. Retoux, Journal of Inorganic and General Chemistry, 2005, 631, 1831.

[120] J. A. Bland, Acta Crystallogr., 1961, 14, 875

[121] A. R. West, Solid State Chemistry and its Applications, Wiley and Sons, 2005

[122] C. J. Brinker and G. W. Scherer, Sol-gel Science: the Physics and Chemistry of Sol-gel Processing, Academic Press, Boston, 1993.

[123] R. J. D. Tilley, Crystals and Crystal Structures, John Wiley & Sons, Chichester, 2007.

[124] V. K. Pecharsky and P. Y. Zavalij, Fundamentals of Powder Diffraction and Structural Characterization of Materials, Springer, New York, 2009.

[125] https://cnx.org/contents/6Q1RYWaw@10/Crystal-Structure

[126] H. Rietveld, Journal of Applied Crystallography, 1969, 2, 65.

[127] L. B. McCusker, R. B. Von Dreele, D. E. Cox, D. Louer and P. Scardi, Journal of Applied Crystallography, 1999, 32, 36.

[128] R. Von, Journal of Applied Crystallography, 1997, 30, 517.

[129] S. A. Maher Raman Spectroscopy for Soft Matter Application, Wiley and Sons, New York, 2008.

[130] P. J. Haines, Principles of Thermal Analysis and Calorimtery, Royal Society of Chemistry, Cambridge, 2002.

[131] C. Greaves, P. R. Slater, J. Mater. Chem., 1991, 1, 17.

[132] C. Greaves, P. R. Slater, Physica C, 1991, 175, 172.

[133] P. R. Slater, C. Greaves, M. Slaski, C. M. Muirhead, Physica C, 1993, 208, 193.

[134] A. Maignan, M. Hervieu, C. Michel, B. Raveau, Physica C, 1993, 208, 116.

[135] K. Kinochita, T. Yamada, Nature, 1992, 357, 313.

[136] M. G. Francesconi, C. Greaves, Supercond. Sci. & Technol., 1997, 10, A29.

[137] M. Uehara, H. Nakata, J. Akimitsu, Physica C, 1993, 216, 453.

[138] R. Li, R.K. Kremer, J. Maier, J. Solid State Chem., 1993, 105, 609.

[139] Y. Miyazaki, H. Yamane, T. Kajitani, N. Kobayashi, K. Hiraga, Y. Morii, S. Funahashi, T. Hirai, Physica C, 1994, 230, 89.

[140] J. Akimitsu, M. Uehara, M. Ogawa, H. Nakata, K. Tomimoto, Y. Miyazaki, H. Yamane, T. Hirai, K. Kinoshita, Y. Matsui, Physica C, 1992, 201, 320.

[141] B. Domenges, M. Hervieu, B. Raveau, Physica C, 1993, 207, 65.

[142] Y. Shimakawa, J. D. Jorgensen, D. G. Hinks, H. Shaked, R. L. Hitterman, Phys. Rev. B, 1994, 50, 16008.

[143] C.A. Hancock, J.M. Porras-Vazquez, P.A. Keenan, P.R. Slater, Dalton Trans., 2015, 44, 10559.

[144] V. Caignaert, B. Domenges, B. Raveau, J. Solid State Chem., 1995, 120, 279.

[145] D. Pelloquin, M. Hervieu, C. Michel, N. Nguyen, B.Raveau, J. Solid State Chem., 1997, 134, 395.

[146] M. Hervieu, C. Michel, D. Pelloquin, A. Maignan, B. Raveau, J. Solid State Chem., 2000, 149, 226.

[147] Y. Breard, C. Michel, M. Hervieu, N. Nguyen, A. Ducouret, V. Hardy, A. Maignan, B. Raveau, F. Bouree, G. Andre, Chem. Mater., 2004, 16, 2895.

[148] B. Raveau, M. Hervieu, D. Pelloquin, C. Michel, R. Retoux, Z. Anorg. Allg. Chem., 2005, 631, 1831.

[149] J. F. Shin, L. Hussey, A. Orera, P. R. Slater, Chem. Commun., 2010, 46, 4613.

[150] J. F. Shin, D. C. Apperley, P.R. Slater, Chem. Mater., 2010, 22, 5945.

[151] J. F. Shin, P. R. Slater, J. Power Sources, 2011, 196, 8539.

[152] C. A. Hancock, R. C. T. Slade, J. R Varcoe, P. R Slater, J. Solid State Chem., 2011, 184, 2972.

[153] J. M. Porras-Vazquez, P. R. Slater, J. Power Sources, 2012, 209, 180.

[154] J. M. Porras-Vazquez, T. F. Kemp, J. V. Hanna, P. R. Slater, J. Mater. Chem., 2012, 22, 8287.

[155] J. M. Porras-Vazquez, P. R. Slater, Fuel Cells, 2012, 12, 1056.

[156] C. A. Hancock, P. R. Slater, Dalton Trans., 2011, 40, 5599.

[157] J. M. Porras-Vazquez, E. R. Losilla, P. J. Keenan, C. A. Hancock, T. F. Kemp, J. V. Hanna, P. R. Slater, Dalton Trans., 2013, 42, 5421.

[158] J. M. Porras-Vazquez, T. Pike, C. A. Hancock, J. F. Marco, F. J. Berry, P. R. Slater, J. Mater. Chem. A, 2013, 1, 11834.

[159] J. M. Porras-Vazquez, R. I. Smith, P. R. Slater, J. Solid State Chem., 2014, 1, 132.

[160] J. F. Shin, K. Joubel, D. C. Apperley, P. R. Slater, Dalton Trans., 2012, 41, 261.

[161] J. F. Shin, A. Orera, D. C. Apperley, P. R. Slater; J. Mater. Chem., 2011, 21, 874.

[162] A. D. Smith, P. R. Slater, Inorganics, 2014, 2, 16.

[163] B. H. Toby, R. B. Von Dreele, J. Appl. Crystallogr., 2013, 46, 544.

[164] Buzgar, Nicolae & Apopei, Andrei., Anal. Şt. Univ. „Al. I. Cuza” Iaşi., 2009, LV, 97.

[165] R. D. Shannon, Acta Crystallographica, 1976, A32, 751.

[166] V. V. Halyan, I. A. Ivanshchenko, IntechOpen, 2018, 81445.

[167] Omori. K., Mineralogical Journal, 1968, 5, 334

[168] A. Choudhury, H. Chandra, A. Arora, Renew. Sust. Energ. Rev., 2013, 20, 430.

[169] S. D. Peter, e. Garbowski, N. Guilhaume, V. Perrichon, M. Primet, Catalysis Letters, 1998, 54, 79.

[170] D. Dalz, K. Plieth, Z. Elektrchem, 1955, 59, 545.

[171] M. T. Robinson, J. Phys. Chem., 1958, 62, 925.

[172] N. Hamao, N. Kitamura, N. Ishida, T. Kamiyama, S. Torii, M. Yonemura, Y. Idemoto, Electrochem., 2014, 82, 550.

[173] N. Hamao, N. Kitamura, T. Itoh, N. Igawa, Y. Idemoto, Solid State Ionics, 2013, 253, 123.

[174] N. Jalarvo, L. Stingaciu, D. Gout, Z. Bi, M.P. Paranthaman, M. Ohl, Solid State Ionics, 2013, 252, 12.

[175] N. Jalarvo, O. Gourdon, Z. Bi, D. Gout, M. Ohl, M. P. Paranthaman, Chem. Mater., 2013, 25, 2741.

[176] E. Kendrick, J. Kendrick, A. Orera, M. Panchmatia, M. S. Islam, P. R. Slater, Fuel Cells, 2011, 11, 38.

[177] F. Giannici, D. Messana, A. Longo, A. Martorana, J. Phys. Chem. C., 2011, 115, 298.

[178] A. Orera, P. R. Slater, Chem. Mater., 2010, 22, 675.

[179] E. Kendrick, K. S. Knight, M. S. Islam, P. R. Slater, J. Mater. Chem., 2010, 20, 10412.

[180] N. Kitamura, T. Usukim Y. Idemoto, Electrochem., 2009, 77, 158.

[181] E. Kendrick, J. Kendrick, K. S. Knight, M. S. Islam, P. R. Slater, Nat. Mater., 2007, 6, 871.

[182] P. L. Russo, J. Sugiyama, J. H. Brewer, E. J. Ansaldo, S. L. Stubbs, K. H. Chow, R. Y. Jin, H. Shas, J. Zhang, Phys. Rev. B., 2009, 80, 104421.

[183] H. J. Koo, K. S. Lee, M. H. Whangbo, Inorg. Chem., 2009, 45, 10743.

[184] K. Boulahya, M. Parras, J. M. Gonzalez-Calbet, U. Amador, J. L. Martinez, M. T. Fernandez-Diaz, Chem. Mater., 2006, 18, 3898.

[185] R. Jin, H. Sha, P. G. Khalifa, R. E. Sykora, B. C. Sales, D. Mandrus, J. Zhang, Phys. Rev. B., 2006, 73, 174404.

[186] K. Boulahya, M. Parras, A. Vegas, J. M. Gonzalez, Solid State Sci., 2000, 2, 57.

[187] J. A. Bland, Acta Crystallogr., 1961, 14, 875.

[188] J. Li, A. E. Smith, P. Jiang, J. K. Stalick, A. W. Sleight, M. A. Subramanian, Inorg. Chem., 2015, 54, 837.

[189] A. J. McSloy, I. Trussov, A. Jarvis, D. J. Cooke, P. R. Slater, P. M. Panchmatia, J. Phys. Chem. C., 2018, 122, 1061.

[190] J. Deakin, I. Trussov, A. Gibbs, E. Kendrick, P. R. Slater, Dalton Trans., 2018, 47, 12901.

[191] K. Boulahya, U. Amador, M. Parras, J. M. Gonzalez-Calbet, Chem. Mater, 2000, 12, 966.

[192] W. Acuna, J. F. Tellez, M. A. Macias, P. Roussel, S. Ricote, G. H. Gauthier, Solid State Sciences, 2017, 71, 61.

[193] L. Wu, X. L. Chen, H. Li, M. He, Y. P. Xu, X. Z. Li, Inorg. Chem., 2005, 44, 6409.

[194] J. Huang, J. Dai, D. Deng, H. Yu, Y. Li, Y. Hua, S. Zhao, C. Li, S. Xu, RSC Adv., 2015, 5, 85682.

[195] X. Zhang, X. Qiao, H. J. Seo, Current Applied Physics, 2011, 11, 442.

[196] I. Pekgozlu, Optik, 127 (2016), 4114.

[197] Z. W. Zhang, X. Y. Sun. L. Liu, Y. S. Peng, X. H. Shen, W. G. Zhang, D. J. Wang, Ceramics International, 2013, 39, 1723.

[198] I. Pekgozlu, Journal of Luminescence, 2016, 169, 182.

[199] C. Greaves, S. M. A. Katib, J. Solid State Chem., 1990, 84, 82.

[200] J. A. Alonso, E. Mzayek, I. Rasines, Mater. Res. Bull., 1987, 69.

[201] A. Jarvis, P. R. Slater, Crystals, 2017, 7, 169

[202] Li Rukang, R. K. Kremer, J. Maier, J. Sold State Chem., 2013, 105, 609.

[203] P. R. Slater, C. Greaves, Physica C, 1993, 215, 191.

[204] R. Mahesh, R. Nagarajan, C. N. R. Rao, Solid Sate Commun., 1994, 90, 435.

[205] J. P. Chapman, W. Z. Zhou, J. P. Attfield, J. Alloys Compd., 1997, 261, 187.

[206] E. Takayama-Muromachi, Y. Matsui, K. Kosada, Physica C, !995, 241, 137.

[207] E. Takayama-Muromachi, Y. Matsui, J. Ramirez-Catellanos, Physica C, 1995, 252, 221.

[208] E. A. Donlan, H. L. B. Boström, H. S. Gedded, E. M. Reynolds, A. L. Goodwin, Chem. Commun., 2017, 53, 11236.

[209] H. L. B. Boström, J. Bruckmoser, A. L. Goodwin, J. Am. Chem. Soc., 2019, 141, 45, 17978.

[210] S. Yamauchi, S. Doi, J. Wood Sci., 2003, 49, 227-234

[211] A. K. Yadav, P. Singh, RSC Adv., 2015, 5, 67583

[212] [213]M. Iliescu, V. Nelea, J. Werckmann, G. Socol, I.N. Mihailescu, I. Mayer, F.Cuisinier, Mater. Sci. Eng., 2007, C27, 105.

[213] A. Yasukawa, S. Ouchi, K. Kandori, T. Ishikawa, J. Mater. Chem., 1996, 6, 1401.

[214] I.R. Gibson, W. Bonfield, J. Mater. Sci. Mater. Med., 2002, 13, 685.

[215] S.B. Abdelkader, I. Khattech, C. Rey, M. Jemal, Thermochim. Acta., 2001, 37625.

[216] J. Mayer, R. Schlam, D.B. Featherstone, J. Inorg. Biochem., 1997, 66, 1.

[217] S.M. Barinov et al., Mater. Res. Bull., 2006, 41, 485.

[218] R.Z. Legeros, T. Sakae, C. Bautista, M. Retino, J.P. Legeros, Adv. Dent. Res., 1996, 10, 225.

[219] D. Eichert, C. Combes, C. Drouet, C. Rey, Key Eng. Mater., 2005, 3, 284.

[220] T. B. Ghosh, S. Dhabal, A. K. Datta, J. Appl. Phys., 2003, 94, 4577.

[221] G. Li, L. Li, J. Boerio-Goates, B. F. Woodfield, J. Am. Chem. Soc., 2005, 127, 8659.

[222] M. Hirano, N. Nakahara, K. Ota, O. Tanaike, N. Inagaki, J. Solid State. Chem., 2003, 170, 39.

[223] O. Carp, C. L. Huisman, A. Reller, Prog. Solid State Chem., 2004, 21, 33.

[224] J. Kim, K. C. Song, S. Foncillas, S. Pratsinis, J. Eur. Ceram. Soc., 2001, 21, 2863.

[225] R. D. Shannon, J. A. Pask, J. Am. Ceram. Soc., 2000, 48, 391.

[226] H. Zhang, J. F. Banfield, J. Mater. Res., 2000, 15, 437.

[227] P. I. Gouma, M. J. Mills, J. Am. Ceram. Soc., 2001, 84, 619.

[228] Z. Jing, X. Qian, F. Zhaochi, L. Meijun, L. Can, Angew Chem. Int. Ed., 2008, 47, 1766.

[229] F. Holtzberg, A. Reisman, M. Berry, M. Berkenblit, J. Am. Chem. Soc., 1957, 79, 2039.

[230] G. Brauer, Z. Anorg. Allg. Chem., 1941, 248, 1.

[231] I. Nowak, A. M. Ziolek, Chem. Rev. , 1999, 99, 3603.

[232] M. Palanitkov, O. Shcherbina, N. Sidorov, K. Bormanis, Ukr. J. Phys. Opt., 2012, 13, 207.

[233] W. Wertin, S. Andersson, R. Gruehn, J. Solid State Chem., 1970, 1, 419.

[234] S. Georges, F. Goutenoire, F. Altorfer, D. Sheptyakov, F. Fauth, E. Suard, P. Lacorre, Solid State Ionics, 2003, 161, 231.

[235] T. Paul, A. Ghosh, J. Appl. Phys. 2018, 124, 225102.

[236] T. Paul, A. Ghosh, J. Alloys Compd., 2014, 613, 146.

[237] T. Paul, A. Ghosh, J. Appl. Phys. 2018, 123, 045107.

[238] B. M. van der Ende, L. Aarts, and A. Meijerink, Adv. Mater., 2009, 21, 3073.

[239] L. Xie, Y. Wang, and H. Zhang, Appl. Phys. Lett., 2009, 94, 061905.

[240] P. Vergeer, T. J. H. Vlugt, M. H. F. Kox, M. I. den Hertog, J. P. J. M. van der Eerden, and A. Meijerink, Phys. Rev. B, 2005, 71, 014119.

[241] Z. Liu, J. Li, L. Yang, Q. Chen, Y. Chu, and N. Dai, Sol. Energy Mater. Sol. Cells, 2014, 122, 46.

[242] J. Chen, H. Zhang, F. Li, and H. Guo, Mater. Chem. Phys., 2011, 128, 191.

[243] D. C. Yu, F. T. Rabouw, W. Q. Boon, T. Kieboom, S. Ye, Q. Y. Zhang, and A. Meijerink, Phys. Rev., 2014, B 90, 165126.

[244] N. S. Bajaj, S. K. Omanwar, Journal of Luminescence, 2014, 148, 169.

[245] L. Wu, Y. Zhang, M. Gui, P. Lu, L. Zhao, S. Tian, Y. Kong, Jing jun, J. Mater. Chem., 2012, 22, 6463.

[246] X. Zhang, H. Lang, H.J. Seo, J. Fluoresc. 2011, 21 1111.

[247] X. Zhang, X. Qiao, H.J. Seo, Curr. Appl. Phys., 2011, 11, 442.

[248] X. Ding, H. Liang, D. Hou, S. Jia, Q. Su, S. Sun, Y. Tao., J. Phys. D: Appl. Phys, 2012, 45, 365301.

[249] C.F. Guo, X. Ding, H.J. Seo, Z.Y. Ren, J.T. Bai, J. Alloys Compd., 2011, 509 4871.

[250] J. Deakin, P. R. Slater, Journal of Solid State Chemistry, 2021, 294, 121870.